Dynamic Modeling and Performance Analysis of Rotary Drilling Systems with a Downhole Passive Regulator

Arviandy Gustrianto Aribowo

The work described in this thesis was carried out in the Dynamics and Control (D&C) research group under the Department of Mechanical Engineering at the Eindhoven University of Technology (TU/e). This research was supported by the Ministry of Finance of the Republic of Indonesia through the Indonesia Endowment Fund for Education (LPDP) program under grant no. PRJ-4653/LPDP.3/2016 and the Norwegian company Tomax AS.

The research reported in this thesis is part of the research program of the Dutch Institute of Systems and Control (DISC). The author has successfully completed the educational program of the Graduate School DISC.

A catalogue record is available from the Eindhoven University of Technology Library.
ISBN: xxx-xx-xxx-xxxx-x

Typeset by the author using LaTeX 2_ε and LyX.

Cover Design: Arviandy Gustrianto Aribowo
Reproduction: Ipskamp Printing, Enschede, The Netherlands

Dynamic Modeling and Performance Analysis of Rotary Drilling Systems with a Downhole Passive Regulator

PROEFSCHRIFT

ter verkrijging van de graad van doctor aan de
Technische Universiteit Eindhoven, op gezag van de
rector magnificus, prof.dr. S.K. Lenaerts, voor een
commissie aangewezen door het College voor
Promoties, in het openbaar te verdedigen
op donderdag 17 oktober 2024 om 13.30 uur

door

Arviandy Gustrianto Aribowo

geboren te Madioen, Oost-Java, de Republiek Indonesië

Dit proefschrift is goedgekeurd door de promotoren en de samenstelling van de promotiecommissie is als volgt:

voorzitter:	prof.dr.ir L.E. Govaert
1e promotor:	prof.dr.ir. N. van de Wouw
2e promotor:	prof.dr. E. Detournay (University of Minnesota)
leden:	prof.dr.-ing.habil. R.I. Leine (University of Stuttgart)
	prof.dr. W.H.A. Schilders
	prof.dr.ir. A.V. Pavlov (Norwegian University of Science and Technology)
	prof.dr. B. Balachandran (University of Maryland)
adviseur:	ing. N. Reimers (Tomax AS)

Het onderzoek dat in dit proefschrift wordt beschreven is uitgevoerd in overeenstemming met de TU/e Gedragscode Wetenschapsbeoefening.

Summary

Dynamic Modeling and Performance Analysis of Rotary Drilling Systems with a Downhole Passive Regulator

The exploration and production of energy resources (i.e., hydrocarbon-, geothermal-based) trapped in the subsurface rock formations require drilling deep well-bores. Besides, in an effort to mitigate the effects of global climate change by reducing CO_2 emission into the atmosphere, the sequestration of CO_2 in depleted hydrocarbon reservoirs is being developed at an industrial scale. Injection of CO_2 in the subsurface also requires extensive drilling of boreholes.

For all these purposes of drilling, it is essential that the rate-of-penetration (ROP) is increased to minimize the cost of operation. To this end, innovative drilling technologies have been pursued within the energy industry. One of such technologies, which is the focus of this research, is the downhole regulator AST developed by Tomax AS – a Norwegian drilling supporting service company. This regulator is installed in the bottom-hole-assembly (BHA, the lower part of the drill-string), about $40-60$ m above the drill-bit. By design, the main components of AST consist of an internal preloaded spring and a helical spline designed with a particular lead angle and radius. Based on reported field results, use of the AST significantly improves the drilling performance in deviated well-bore and in heterogeneous rock formations.

Recent research efforts have shed some lights on the mechanisms by which this downhole regulator enables the increase in drilling performance for vertical boreholes and homogeneous rock formations. However, some open challenges still exist, particularly related on understanding how such performance increase can also be expected when drilling deviated well-bores and/or drilling in interbedded formations. Also, the lumped-parameter model of the drill-string, used so far to analyze the role of the AST, fails to capture the complex, distributed dynamics of the drill-string. Therefore, this thesis primarily contributes to the dynamic modeling of drilling systems equipped with the AST in the separated cases involving deviated well-bore, heterogeneous rock formations, and/or distributed dynamics of the drill-string. Development of the necessary numerical tools and the associated performance analyses are also performed to reveal the underlying mechanisms of such performance increase with the regulator.

The thesis consists of three main parts. In the first part, dynamic models of the drill-string system with and without AST are developed for the case of deviated drilling trajectory in a homogeneous rock formation. In particular, this drilling scenario induces frictional contact between the BHA and the borehole wall. A lumped-parameter (discrete) modeling approach is employed to focus on the first dominant modes of the axial and torsional dynamics of the drilling system, which are coupled at the bit-rock interface as well as at the downhole regulator. This leads to models formulated in terms of discontinuous delay differential equations with state-dependent delays. Time stepping-based methods are formulated to conduct numerical analysis of these models. Moreover, the effect of AST on drilling performance is evaluated for varying deviation angles of the drilling trajectory. This analysis shows that the downhole regulator can also improve drilling performance significantly with deviated well scenarios. In addition, a study of the tool design concluded that lowering the stiffness value of the AST internal spring can improve drilling performance, while the optimal lead angle of the helical spline for drilling performance is achieved at 30°.

In the second part of the thesis, the scenario of drilling in interbedded formations, i.e., drilling through rock layers with distinct properties, is considered. As a first step, novel bit-rock interface laws for a two-rock-layers system are constructed under a quasi-stationary drilling condition. These interface laws establish the relationship between the forces acting on the bit (namely, weight-on-bit and torque-on-bit) and the depth-of-cut as a function of the bit engagement in the two-layers system, which is treated as an evolution parameter. These interface laws take into account the bit shape profile. As a second step, these bit-rock interaction laws are employed to construct a dynamic (lumped-parameter) model for drilling systems in interbedded formations (for the cases with and without the downhole regulator). Using this model, the effect of AST on drilling performance is studied in the context of interbedded rock formations. In particular, the dynamic analyses on the limit-cycling behavior reveal how the increased axial vibrations induced by the AST lead to reduced frictional losses in the bit-rock interaction. This reduction in frictional dissipation leads to an increase of drilling performance. In addition, the so-called $E-S$ diagrams for drilling in interbedded formation are constructed to support the analysis on the effect of AST on drilling performance.

In the last part of the thesis, a distributed parameter model for the drill-string system with the AST is constructed. In this modeling framework, the drill-pipe is represented as a continuum model in the form of partial differential equations (PDEs), capturing all axial and torsional dynamic modes. The BHA is described by a discrete model governed by discontinuous ordinary differential equations (ODEs) and the evolution of the rock surface under the bit is characterized by a PDE. These sub-systems are assembled and form a discontinuous coupled PDE-ODE-PDE system model, including a non-smooth bit-rock interaction model.

Simulation-based studies on this model are pursued for cases without and with the AST, in which the drilling performance in both cases is analyzed. These numerical studies show that the use of the AST regulator can assist to improve the drilling performance and to decrease both the frictional loading at the drill-bit and the dynamic loading on the drill-string. Moreover, a robust performance-based design of the AST is investigated using the proposed model under the variations of drill-string and rock parameters. Based on the numerical studies, this AST design is robust in terms of drilling performance under a realistic parametric space of the drilling operations, the drill-string, and the rock formation.

As the final summary, the thesis presents novel models and dynamic analyses of the performance of drilling systems including a downhole regulator, in the presence of closer-to-real drilling conditions, such as deviated wells, interbedded formations, and distributed dynamics of long drill-string structure. It is shown that the downhole regulator consistently improves the rate of penetration and drilling efficiency.

Contents

Nomenclature

Acronyms and Abbreviations

BM model : Benchmark drill-string model (without the AST)

BHA : Bottom Hole Assembly

DOC : Depth of Cut

AST model : Drill-string model with the AST

EOM(s) : Equation(s) of motion

NPT : Non-Productive Time

ODE(s) : Ordinary Differential Equation(s)

PDE(s) : Partial Differential Equation(s)

PDC : Polycrystaline Diamond Compact

ROP : Rate of Penetration

RPM : Revolutions per minute

RGD model : Richard-Germay-Detournay model

TOB : Torque-On-Bit

TOI : Torque-On-Interface

WOB : Weight-On-Bit

Chapter 1

Introduction

Abstract - This chapter presents a high-level introduction to this thesis. It starts with a brief description of energy resources and the drilling process in Section 1.1, and describes drilling systems, the AST downhole regulator and the motivation for the research in this thesis in Section 1.2. Next, in Section 1.3, it provides a high-level literature review on dynamic modeling and analysis of (rotary) drilling systems without and with the presence of AST regulator and also on physical models for the bit-rock interaction. More detailed literature reviews on dedicated topics are included in the introductory sections of the individual chapters. This chapter also presents, in Sections 1.4 and 1.5, the objectives and main contributions of the thesis. A list of the publications is provided in Section 1.6. Finally, an outline of the thesis is given in Section 1.7.

1.1 Energy resources and drilling process

The exploration and production of the energy resources trapped in the subsurface rock formations have been an essential endeavour for the development of industry and society. Nevertheless, global climate change requires urgent reduction of CO_2 emissions into the atmosphere, which is now also gradually affecting current strategies of energy exploration and production (E&P) companies [11]. As such, both industry and society now recognize the urgent need for making the energy transition and for implementing specific targets and measures of carbon footprint reduction (decarbonization).

In the context of energy transition, renewable energy resources (such as wind and solar energies, but also geothermal energy) have been explored intensively and utilized gradually for heating and electrification [133, 61, 139, 161]. Such efforts work at the frontier of decreasing our dependencies on the conventional energy resources (e.g., crude oils, coals). Moreover, several examples of carbon footprint reduction strategies are the development of hydrogen-based resources (the so-called blue and green hydrogen energy generations) and carbon capture and sequestration (CCS). In the past decades, renewable hydrogen resources have been extensively explored as fuel and energy carriers that can be developed jointly with conventional energy resources and other renewable resources to form a hydrogen value chain [29]. In CCS, the CO_2 is sequestered in depleted hydrocarbon reservoirs where this process has also been developed to reach an industrial scale [130]. In addition, CCS can be potentially combined in the hydrogen value chain, particularly for producing the blue hydrogen.

To accommodate all the strategic purposes above, extensive drilling and well operations play important roles as the key to success in the exploration-production activities of (conventional) oil-gas and (renewable) geothermal reservoirs (as depicted in Figures 1.1 and 1.2, respectively) and also in the realization of the CO_2 emissions reduction via the injection of CO_2 in the subsurface on CCS projects (as depicted in Figure 1.3). In fact, already since the early 1900s drilling technologies have been developed extensively to produce oil and gas in both offshore and onshore fields. In such drilling operations, challenging well-bore trajectories often need to be created under highly uncertain and extreme environmental conditions related to the subsurface formations. For example, a drilling process in the Valemon gas and condensate field (located in the northern part of the North Sea within the Norwegian sector) has to manage the extraction of resources from the rock in high-pressure and high-temperature (HPHT) reservoirs with an expected reservoir pressure of 865 bar ($\approx 8.65 \times 10^7$ Pa) and reservoir temperature of 170°Celsius located at approximately 4423 m-TVDSS (meter-True Vertical Depth Sub Sea) [135].

Consequently, to recover resources from the subsurface, robust and reliable drilling technologies are required, particularly to deliver optimal drilling performance (e.g., in terms of rate of penetration and drilling efficiency) to warrant economically feasible operations and simultaneously ensure safe drilling processes. We care to stress that the reduction of drilling costs is an important factor in upscaling drilling technology for the development of geothermal energy and CCS, as drilling costs make up a significant portion of the total operational cost [138, 193].

1.2 Drilling systems and the AST downhole regulator

Rotary drilling systems with the Polycrystalline-Diamond-Compact (PDC) bit technology at the bottom-end, as depicted in Figure 1.4, is the common tool used for drilling process into the subsurface in the exploration and production of energy resources. PDC bits, as depicted in Figure 1.5, are recognized as the most efficient drill bit types [9]; yet they are prone to severe self-excited vibrations induced by the bit-rock interaction [54, 72].

In general, a rotary drilling system is composed of three major parts: a drilling

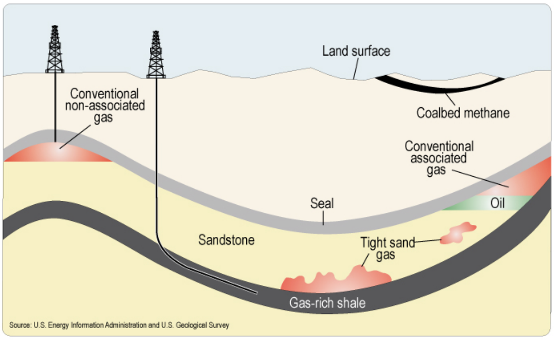

Figure 1.1: Hydrocarbon resources [176].

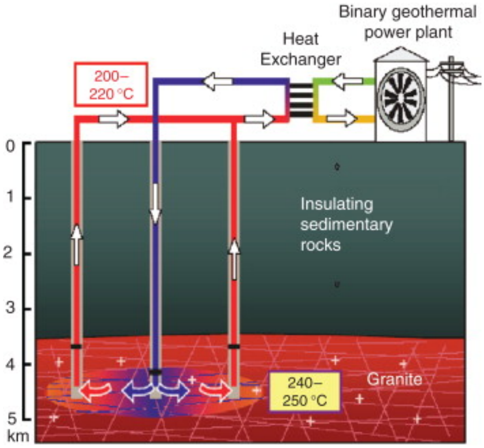

Figure 1.2: Enhanced geothermal systems (EGS) schematic [62].

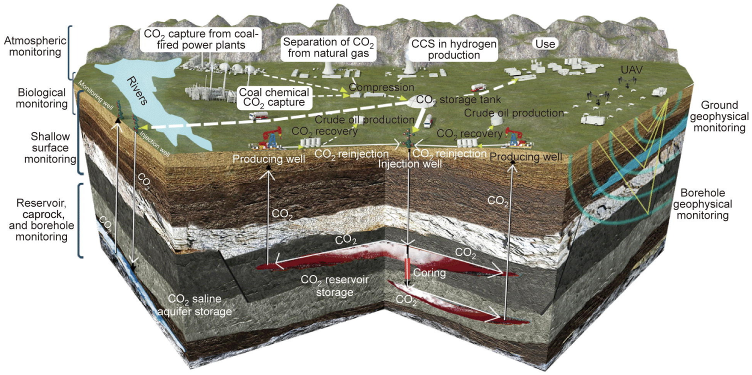

Figure 1.3: Carbon capture and storage (CCS) chain [110] – an example of carbon footprint reduction strategies.

rig at the surface, a drill-string and a drill-bit as depicted in Figure 1.4. The rig consists of two major sub-parts, namely a hoisting system and a top-drive system. The hoisting system acts to adjust the hook-load (the axial force in the upward direction) in order to optimally transfer the downward force, due to the total weight of the drill-string, through the drill-pipes to the drill-bit. The top-drive system generates the required torque and also imposes a nominal angular velocity to rotate the drill-string and the bit for cutting rock at the bit.

Moreover, the drill-string consists of two main parts: the upper part is mainly composed by a serial connection of drill-pipes with different sizes, and the lower part is known as the bottom-hole-assembly (BHA) with characteristic lengths indicated in Figure 1.4. The BHA is the heaviest part of the drill-string as it is composed of a set of heavy tubes, called drill-collar, which are designed to transmit the weight to the bit. This assembly is connected to the drill-bit and used to transfer the force and torque imposed at the surface to the bit for the rock-cutting process. Some downhole tools can be installed at specific locations on the BHA in order to improve the drilling performance.

In drilling processes, the key performance indicators are the drilling efficiency and the rate-of-penetration (ROP). The drilling efficiency is defined as the ratio between the energy devoted to the cutting process and the total energy dissipated at the bit. This efficiency is influenced by the wear state of the drill-bit, which can be affected by the frictional contact force at the interface between the rock and the bit (wearflat). Therefore, this efficiency can be equivalently defined as the ratio between the intrinsic specific energy of the associated rock layer and the mechanical-specific-energy (MSE) [58, 145, 59]. Note that MSE is the quantity (in the unit of pressure) representing the amount of energy dissipated to drill a unit volume of rock, where it accounts for both the work spent to cut the rock and for frictional dissipation. In drilling practice, a lower MSE quantity is desirable by engineers and operators, as it indicates higher efficiency in rock cutting process. On the other hand, the ROP (also known as drilling speed) measures how quickly the drill-string advances the drill bit through the subsurface formations. This quantity is expressed in feet per hour ($^{\mathrm{ft}}/_{\mathrm{hr}}$) or meters per hour ($^{\mathrm{m}}/_{\mathrm{hr}}$). It directly affects the cost-effectiveness of drilling operations.

As a matter of fact, one of the factors that can reduce drilling performance is self-excited vibrations. Drilling systems experience different types of self-excited vibrations, such as axial, lateral, and torsional vibrations, which lead to bit bouncing, whirling, and torsional stick-slip, respectively [190]. These types of vibrations lead to damage to the drilling equipment (i.e., in the BHA), early fatigue of drill pipes, and premature failure of the bits [101, 37], which consequently cause a decrease in drilling efficiency and ROP and increased rig down-time. It is worth noting that purely eliminating such vibrations in drilling systems is inconceivable in practice; therefore, limiting the magnitude of these vibrations is desirable.

As an example of drilling efficiency improvement, it is desired to have the ability to manage the dynamics of the drill-string such that the contact force and frictional

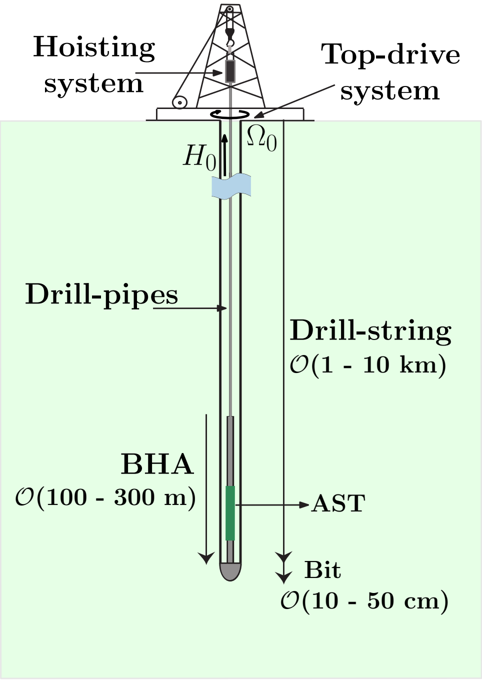

Figure 1.4: Schematic overview of rotary drilling system equipped with the AST and the PDC bit in a vertical well-bore.

Figure 1.5: Polycrystalline-Diamond-Compact (PDC) bit [162].

torque at the bit-rock interface become lower, which would consequently decrease the frictional losses at the bit and allow for more energy to be used for the rock cutting process. This thesis investigates whether, how and to which extent such a goal can be achieved by the presence of a particular downhole tool in the BHA.

In the next section, we review different types of measures employed in drilling system design to improve (optimize) drilling performance indicators, such as efficiency and ROP. Nevertheless, the main focus of this thesis is on the modeling and analysis of a particular downhole tool, the AST [158, 140, 141]. The AST acts as the passive downhole regulator mechanism for drilling performance and has been started to be formally modeled and analyzed in [182, 181]. This downhole tool has been developed by Tomax AS – a Norwegian drilling supporting service company [173], and has been deployed in field since 2005.

1.2.1 Drill-string system design for drilling performance

The energy industry has developed a wide range of innovative technologies in many parts of the drilling system for improving drilling performance in terms of rate of penetration (ROP) and drilling efficiency. Based on field operations, performance can be improved in various ways: drill-string (BHA) system design (including bit design), active feedback control strategies implemented at the surface and downhole, and the use of passive downhole tools (e.g., a mechanical regulator mechanism) — that will be summarized below.

Drill-string (BHA) system design Field case studies in [26, 135] show that drilling performance improvement can be obtained via drill-string (BHA) design, e.g., by utilizing advanced bit design and employing a rotary-steerable-system (RSS) and a downhole drilling mechanics module. Advanced bit design is considered to balance drilling processes with low aggressiveness, particularly through HPHT rock formations, for controlling the depth-of-cut and mitigating the downhole shocks. The RSS provides a steering capability (i.e., sufficient power with better weight transfer) to drive the bit performance allowing for drilling more complex wellbores (i.e., horizontal/deviated wellbores). A downhole drilling mechanics module is able to provide real-time axial, lateral, and torsional shock and vibration data. This module is installed below the measurement-while-drilling (MWD) tool in the BHA and enables to tune surface drilling parameters, i.e., applied weight and top angular velocity.

Active feedback control strategies Furthermore, improving drilling performance can be also carried out by implementing active feedback control strategies for optimizing drilling operational parameters to mitigate (torsional) stick-slip vibrations [100, 65], which may be detrimental to drilling performance. These active control systems are the automation technologies commonly installed in drilling rigs at surface (e.g., on the top drive systems) and aimed at optimizing the RPM of the top drive systems.

Application examples of these drilling automation technologies in the field are Torque-Feedback [84], Soft-Torque [150], Soft-Speed [102], and Z-Torque [64]. In addition, the studies in [52, 88] show some field results on the applications of automatic trajectory control algorithms applied in downhole rotary steerable systems (RSS) to deliver improved ROP and geosteering capability in drilling operations. As motivated by these implementation results of drilling automation technologies in fields, further theoretical and experimental studies have also been conducted that lead to the development of model-based active control designs to mitigate torsional stick-slip vibrations; see for example [91, 92, 159, 51, 126, 124, 123, 40, 125, 122, 39, 35, 36, 177, 149, 183, 49] where models of torsional dynamics were considered, and [189, 32, 107, 28, 34, 155, 24, 166] where models of coupled axial-torsional dynamics were used.

Passive downhole tools In real drilling operations, the utilization of passive mechanical regulators installed downhole (i.e., in the BHA) has also been considered as another strategy for improving drilling performance. In [25, 12], the use of a downhole tool, namely the drilling agitator tool (DAT, also known as an axial oscillation tool), in field operations has been reported. This downhole tool regulates the weight transfer to the drill bit by inducing a low frequency and low amplitude of axial vibrations, and such a mechanism improves the ROP. Some other downhole tools and mechanisms have been designed mainly for attenuating the torsional stick-slip vibrations, e.g., the shock sub [126, 4], the nonlinear energy sink (NES) with a nonlinear passive targeted energy transfer mechanism [178, 179, 180], and damping subs with a distributed vibration damping mechanism [41].

As the main focus of this thesis, the AST of Tomax AS has been widely used in drilling operations world-wide [158, 140, 10], particularly for suppressing the occurrence of stick-slip vibrations and improving drilling performance (i.e., in terms of ROP and MSE), also involving horizontal drilling (i.e., for deviated wellbore) and heterogeneous rock formations. In [99], a combined implementation of PDC bits, Z-Torque, and AST technologies in drilling operations involving carbonate and interbedded shale lithology has been shown to be the most effective strategy for achieving ROP improvement that led to a reduction in the overall drilling cost. In the next section, a brief introduction to the AST regulator is presented.

1.2.2 The AST downhole regulator

In this section, we describe the design of the AST downhole regulator developed by the company Tomax AS [173]. We will also discuss field observations on the influence of deploying this tool in drilling systems with PDC bits on drilling performance.

Modern fixed-cutter PDC drill-bit technology has shown high efficiency in the rock cutting process; however, its interaction with the rock formation has also proven to be a potential source for vibrations leading to dynamic forces and shocks with significant destructive levels to the bit itself, the instrumented BHA, and the drill-

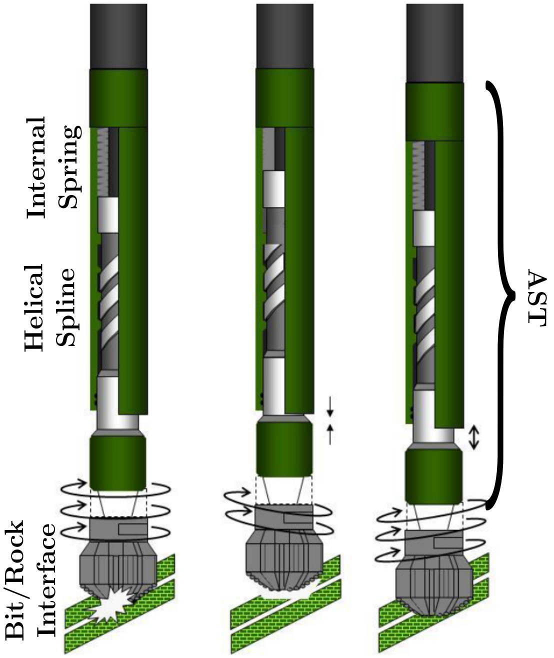

Figure 1.6: The schematic of AST design, see further in [158, 140, 141].

string connections [72]. To overcome this operational challenge of the PDC bit, the AST is designed as a passive downhole tool to prolong the bit life (i.e., less damage) and thus enable drilling performance to be maintained in an optimal way [158, 140, 141].

An impression of the AST regulator developed by Tomax AS is depicted in Figure 1.6. By design, this downhole regulator consists of two main components: an internal preloaded spring and a helical spline designed with a particular lead angle and radius. The helical spline introduces an holonomic constraint on the AST that couples the axial and torsional dynamics of the drill-string system. The internal spring of AST is used for storing and releasing excessive energy from the bit/rock interaction that involves the cutting process and the frictional contact between the drill-bit and the rock layers. This downhole regulator is typically installed in the BHA (the lower part of the drill-string, see Figure 1.4), about 40 – 60 m above the drill-bit.

The first testing of a prototype of this AST regulator took place in 2005 at the Ullrigg test facility in Stavanger supported by two Norwegian operators (Statoil and Norsk Hydro); these same companies later merged and became what is known today as Equinor. In this test, the recorded results have shown that the regulator led to a significant reduction in the torque-on-bit (TOB) and a measurable improvement in drilling performance (ROP) [158]. Together with BP, these three

Figure 1.7: Schematic overview of the limited-range AST type (TT-series) [173].

Figure 1.8: Schematic overview of the full-range AST type (X-series) [173].

companies continued to implement this regulator in the field.

Figures 1.7 and 1.8 show two types of AST regulators commonly used in drilling activities. The first one in Figure 1.7 is the limited-range type AST (a TT series), which has a specific operational threshold in terms of weight- and/or torque-on-bit. Figure 1.8 shows the second type as the next generation of AST with a full-range type (a X series). The latter type provides a more extensive operational capability in terms of drilling parameters and well curvature [173].

Figure 1.9 shows the comparison of post-drilling conditions of the drill bits conducted in Ullrig drilling test facility in Norway for the cases without and with the AST as reported in [158]. This comparison gives field-based validation for an improved condition of the bit is obtained when the drilling system is equipped with the AST.

In [14], Equinor, which has used the AST technology since 2006, also shared relevant drilling records that cover the full field implementations of the two types of AST regulators (the limited-range and full-range types) for drilling operations in the Gullfaks platforms located in the Norwegian Continental Self (NCS). Based on these reported field results, the use of the AST downhole regulators significantly improved the drilling performance in terms of ROP and drilling efficiency, particularly more positive results were achieved with the full-range type of AST. This also shows the potential for a design improvement (towards the full-range regulator) on such a downhole regulator that can deliver an increased positive effect on drilling performance. Moreover, the drilling processes included in these records involved not only vertical wells but also deviated well trajectories and interbedded formations with heterogeneous rock properties.

These findings of field implementations motivate the goal of this thesis, where we aim to use a physics-based dynamical modeling approach to gain insight into possible mechanisms that may explain the improved performance brought by the AST as observed in the field. The state of the art on the modelling and analysis of the dynamics of drilling systems (with and without the AST downhole regulator) is described in the next section.

a) Without the AST

b) With the AST

Figure 1.9: Comparison of post-drilling conditions of the drill bits conducted in Ullrig drilling test facility in Norway for the cases without and with the AST [158].

1.3 State of the art on the modeling and analysis of the dynamics of drilling systems

Models for drilling systems can (coarsely) be categorized based on: (i) the type of model used for the bit-rock interaction and (ii) the type of model used for the drill-string dynamics. In Section 1.3.1, a summary of the development of bit-rock interaction models (also known as the bit-rock interface laws) that support the dynamical modeling of drilling systems is presented. This interaction model enables the determination of the reaction forces and torques at the bit that act as the bottom boundary conditions for the models of the drill-string dynamics. In Section 1.3.2, we will concisely discuss the most important types of dynamical models for drilling systems. In Section 1.3.3, we will extend the description of the state of the art to drilling systems equipped with the AST downhole regulator.

1.3.1 Bit-rock interaction

In rock cutting mechanics involving PDC bits, the bit-rock interaction involves two coexistent phenomena, namely cutting and frictional contact [71].

As motivated by field observations indicating a decreasing reactive torque-on-bit with increasing angular velocity of the bit [37], velocity-weakening bit-rock interface laws were developed and studied to explain the occurrence of torsional stick-slip vibrations [136, 174, 42, 175, 94, 157, 148]. These rate-dependent interface laws postulate this inherent velocity-weakening characteristic in the bit-rock interface as the causal effect of the onset of torsional stick-slip vibrations and typically are of frictional type (i.e., attributed to the Stribeck effect).

In [58], a phenomenological model (also known as the “DD model”) of the bit-rock interaction was proposed, where it is derived based on the reaction forces acting on a single PDC cutter, each decomposed into two components associated with these basic phenomena: cutting and friction. [59, 194] completed the formulation of the bit-rock interface laws based on this DD model that was utilized to analyze the response of the PDC bit for steady-state drilling conditions in homogeneous rock formations. In these interface laws, the reaction force and torque associated with the cutting process and frictional contact are rate-independent, as supported by the experimental evidence on the absence of a rate effect in the bit-rock interaction reported in [127, 144, 75, 142]. Moreover, the reaction force and torque exerted on the bit are dependent on rock and bit design parameters related to the cutting and frictional components of the bit-rock interaction. In [59], a deterministic parameter estimation technique (i.e., a least-square based method) was proposed to estimate these bit-rock parameters based on downhole data of real drilling process: weight-on-bit, torque-on-bit, bit axial and angular velocities; see further implementation in [30].

The interface laws are an essential ingredient in the vibrational modeling of drilling systems. This will be discussed further in the next section.

1.3.2 Modeling and analysis of drilling systems

In order to analyze and optimize drilling performance (i.e., in terms of ROP and efficiency as the key performance indicators), suitable values of operational drilling parameters imposed at the surface, such as weight-on-bit (WOB) and angular speed, must be set by drilling operators on the rig. For this optimization purpose, a dynamic model of drill-string dynamics is required. Another reason for the development of dynamical models for drilling systems is the desire to gain insight into the mechanisms leading to axial, torsional, and lateral vibrations – as discussed in Section 1.2. For example, the severity of torsional stick-slip vibrations increases with higher applied weight on the drill bit and lower rotary speeds imposed at the surface [37]. Therefore, a physical model that describes the dynamical characteristics of drilling systems can shed light on the optimal solutions for drilling rig operators on how to mitigate or suppress such stick-slip vibrations and improve drilling performance.

Based on [154], two model classifications of the drill-string dynamics are considered, namely the lumped-parameter and the distributed-parameter models. For the description of low-dimensional drill-string dynamics, lumped-parameter models have been used. Distributed-parameter models (or discretized variants of those) include a much richer description of the vibrational dynamics, at the cost of model complexity, and they are infinite-dimensional system models.

We care to stress that this thesis focuses on the axial and torsional dynamics of drill-string that are coupled by rate-independent interface laws. The modeling of drilling system dynamics has received wide attention in the literature and wide variety of models has been developed: models of drill-string dynamics as proposed in previous works, e.g., models of torsional dynamics in [37, 92, 91, 126, 116, 114, 123, 124, 122, 149, 132, 42, 152, 151, 156, 23, 35, 36, 83, 109], models of coupled lateral-torsional dynamics of drill-string in [7, 188, 105, 115], models of coupled axial-lateral dynamics in [50], models of coupled axial-torsional dynamics with rate-dependent interface laws in [33, 153, 151, 155, 24], and models of coupled axial, torsional, and lateral dynamics in [174, 175, 51]. In the next sections, we summarize the modeling and analysis of drill-string dynamics incorporated with rate-independent bit-rock interface laws for both modeling approaches: lumped- and distributed-parameter approaches.

1.3.2.1 Lumped-parameter models with rate-independent interface laws

In the early 2000s, [143, 145, 146, 147] have presented a two degrees-of-freedom (DOFs) lumped-parameter model of drill-string dynamics, where the axial and torsional dynamics are coupled by the rate-independent bit-rock interface laws developed in [58, 59]. This modeling approach, also known as the “RGD model” in this work, has been the *avant-garde* work to investigate the onset of self-excited torsional stick-slip vibrations on the drill-string due to the coupling between its axial and torsional dynamics via the rate-independent interface laws.

We follow the argument summarized in [147, 192], based on the simulation studies considering the rate-independent interface laws, that the observed velocity-weakening torque-on-bit is an actual consequence, rather than a cause, of the self-excited torsional stick-slip vibrations. The occurrence of these stick-slip vibrations is argued to be due to a complex dynamic coupling between the axial and torsional degrees-of-freedom (DOFs) of the drilling system.

In more detail, the velocity-weakening effect on the torque-on-bit is affected by a combination of the physical properties of the bit-rock interface (i.e., a combination of rock and bit design parameters associated with the cutting and frictional components) and of the drill-string. Therefore, this velocity-weakening effect is not a constitutive (intrinsic) property of the bit-rock interface as assumed in the rate-dependent laws, where this assumption is not supported by experimental evidence.

This reasoning based on the rate-independent bit-rock interaction laws is supported by two facts. First, kinematically controlled lab experiments with a single PDC cutter [85, 44, 43] and a PDC bit [75] show no significant dependency of the reactive force response on cutter (bit) velocities. Second, the significant influence of the bit design on the onset of the torsional stick-slip vibrations was reported based on real field cases [72, 48].

In [78], the RGD model was further analyzed, particularly to reveal that the apparent velocity-weakening effect on the mean torque applied on the bit (being responsible for the growth of the amplitude of the torsional stick-slip vibrations) is a consequence of the axial stick-slip, i.e., due to the intermittent decrease of the frictional contact force on the bit-rock interaction. Moreover, the regenerative effect associated with the rock cutting process acts as the main actor responsible for the coupling of axial and torsional oscillations and for the existence of self-excited stick-slip vibrations on the drilling system.

In more detail, as the motion of the PDC bit follows a helical path in the rock cutting process, the depth-of-cut and, consequently, the cutting force are dependent on the current and delayed axial positions of the bit, and this process is repeated such that it creates a complex dynamic coupling of the two modes of oscillations. This phenomenon is an analogue of the chattering phenomena in metal machining (cutting) processes [172, 163, 67, 89]. In addition, a discontinuous (nonlinearity) term present at the boundary condition of the RGD model is due to the frictional contact taking place at the bit wearflat-rock interface; note that the wearflat is the blunt part of the cutter (bit). More detailed explanations that support this mechanism underlying the onset of self-excited torsional stick-slip vibrations due to the regenerative effect associated with the rock cutting process are the stability analysis based on the simulation study in [98] and its associated experimental work in [97].

In [57], the RGD model was used to study further the torsional stick-slip vibrations via a linear stability analysis involving the state-dependent delay arising from the cutting process on the bit-rock interaction. This work revealed two regimes, slow and fast, of instability with a transition located at a critical angular velocity. In [27], the RGD model was extended into a more realistic model by considering axial stiffness and damping of the drill-string but without torsional damping. The conclusion of the simulation studies in this work is qualitatively the same as reported in [78] regarding the mechanisms responsible for the onset of torsional stick-slip vibrations, i.e., it is driven by the axial dynamics (via the regenerative effect of rock cutting process). Following this finding, this work also suggested a mechanism for mitigating these torsional vibrations via a stabilization of the axial dynamics of drill-string system that is inline with the recommendations in [66, 189]. The latest studies reported in [171, 168, 169, 170] have utilized the RGD model to investigate the influence of bit design in mitigating the occurrence of torsional stick-slip vibrations.

The study [107] has extended the RGD model in [27] by also taking into account torsional damping on the drill-string dynamics due to the drill mud. The goal of this study was to investigate the effect of varying drilling operational parameters (i.e., the angular velocity imposed at surface) on the range of stability for the coupled axial-torsional motions in the presence of state-dependent delay, which could be useful for analyzing the effectiveness of an active feedback controller to suppress torsional stick-slip vibrations. In [108], a higher-dimensional version of the lumped-parameter model in [107] was proposed. The analysis of this higher-dimensional model suggested that an increase in the resolution of the spatial discretization leads to a significant reduction of the stable region and that the system is prone to self-excited vibrations due to the regenerative effect.

In the work [120], a comprehensive stability analysis on the drill-string model in [27] extended with torsional damping was conducted in order to develop a stability chart for deducing the stable operating regime on a drilling operational parameter-based plane (i.e., in terms of weight-on-bit and top angular velocity at surface). [119] studied the application of the Galerkin projection scheme to solve the state-dependent delay (of the rock cutting process) in the drill-string dynamic model of [120].

Inspired by the study of the global dynamics of the regenerative metal cutting process in [184], a novel approach was introduced in [80] for the calculation of depth-of-cut (in the rock cutting process) based on the evolution of a representative cut surface between two successive (adjacent) cutters. The evolution of this cut surface is governed by a nonlinear partial differential equation (PDE) and has been used for the stability analysis of the coupled axial-torsional dynamics of drilling systems [81, 82]. This approach is supported by the fact that the depth-of-cut formulation in terms of a coupled state-dependent delay differential equation [147] is only valid for drill-bit motions continuously in contact with the drilling surface [80].

1.3.2.2 Distributed-parameter models with rate-independent interface laws

The modeling approach of the drilling system in [77] has considered taking into account the higher (multiple) modes of the axial and torsional dynamics of the drill-string while also incorporating the rate-independent bit-rock interaction law of [58, 59] – as an extension of the RGD model. The study [192] has led to the development of a multiple DOFs model of rotary drilling systems with a rate-independent interface law and the PDE-based evolution of the cut surface for estimating the depth-of-cut [80]. This multiple DOFs model was used to investigate the self-excited axial and torsional vibrations of rotary drilling systems via linear stability analysis and parametric studies. In this study, it was found that the bit-design parameter related to the wearflat plays an important role in delaying or even suppressing the occurrence of torsional stick-slip oscillations.

In [60, 2], distributed models of drill-string dynamics were rewritten as a system of transport equations, and these transport equations were represented as a transfer function matrix by employing the transmission line model formulation (the transfer matrix approach). This approach is useful for conducting a local stability analysis (i.e., around nominal constant axial and torsional velocities). In [2, 5, 3, 6], this transfer function matrix of distributed drill-string dynamics was coupled with the transfer function of the linearized rate-independent interface laws into a feedback representation (i.e., in a block diagram of the full interconnected system) to show the regenerative effect of the bit-rock interaction on the drill-string dynamics in the Laplace domain. In addition, the stability analysis on the local dynamics of this interconnected system was performed via the Nyquist stability criterion.

In [3, 6], the new representation of the depth-of-cut evolution in [80] was considered, while in [2, 5], the coupled state-dependent delay differential equation in [147] was used. In [3], time-domain simulation studies for the full coupled distributed models of drill-string dynamics and rate-independent interface laws were conducted for analyzing the behavioral characteristics of the non-local dynamics (limit cycle behavior). This distributed model of drill-string dynamics was also extended by adding a shock absorber, namely shock sub, to study its effect on the occurrence of axial and torsional self-excited vibrations via both local and non-local dynamic analyses [4].

As another distributed-parameter modeling approach, the infinite-dimensional neutral-type delay (NTD) model that couples the axial and torsional dynamics of drilling systems with rate-independent interface laws was formulated in [167]. This model takes into account two types of delays related to the wave propagation speeds along the drill-string (namely the constant input delays and constant state delays) and the state-dependent delay induced by the bit-rock interaction following [147]. This model is also used in [69, 166, 70] for the development of mitigation strategy on the occurrence of torsional stick-slip vibrations via active state feedback controllers with an observer-like predictor designed for state estimation.

In [68], the infinite-dimensional NTD model was extended by modifying the estimation of depth-of-cut while taking into account the case of bit bounce and the bit reverse (backward) rotation. For a worthy comparison with the previous distributed modeling approaches, a coupled PDE-ODE model is considered in [34], where the distributed characteristic of the drill-string is coupled with the lumped BHA section and the state-dependent delay in [147] is used to couple the axial and torsional dynamics.

Clearly, all these models display a more complex vibrational signature than their lumped-parameter counterparts. Still, they confirm the same root cause for axial and torsional instabilities - that the regenerative effect associated with the rock cutting process acts as the root cause of these instabilities. All these models, developed both by lumped-parameter and distributed-parameter (or finite-element based) approaches, still mostly consider a scenario of drilling vertical boreholes in homogeneous rock formations – still a simplified abstraction of real operational conditions in the field.

1.3.3 Modeling and analysis of drilling systems with downhole regulator

The two degrees-of-freedom (DOFs) lumped-parameter model of the rotary drilling system (RGD model) developed in [147] was extended to incorporate the downhole regulator AST [182, 181]. The AST model is represented by an internal stiffness and damping, and a kinematic constraint (induced by its helical spline) that couples the axial and torsional dynamics of the drill-string. In addition, a lead angle and spline radius were also introduced in this model to quantify the slope of the AST spline. These studies successfully revealed the mechanisms of how the AST improves drilling performance in terms of ROP and efficiency of the rock cutting process. In more detail, these studies showed that the inclusion of the AST regulator increases the axial instabilities of the drill-string system, particularly at the bit-rock interaction level. As a consequence, the wearflat (contact) force levels at the bit (on average) decrease. In turn, this leads to reduced frictional losses at the bit, thereby leaving more torque available for the rock cutting process at the bit. This is the key mechanism by which the AST enables improved ROP and drilling efficiency.

Moreover, the studies [55, 131] have proposed a modification in the internal modeling of AST by considering the effect of internal friction on the helical spline (e.g., a nonsmooth (frictional) contact and dry friction) and a preload of the internal spring. The results of parametric studies in these works suggest including the preload and internal friction of AST for obtaining more accurate dynamic responses, particularly with the aim of optimizing the tool design to improve drilling performance.

Again, none of these works considered drilling scenarios with deviated wells, and all of these works focused on the simplified case of homogeneous rock formations. Finally, we want to emphasize that none of the works above consider the infinite-dimensional (distributed) characteristics of drill-string dynamics.

1.4 Open challenges and research objectives

Previous research efforts, reviewed in Section 1.3, have shed light on 1) the root cause for axial and torsional vibrations in drilling systems (without AST regulator) and 2) the core mechanism by which the AST regulator enables the increase in drilling performance for vertical boreholes and homogeneous rock formations.

However, based on the above descriptions of the state of the art, we identify several essential open challenges. These open challenges particularly relate to gaining understanding on whether and, if so, why such drilling performance increases can also be expected for drilling scenarios closer to real field implementations, as reported in [158, 140, 141].

In this thesis, we focus on two aspects of real-life drilling scenarios. Firstly, many wells involve deviated (not vertical) borehole trajectories. Therefore, it is an open question whether and how the interaction between the borehole and drill-string in such scenarios affects the potential improvement in drilling performance that can be gained by the use of the AST regulator in such scenarios. Secondly, many wells need to be drilled through layered, heterogeneous rock formations. Again, it is an open question whether and how the varying loading on the bit when transitioning between distinct rock layers affects the potential improvement in drilling performance that can be gained by the use of the AST regulator in such scenarios. Also, the lumped-parameter model of the drill-string, used so far to analyze the role of the AST [182, 181], is unable to capture the complex, distributed dynamics of the drill-string. It is, therefore, an open question how such richer, infinite-dimensional (distributed) drill-string dynamics affect the potential improvement in drilling performance that can be gained by the use of the AST regulator.

Summarizing, the main objectives of this thesis can be stated as follows:

1. To extend the dynamic modeling of drilling systems equipped with the AST downhole regulator toward scenarios involving, firstly, deviated well-bore trajectories inducing the contact between drill-string and borehole, secondly, interbedded formations with heterogeneous rock properties, and thirdly, distributed dynamics of the long, slender drill-string.

2. To perform the dynamic analysis on the effect of such regulator on drilling performance (in terms of ROP and efficiency in the rock cutting process) by developing numerical simulators for the models pursued in point 1. Another objective is to shed light on the core mechanism underlying the way in which the AST downhole regulator affects the drilling performance in the scenarios mentioned in point 1.

3. To conduct a parametric study utilizing the extended models and developed simulators to understand which operational conditions and parametric settings of AST are significant factors in terms of drilling performance.

1.5 Contributions of thesis

The effort made to accomplish the research objectives has led to findings that can be split into three categories: contributions to the extension of the dynamic modeling of drilling systems equipped with the downhole regulator AST (including the development of the associated numerical simulators) for the drilling scenarios mentioned in Section 1.4, contributions to the dynamic analysis on the effects of the regulator AST on drilling performance (in terms of ROP and drilling efficiency), and contributions concerning the parametric study to find the operational conditions and the settings of AST that significantly affect the drilling performance.

A more detailed description of the contributions of this thesis is as follows:

1. In **Chapter 2**, lumped-parameter models of drilling systems without and with the downhole regulator AST have been developed for drilling in deviated well-bore trajectories. A comparative dynamic analysis of these extended models has been performed utilizing the associated numerical simulators to investigate (i) the effect of the deviated well-bore (particularly the contact between the BHA part and the well-bore wall) on the drilling response and (ii) the effect of the AST on the drilling performance.
2. In **Chapter 3**, novel bit-rock interface laws are developed for scenarios in which a PDC bit transitions between two rock layers (e.g., soft and hard layers of an interbedded formation). These interface laws are a necessary stepping stone towards dynamic drill-string models for scenarios in which heterogeneous rock formations are drilled.
3. In **Chapter 4**, lumped-parameter models of drilling systems without and with the AST are developed for drilling scenarios in interbedded formation by taking into account the extended bit-rock interface laws developed in **Chapter 3**. A comparative dynamic analysis of these two models is also performed utilizing the associated numerical simulators to investigate (i) the effect of the interbedded rock formation on the drilling response and (ii) the effect of the AST on the drilling performance in such scenario.
4. In **Chapter 5**, a distributed model of drill-string dynamics equipped with the regulator AST is developed, including the associated numerical simulator. A comparative analysis of the distributed drill-string models without and with the regulator AST is performed to investigate the effect of the AST on the drilling performance under the influence of such distributed dynamics of the drill-string.
5. In **Chapters 2** and **5**, a parametric performance study utilizing the extended models and developed simulators is pursued to investigate the operational conditions and settings of AST that significantly affect the drilling performance.

1.6 Publications

The main contributions of this thesis have been published (or based on publications still in preparation) as the following journal articles and conference papers.

1.6.1 Peer-reviewed journal articles

Below is a list of of the published journal articles.

- R. Wildemans, **A.G. Aribowo**, E. Detournay, N. van de Wouw, “Modelling and dynamic analysis of an anti-stall tool in a drilling system including spatial friction", *Nonlinear Dynamics*, Volume 98, Issue number 4, pp. 2631 – 2650, 2019.
- **A.G. Aribowo**, R. Wildemans, E. Detournay, N. van de Wouw, “Drag bit/rock interface laws for the transition between two layers", *International Journal of Rock Mechanics and Mining Sciences*, Volume 150, Article number 104980, 2022.
- **A.G. Aribowo**, R. Wildemans, E. Detournay, N. van de Wouw, “Dynamic analysis of a downhole regulator for drilling in interbedded formations", *Society of Petroleum Engineers (SPE) Journal*, Volume 28, Issue number 04, pp. 1611–1635, Paper number: SPE-214310-PA, 2023.
- **A.G. Aribowo**, U. J. F. Aarsnes, K. Chen, E. Detournay, N. van de Wouw, “Analysis of a downhole passive regulator in drilling: a distributed parameter modeling approach", to be submitted to the Journal of Sound and Vibration.

1.6.2 Peer-reviewed papers and abstracts in conferences

Below is a list of of the papers and abstracts published and presented in conferences.

- R. Wildemans, **A.G. Aribowo**, E. Detournay, N. van de Wouw, “Modelling and analysis of a down-hole tool in a drilling system including spatial friction", in *Proceedings of the First International Nonlinear Dynamics Conference (NODYCON 2019)*, Rome, Italy, 2019.
- **A.G. Aribowo**, R. Wildemans, E. Detournay, N. van de Wouw, “Dynamic modeling of drill-string systems for layered rock formations", in *Proceedings of the Fifth International Colloquium on Nonlinear Dynamics and Control of Deep Drilling Systems*, pp. 79-92, University of Maryland, College Park, United States, 2022.
- **A.G. Aribowo**, R. Wildemans, E. Detournay, N. van de Wouw, “Nonsmooth dynamics modeling of drill-string systems in heterogeneous formations", in 10^{th} *European Nonlinear Dynamics Conference (ENOC 2022)*, Lyon, France, 2022.
- **A.G. Aribowo**, U. J. F. Aarsnes, E. Detournay, N. van de Wouw, N. Reimers, “Performance analysis of a downhole regulator on rate-of-penetration

and drilling efficiency: an autonomous load management at *bit*", in *SPE/IADC International Drilling Conference and Exhibition*, Stavanger Forum, Stavanger, Norway, 2023.

- **A.G. Aribowo**, U. J. F. Aarsnes, K. Chen, E. Detournay, N. van de Wouw, "Model-based drilling performance analysis of a downhole regulator", in *Proceedings of the Sixth International Colloquium on Nonlinear Dynamics and Control of Deep Drilling Systems*, Universidade Federal do Rio de Janeiro (UFRJ), Rio de Janeiro, RJ, Brazil, July 1st - 3rd, 2024.

1.6.3 Non peer-reviewed papers and abstracts in conferences

Below is a list of non peer-reviewed papers and abstracts published and presented in conferences.

- **A.G. Aribowo**, R. Wildemans, E. Detournay, N. van de Wouw, "Non-smooth dynamics modeling of drill-string systems in interbedded formations", in 40^{th} *Benelux Meeting on Systems and Control 2021*, Rotterdam, Netherlands, June 2021.

1.7 Outline

The remainder of this thesis consists of five chapters in total. Each chapter, except for the last chapter, is based on the published or submitted papers in Section 1.6 and is, thus, self-contained, including more detailed and dedicated descriptions of the relevant literature.

Chapters 2, **3** and **4** cover the contributions of the thesis to the extension of lumped-parameter models and dynamic analysis of drill-string dynamics without and with the AST for the drilling scenarios involving deviated well-bore trajectories and heterogeneous rock formation. Specifically, **Chapter 2** focuses on the model for the drilling scenario of deviated well-bore. **Chapters 3** and **4** present the models related to the drilling scenario of heterogeneous formations. As a stepping stone to **Chapter 4**, in **Chapter 3**, the extended bit-rock interface laws involving the transition between two rock layers are presented.

Chapter 5 reports on the distributed model of drill-string dynamics and the parametric study of the operational conditions and key settings of AST in the light of drilling performance analysis. In particular, this chapter focuses on the development of the distributed model of the drill-string equipped with the downhole regulator AST, which is used as the basis for the parametric study. Finally, conclusion and recommendations for future research are presented in **Chapter 6**.

Chapter 2

Modelling and dynamic analysis of a down-hole regulator in a drilling system including spatial friction

Abstract[1] - This chapter investigates the effects of a down-hole anti-stall tool (AST) in deviated wells on the drilling performance of a rotary drilling system. Deviated wells typically induce frictional contact between the drill-string and the borehole, which affects the drill-string dynamics. In order to study the influence of such frictional effects on the effectiveness of the AST in improving the rate-of-penetration and drilling efficiency, a model-based approach is proposed. A dynamic model with coupled axial and torsional dynamics of a drilling system including the down-hole tool in an inclined well is constructed. Furthermore, the frictional contact between the drill-string and the borehole is modeled by a set-valued spatial Coulomb friction law affecting both the axial and torsional dynamics. These dynamics are described by state-dependent delay differential inclusions. Numerical analysis of this model shows that the rate-of-penetration and drilling efficiency increases by inclusion of the AST, both in the case with and without spatial Coulomb friction. Furthermore, a parametric design study of the AST in different inclined drilling scenarios is performed. This study reveals a design for the AST, which gives optimal drilling efficiency, robustly over a broad range of inclined drilling scenarios.

2.1 Introduction

Drilling is used for the exploration of oil, gas, minerals and increasingly for geothermal energy. Current drilling operations are challenging as often complex, deviated wells need to be drilled, for oil and gas exploration, while, for geothermal

---

[1] This chapter is based on [187] R. Wildemans, **A.G. Aribowo**, E. Detournay, N. van de Wouw, "Modelling and dynamic analysis of an anti-stall tool in a drilling system including spatial friction", *Nonlinear Dynamics*, Volume 98, Issue number 4, pp. 2631 – 2650, 2019. The main findings of this chapter are summarized in [14].

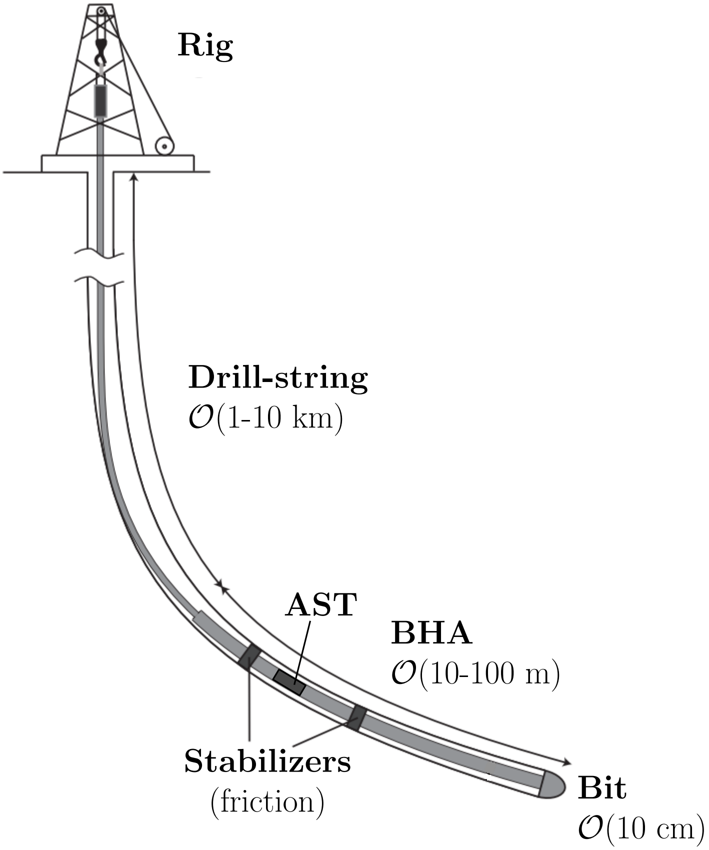

Figure 2.1: Schematic overview of a drilling system in an inclined well (adapted from [111]).

applications, drilling into hard rock is required. Improving the efficiency of these drilling operations will significantly reduce the costs. Particularly in geothermal drilling operations, where $30-50\%$ of the total development costs are from drilling [10, 13, 73]. Therefore, the development of new technologies to improve drilling performance is key to increase the economic feasibility of geothermal drilling operations.

Rotary drilling with PDC bits is widely accepted as most efficient for exploration and production drilling operations. Figure 2.1 depicts the major components of a rotary drilling system: rig, drill-string, bottom hole assembly (BHA), including stabilizers and downhole tools, and drill-bit. In a rotary drilling system, a key indicator of its efficiency is the ROP, which is the speed at which the bit is drilling into the sub-surface formation. In order to optimize the ROP, suitable values of the hook-load, which translates into an axial force on the bit referred to as weight-on-bit (WOB), and rotation speed (RPM) imposed at the surface (rig) must be set by drilling operators. For this ROP optimization purpose, the Bourgoyne and Young ROP model is widely used in industry [22, 121]. This model takes into account different aspects, such as formation strength, WOB, angular velocity and bit wear, which influence the ROP. Based on the optimal operational parameters, the ROP is then optimized by using various controllers [20]. However, the dynamics of the drill-string, the bit– rock interaction and the (frictional) contact along the drill-string in a deviated well are not taken into account in this modelling approach. A different approach for ROP improvement is the selection of drill-string components, such as drill-bits or down-hole tools located at the BHA of the drill-string [10, 25, 21, 74]. Down-hole tools can be either active [25, 74, 21] or passive [10, 140, 181]. Active tools typically provide axial excitation during drilling, which can alter the effect of axial friction and consequently improve the drilling efficiency. The current chapter aims to model and analyze the effect of a passive down-hole tool on the drilling efficiency in presence of friction between the drill-string and borehole wall. This work is motivated by field data that show evidence that the AST can increase the drilling efficiency in terms of ROP, also in deviated wells [140, 158].

In particular, this chapter focuses on the modelling and analysis of the coupling of axial and torsional vibrations in drill-string dynamics, and studies how a down-hole tool, called the AST [140], affects the drilling performance (in terms of ROP) in a deviated borehole. Previous works, e.g., [27, 57, 147] have shown that a rate-independent bit–rock interaction model [58], including both cutting and frictional contact processes, is essential in the coupling between the axial and torsional dynamics. In this chapter, we also pursue such type of modelling approach, further motivated by the fact that the AST also operates by coupling the axial and torsional dynamics [140, 181]. The dynamics of drill-string systems, including such rate-independent bit-rock interaction model, has been described by a variety of dynamical models. In [27, 57, 78, 80, 82, 106, 107, 108, 120, 118, 147] lumped-parameter models for the axial-torsional drill-string dynamics have been proposed, while in [2, 5, 60, 77] both finite-element based and distributed models have been developed. These models have been employed to study instabilities and axial and torsional vibrations of drill-string systems, and recently to investigate the effect of the AST on the ROP [181]. However, the effect of friction between the drill-string and the borehole due to deviated well scenarios has not yet been taken into account.

The modelling of the frictional contact along the drill-string has been considered extensively in the scope of so-called torque and drag models [1, 93, 160]. The magnitude of the frictional forces mainly depends on the normal force acting between the drill-string and the borehole wall. Hence, in highly deviated wells the effects of this friction indeed becomes more prominent, because the drill-string is resting under its own weight on the borehole wall. However, in these models no vibrational dynamics and down-hole tooling have been taken into account, while it has been shown that the functioning of the AST is intrinsically related to the drill-string dynamics [181].

This work builds on and extends the developments in [181] by modelling and analysis of the (frictional) contact between the BHA and the borehole wall, thereby broadening its applicability to deviated well scenarios. The main contributions of this chapter are as follows:

- Firstly, a benchmark model of the drill-string dynamics (without AST) and a drill-string model including AST, both with spatial friction between the borehole and drill-string, are developed. Herein, both unilateral contact and frictional characteristics of the bit-rock interaction and the spatial friction between the borehole and drill-string have been modeled by set-valued force laws. This allows for a unified treatment of these nonlinear model features in a time-stepping-based simulation tool for the resulting delay differential inclusion model;
- Secondly, a model-based analysis of the effect of frictional contact between BHA and borehole wall on the drilling performance (in terms of ROP and drilling efficiency) is performed;
- Finally, a parametric performance study on the AST design is performed leading to an optimal design to maintain a high drilling efficiency, which is robust for a wide range of deviated wells.

The outline of this chapter is as follows. In Section 2.2, the dynamic models of a drill-string system without and with AST for drilling in a deviated well are derived. In Section 2.3, a dynamic analysis is performed with a focus on the effect of the spatial frictional contact on drilling performance (ROP and drilling efficiency; for both cases without and with AST). Subsequently, a parametric design study on the AST design is presented in Section 2.4. Finally, conclusions are drawn in Section 2.5.

2.2 Dynamic modelling

In this section, two models of a drill-string including spatial friction between the BHA and the borehole are presented. In Section 2.2.1, two drill-string models, with and without AST, are introduced, enabling the comparative analysis of systems with and without the AST. In Section 2.2.2, the bit–rock interaction model is discussed. In Section 2.2.3, the model that describes the frictional contact between the borehole and the BHA is presented. Finally, in Section 2.2.4 the two dynamic models, with and without AST, are expressed in dimensionless perturbation coordinates around their nominal solutions in order to identify a minimum set of parameters characterizing the dynamics.

A total overview of a drilling system in a deviated well is depicted in Figure 2.1. A typical drilling system is operated from the rig located at the surface,

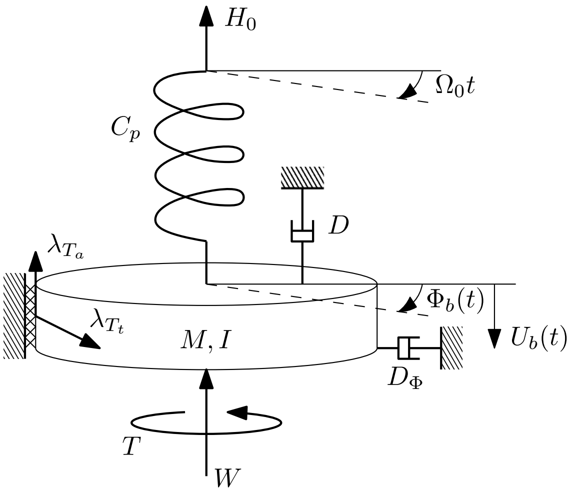

Figure 2.2: Schematic representation of the benchmark model.

where the top-drive equipment sets the angular speed and adjusts the weight by regulating the hookload. These operational conditions are transmitted via slender drill-pipes and a BHA to the drill-bit. The BHA is specifically designed to fulfill a particular drilling objective(s) based on the subsurface geological conditions and can be composed by several down-hole components, such as stabilizer(s), rotary steerable system (RSS), logging tools, mud motor(s), etc. Due to the larger diameter of the stabilizers compared to the rest of the BHA components, the stabilizers are in contact with the borehole wall, which consequently results in additional friction affecting the drill-string dynamics. The physical aspects to be considered in the modelling are the boundary conditions at the rig, the drill-string dynamics including the AST, the bit–rock interaction as the down-hole boundary conditions and the frictional contact between the stabilizers and the borehole.

2.2.1 Drill-string dynamics

In this section, the dynamic models of the drill-string systems are presented. First the benchmark model, excluding the AST, is discussed. Thereafter, the model including the AST is discussed.

2.2.1.1 Benchmark drill-string dynamics

In Figure 2.2, the lumped-parameter benchmark model (i.e., without the AST) is schematically depicted. The axial and torsional dynamics are described by this model, which consists of two degrees-of-freedom (DOFs), namely the axial displacement of the bit U_b and the angular displacement of the bit Φ_b.

At the rig, the boundary conditions are given by an imposed constant angular velocity Ω_0 and a constant upward force H_0, the so-called hookload. The total mass and inertia of the drill-string including the BHA are lumped in the discrete mass M and inertia I. The torsional stiffness of the drill-pipes is modelled as a torsional spring with stiffness C_p. The viscous friction along the drill-string and BHA in axial and angular directions are characterized by the parameters D and D_Φ, respectively. The parameters λ_{T_a} and λ_{T_t} are associated with the spatial Coulomb friction between the stabilizers and the borehole in axial and torsional direction, respectively, which is discussed in more detail in Section 2.2.3. The weight acting on the bit is denoted by W and the torque acting on the bit is denoted by T.

The bit–rock interaction model, which is discussed in more detail in Section 2.2.2, relates the weight-on-bit (WOB) W and the torque-on-bit (TOB) T to the axial and angular motion of the bit. This bit–rock law considers two independent processes, namely a pure cutting process and a frictional contact. Hence, the force and torque can be decomposed in a cutting and frictional component, denoted by the superscripts c and f, respectively, i.e., for the total WOB $W = W^c + W^f$, and for the total TOB $T = T^c + T^f$. The force and torque contributions associated with the wearflat will from now on be denoted as follows:

$$W^f = -\lambda_{b_a}, \qquad\qquad T^f = -\lambda_{b_t}. \tag{2.1}$$

By using a Lagrangian approach, the equations of motion (EOMs) for this model are obtained. In general, these can be written in the following form:

$$\mathbf{M}\ddot{\mathbf{q}} - \mathbf{h}(t, \mathbf{q}, \dot{\mathbf{q}}) = \mathbf{W}\boldsymbol{\lambda}, \tag{2.2}$$

where $\mathbf{q}$ represents the column with generalized coordinates. M is the mass matrix and the column $\mathbf{h}(t, \mathbf{q}, \dot{\mathbf{q}})$ contains all generalized forces except the friction forces (both due to frictional contacts at the bit and between the borehole and the stabilizers at the BHA). The vector $\boldsymbol{\lambda}$ contains the generalized forces associated with the set-valued force laws, characterizing both due to frictional contacts at the bit and between the borehole and the stabilizers at the BHA, see Sections 2.2.2 and 2.2.3, and the matrix $\mathbf{W}$ contains the associated generalized force directions. In case of the benchmark model with the generalized coordinates $\mathbf{q} = \begin{bmatrix} U_b & \Phi_b \end{bmatrix}^\top$, this results in the following matrices and columns in Eq. (2.2):

$$\begin{aligned}
\mathbf{M} &= \begin{bmatrix} M & 0 \\ 0 & I \end{bmatrix}, \\
\mathbf{h}(t, \mathbf{q}, \dot{\mathbf{q}}) &= \begin{bmatrix} -D\dot{U}_b - H_0 + W_s - W^c \\ -D_\Phi \dot{\Phi}_b + C_p \left(\Omega_0 t - \Phi_b\right) - T^c \end{bmatrix}, \\
\mathbf{W} &= \begin{bmatrix} 1 & 0 & 1 & 0 \\ 0 & 1 & 0 & R \end{bmatrix}, \\
\boldsymbol{\lambda} &= \begin{bmatrix} \lambda_{b_a} & \lambda_{b_t} & \lambda_{T_a} & \lambda_{T_t} \end{bmatrix}^\top,
\end{aligned} \tag{2.3}$$

where W^c and T^c are satisfying Eqs. (2.6), 2.7, and 2.8, and the vector $\boldsymbol{\lambda}$ is satisfying Eqs. (2.9), (2.12), and 2.25, and W_s represents the submerged weight

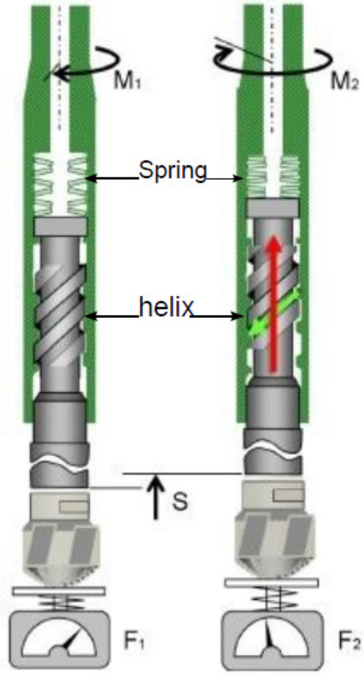

Figure 2.3: The working principle of the AST: an increase in torque (M_2) will cause a contraction (S) to off-load the weight from the cutters (F_2) [10].

of the drill-string. A detailed derivation of the equations of motion can be found in [186].

2.2.1.2 Drill-string dynamics including AST

The AST is designed to influence the coupling between the axial and torsional displacement. The AST consists of two tool bodies connected by a helical spline and an axial internal spring, as viewed in Figure 2.3. According to [158], the working principle of the tool is that a torsional load with sufficient magnitude to overcome the compressed spring will make the upper tool body, with the internal helical spline, rotate on the mating lower body. When the upper and lower part screw together in this manner, the tool telescopically contracts. Consequently, this results in an adjustment of the axial and torsional loading acting on the bit. Hence, the tool prevents dynamic forces from reaching destructive levels.

In Figure 2.4, the lumped-parameter model including AST is schematically depicted. The AST separates the drill-string in two parts, where the coordinates U and Φ are related to the displacements of the top part and U_b and Φ_b to the

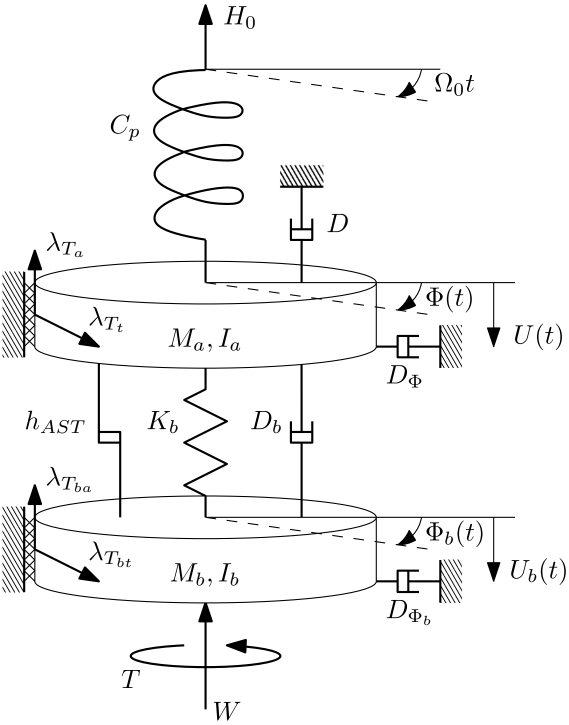

Figure 2.4: Schematic representation of the drill-string model including the AST.

displacements of the part below the tool. The mass and inertia of the drill-string including the part of the BHA above the tool are lumped into a discrete mass M_a and inertia I_a, while the mass and inertia of the part of the BHA below the tool are lumped into a discrete mass M_b and inertia I_b. The torsional stiffness of the drill-pipes and the viscous friction components are identical to the benchmark model. However, the axial viscous friction only acts on the part above the tool (characterized by the damping parameter D). The viscous friction in the angular direction is modelled by two dampers characterized by D_Φ and D_{Φ_b}. The spatial friction acts both on the DOFs above the tool and on the DOFs at the bit, and the distribution of the friction between the two parts of the drill-string is denoted by $\Delta \in [0, 1]$, as introduced in Eqs. (2.22) and (2.23). The radius of the stabilizer below the tool is assumed to be the same as above the tool.

Let us now introduce the model of the AST, which introduces an additional axial spring K_b and damper D_b, see Figure 2.4. Furthermore, the helical spline in the tool introduces a kinematic constraint, which is characterized by the lead p, lead angle β, and the radius r_{spline} of the helical spline, and can be written as

$$\begin{aligned} U - U_b &= \frac{p}{2\pi r_{spline}} \left(\Phi r_{spline} - \Phi_b r_{spline} \right) \\ &= \frac{p}{2\pi} \left(\Phi - \Phi_b \right) =: \alpha \left(\Phi - \Phi_b \right). \end{aligned} \tag{2.4}$$

Herein $U(\Phi)$ and $U_b(\Phi_b)$ represent the axial (angular) positions above the tool and at the bit/below the tool, respectively (see Figure 2.4). The lead is given by $p = 2\pi r_{spline} \tan\beta$.

The generalized coordinates of the model including AST are given by $\mathbf{q}^c = \left[\begin{array}{cccc} U & \Phi & U_b & \Phi_b \end{array} \right]^\top$. However, due to the kinematic, holonomic constraint of the AST, this model can be alternatively formulated in terms of three independent generalized coordinates $\mathbf{q} = \left[\begin{array}{ccc} U & U_b & \Phi_b \end{array} \right]^\top$. This coordinate transformation is discussed in detail in Appendix A.1. Using a Lagrangian approach for systems with constraints and after eliminating the DOF Φ, the obtained EOMs can be written in the general form of Eq. (2.2), with the following matrices and columns:

$$\begin{aligned} \mathbf{M} &= \left[\begin{array}{ccc} M_a + \frac{I_a}{\alpha^2} & -\frac{I_a}{\alpha^2} & \frac{I_a}{\alpha} \\ -\frac{I_a}{\alpha^2} & M_b + \frac{I_a}{\alpha^2} & -\frac{I_a}{\alpha} \\ \frac{I_a}{\alpha} & -\frac{I_a}{\alpha} & I_a + I_b \end{array} \right], \\ \mathbf{h}(t, \mathbf{q}, \dot{\mathbf{q}}) &= \left[\begin{array}{c} -K_b \left(U - U_b \right) - \frac{1}{\alpha} C_p Y - \frac{1}{\alpha} D_\Phi \dot{Y} - D \dot{U} \cdots \\ K_b \left(U - U_b \right) + \frac{1}{\alpha} C_p Y + \frac{1}{\alpha} D_\Phi \dot{Y} \cdots \\ -C_p Y - D_\Phi \dot{Y} - D_{\Phi_b} \dot{\Phi}_b \cdots \end{array} \right. \\ &= \left. \begin{array}{c} \cdots - D_b \left(\dot{U} - \dot{U}_b \right) + \frac{1}{\alpha} C_p \Omega_0 t + W_s - H_0 \\ \cdots + D_b \left(\dot{U} - \dot{U}_b \right) - W^c - \frac{1}{\alpha} C_p \Omega_0 t + W_{bs} \\ \cdots - T^c + C_p \Omega_0 t \end{array} \right], \\ \mathbf{W} &= \left[\begin{array}{cccccc} 0 & 0 & 1 & \frac{R}{\alpha} & 0 & 0 \\ 1 & 0 & 0 & -\frac{R}{\alpha} & 1 & 0 \\ 0 & 1 & 0 & R & 0 & R \end{array} \right], \\ \boldsymbol{\lambda} &= \left[\begin{array}{cccccc} \lambda_{b_a} & \lambda_{b_t} & \lambda_{T_a} & \lambda_{T_t} & \lambda_{T_{ba}} & \lambda_{T_{bt}} \end{array} \right]^\top, \end{aligned} \tag{2.5}$$

with the auxiliary variables $Y = \Phi_b + \frac{1}{\alpha} \left(U - U_b \right)$ and $\dot{Y} = \dot{\Phi}_b + \frac{1}{\alpha} \left(\dot{U} - \dot{U}_b \right)$ in the expression for $\mathbf{h}(t, \mathbf{q}, \dot{\mathbf{q}})$, while W^c and T^c satisfy Eqs. (2.6), 2.7, and 2.8 and $\boldsymbol{\lambda}$ satisfies Eqs. (2.9), (2.12), and 2.25. The parameters W_s and W_{bs} denote the submerged weights of the drill-string parts above and below the tool, respectively. A detailed derivation of the equations of motion can be found in [186].

2.2.2 Bit-rock interaction model

In this chapter, the rate-independent bit–rock interaction law as introduced in [58, 59] is adopted, which relates the WOB and the TOB to the axial and angular motions of the bit. The bit-rock interaction involves two independent processes: a pure cutting process taking place at the front of the cutters and a frictional contact between the rock and the so-called wearflat underneath the cutters. According to [58, 59], the cutting contributions for a bit consisting of n identical and symmetrically distributed blades of cutters around the axis of revolution and a bit radius of a, can be written as

$$W^c = na\varepsilon\zeta d_n, \qquad\qquad T^c = \frac{1}{2}na^2\varepsilon d_n, \tag{2.6}$$

where ε is the intrinsic specific energy related to the rock strength and ζ is related to the orientation of the cutting face. The cutting force and torque are proportional to the depth-of-cut (DOC) d_n produced by a single blade, which is in general not constant. The DOC depends on the axial position of the bit and the rock surface generated by the previous blade according to

$$d_n = U_b(t) - U_b(t - t_n(t)), \tag{2.7}$$

where $U_b(t)$ is the axial bit position and t denotes time, see Figure 2.5. Furthermore, $t_n(t)$ is the time required for the bit to rotate by an angle of ${}^{2\pi}/_{n}$, which is the angle between two successive blades. This time-dependent delay $t_n(t)$ (actually state-dependent) is characterized by the implicit equation:

$$\int\limits_{t-t_n(t)}^{t} \frac{\mathrm{d}\Phi_b(s)}{\mathrm{d}s}\mathrm{d}s = \Phi_b(t) - \Phi_b(t - t_n(t)) = \frac{2\pi}{n}, \tag{2.8}$$

where $\Phi_b(t)$ denotes the angular position of the bit at time t.

In the contributions associated with the wearflat as introduced in Eq. (2.1), the wearflat reaction force λ_{b_a} is essentially discontinuous in terms of the bit axial velocity. When the bit moves downwards, the contact between the wearflat and the rock is fully mobilized. However, when the bit moves upwards, the contact is lost and consequently the reaction force vanishes. Hence, the wearflat reaction force can be described in a set-valued force law by the following inclusion:

$$\lambda_{b_a} \in -na\bar{\sigma}l_n \frac{1 + \mathrm{Sign}\left(\dot{U}_b\right)}{2}, \tag{2.9}$$

where $\bar{\sigma}$ is the maximum contact stress and l_n is the wearflat length per blade. The axial velocity of the bit is denoted by $\dot{U}_b$ and the set-valued sign-function in Eq. 2.9 is defined as

$$\mathrm{Sign}\,(y) := \begin{cases} \quad 1 & y > 0 \\ [-1,1] \quad , & y = 0 \quad , \\ \ -1 & y < 0 \end{cases} \tag{2.10}$$

As a consequence of the set-valued nature of the law in Eq. 2.9, the admissible values of the wearflat reaction force form a convex set C_a given by

$$C_a = \{\lambda_{b_a} \mid -na\bar{\sigma}l_n \leq \lambda_{b_a} \leq 0\}\,. \tag{2.11}$$

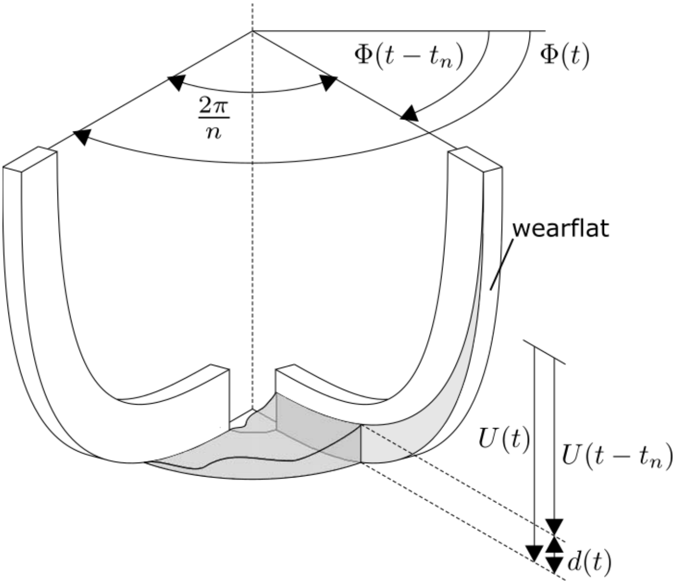

Figure 2.5: Bottom hole profile between two successive blades [27].

The force acting on the wearflat also induces a frictional torque λ_{b_t}. Since the friction always acts in opposite direction compared to the bit rotational velocity, this frictional torque is discontinuous with respect to the rotational velocity and can be modelled by the following inclusion:

$$\lambda_{b_t} \in \frac{1}{2} a\mu\xi\lambda_{b_a} \mathrm{Sign}\left(\dot{\Phi}_b\right). \tag{2.12}$$

Herein, μ is a rate-independent friction coefficient and ξ characterizes the orientation and spatial distribution of the frictional contact of the surfaces along the bit blade(s). The angular velocity of the bit is denoted by $\dot{\Phi}_b$. The admissible values of the frictional torque forms a convex set C_t, which depends on the wearflat(normal) reaction force λ_{b_a}. This set is given by

$$C_t(\lambda_{b_a}) = \left\{ \lambda_{b_t} \mid \frac{1}{2} a\mu\xi\lambda_{b_a} \leq \lambda_{b_t} \leq -\frac{1}{2} a\mu\xi\lambda_{b_a} \right\}. \tag{2.13}$$

The set-valued force laws for reaction force λ_{b_a} and frictional torque λ_{b_t} can be formulated by using normal cones of the convex sets Eqs. (2.11) and (2.13), respectively [79, 104]:

$$-\dot{U}_b \in N_{C_a}(\lambda_{b_a}), \tag{2.14}$$

$$-\dot{\Phi}_b \in N_{C_t}(\lambda_{b_t}). \tag{2.15}$$

From convex analysis, these inclusions are equivalent to implicit proximal point formulations [104]. Hence, these formulations transform the associated inclusions into nonlinear implicit equations, which are ultimately used in the (time-stepping-based) numerical solver which is developed in this work. These read as

$$\lambda_{b_a} = \mathrm{prox}_{C_a}\left(\lambda_{b_a} - r_1 \dot{U}_b\right), \tag{2.16}$$

$$\lambda_{b_t} = \mathrm{prox}_{C_t}\left(\lambda_{b_t} - r_2 \dot{\Phi}_b\right), \tag{2.17}$$

for $r_1, r_2 > 0$ arbitrary, positive constants.

Remarks During a torsional slip phase, the cutting edge is in full contact with the rock. However, during torsional stick, this contact is not necessarily fully mobilized, which results in an unknown distribution between torque associated with cutting and friction in this case. To include torsional stick in the model, it is assumed that during torsional stick the contact between the cutting edge of the bit blade and the rock remains fully mobilized. Therefore, this assumption has conditioned that the cutting component of the model in Eq. 2.6 is only valid under the conditions of a non-negative angular motion of the bit ($\dot{\Phi}_b \geq 0$) and with non-negative DOC ($d_n \geq 0$). Furthermore, a negative DOC is associated with bouncing of the bit, which indicates total loss of contact between the bit and the rock. Hence, bit-bouncing is not analyzed in this work.

2.2.3 Spatial Coulomb friction model

In drilling operations in inclined wells, the drill-string rests on the borehole wall with its own weight, resulting in additional frictional contact between the drill-string and borehole. This contact is mainly generated by a specific BHA component, the stabilizers, due to their larger diameter compared to the rest of the BHA components (see Figure 2.6). The frictional contact between the drill-string and borehole has been modelled by torque and drag models [93, 160]. In these models, the frictional contact forces depend on the normal force and the frictional coefficient between contact surfaces. In a drilling operation, the drill-string rotates and translates in axial direction. Hence, the sliding velocity of the contact point has two components, both in axial and tangential direction. Due to this spatial contact, the spatial Coulomb's friction law involves a two-dimensional force $\boldsymbol{\lambda}_T = \begin{bmatrix} \lambda_{T_a} & \lambda_{T_t} \end{bmatrix}^\top$. In Figure 2.6 a schematic representation of the forces acting on the BHA is depicted. Figure 2.6 also depicts the AST located in between the top and bottom stabilizer of the BHA. In this case, the normal force F_N is distributed over the two stabilizers. In the benchmark model (excluding AST), all friction force acts on a single stabilizer, because in the benchmark model both stabilizers related to the same DOF. Furthermore, homogeneous rock formations are considered in this study, such that the spatial friction law is assumed to be isotropic and its force reservoir is represented by a disc. The admissible values of the spatial Coulomb friction force for a single frictional contact point (i.e., as in the benchmark model) are given by the convex set C_T:

$$C_T = \left\{\boldsymbol{\lambda}_T \in \mathbb{R}^2 \mid \|\boldsymbol{\lambda}_T\| \leq \mu_w F_N\right\}, \tag{2.18}$$

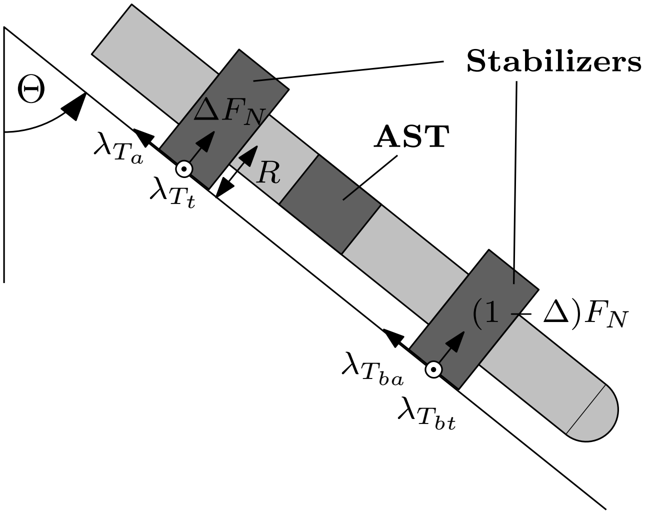

Figure 2.6: The BHA resting on its own weight in an inclined well with the axial (λ_{T_a}, $\lambda_{T_{ba}}$) and tangential (λ_{T_t}, $\lambda_{T_{bt}}$, pointing out the plane) components of the spatial friction acting on the stabilizers and the distributed normal force F_N with distribution Δ.

where μ_w is the friction coefficient and F_N denotes the normal force between the stabilizer in the BHA and the borehole wall.

Low-order lumped-parameter models for the drill-string dynamics are used in this study, such that only the gravitational effect (represented by the drill-string weight) is considered to contribute to the normal force. Thus, the possible force contributions due to the curvature of the borehole are neglected. Furthermore, it is assumed that the stabilizers are always in contact with the borehole wall. However, when the geometrical structure of the borehole is perfectly vertical ($\mathit{\Theta} = 0°$), the spatial friction force vanishes. As the normal force presumptively depends on the buoyed weight of the BHA and the inclination of the borehole structure $\mathit{\Theta}$, as depicted in Figure 2.6, this normal force is defined as

$$F_N = B_F M_{BHA} g \sin \mathit{\Theta}, \tag{2.19}$$

where M_{BHA} denotes the total mass of the BHA, g is the gravitational acceleration, and B_F is the buoyancy factor given by

$$B_F = \frac{\rho - \rho_m}{\rho}. \tag{2.20}$$

Herein, ρ is the density of the BHA and ρ_m is the density of the mud in which the BHA is submerged below the surface. Hence, the magnitude of the normal force increases as the borehole inclination ($\mathit{\Theta}$) increases.

In the benchmark model without the tool, the sliding velocity γ_T at the frictional contact between borehole and BHA is given by

$$\boldsymbol{\gamma}_T = \begin{bmatrix} \dot{U}_b \\ \dot{\Phi}_b R \end{bmatrix}, \tag{2.21}$$

where the first component is associated with the axial and the second with the tangential velocity component. In this definition, R is the outer radius of the stabilizers.

In the drill-string model with the AST tool, the BHA is separated in two parts, such that the spatial friction can act partly above and partly below the tool as shown in Figure 2.6. Essentially, the normal force F_N is distributed between the two locations, namely above and below the AST. As a consequence, the force reservoir C_T can be segregated into two smaller isotropic reservoirs. In order to enable the analysis of the cases where all the friction acts only above or below the tool, a linear distribution parameter $\Delta \in [0, 1]$ is introduced. The admissible friction force reservoirs associated to the friction forces above and below the tool are, respectively, given by the following convex sets:

$$C_T = \left\{\boldsymbol{\lambda}_T \in \mathbb{R}^2 \mid \|\boldsymbol{\lambda}_T\| \leq \Delta \mu_w F_N\right\}, \tag{2.22}$$

$$C_{T_b} = \left\{\boldsymbol{\lambda}_{T_b} \in \mathbb{R}^2 \mid \|\boldsymbol{\lambda}_{T_b}\| \leq (1-\Delta) \mu_w F_N\right\}. \tag{2.23}$$

The index b denotes the contributions, which are lumped at the bit. Note that for a straightforward comparison between the model with and without the tool, the sum of maximal allowable friction forces are equal. When $\Delta = 1$ holds, the spatial friction only acts above the AST; when $\Delta = 0$ holds, all spatial friction acts below the tool. The corresponding sliding velocities are given by

$$\boldsymbol{\gamma}_T = \begin{bmatrix} \dot{U} \\ \dot{\Phi} R \end{bmatrix}, \qquad \boldsymbol{\gamma}_{T_b} = \begin{bmatrix} \dot{U}_b \\ \dot{\Phi}_b R \end{bmatrix}. \tag{2.24}$$

The relation between the sliding velocity and the spatial friction force can be expressed by the following inclusion, using the normal cone formulation of the set-valued spatial Coulomb friction law [104]

$$-\boldsymbol{\gamma}_T \in N_{C_T}(\boldsymbol{\lambda}_T). \tag{2.25}$$

This inclusion can equivalently be written as an implicit proximal point formulation:

$$\boldsymbol{\lambda}_T = \mathrm{prox}_{C_T}\left(\boldsymbol{\lambda}_T - r\boldsymbol{\gamma}_T\right), \tag{2.26}$$

where $r > 0$ is an arbitrary positive constant.

2.2.4 Dimensionless perturbation models

The EOMs, given by Eq. (2.2), are scaled in order to reduce the number of parameters. Furthermore, the dynamics are expressed around its nominal solution (reflected by a constant angular velocity and ROP) by introducing perturbation coordinates. Following [147], a timescale t_* and a characteristic length L_* are introduced, which are defined by

$$t_* = \sqrt{\frac{I_{tot}}{C_p}}, \qquad L_* = \frac{2C_p}{\varepsilon a^2}, \tag{2.27}$$

with the total inertia in the benchmark model $I_{tot} = I$ and in the model including AST $I_{tot} = I_a + I_b$. Since the total inertia is equal in both models, the timescale is the same in both models. By using these scaling parameters, the following dimensionless perturbation coordinates are introduced

$$\begin{aligned} u(\tau) &= \frac{U - U_0}{L_*}, & u_b(\tau) &= \frac{U_b - U_{b0}}{L_*}, \\ \phi_b(\tau) &= \phi_b - \phi_{b0}, \end{aligned} \tag{2.28}$$

which are functions of the dimensionless time

$$\tau = \frac{t}{t_*}. \tag{2.29}$$

These coordinates represent the dimensionless axial and torsional perturbations with respect to its nominal responses, where the coordinates denoted with subscript b are associated with the bit. Explicit expressions for the nominal displacements U_0, U_{b0}, and Φ_{b0} in both models are given in the subsequent sections.

The generalized forces associated with set-valued force laws are scaled by a characteristic cutting force corresponding to a DOC equal to the characteristic length L_*. This results in the following dimensionless perturbation forces and torque associated to the set-valued force laws introduced in Sections 2.2.2 and 2.2.3:

$$\begin{aligned} \hat{\lambda}_{b_a} &= \frac{a}{2\zeta C_p}\left(\lambda_{b_a} - \lambda_{b_{a0}}\right), & \hat{\lambda}_{b_t} &= \frac{1}{C_p}\left(\lambda_{b_t} - \lambda_{b_{t0}}\right), \\ \hat{\boldsymbol{\lambda}}_T &= \frac{a}{2\zeta C_p}\left(\boldsymbol{\lambda}_T - \boldsymbol{\lambda}_{T_0}\right). \end{aligned} \tag{2.30}$$

Note that $\hat{\boldsymbol{\lambda}}_T$ is a column containing the dimensionless axial and tangential components of the spatial Coulomb friction. Furthermore, in the model including the AST tool, the spatial Coulomb friction acting above and below the tool both satisfy the same dimensionless perturbed form as above for $\hat{\boldsymbol{\lambda}}_T$. However, the values of each associated friction forces can be different as these are scaled by the parameter Δ in Eqs. (2.22) - (2.23). Furthermore, the nominal values of the frictional contact component in the bit–rock interaction law are $\lambda_{b_{a0}} = -na\bar{\sigma}l_n$ and $\lambda_{b_{t0}} = -\frac{1}{2}na^2\mu\xi\bar{\sigma}l_n$. Expressions for $\boldsymbol{\lambda}_{T0}$ for both models are given in the subsequent sections.

The dimensionless form of the time delay, depth-of-cut and axial and torsional nominal velocities are given by

$$\begin{aligned}\tau_n &= \frac{t_n}{t_*}, & \delta &= \frac{d}{L_*},\\ v_0 &= \frac{V_0 t_*}{L_*}, & \omega_0 &= \Omega_0 t_*. \end{aligned} \tag{2.31}$$

The nominal axial velocity V_0 (in original coordinates) in both models is given by

$$V_0 = \frac{1}{D}\left(-H_0 + M_s g - na\varepsilon\zeta d_{n0} + \lambda_{b_{a0}} + \lambda_{T_{a0}}\right). \tag{2.32}$$

The nominal DOC d_0 and the axial component of the nominal spatial friction $\lambda_{T_{a0}}$ are both functions of the nominal velocity V_0 and given by

$$d_{n0} = V_0 t_{n0}, \tag{2.33}$$

$$\lambda_{T_{a0}} = -\frac{V_0}{\Omega_0 R}\sqrt{\frac{\mu_w^2 F_N^2}{1+\left(\frac{V_0}{\Omega_0 R}\right)^2}}, \tag{2.34}$$

with $t_{n0} = {}^{2\pi}\!/\!_{(n\Omega_0)}$. Substitution of these expressions results in a fourth-order polynomial in V_0, which is monotone for positive values of V_0. Hence, Eq. (2.32) exhibits a unique solution for normal drilling operations (reflected by a positive nominal axial velocity V_0).

Moreover, the dimensionless nominal time delay is defined as $\tau_{n0} = {}^{t_{n0}}\!/\!_{t_*} = {}^{2\pi}\!/\!_{(n\omega_0)}$. The dimensionless depth-of-cut (δ) can be expressed in terms of a perturbation $\hat{\delta}$ from the nominal depth-of-cut per revolution ($\delta_0 = {}^{2\pi v_0}\!/\!_{\omega_0}$):

$$\delta = \hat{\delta} + \delta_0. \tag{2.35}$$

The dimensionless perturbed DOC $\hat{\delta}$ is given by

$$\hat{\delta} = n\left(u_b\left(\tau\right) - u_b\left(\tau - \tau_n\right)\right) + nv_0\hat{\tau}_n. \tag{2.36}$$

Note also that the dimensionless perturbed DOC produced by a single blade is given by $\hat{\delta}_n = \left(u_b\left(\tau\right) - u_b\left(\tau - \tau_n\right)\right) + v_0\hat{\tau}_n$, such that this relation $\hat{\delta} = n\hat{\delta}_n$ holds. Herein, τ_n is the dimensionless time delay, equal to $\tau_n = \hat{\tau}_n + \tau_{n0}$, where $\hat{\tau}_n$ is its perturbation from the nominal time delay τ_{n0}. This time delay is obtained with the implicit delay equation, given in Eq. (2.8), which reads in a dimensionless formulation:

$$\phi_b(\tau) - \phi_b(\tau - \tau_n) + \omega_0\hat{\tau}_n = 0. \tag{2.37}$$

2.2.4.1 Benchmark drill-string model

The column with the dimensionless perturbation coordinates in the benchmark model is given by $\mathbf{z} = \begin{bmatrix} u_b & \phi_b \end{bmatrix}^\top$. In the case of a nominal drilling operation, there are no vibrations; thus, the axial and torsional velocities are constant and positive. Due to the constant velocities, the accelerations are equal to zero. By substitution of the constant velocities and zero accelerations in the dynamic models, expressions for the nominal values of the displacements, velocities and forces are obtained. The nominal values of the axial and angular bit displacement, U_{b0} and Φ_{b0} (see Eq. (2.28)), are given by

$$U_{b0} = V_0 t, \tag{2.38}$$

$$\Phi_{b0} = \Omega_0 t + \frac{1}{C_p}\left(-D_\Phi \Omega_0 - \frac{1}{2} n a^2 \varepsilon d_{n0} + \lambda_{b_{t0}} + R\lambda_{T_{t0}}\right). \tag{2.39}$$

The nominal values of the spatial Coulomb friction ($\boldsymbol{\lambda}_{T_0} = \left[\begin{array}{cc} \lambda_{T_{a0}} & \lambda_{T_{t0}} \end{array}\right]^\top$) are given by

$$\lambda_{T_{a0}} = -\frac{V_0}{\Omega_0 R}\sqrt{\frac{\mu_w^2 F_N^2}{1+\left(\frac{V_0}{\Omega_0 R}\right)^2}}, \tag{2.40}$$

$$\lambda_{T_{t0}} = -\sqrt{\frac{\mu_w^2 F_N^2}{1+\left(\frac{V_0}{\Omega_0 R}\right)^2}}. \tag{2.41}$$

The scaling and introduction of the perturbation coordinates lead to the dimensionless EOMs in general form:

$$\mathscr{M}\mathbf{z}'' - \mathscr{H}(t,\mathbf{z},\mathbf{z}') = \mathscr{W}\hat{\boldsymbol{\lambda}}. \tag{2.42}$$

Then, the corresponding matrices and columns in Eq. (2.42) for the benchmark model are given by

$$\begin{aligned} \mathscr{M} &= \left[\begin{array}{cc} 1 & 0 \\ 0 & 1 \end{array}\right], \\ \mathscr{H}(t,\mathbf{z},\mathbf{z}') &= \left[\begin{array}{c} -\gamma u_b' - \psi\hat{\delta} \\ -\gamma_\phi \phi_b' - \phi_b - \hat{\delta} \end{array}\right], \\ \mathscr{W} &= \left[\begin{array}{cccc} \psi & 0 & \psi & 0 \\ 0 & \psi & 0 & \chi \end{array}\right], \\ \hat{\boldsymbol{\lambda}} &= \left[\begin{array}{cccc} \hat{\lambda}_{b_a} & \hat{\lambda}_{b_t} & \hat{\lambda}_{T_a} & \hat{\lambda}_{T_t} \end{array}\right]^\top. \end{aligned} \tag{2.43}$$

By using the perturbation variables, the proximal point formulations of the set-valued force laws, given by Eqs. (2.16), (2.17), and (2.26), are transformed into dimensionless perturbation coordinates. Thereto, the sliding velocity $\boldsymbol{\gamma}_T$, given for the benchmark model by Eq. 2.21, is written in terms of the dimensionless perturbation velocities. After performing the substitution of the dimensionless velocities (see Eq. (2.28) for the dimensionless perturbation coordinates) and pre-multiplying it with ${}^{t_*}/_{L_*}$, the dimensionless sliding velocity is obtained:

$$\boldsymbol{\zeta}_T = \left[\begin{array}{c} \dot{u}_b + v_0 \\ r_*\left(\dot{\phi}_b + \omega_0\right) \end{array}\right], \tag{2.44}$$

where $r_* = {}^{R}\!/_{L_*}$ is the dimensionless radius of the BHA. Thus, the set-valued force laws in terms of the dimensionless perturbation variables are given by

$$\hat{\lambda}_{b_a} = \mathrm{prox}_{\hat{C}_a}\left(\hat{\lambda}_{b_a} - r_1\left(\dot{u}_b + v_0\right)\right), \quad \text{with } \hat{C}_a = \left\{\hat{\lambda}_{b_a} \mid -na\bar{\sigma}l_n \leq \lambda_{b_a} \leq 0\right\}, \tag{2.45}$$

$$\begin{aligned} \hat{\lambda}_{b_t} &= \mathrm{prox}_{\hat{C}_t}\left(\hat{\lambda}_{b_t} - r_2\left(\dot{\phi}_b + \omega_0\right)\right), \cdots \\ &\cdots \quad \text{with } \hat{C}_t(\hat{\lambda}_{b_a}) = \left\{\hat{\lambda}_{b_t} \mid \beta\hat{\lambda}_{b_a} \leq \hat{\lambda}_{b_t} \leq \beta\hat{\lambda}_{b_a} + 2\lambda\beta\right\}, \end{aligned} \tag{2.46}$$

$$\begin{aligned} \hat{\boldsymbol{\lambda}}_T &= \mathrm{prox}_{\hat{C}_T}\left(\hat{\boldsymbol{\lambda}}_T - r_3\boldsymbol{\zeta}_T\right), \cdots \\ &\cdots \quad \text{with } \hat{C}_T = \left\{\hat{\boldsymbol{\lambda}}_T \in \mathbb{R}^2 \mid \left\|\hat{\boldsymbol{\lambda}}_T + \frac{a}{2\zeta C_p}\boldsymbol{\lambda}_{T0}\right\| \leq \frac{a}{2\zeta C_p}\mu_w F_N\right\}. \end{aligned} \tag{2.47}$$

The constants $r_1, r_2, r_3 > 0$ are not necessarily equal in both models.

2.2.4.2 Drill-string model including AST

The column with the dimensionless perturbation coordinates in the model including AST is given by $\mathbf{z} = [\begin{matrix} u & u_b & \phi_b \end{matrix}]^\top$. The nominal values of the axial and angular displacements, U_0, U_{b0}, and Φ_{b0}, are given by

$$\begin{aligned} U_0 &= V_0 t + \frac{1}{\alpha K_b}\left(\frac{1}{2}na^2\varepsilon d_{n0} + \alpha na\varepsilon\zeta d_{n0} + D_{\Phi_b}\Omega_0 \cdots\right. \\ &\quad \left.\cdots - \alpha M_{bs}g - \alpha\lambda_{b_{a0}} - \lambda_{b_{t0}} - \alpha\lambda_{T_{ba0}} - R\lambda_{T_{bt0}}\right), \end{aligned} \tag{2.48}$$

$$U_{b0} = V_0 t, \tag{2.49}$$

$$\begin{aligned} \Phi_{b0} &= \frac{1}{\alpha K_b}\left(-na\varepsilon\zeta d_{n0} + M_{bs}g + \frac{1}{\alpha}D_\Phi\Omega_0 + \lambda_{b_{a0}} + \lambda_{T_{ba0}}\right)\cdots. \\ &\quad \cdots + \left(\frac{1}{C_p} + \frac{1}{\alpha^2 K_b}\right)\left(-\frac{1}{2}na^2\varepsilon d_{n0} - \left(D_\Phi + D_{\Phi_b}\right)\Omega_0 + \lambda_{b_{t0}} + R\lambda_{T_{bt0}}\right)\cdots \\ &\quad \cdots + \frac{R}{C_p}\lambda_{T_{t0}} + \Omega_0 t. \end{aligned} \tag{2.50}$$

The nominal values of the spatial Coulomb friction located above and below the AST ($\boldsymbol{\lambda}_{T_0} = [\ \lambda_{T_{a0}} \quad \lambda_{T_{t0}} \quad \lambda_{T_{ba0}} \quad \lambda_{T_{bt0}}\ ]^\top$) are given by

$$\lambda_{T_{a0}} = -\frac{V_0}{\Omega_0 R}\sqrt{\frac{\Delta^2 \mu_w^2 F_N^2}{1+\left(\frac{V_0}{\Omega_0 R}\right)^2}}, \tag{2.51}$$

$$\lambda_{T_{t0}} = -\sqrt{\frac{\Delta^2 \mu_w^2 F_N^2}{1+\left(\frac{V_0}{\Omega_0 R}\right)^2}}, \tag{2.52}$$

$$\lambda_{T_{ba0}} = -\frac{V_0}{\Omega_0 R}\sqrt{\frac{(1-\Delta)^2 \mu_w^2 F_N^2}{1+\left(\frac{V_0}{\Omega_0 R}\right)^2}}, \tag{2.53}$$

$$\lambda_{T_{bt0}} = -\sqrt{\frac{(1-\Delta)^2 \mu_w^2 F_N^2}{1+\left(\frac{V_0}{\Omega_0 R}\right)^2}}. \tag{2.54}$$

Then, the scaled EOMs in dimensionless perturbation coordinates for the model including AST can be written in the general form of Eq. (2.42). The corresponding matrices and columns are given by

$$\begin{aligned}
\mathscr{M} &= \begin{bmatrix} m_* + \kappa\iota & -\kappa\iota & \nu\iota \\ -\kappa\iota & -m_* + \kappa\iota + 1 & -\nu\iota \\ \frac{\kappa}{\nu}\iota & -\frac{\kappa}{\nu}\iota & 1 \end{bmatrix}, \\
\mathscr{H}(t,\mathbf{z},\mathbf{z}') &= \left[\begin{array}{c} -\eta_b^2(u-u_b) - \gamma u' - \gamma_b(u'-u_b') - \nu\phi_b \cdots \\ \nu\phi_b + \kappa(u-u_b) + \nu\gamma_{\phi_1}\phi_b' + \kappa\gamma_{\phi_1}(u'-u_b') \cdots \\ -\phi_b - \frac{\kappa}{\nu}(u-u_b) - \gamma_{\phi_1}\phi_b' \cdots \end{array} \right. \\
&\qquad \left. \begin{array}{c} \cdots - \kappa(u-u_b) - \nu\gamma_{\phi_1}\phi_b' - \kappa\gamma_{\phi_1}(u'-u_b') \\ \cdots + \eta_b^2(u-u_b) + \gamma_b(u'-u_b') - \psi\hat{\delta} \\ \cdots - \gamma_{\phi_1}\frac{\kappa}{\nu}(u'-u_b') - \gamma_{\phi_2}\phi_b' - \hat{\delta} \end{array} \right], \\
\mathscr{W} &= \begin{bmatrix} 0 & 0 & \psi & \nu\chi & 0 & 0 \\ \psi & 0 & 0 & -\nu\chi & \psi & 0 \\ 0 & 1 & 0 & \chi & 0 & \chi \end{bmatrix}, \\
\hat{\boldsymbol{\lambda}} &= [\ \hat{\lambda}_{b_a} \quad \hat{\lambda}_{b_t} \quad \hat{\lambda}_{T_a} \quad \hat{\lambda}_{T_t} \quad \hat{\lambda}_{T_{ba}} \quad \hat{\lambda}_{T_{bt}}\ ]^\top,
\end{aligned} \tag{2.55}$$

with $\hat{\boldsymbol{\lambda}}$ satisfying Eqs. (2.45) – (2.47). The sliding velocities $\boldsymbol{\zeta}_T$ and $\boldsymbol{\zeta}_{T_b}$ (above and below the AST, respectively) in Eq. 2.47 are given by

$$\boldsymbol{\zeta}_T = \begin{bmatrix} \dot{u} + v_0 \\ r_*\left(\frac{\kappa}{\nu}(u'-u_b') + \dot{\phi} + \omega_0\right) \end{bmatrix}, \qquad \boldsymbol{\zeta}_{T_b} = \begin{bmatrix} \dot{u}_b + v_0 \\ r_*\left(\dot{\phi}_b + \omega_0\right) \end{bmatrix}. \tag{2.56}$$

The definitions of the characterizing dimensionless parameters in Eqs. (2.43) and (2.55) are given in Table 2.1, along with their values used in Section 2.3. The models presented in this section will now be used to analyze their dynamics, in particular to study the effect of the AST and spatial frictional on the drilling performance.

Table 2.1: Characteristic system parameters.

Parameter Name	Symbol	Value
Characteristic length	$L_* = \frac{2C_p}{\varepsilon a^2}$	7.13×10^{-4}
Characteristic time	$t_* = \sqrt{\frac{I_{tot}}{C_p}}$	0.45
Mass ratio	$m_* = \frac{M_a}{M_{tot}}$	0.92
Inertia ratio	$\iota = \frac{I_a}{I_{tot}}$	0.86
Scaled axial damping	$\gamma = \frac{D}{M_{tot}}\sqrt{\frac{I_{tot}}{C_p}}$	6.43×10^{-3}
Torsional damping above AST	$\gamma_{\phi_1} = \frac{D_\Phi}{\sqrt{I_{tot}C_p}}$	2.05×10^{-4}
Torsional damping below AST	$\gamma_{\phi_2} = \frac{D_{\Phi_b}}{\sqrt{I_{tot}C_p}}$	7.39×10^{-6}
Drill-string design	$\psi = \frac{I_{tot}a\varepsilon\zeta}{M_{tot}C_p}$	37.5
Arm Coulomb friction force	$\chi = \frac{2\zeta R}{a}$	0.96
Wearflat friction	$\lambda = \frac{a^2\bar{\sigma}l_n}{2\zeta C_p}$	16.15
Drill bit design	$\beta = \mu\xi\zeta$	0.81
Inertia mass ratio	$\kappa = \frac{I_{tot}}{\alpha^2 M_{tot}}$	0.56
Scaled lead of AST	$\nu = \frac{\alpha\kappa}{L_*}$	50.64
Scaled axial stiffness of AST	$\eta_b = \sqrt{\frac{K_b I_{tot}}{M_{tot}C_p}}$	2.06
Scaled axial damping of AST	$\gamma_b = \frac{D_b}{M_{tot}}\sqrt{\frac{I_{tot}}{C_p}}$	0.45

2.3 Drilling performance analysis

In this section, the effect of spatial Coulomb friction on the drilling performance is investigated. The drilling performance is characterized by the drilling efficiency and ROP. This chapter focuses on the effect of friction on the drilling performance under different operational conditions, namely the prescribed angular speed and the hookload at the surface. The characterizing parameters are introduced in Section 2.3.1. Next, in Section 2.3.2 the drilling performance of the benchmark model is investigated. In Section 2.3.3, the drilling performance of the model including AST is investigated and these results are compared to the benchmark model in order to investigate the effectiveness of the AST.

2.3.1 Drilling performance variables

From stability analyses of the benchmark model in the absence of spatial Coulomb friction, it is observed that the nominal solution is typically unstable for realistic operating conditions [147, 57, 182]. As a consequence, solutions diverge away from the unstable nominal response and result in a time-varying steady-state response from the nonlinear dynamics, where the nonlinearities are related to the set-valued nonlinearities in the bit-rock interaction law, the set-valued spatial friction law, and the state-dependent delay effect. The drill-string system exhibits both axial and torsional vibrations, where the torsional vibrations typically evolve over a significantly slower timescale compared to the axial vibrations. Since the torsional vibrations typically converge to a steady-state torsional limit cycle, in this section, the performance characterization variables are averaged over a torsional limit cycle.

The performance of a drilling operation is mainly characterized by the drilling efficiency [112]. The drilling efficiency reflects how much of the total torque provided to the bit is used for cutting.

Remark Note that the torque provided at the bit is in general not equal to the torque applied at the surface due to frictional losses along the drill-string.

In line with previous studies [147, 181], this efficiency is defined as the ratio between the energy devoted to the cutting process and the total energy dissipated at the bit (i.e., by cutting and frictional forces). The average drilling efficiency η is given by

$$\eta = \frac{\langle T^c \rangle}{\langle T^c \rangle + \langle T^f \rangle}. \tag{2.57}$$

Herein T^c represents the cutting torque and T^f denotes the frictional torque at the bit. The brackets $\langle \cdot \rangle$ denote the average over a torsional limit cycle. However, the averaged frictional torque at the bit, $\left\langle T^f \right\rangle$, is not directly obtained from the numerical simulation, since the frictional torque at the wearflat, T^f, acts on the same DOF as the tangential component of the set-valued Coulomb friction force below the AST, $\lambda_{T_{bt}}$ (see Eq. (2.3) and Figure 2.2 for the benchmark model and Eq. (2.5) and Figure 2.4 for the model including AST). Besides, both torques are governed by a similar set-valued force law, see Eqs. (2.15) and (2.25). As a consequence, it is not possible to distinguish between the wearflat torque and the set-valued frictional torque below the AST in numerical simulations with the model.

Let us now explain how we obtain an accurate measure for the frictional losses acting at the bit in order to assess the efficiency in Eq. (2.57). According to Eq. (2.12), the frictional torque at the bit is proportional to the wearflat reaction force W^f with a factor $\frac{1}{2}a\mu\xi$. From the model including the tool, as depicted in Figure 2.4, the average of the sum of the wearflat force and the axial set-valued friction force below the AST, $\left\langle W^f + \lambda_{T_{ba}} \right\rangle$, can directly be computed. Since the averaged axial velocity is much smaller compared to the averaged tangential velocity (i.e., $\langle \dot{U}_b \rangle / \langle \dot{\Phi}_b R \rangle = \mathcal{O}\left(10^{-4} - 10^{-2}\right)$), the frictional contact basically only produces a frictional torque and thus the axial component $\lambda_{T_{ba}}$ is negligible. Hence, the average wearflat force $\left\langle W^f \right\rangle$ is approximated by $\left\langle W^f + \lambda_{T_{ba}} \right\rangle$ and can be used to calculate the average frictional torque at the bit $\left\langle T^f \right\rangle$.

A higher drilling efficiency will result in more efficient drilling and consequently in saving drilling costs. Moreover, a higher drilling efficiency, as defined in Eq. (2.57), implies less frictional dissipation at the bit, which is generally favorable from a bit wear perspective (i.e., longer bit life-time or maintaining bit sharpness).

A control parameter in both models is the hookload H_0 at the surface (an upward force). It can be deduced that an increase in the hook-load is causing a decrease in the total weight applied to the bit, and this consequently will decrease the ROP. However, the total weight applied on the bit is not only defined by the hook-load, but also by the gravitational forces acting on the submerged drill-string. Therefore, instead of varying the hook-load, the total nominal weight applied on the bit W_0 is varied as a control parameter in the simulations. The total weight applied on the bit is defined as

$$W_0 = W_s - H_0, \tag{2.58}$$

with W_s the submerged weight of the drill-string.

Remark In general, the WOB depends on the inclination of the well, since the submerged weight of a drill-string decreases when the inclination increases. However, it is beyond the scope of this chapter to study how all individual force components vary with the inclination. Therefore, it is assumed that the hook-load is adjusted when the inclination changes such that the WOB remains constant.

2.3.2 Drilling performance of the benchmark model

The performance analysis pursued in this section focuses on the axial bit velocity, because this ultimately determines the ROP. The dynamic models as presented in Section 2.2 are simulated with a time-stepping-based numerical simulator. The structure of the numerical simulator is based on [164].

Time-domain responses of the axial bit velocity of the benchmark model with and without spatial friction between the BHA and the borehole wall are depicted in Figure 2.7. In both simulations, the same boundary conditions are applied (the total weight applied on the bit $W_0 = 171$ kN and the angular velocity at the top-drive $\Omega_0 = 80$ RPM). The initial conditions in both simulations are chosen close to the desired nominal operating conditions ($u_b(0) = \phi_b(0) = 10^{-4}$ and $\dot{u}_b(0) = \dot{\phi}_b(0) = 0$), such that the initial perturbations are small with respect to the nominal solution. Figure 2.7 (a) and (b) show the axial bit velocity without and with spatial friction, respectively. Both cases show unstable transient behavior where the oscillations grow until the bit experiences an axial (and a torsional) stick-slip limit cycle. Furthermore, the transient phase in the case with friction is longer, i.e., it requires more time to reach the axial (and torsional) limit cycle. This implies that the friction has a stabilizing effect on the drill-string dynamics, which reduces the growth rate of the axial (and torsional) vibrations. The spatial

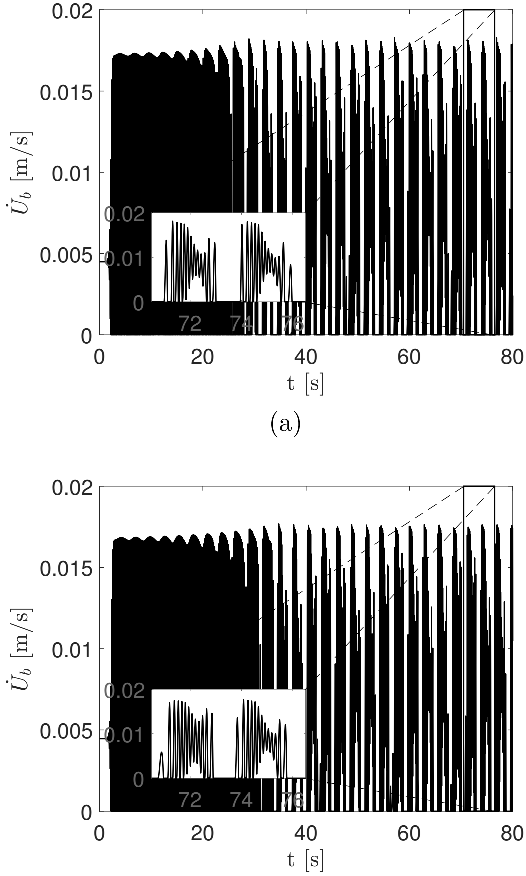

(a)

(b)

Figure 2.7: (a) The axial bit velocity for the benchmark model without friction between the BHA and borehole wall ($\Theta = 0°$) and (b) with the Coulomb friction ($\Theta = 90°$) ($W_0 = 171$ kN and $\Omega_0 = 80$ RPM).

Coulomb friction does not qualitatively change the drill-string system response of the benchmark model for this specific set of operation conditions.

Next, the effect of the spatial friction is investigated for a broad range of operation conditions. The range of the nominal WOB (W_0) corresponds with the range of hookload forces of $H_0 = 370-440$ kN. This range is chosen such that lower values result in bit-bouncing and higher values in a negative nominal axial velocity (see Eq. (2.32) for the relation between H_0 and V_0). The range of angular velocities corresponds with $\Omega_0 = 30-150$ RPM. The drilling efficiency η and averaged ROP for this range of operation conditions are depicted in Figures 2.8, 2.9 and 2.10 for different inclined scenarios with $\Theta = 0°$, $\Theta = 45°$, and $\Theta = 90°$, respectively.

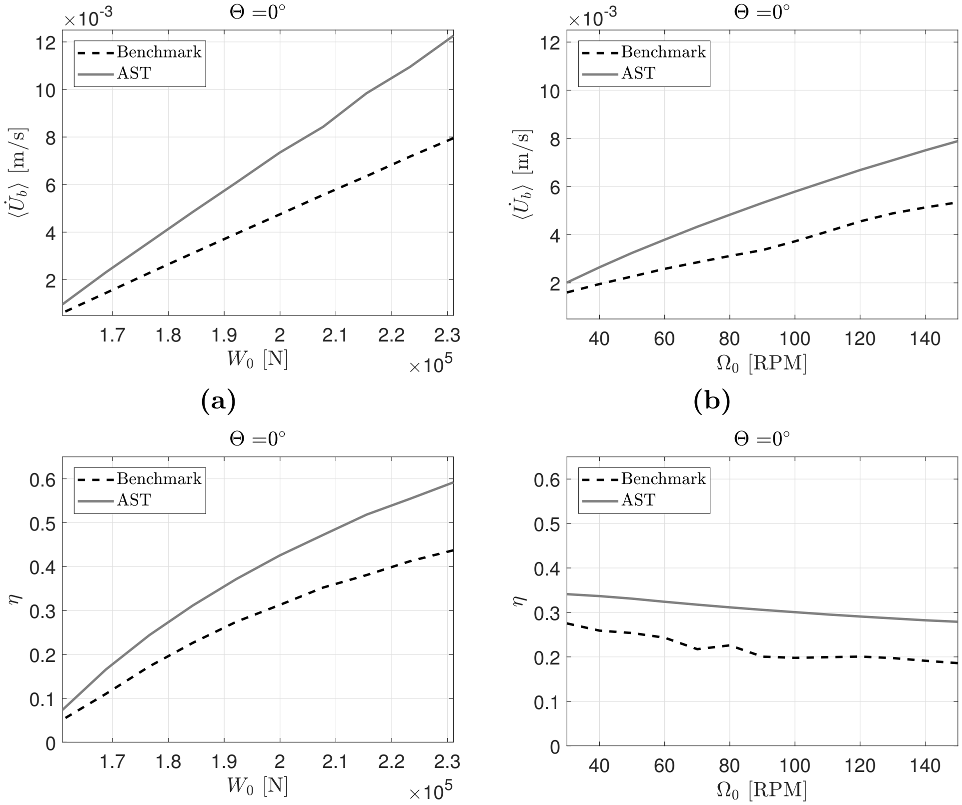

(a) **(b)**

(c) **(d)**

Figure 2.8: Drilling performance without and with AST in a vertical well with inclination angle $\Theta = 0°$. The rate-of-penetration as function of **(a)** applied WOB W_0 and **(b)** rotational velocity Ω_0 and drilling efficiency as function of **(c)** applied WOB W_0 and **(d)** rotational velocity Ω_0 ($W_0 = 171$ kN and $\Omega_0 = 80$ RPM, unless parameter is varied).

In Figures 2.8 (a) – (b), 2.9 (a) – (b) and 2.10 (a) – (b), it can be observed that the ROP increases with increasing nominal WOB and prescribed angular velocity. An increase in W_0, under a prescribed constant angular velocity, results in an increased ratio between the cutting and frictional forces. Also with faster rotation (higher values of Ω_0) more volume of rock is cut in a given time window. Furthermore, the spatial Coulomb friction has a small effect on the ROP, implying that the portion of the total force used for the cutting process is not affected significantly by the spatial friction between the BHA and borehole.

The drilling efficiency for different operation conditions is shown in Figures 2.8 (c) – (d), 2.9 (c) – (d) and 2.10 (c) – (d). An increase in the nominal WOB results in a higher drilling efficiency. This indicates that for a higher W_0 more energy is

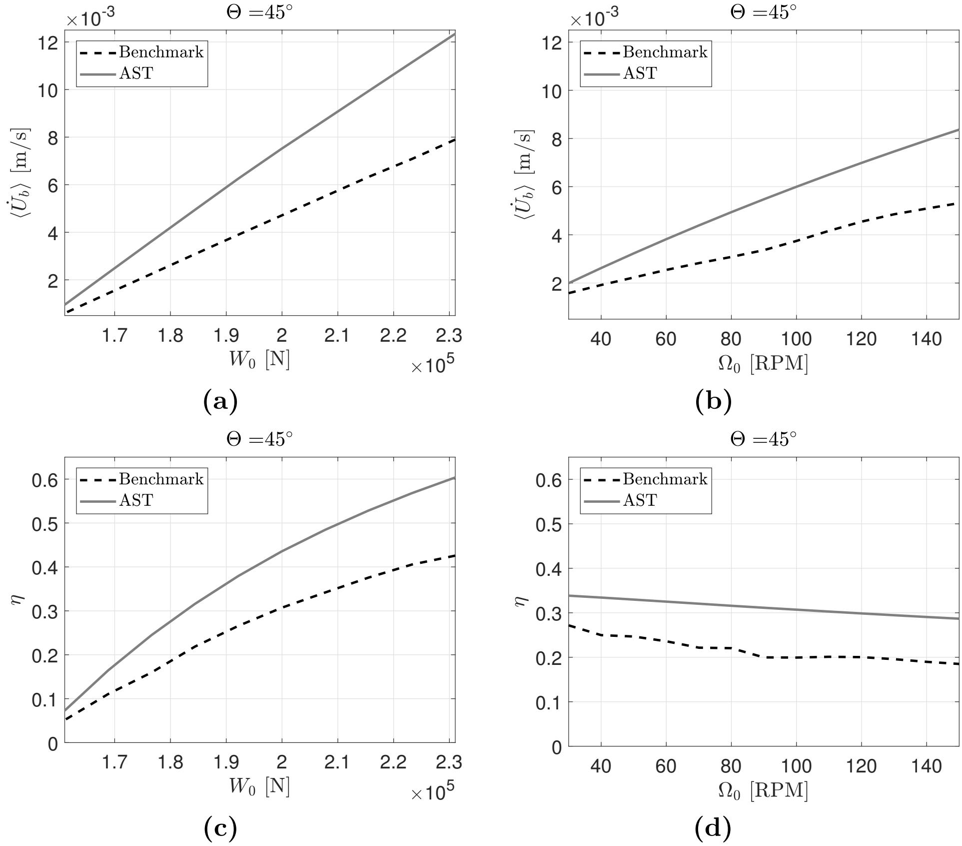

(a) **(b)**

(c) **(d)**

Figure 2.9: Drilling performance without and with AST in an inclined well with inclination angle $\Theta = 45°$. The rate-of-penetration as function of **(a)** applied WOB W_0 and **(b)** rotational velocity Ω_0 and drilling efficiency as function of **(c)** applied WOB W_0 and **(d)** rotational velocity Ω_0 ($W_0 = 171$ kN and $\Omega_0 = 80$ RPM, unless parameter is varied).

used for the cutting process, which is in line with the results in Figures 2.8 (a), 2.9 (a) and 2.10 (a). However, an increasing prescribed angular velocity results in a decreasing drilling efficiency, which indicates that less energy is used for cutting. This implies a decrease in DOC. Even with the decrease in DOC, an increased ROP is still maintained. This consequently happens since with a higher angular velocity more volume of rock is removed by cutting in a given amount of time. From these results, it can be concluded that the spatial Coulomb friction mainly acts in tangential direction.

This is a direct consequence of the large angular velocity compared to the axial velocity of the drill-string, which results in a sliding velocity (between stabilizer and borehole) with a relative small axial component compared to the tangential

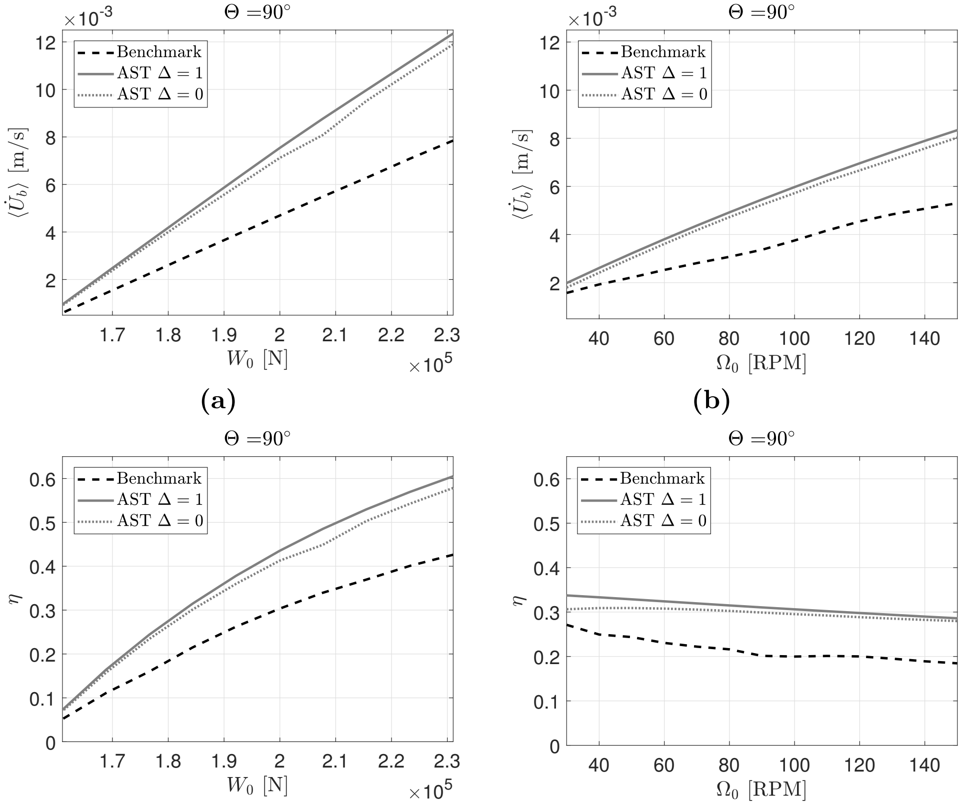

(a) **(b)**

(c) **(d)**

Figure 2.10: Drilling performance without and with AST in an inclined well with inclination angle $\Theta = 90°$. The rate-of-penetration as function of **(a)** applied WOB W_0 and **(b)** rotational velocity Ω_0 and drilling efficiency as function of **(c)** applied WOB W_0 and **(d)** rotational velocity Ω_0 ($W_0 = 171$ kN and $\Omega_0 = 80$ RPM, unless parameter is varied).

component. Consequently, this is reflected by the ratio between the axial and tangential components of the spatial Coulomb friction ($\boldsymbol{\lambda}_T = \lambda_{T_a}/\lambda_{T_t}$), which is of $\mathcal{O}\left(10^{-4} - 10^{-2}\right)$. This observation indicates that the spatial Coulomb friction basically only produces a torsional friction and consequently hardly influences the axial motion of the bit, as reflected in the ROP observations.

2.3.3 Drilling performance of the model including AST

In this section, we analyze the drilling performance of the system with AST in the presence of spatial friction between borehole and stabilizers.

Steady-state time-domain responses of the axial bit velocity for the drill-string

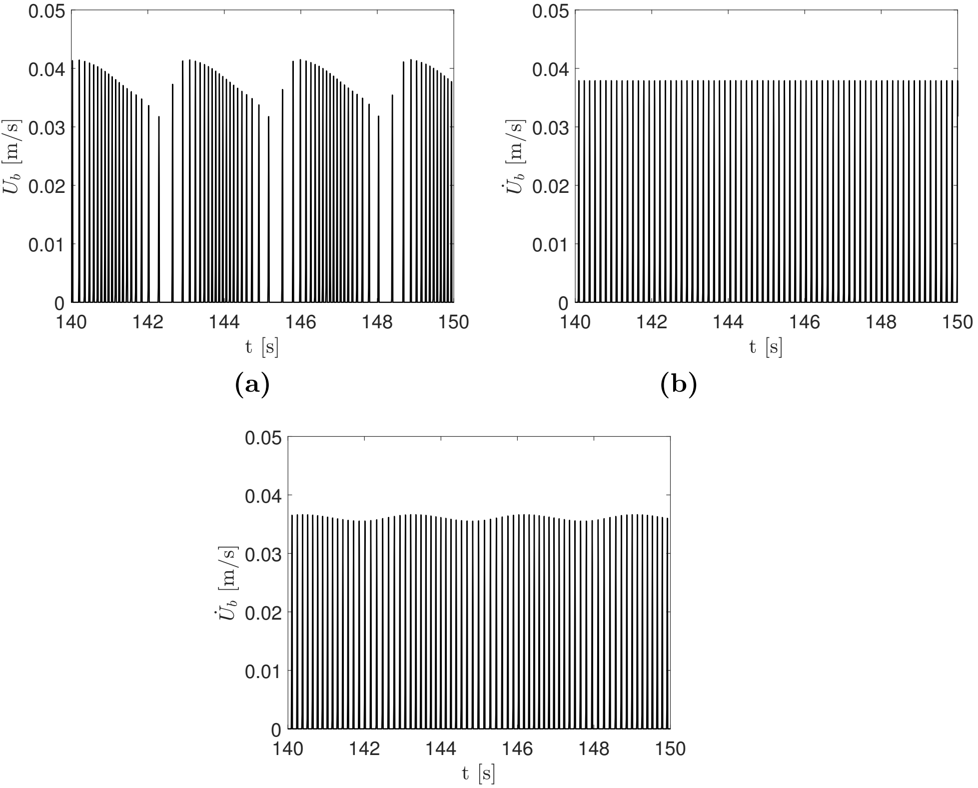

(a)

(b)

(c)

Figure 2.11: (a) The steady-state axial bit velocity for the model including AST without friction between the BHA and borehole wall ($\Theta = 0°$), (b) with Coulomb friction ($\Theta = 90°$) acting fully above the AST $\Delta = 1$, and (c) with Coulomb friction ($\Theta = 90°$) acting with fully below the AST $\Delta = 0$ ($W_0 = 171$ kN and $\Omega_0 = 80$ RPM).

model including the AST with and without spatial friction are depicted in Figure 2.11. These responses are obtained with the same boundary conditions as used in benchmark model ($W_0 = 171$ kN and $\Omega_0 = 80$ RPM). The initial conditions are chosen close to the nominal operating conditions ($u(0) = u_b(0) = \phi_b(0) = 10^{-4}$ and $\dot{u}(0) = \dot{u}_b(0) = \dot{\phi}_b(0) = 0$). In the absence of spatial Coulomb friction, the axial vibrations have a larger amplitude compared to the cases with spatial Coulomb friction. Furthermore, the axial bit velocity exhibits stick-slip transitions in cases with and without spatial friction. Comparing the response of the model including AST with response of the benchmark shows a significant difference between the axial responses. In particular, the amplitude of the axial bit velocity ($\dot{U}_b$) increases by including the AST up to two times the amplitude of the axial bit velocity obtained with the benchmark model.

The drilling performance for a range of operational conditions is depicted in Figures 2.8, 2.9 and 2.10 for different inclined scenarios with $\Theta = 0°$, $\Theta = 45°$, and $\Theta = 90°$, respectively. The trends are comparable with the benchmark model, since the increase of the nominal WOB and prescribed angular velocity result in an increasing ROP, while the drilling efficiency increases with W_0 and decreases with increasing Ω_0. These figures also indicate that the spatial friction hardly affects the ROP. However, Figure 2.10 shows that it makes a difference if the spatial Coulomb friction fully acts below ($\Delta = 0$) or above ($\Delta = 1$) the AST. In the simulations, it is observed that the axial vibrations above the tool ($\dot{U}$) decreases when the spatial friction acts fully above the tool ($\Delta = 1$). This indicates that smaller vibrations above the AST have a positive effect on the effectiveness of the tool, since it results in a slight improvement of ROP. When the friction fully acts below the tool ($\Delta = 0$), the ROP is slightly lower compared to the case without spatial friction. Furthermore, the influence of the location where the spatial friction acts is also observed in the drilling efficiency, which is lower in the case when all spatial friction acts below the tool. Hence, it can be concluded that the effect of the spatial friction on the axial vibrations, which are related to the improved drilling performance, depends on the location where the spatial friction acts. For various operational conditions (W_0 and Ω_0), the drilling performance is higher for the case where all the additional friction acts above the tool. This insight reveals that it is more beneficial in practice to place the AST closer to the bit, such that the friction acts mainly above the tool.

A comparison between the ROP and drilling efficiency obtained with the benchmark model and with the model including AST shows that incorporating the AST significantly improves the ROP and the drilling efficiency for a broad range of spatial friction levels. For example, in the case of a prescribed angular velocity $\Omega_0 = 80$ RPM and a nominal WOB of $W_0 = 192$ kN, the benchmark model results in the absence of spatial friction in a ROP of $\langle \dot{U}_b \rangle = 3.94 \times 10^{-3}$ ${}^{m}\!/{}_{s}$ and a drilling efficiency $\eta = 0.28$, see Figure 2.8. Under the same operational condition, a ROP of $\langle \dot{U}_b \rangle = 6.08 \times 10^{-3}$ ${}^{m}\!/{}_{s}$ and a drilling efficiency $\eta = 0.37$ are obtained with the model including AST. In this specific case, an increase of more than 50% in ROP and more than 30% in drilling efficiency is achieved by incorporating the AST. In the presence of spatial friction, the increase in ROP and drilling efficiency are comparable.

2.3.4 Discussion

From the performance analysis, it is concluded that the spatial friction hardly affects the ROP, since the axial component of the friction is relatively small compared to the tangential component. Furthermore, simulation results have revealed that incorporating the AST in the drill-string results in an improved drilling efficiency and ROP for a broad range of deviated wells. In case when the spatial friction acts fully above the AST, a slight improvement of drilling performance is observed compared to the case without spatial friction and when all friction acts below the tool.

2.4 Parametric study of the AST design

Based on the analysis performed in the previous section, incorporating the AST can provide a solution to improve the drilling efficiency, also in inclined drilling scenarios with increased frictional contact. From this point of view, the question arises how to find the optimal tool settings that provide the highest drilling efficiency. A parametric design study is performed in order to investigate the optimal tool design and to understand whether the optimality of this design is influenced by the frictional contacts between the BHA and the borehole wall (i.e., whether optimal tool settings can be found that robustly optimize performance for a broad range of deviated wells).

In practical field cases, the tool is placed in the bottom part of the BHA [158], which results in more mass of the BHA above the tool than below the tool. Since the largest contribution to the spatial friction comes from the heaviest part of the BHA, all simulations in this section are performed under the assumption that all spatial Coulomb friction forces fully act above the tool ($\Delta = 1$).

The tool design is mainly reflected by two parameters, namely the lead of the helical spline β and the spring stiffness K_b. In the current design of the AST, a lead angle of $\beta = 45°$ and a spring stiffness $Kb = 1522.5$ kN/m are used. The investigated range of the lead angle is in between $\beta = 10° - 70°$ and the spring stiffness range is in between $50 - 11,133$ kN/m. Higher values of spring stiffness results in bit-bouncing in absence of spatial friction. Two different operational scenarios are investigated, namely with a low angular velocity, where $\Omega_0 = 50$ RPM, and a high angular velocity, where $\Omega_0 = 120$ RPM. By considering these two operation scenarios, it can be investigated if the tool design is robust for different operational conditions. In all simulations, $W_0 = 201$ kN is used.

From the resulting parametric study, it is observed that a higher spring stiffness results in a higher frequency of the vibrations induced by the tool contraction. Furthermore, a smaller value of the lead will result in less contraction at a certain torsional displacement.

In Figure 2.12, the drilling efficiency is plotted against the lead angle and the spring stiffness for different well inclination angles with the low angular velocity case ($\Omega_0 = 50$ RPM). The shape of the surfaces characterizing the drilling efficiency have similar trends for different values of the inclination Θ, indicating that the influence of the spring stiffness and the lead on the drilling efficiency is comparable under various levels of spatial Coulomb friction. Figure 2.12 shows that for various spatial Coulomb frictions, the optimal value for the lead angle β is around 30°. Since in the current designs a lead angle of 45° is used, between 2% and 7% in drilling efficiency can be gained by changing the lead angle to 30° in this specific case with the above-mentioned operational conditions. Furthermore, it is observed that for lower values of the spring stiffness, the tool provides a higher drilling efficiency. However, the influence of the spring stiffness is relatively small compared to the influence of the lead angle.

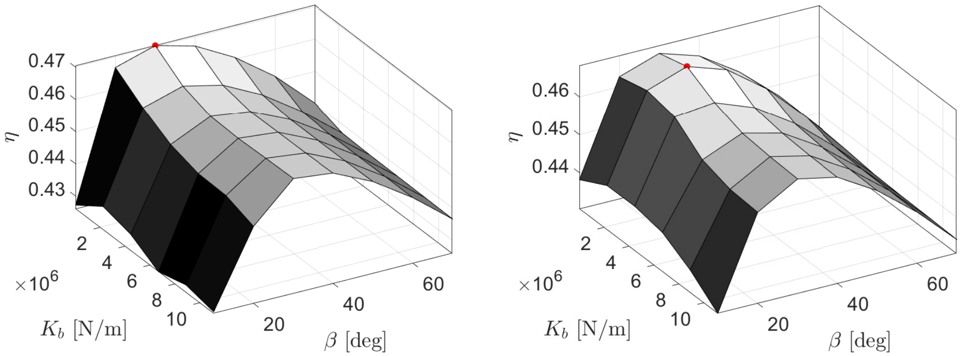

(a) $\Theta = 0°$

(b) $\Theta = 45°$

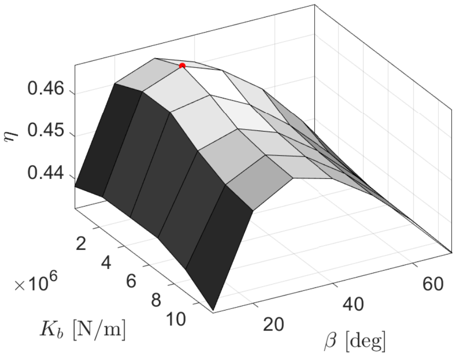

(c) $\Theta = 90°$

Figure 2.12: Drilling efficiency for different tool settings at (a) $\Theta = 0°$, (b) $\Theta = 45°$, and (c) $\Theta = 90°$ with $\Omega_0 = 50$ RPM (the low angular velocity case) and $W_0 = 201$ kN. The highest drilling efficiency is denoted by the red dots.

In Figure 2.13, the drilling efficiency for the high angular velocity case ($\Omega_0 = 120$ RPM) is depicted for various values of the lead angle and spring stiffness and for different values of inclination Θ. The shapes in these figures are slightly different compared to the low angular velocity case. The dependency of the drilling efficiency η on the spring stiffness K_b reveals a less clear trend compared to the low angular velocity case. The optimal lead angle in this case is also around $\beta = 30°$, which is equal to the low angular velocity case. However, it is observed that in the high angular velocity case the drilling efficiency is less sensitive for an increase in lead angle compared to the low angular velocity case.

Based on these results, the general conclusion is that the optimal values of the tool design are robust for different friction levels and a range of angular velocities imposed at the surface (rig). Hence, an optimal design for the AST that gives optimal drilling efficiency over a broad range of inclined scenarios is feasible.

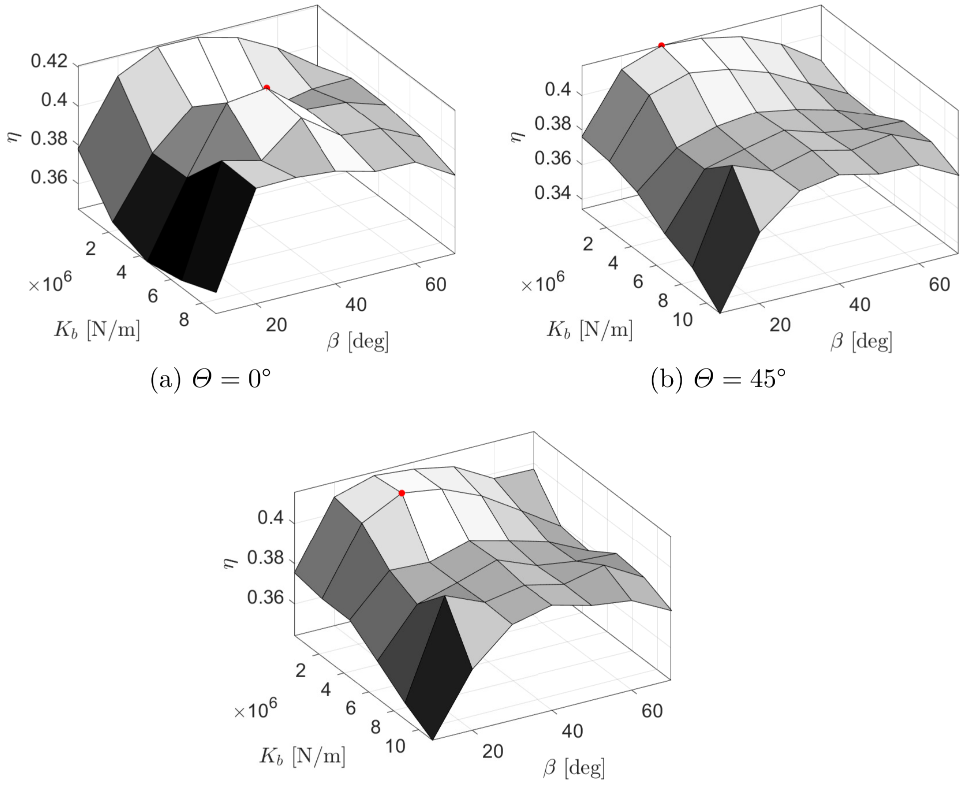

(a) $\Theta = 0°$

(b) $\Theta = 45°$

(c) $\Theta = 90°$

Figure 2.13: Drilling efficiency for different tool settings at (a) $\Theta = 0°$, (b) $\Theta = 45°$, and (c) $\Theta = 90°$ with $\Omega_0 = 120$ RPM (the high angular velocity case) and $W_0 = 201$ kN. The highest drilling efficiency is denoted by the red dots.

2.5 Conclusions

In this chapter, the effect of a passive down-hole anti-stall tool on the drilling performance of rotary drilling systems has been investigated for deviated well scenarios. A model including the coupled axial-torsional drill-string dynamics, the bit-rock interaction, the tool and the frictional effects of the stabilizers, due to borehole inclination, has been developed. A set-valued modelling approach for all contact and frictional effects has been pursued leading to a model in terms of a delay differential inclusion for which a time-stepping method is employed for simulation purposes. Numerical analysis results revealed that the down-hole tool significantly improves drilling efficiency and ROP for a broad range of deviated wells. Moreover, based on a parametric design study it is concluded that an optimal tool design, in terms of drilling efficiency, can be found that is robust for a large range of borehole inclinations and operational conditions.

Chapter 3

Bit/rock interface laws for the transition between two layers

Abstract[1] - This chapter extends bit/rock interface laws for drag (PDC) bits, originally formulated for homogeneous rocks, to the transition between two rock layers with distinct mechanical properties. It formulates a set of relations between the weight-on-bit, the torque-on-bit, the depth-of-cut per bit revolution, and the engagement parameter of the bit in the lower rock layer. This model enables us to extend the 2D $E - S$ diagram for the homogeneous case to a 3D $E - S$ diagram for the transitional case, where the third dimension is related to the engagement parameter. Moreover, this model is used to derive an expression for the drilling efficiency for the transitional phase. Examples are provided for describing the 3D $E - S$ diagram and drilling efficiency under the condition of quasi-stationary drilling (i.e., constant angular velocity, constant weight-on-bit). These examples show that the drilling efficiency depends nonlinearly on the bit engagement between the two rock layers. This intrinsic dependency is closely related to the bit shape.

3.1 Introduction

Exploration and production activities for the discovery and extraction of hydrocarbon and geothermal energy resources require to drill deep (even ultra-deep-water) well-bores into the targeted reservoir zones in the earth's crust where the resources are accumulated. Down-hole, self-excited vibrations are omnipresent phenomena when performing these drilling operations, which are typically done by rotary drilling systems equipped with Polycrystalline-Diamond-Compact (PDC) bits as sketched in Figure 3.1. PDC bits (also known as a class-type of fixed cutter

---

[1] This chapter is based on: [17] **A.G. Aribowo**, R. Wildemans, E. Detournay, N. van de Wouw, "Drag bit/rock interface laws for the transition between two layers", *International Journal of Rock Mechanics and Mining Sciences*, Volume 150, Article number 104980, 2022. Related preliminary results are reported in [18].

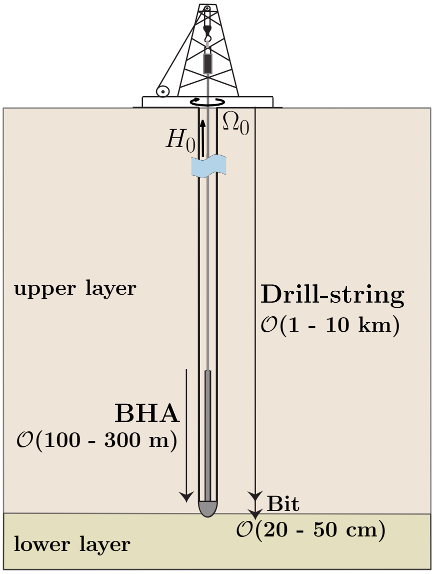

Figure 3.1: Schematic overview of a rotary drilling system with a PDC bit in drilling a vertical well-bore during a transitional phase between two rock layers.

Figure 3.2: PDC bit (after [162]).

or drag bits) consist of several bit blades on which the PDC cutters are attached (see Figure 3.2).

The vibrations at the bit are primarily caused by the interaction between the bit and the rock formation [190, 54, 76]. In addition, the bit experiences transient vibrations when transitioning between two distinct layers [87, 26, 63]. Such drilling conditions can lead to fast changes in the weight-on-bit (WOB) and torque-on-bit (TOB) arising from the bit/rock interaction, and consequently affect the total dynamics of the drill-string system. These rapid load changes on the bit may lead to bit damage and drilling in interbedding formations may significantly affect drilling efficiency [38, 31, 113, 9]. These observations motivate the development of a bit/rock interaction model for PDC bits transitioning between two layers.

The interface laws, originally introduced in [58, 59, 194] to describe the interaction between the rock and bit, have been used to analyze the response of drilling systems with PDC bits in *homogeneous* formations. In [147, 78, 27, 57, 107], these interface laws are utilized in the modeling and dynamic analyses of drill-string systems to explain the root-cause of the vibrations for drilling scenarios with PDC bits in *homogeneous* rock formations. The interface laws, being parameterized by the rock mechanical properties and the bit-design properties, couple the axial and torsional dynamics of the drill-string through both the regenerative effect (well-known in the scope of chatter phenomenon in the milling process [89]) and frictional contact. However, such interface laws for the case of the bit transitioning between two distinct rock layers are still missing in the literature.

The main contributions of this chapter are as follows:

- Firstly, we extend the bit/rock interface laws for homogeneous formations to the transition between two layers (e.g., soft and hard layers of an interbedded formation as sketched in Figure 3.1). Specifically, we derive a set of relations between the dynamic variables (the WOB W, the TOB T) and the kinematic variable d for the depth-of-cut (DOC) produced per bit revolution and the evolution parameter U for the bit engagement in the associated lower layer during the transition. Parameter U represents how deep the bit has entered the lower layer.
- Secondly, by using this novel model, we extend the 2D $E-S$ diagram (with E being the mechanical-specific-energy (MSE) and S being the drilling strength) for the homogeneous case to 3D $E-S$ diagrams for the transitional case, where the third dimension is related to the engagement parameter U.
- Finally, this model is used to find an analytical expression for the drilling efficiency for the transitional case.

The chapter is organized as follows. Section 3.2 summarizes the foundational formulation of the interface laws for the transitional phase, which consist of two components: *(i)* cutting and *(ii)* frictional contact. In Section 3.3, the dynamic variables in these components are explicitly formulated as function of the depth-of-cut and parameterized by the bit characteristics and the rock properties associated to the layer(s) with which the bit currently engages. Section 3.4 presents the extension of the $E-S$ diagram and of the drilling efficiency for the transitional phase. In Section 3.5, the MSE and the drilling efficiency are numerically investigated within a scenario of the transitional phase. Furthermore, the effect of the bit shape on the drilling efficiency is also explored. Finally, Section 3.6 draws conclusions.

3.2 Problem formulation

In this section, we formulate the foundations over which the interface laws are extended for the transitional phase between two rock layers. We recall some well-established concepts related to bit/rock interaction in *isotropic-homogeneous* rock formations. We also introduce some novel parameters related to the transitional phase that will be used in extending the interface laws.

3.2.1 Rate-independent interface laws and penetration per revolution of the bit

We consider the normal mode of bit/rock interaction, where the bit is drilling straight ahead. The response model of drilling with drag bits in this normal mode consists of a set of relations between the weight-on-bit W, the torque-on-bit T, the rate of penetration (ROP) V, and the angular velocity Ω [59, 194]. In this work, we use the coordinate basis $(\mathbf{i}_x, \mathbf{i}_y, \mathbf{i}_z)$ of the PDC bit system (see Figure 3.3). The $\mathbf{i}_z$-axis coincides with the bit axis of symmetry while pointing ahead of the bit and the origin is selected at the reference point of the bit (located at the lowest point on the bit profile). The coordinate basis of the bit system can also be represented in the cylindrical coordinate basis $(\mathbf{i}_r, \mathbf{i}_\omega, \mathbf{i}_z)$ as depicted in Figure 3.3.

The rate-independent bit/rock interface laws relate these dynamic variables (W, T) to the kinematic variable d. During the transitional phase between two rock layers, the extension of these interface laws are formulated to be parameterized by the bit engagement U in the lower layer (as the evolution parameter), such that

$$W = \widetilde{W}(d; U), \qquad\qquad T = \widetilde{T}(d; U). \tag{3.1}$$

These functions $\widetilde{W}$, $\widetilde{T}$ in Eq. (3.1) are averaged over at least one revolution of the bit. The relations are assumed to be rate-independent, as supported by experimental evidence from laboratory single cutter and drilling tests conducted under kinematic control [56, 127, 75, 142]. The kinematic variable d can also be understood as the penetration per revolution of the bit, which represents the advance of the bit in the $\mathbf{i_z}$ direction; see Figure 3.4. On the other hand, the parameter U determines the portion of the bit engaged in the lower layer during the transitional phase (to be detailed in Section 3.2.5). Herein, we assume *quasi-stationary* drilling conditions where the total WOB and the angular velocity (RPM) of the bit are constant.

3.2.2 Equivalent blade concept

The concept of *equivalent blade* introduced in [137, 194] is adopted to simplify the description of the interaction of the bit with the rock. To illustrate this concept, first we consider that all PDC cutters mounted along a bit blade on the bit body

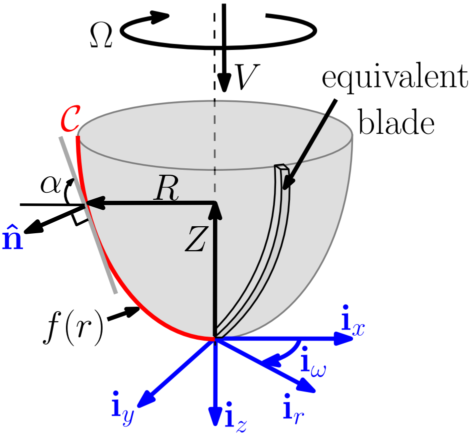

Figure 3.3: The coordinate basis for the PDC bit and an illustration of equivalent blade for a parabolic bit shape.

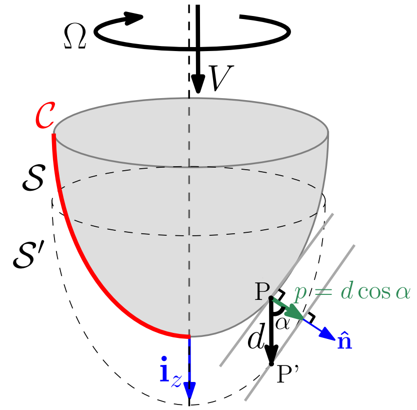

Figure 3.4: The penetration (kinematic) variable d (after [137]).

are as the outer (cutting) edge of the bit defined by a two-dimensional curve $\mathcal{C}$ (red line) illustrated in Figure 3.3. Then let us imagine that as this curve $\mathcal{C}$ fully rotates about the axis $\mathbf{i}_z$ (without the bit advancing), the cutting profile surface (i.e., $\mathcal{S}$ or $\mathcal{S}'$ as illustrated in Figure 3.4) generated by the bit can be *equivalently replaced* by a rotation of the blade depicted in Figure 3.3. Therefore, this curve describes the geometry of the *bit equivalent blade* and thus the bit shape.

In order to connect the concept of penetration per revolution and *equivalent blade*, we note that in the nominal case (steady drilling condition) the kinematic variable d_0 (produced per bit revolution in the time period $t_0 = {}^{2\pi}/_{\Omega_0}$ with a nominal RPM Ω_0) is also the instantaneous depth-of-cut produced by the *equivalent blade.* Trivially, the rate of volume of rock excavated is equal to

$\mathcal{Q}_0 = \Omega_0 d_0 \int\limits_0^a r \mathrm{d}r = \frac{1}{2} a^2 d_0 \Omega_0$, and hence the total excavated rock volume rate per revolution is $\delta \mathcal{V}_0 = t_0 \mathcal{Q}_0 = \pi a^2 d_0$. If the interface laws are indeed rate-independent, the instantaneous depth-of-cut d associated with the rotation of the *bit equivalent blade* is the only kinematic variable needed. The laws account for the effect of bit shape (to represent all contributions of the orientations of PDC cutters on the bit).

3.2.3 Bit profile

A PDC bit is characterized by its height b and its radius a. A radial coordinate R is the radial distance of a point located along the curve of the blade profile from the bit axis of symmetry (i.e., $0 \leq R \leq a$), while an axial coordinate Z is on the bit axis of symmetry with its origin at the lowest point on the bit (i.e., $0 \leq Z \leq b$); see Figure 3.3. The function

$$z := f\left(r\right) \tag{3.2}$$

characterizes the bit profile (shape). This function maps the axial coordinate $z = {}^{Z}\!/_{a}$ on the radial coordinate $r = {}^{R}\!/_{a}$. In this work, we consider a parabolic bit shape function $f(r)$ as an illustrative example; see Figure 3.3. However, these extended bit/rock interface laws are valid for a generic class of bit shapes, where we restrict the formulation of the interface laws to bit profiles with $f'(r) = {}^{\mathrm{d}f}\!/_{\mathrm{d}r} > 0$, for $0 \leq r \leq 1$. Note that if the bit has a re-entrant (nose) shape (for which $f(\cdot)$ is not invertible), the values of r can be multi-valued.

3.2.4 Local penetration

By reference to Figure 3.4, let P be a point on the bit cutting profile $\mathcal{S}$, and P' the point on the cutting profile $\mathcal{S}'$ produced after the axial translation d by the rotation of the cutting edge curve $\mathcal{C}$. The local penetration variable p is then defined as the projection of vector $\overrightarrow{PP'}$ onto $\hat{\mathbf{n}}$, and equal to

$$p = d \cos \alpha, \tag{3.3}$$

where α is the angle between the external normal direction $\hat{\mathbf{n}}$ of the curve $\mathcal{C}$ and the direction $\mathbf{i}_z$ (see Figure 3.3), i.e., $\tan \alpha = {}^{\mathrm{d}f}\!/_{\mathrm{d}r}$. Hence we have

$$\cos \alpha = \frac{1}{\sqrt{(f'(r))^2 + 1}}. \tag{3.4}$$

The local penetration p varies along the cutting profile of the blade due to the effect of the bit shape (i.e., the profile function $f(r)$). Consequently, each elementary part of the *equivalent blade* only considers this local depth produced per revolution (in the view of local symmetry between the rotational axis of the bit $\mathbf{i}_z$ and the normal direction $\hat{\mathbf{n}}$ of the cutting profiles).

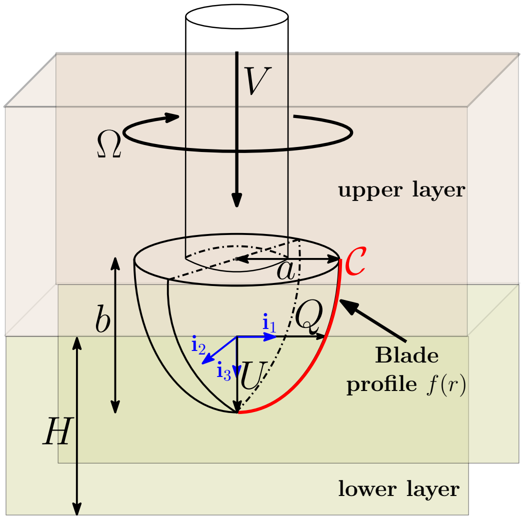

Figure 3.5: The PDC bit systems during the transitional phase and the bit engagement.

3.2.5 Bit Engagement

We introduce an engagement parameter U that identifies the bit portion being engaged in the lower layer (as depicted in Figure 3.5) and acts as the evolution parameter for the weight and torque during the transitional phase. The dimensionless engagement parameter $u \in [0, {}^{b}\!/\!{}_{a}]$ is also introduced and is related to the parameter U scaled by the bit radius a:

$$u = \frac{U}{a}, \text{ for } 0 \leq U \leq b. \tag{3.5}$$

In its initial position, the bit is assumed to be fully engaged in the upper layer (i.e., $u = 0$) with its reference point located on the interface between the two layers. We also assume that the layer thickness $H \geq b$, which implies that the bit is at most engaging in these two consecutive layers during the transitional phase.

An alternative evolution parameter, $Q \in [0, a]$, is also considered. It is defined as the radial coordinate R of the point on the blade profile located at the interface, see Figure 3.5. We consider its dimensionless form, $q = Q/a$, and use Eq. (3.2) to relate it with u in Eq. (3.5) according to

$$u = f(q), \text{ for } 0 \leq q \leq 1. \tag{3.6}$$

Parameter q is used to identify which part of the bit is engaged in the upper and lower rock layers, and can also be expressed uniquely in terms of u due to the invertibility of $f(\cdot)$ (due to its monotonicity): $q = f^{-1}(u)$, for $0 \leq u \leq {}^{b}\!/\!{}_{a}$.

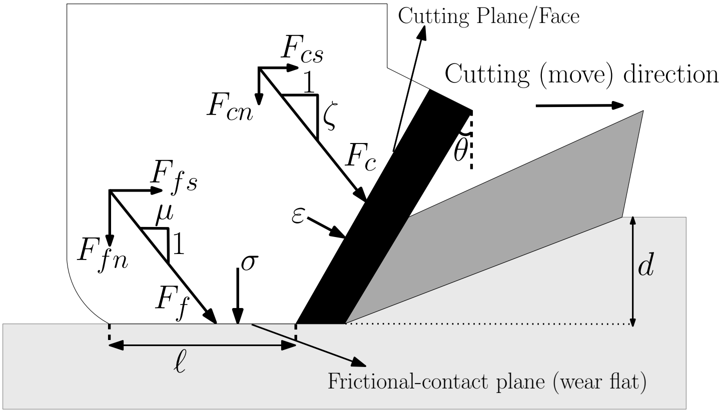

Figure 3.6: A blunt single PDC cutter (after [58, 59]).

3.2.6 Parameters of the cutter/rock interface laws

Previous works in [58, 59] have identified the cutter/rock properties that enter the interface laws when drilling *isotropic-homogeneous* rock formations (Figure 3.6). Firstly, the cutting component is parameterized by: *(i)* the intrinsic specific energy ε (in the unit of pressure), and *(ii)* the constant number ζ, characterizing the inclination of the cutting force. Secondly, the frictional contact component is parameterized by: *(i)* the coefficient of the friction μ (at the contact between the wear flat and rock), *(ii)* the maximum contact pressure σ at the wear flat interface, and *(iii)* the wear flat length ℓ that describes its state of wear (bluntness) of the cutter.

3.3 Bit/rock interface laws in the transitional phase

In this section, the interface laws in [58, 59, 194] will be extended to the transitional phase by relating the WOB and TOB to the depth-of-cut. Herein, we take into account the bit design properties, the state of wear (bluntness) of the bit, the mechanical properties of the rocks being drilled, and the evolution of the bit engagement in the two layers depicted in Figure 3.5. In this extension, the upper and lower layers are characterized by their own distinct mechanical properties denoted by the subscripts u and l, respectively, i.e., ε_u, μ_u, σ_u for the upper layer and ε_l, μ_l, σ_l for the lower one.

3.3.1 Cutting component

Consider the length L of the *equivalent blade* and its length element dL as depicted in Figure 3.7 (the yellow-gold color; top-right). Note also that $\varkappa = {}^{L}\!/_{a}$ as the

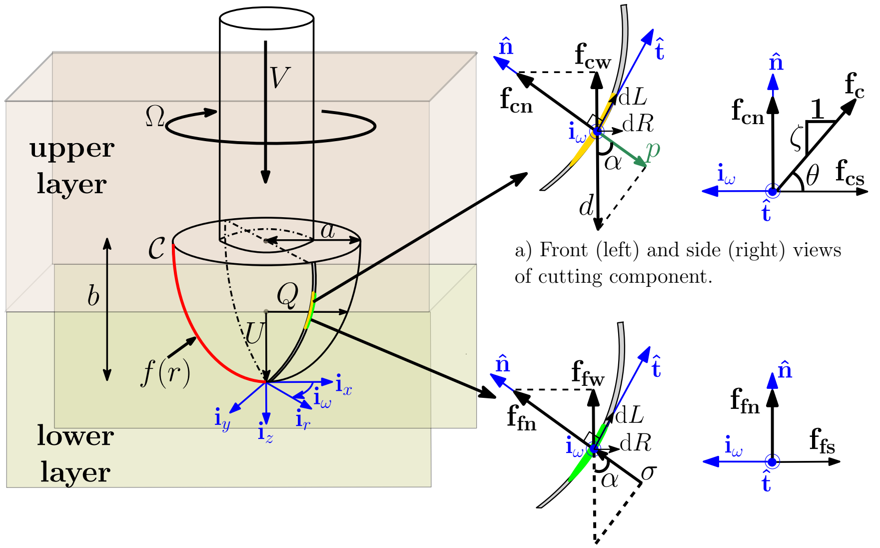

a) Front (left) and side (right) views of cutting component.

b) Front (left) and side (right) views of friction component.

Figure 3.7: Cutting and friction components of the weight-on-bit and torque-on-bit.

scaled length of the blade on the curvilinear coordinate s with respect to the bit profile (in dimensionless). The cutting force acting on this element $\mathrm{d}L$ is $\mathbf{f_c}\mathrm{d}L$, where $\mathbf{f_c}$ is the force density with dimension $[{}^{Force}/_{Length}]$. This force density can be decomposed into the horizontal component $\mathbf{f_{cs}}$ (along the surface) and the normal component $\mathbf{f_{cn}}$, i.e., $\mathbf{f_c} = -f_{cs}\mathbf{i}_\omega + f_{cn}\hat{\mathbf{n}}$; refer to the side view in Figure 3.7. Herein, the torque on bit contributed by the cutting process is generated by the horizontal component, for which its magnitude f_{cs} is given by

$$f_{cs} = \varepsilon p. \tag{3.7}$$

Note that p is the local depth of penetration as described in Eq. (3.3). By considering the relation $\mathrm{d}R = \mathrm{d}L \cos\alpha$ (equivalently $\mathrm{d}r = \mathrm{d}s \cos\alpha$ in dimensionless), the torque (contributed by this horizontal force density) can be expressed by the following integration over the radial coordinate on the bit

$$T_c = a^2 \int_0^{\varkappa} \varepsilon p r \,\mathrm{d}s = a^2 \int_0^1 \varepsilon d r \,\mathrm{d}r = \frac{a^2}{2}\varepsilon d. \tag{3.8}$$

In the transitional phase, the integration process in Eq. (3.8) must take into account the bit engagement in the upper and lower layers, since the intrinsic specific energy ε differs for the two layers. Consequently, this integration is performed for adjusted intervals (i.e., for $r \in [0, q]$ for the lower layer and for $r \in [q, 1]$ for the upper layer), which yields

$$T_c = T_c^u + T_c^l = \frac{a^2}{2} d \left(\varepsilon_u \left(1 - q^2 \right) + \varepsilon_l q^2 \right). \tag{3.9}$$

Next, for the cutting contribution to the weight-on-bit, we focus on the force density $\mathbf{f_{cn}}$ as depicted in the front and side views in Figure 3.7. The vertical component of force density with magnitude $f_{cn} \cos \alpha$ can be integrated over the length element ds on the *equivalent blade* to yield the WOB due to the cutting process

$$W_c = a \int_0^{\varkappa} \zeta \varepsilon p \cos\alpha \, \mathrm{d}s = a \zeta d \int_0^1 \varepsilon \cos\alpha \mathrm{d}r = a \varepsilon d \zeta^*. \tag{3.10}$$

We define the nominal bit design parameter for the cutting component: $\zeta^* := \zeta \, \vartheta_\zeta$ with

$$\vartheta_\zeta := \int_0^1 \frac{1}{\sqrt{\left(f' \left(r \right) \right)^2 + 1}} \mathrm{d}r, \tag{3.11}$$

as we recall Eq. (3.4) to explicitly combine the orientation of the local cutting force and the bit profile function $f(r)$ which both affect the WOB. As for the torque, the integral is split in two parts to account for the different properties of the two rock layers, which gives

$$W_c = W_c^u + W_c^l = a d \zeta \left(\varepsilon_u \int_q^1 \cos\alpha \mathrm{d}r + \varepsilon_l \int_0^q \cos\alpha \mathrm{d}r \right). \tag{3.12}$$

Similarly, from Eqs. (3.12) and (3.4) we define the bit design parameters for both upper and lower layers ($\vartheta_\zeta^u \left(q \right)$ and $\vartheta_\zeta^l \left(q \right)$, respectively) as follows:

$$\vartheta_\zeta^u(q) := \frac{1}{\vartheta_\zeta} \int_q^1 \frac{1}{\sqrt{\left(f' \left(r \right) \right)^2 + 1}} \mathrm{d}r, \quad \vartheta_\zeta^l(q) := \frac{1}{\vartheta_\zeta} \int_0^q \frac{1}{\sqrt{\left(f' \left(r \right) \right)^2 + 1}} \mathrm{d}r, \tag{3.13}$$

such that $\vartheta_\zeta^u \left(q \right) + \vartheta_\zeta^l \left(q \right) = 1$. By using Eqs. (3.11) and (3.13) in combination with Eq. (3.4), W_c in Eq. (3.12) can be rewritten as

$$W_c = a \, \zeta^* \, d \left(\varepsilon_u \, \left(1 - \vartheta_\zeta^l \right) + \varepsilon_l \, \vartheta_\zeta^l \right). \tag{3.14}$$

3.3.2 Frictional contact component

Consider an element of wear flat on the *equivalent blade* in Figure 3.7 with the length element dL (e.g., the green color; bottom-right) for calculating the frictional components of the weight-on-bit and torque-on-bit. Due to the contact stress σ applied on the wear flat element in the normal direction $\hat{\mathbf{n}}$, the force density $\mathbf{f_{fn}}$ generates the weight-on-bit. This normal force density has magnitude

$$f_{fn} = \sigma\lambda. \tag{3.15}$$

In addition, the frictional force density $\mathbf{f_{fs}}$ in the horizontal direction (along the surface) generates to the torque-on-bit, and its has magnitude $f_{fs} = \mu f_{fn}$. Note that λ is the radial distribution of the wear flat length produced by each cutter on the blade. As we assume λ a uniform radial distribution of the wear flat length, the combined wear flat length on the contact surface of the *equivalent blade* is equal to ℓ in the horizontal direction of the blade (i.e., $\ell = \int\limits_0^1 \lambda\,(r)\ \mathrm{d}r = \lambda$).

Herein, the weight acting on the bit due to the frictional contact is calculated along the blade length L using the curvilinear coordinate s with respect to the bit profile. By considering the scaled length $\varkappa = {}^{L}\!/_{a}$ and the relation dr = d$s \cos\alpha$, this frictional component of WOB can be written as the integral of the force density $f_{fw} = f_{fn}\mathrm{cos}\alpha$ with the radial coordinate r in the interval $r \in [0, 1]$:

$$W_f = a \int\limits_0^{\varkappa} \sigma\lambda\mathrm{cos}\alpha\mathrm{d}s = a\sigma \int\limits_0^1 \lambda\mathrm{d}r = a\sigma\ell. \tag{3.16}$$

In the transitional phase, again the integration interval in Eq. (3.16) is adjusted using the coordinate q, and thus the associated rock parameters for the upper and lower layers are used. This leads to

$$W_f = W_f^u + W_f^l = a\,\ell\,(\sigma_u\,(1-q) + \sigma_l q)\,. \tag{3.17}$$

Furthermore, the frictional force density with magnitude f_{fs} (using a Coulomb friction model) contributes to the torque that can be written in the following integral with the coordinate r in the same interval:

$$T_f = a^2 \int\limits_0^{\varkappa} \mu\sigma\lambda r\,\mathrm{d}s = a^2\mu\sigma \int\limits_0^1 \frac{\lambda r}{\mathrm{cos}\alpha}\,\mathrm{d}r = \frac{a^2}{2}\mu\sigma\ell\xi, \tag{3.18}$$

as we consider a uniform radial distribution of the wear flat length ($\lambda = \ell$). We define the nominal bit parameter for the frictional contact (by recalling from Eq. (3.4) that $\sec\alpha = \sqrt{(f'(r))^2 + 1}$):

$$\xi := 2 \int\limits_0^1 r\sqrt{\left(f'\,(r)\right)^2 + 1}\,\mathrm{d}r, \tag{3.19}$$

which is associated to the orientation of the contact force on the wear flat with respect to the bit shape $f(r)$.

In the transitional phase, we again adapt the interval of the integration in Eq. (3.18) for the torque with the coordinate q and use the associated rock parameters. This gives

$$T_f = T_f^u + T_f^l = a^2 \ell \left(\mu_u \sigma_u \int\limits_q^1 \frac{r}{\cos\alpha} \mathrm{d}r + \mu_l \sigma_l \int\limits_0^q \frac{r}{\cos\alpha} \mathrm{d}r \right). \tag{3.20}$$

Similar to the cutting component, we also define the bit parameters of the frictional component for both upper and lower layers ($\vartheta_\xi^u\,(q)$ and $\vartheta_\xi^l\,(q)$, respectively) as follows:

$$\vartheta_\xi^u(q) := \frac{2}{\xi} \int\limits_q^1 r\sqrt{(f'\,(r))^2+1}\,\mathrm{d}r, \quad \vartheta_\xi^l(q) := \frac{2}{\xi} \int\limits_0^q r\sqrt{(f'\,(r))^2+1}\,\mathrm{d}r, \tag{3.21}$$

such that $\vartheta_\xi^u(q) + \vartheta_\xi^l(q) = 1$ holds. Hence, by also considering the following relation obtained from Eq. (3.17):

$$a\,\ell = \frac{W_f}{(\sigma_u\,(1-q) + \sigma_l\,q)}, \tag{3.22}$$

the torque in Eq. (3.20) can be rewritten in terms of the weight W_f,

$$T_f = \frac{(\mu_u\,\sigma_u\,(1-\vartheta_\xi^l) + \mu_l\,\sigma_l\,\vartheta_\xi^l)\,a\,\xi}{2\,(\sigma_u\,(1-q) + \sigma_l\,q)}\,W_f. \tag{3.23}$$

Summarizing, Eqs. (3.9), (3.14), (3.17) and (3.23) represent the bit/rock interface laws, which map the depth-of-cut d to the weight-on-bit and torque-on-bit and also evolve with parameter q during the transitional phase.

3.4 $E-S$ diagram and drilling efficiency in the transitional phase for *quasi-stationary* drilling

In this section, the bit/rock interface laws derived for the transitional case are used to extend the $E-S$ diagram and to derive expressions for the drilling efficiency. Under the assumed *quasi-stationary* drilling conditions, the weight-on-bit W applied by the BHA is in equilibrium with the reaction force resulting from the interaction of the cutters with the rock, i.e., $W = W_c + W_f$,where W_c and W_f are given in Eqs. (3.14) and (3.17), respectively. Hence,

$$W = a\,\zeta\,\vartheta_\zeta\,\left(\varepsilon_u\,\left(1-\vartheta_\zeta^l\right) + \varepsilon_l\,\vartheta_\zeta^l\right)d + a\,l\,(\sigma_u\,(1-q) + \sigma_l q)\,. \tag{3.24}$$

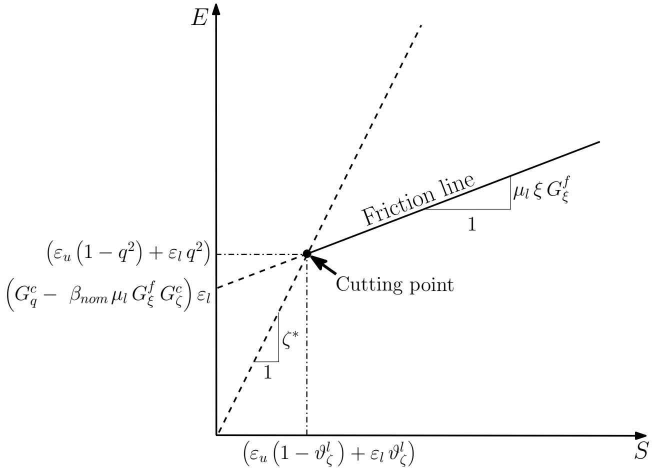

Figure 3.8: $E - S$ diagram for a given value of the bit engagement parameter u under the variations of hook-load H_0 (determining the total weight-on-bit).

Solving (3.24) for the penetration variable d yields

$$d = \frac{\left(W - a \, l \left(\sigma_u \left(1 - q\right) + \sigma_l q\right)\right)}{a \, \zeta \, \vartheta_\zeta \left(\varepsilon_u \left(1 - \vartheta^l_\zeta\right) + \varepsilon_l \, \vartheta^l_\zeta\right)}. \tag{3.25}$$

Here, we see that the kinematic variable d is a continuous function of the engagement u via the parameter q according to Eq. (3.6).

3.4.1 $E - S$ Diagram for the transitional phase

Mechanical-specific-energy (MSE) E is the quantity (in the unit of pressure) representing the amount of energy dissipated to drill a unit volume of rock. It accounts for both the work spent to fragment (cut) the rock and for frictional dissipation, and is defined as follows:

$$E := \frac{2T}{a^2 d}, \tag{3.26}$$

with the total TOB $T = T_c + T_f$, where T_c and T_f are given in Eqs. (3.9) and (3.23), respectively. Drilling strength S is defined as the quantity (in the unit of pressure) that reflects the axial force imposed on the PDC bit for producing the penetration variable d:

$$S := \frac{W}{ad}. \tag{3.27}$$

By noting the relation between the torque T_f and the weight W_f in Eq. (3.23), the definition of MSE E in Eq. (3.26) can be rewritten in terms of drilling strength S with respect to the bit engagement u (or equivalently $q = f^{-1}(u)$) as follows:

$$E = \left(G_q^c - \beta_{nom} \mu_l G_\xi^f G_\zeta^c \right) \varepsilon_l + \mu_l \, \xi \, G_\xi^f \, S, \tag{3.28}$$

with the following definitions:

$$\begin{aligned} G_q^c &:= \left(g_\varepsilon \left(1 - q^2 \right) + q^2 \right), & G_\xi^f &:= \frac{\left(g_\mu \, g_\sigma \left(1 - \vartheta_\xi^l \right) + \vartheta_\xi^l \right)}{\left(g_\sigma \left(1 - q \right) + q \right)}, \\ G_\zeta^c &:= \left(g_\varepsilon \left(1 - \vartheta_\zeta^l \right) + \vartheta_\zeta^l \right), & \beta_{nom} &:= \xi \, \zeta^*. \end{aligned} \tag{3.29}$$

Here, we define the ratio of the associated rock mechanical parameters in the cutting and frictional contact components of the interface laws for two distinct rock layers as follows:

$$g_\varepsilon := \frac{\varepsilon_u}{\varepsilon_l}, \qquad g_\mu := \frac{\mu_u}{\mu_l}, \qquad g_\sigma := \frac{\sigma_u}{\sigma_l}. \tag{3.30}$$

This analytical expression of MSE characterizes the friction line illustrated in Figure 3.8 for a particular value of parameter u; this is what we call the 2D $E - S$ diagram. Visualizing the dependency of E and S on u will lead to a 3D $E - S$ diagram, and an example will be presented in Section 3.5.

3.4.1.1 Cutting point

An ideally sharp bit blade (characterized by a wear flat length $\ell \approx 0$) is represented by the so-called cutting point in the $E - S$ diagram (the left-most point on the friction line in Figure 3.8). At the cutting point, all the energy received by the bit is entirely used for the cutting process without any frictional dissipation ($W_f = T_f = 0$). For $W_f = 0$, the nominal value of depth-of-cut in Eq. (3.25) at the cutting point becomes

$$d_{cp} = \frac{W}{a \, \zeta \, \vartheta_\zeta \left(\varepsilon_u \left(1 - \vartheta_\zeta^l \right) + \varepsilon_l \, \vartheta_\zeta^l \right)}. \tag{3.31}$$

For the cutting point, the MSE E and drilling strength S can be expressed as

$$E_{cp} = \frac{2 T_c}{a^2 d_{cp}} = \left(\varepsilon_u \left(1 - q^2 \right) + \varepsilon_l \, q^2 \right), \tag{3.32}$$

$$S_{cp} = \frac{W_c}{a d_{cp}} = \zeta^* \left(\varepsilon_u \left(1 - \vartheta_\zeta^l \right) + \varepsilon_l \, \vartheta_\zeta^l \right), \tag{3.33}$$

with the nominal bit parameter of the cutting component $\zeta^* = \zeta \, \vartheta_\zeta$; see in Eq. (3.11). This cutting point is also explicitly depicted in Figure 3.8 and depends on the parameter u.

Table 3.1: Bit and rock mechanical properties for soft and hard layers.

Parameter Name	Soft Layer	Hard Layer	Unit
Intrinsic specific energy (ε)	100	200	MPa
Contact pressure (σ)	100	200	MPa
Friction coefficient (μ)	0.5	1.0	[–]
Bit height (b)	22.2	22.2	cm
Bit radius (a)	10.8	10.8	cm

3.4.2 Drilling efficiency

The drilling efficiency is defined as the ratio between the intrinsic specific energy of the associated rock layer and the *apparent* specific energy [58, 59], represented by the MSE E. Thus for the transitional phase considered here, we refer to Eq. (3.32) for the intrinsic specific energy of the two rock layers and Eq. (3.28) for the MSE E. Hence, the drilling efficiency during the transitional phase is given by

$$\eta(q) = \frac{E_{cp}}{E} = \frac{\left(\varepsilon_u \left(1 - q^2\right) + \varepsilon_l q^2\right)}{\left(G^c_q - \beta_{nom}\, \mu_l\, G^f_\xi\, G^c_\zeta\right) \varepsilon_l + \mu_l\, \xi\, G^f_\xi\, S}. \tag{3.34}$$

The drilling efficiency evolves during the transitional phase in view of the dependence of q on the engagement u.

3.5 Illustrative case study and analysis

Next, we illustrate the $E - S$ diagram and the drilling efficiency during the transition of the bit between two rock layers.

3.5.1 $E - S$ diagram for the transitional phase: a transition from soft to hard layers

During the transitional phase, E and S depend on the bit engagement parameter $u \in [0, {}^{b}\!/_{a}]$. For the illustrative case study presented below, we consider the rock mechanical properties and the physical characteristics of the drag bit listed in Table 3.1. A parabolic bit is considered, with $f(r) = A_z r^2$, where A_z is a positive constant.

Figure 3.9 illustrates the evolution of MSE E in terms of drilling strength S as the bit transitions from a soft to a hard layers. Specifically, this 3D E–S diagram is depicted as a *friction surface* that maps all possible 2D *friction lines* for each bit engagement progression u into the lower layer (i.e., the dashed lines for fixed values of u). As such, this 3-D E–S diagram constrains all the possible states of the bit response irrespective of the WOB and the wear state of the bit.

For this particular example, the friction lines for several selected bit engagement u

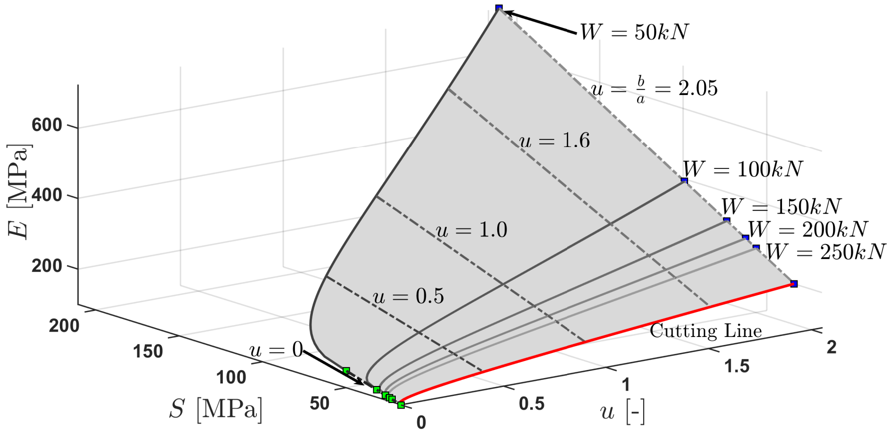

Figure 3.9: 3D $E-S$ diagram under the variations of weight W applied at the top side of PDC bit during the transitional phase from a soft-upper layer (green-square) to a hard-lower layer (blue-square).

values are depicted in dashed-gray lines. The solid lines characterize the transition from the soft-upper layer ($u = 0$ in green-square) to the hard-lower layer ($u = {}^{b}/_{a}$ in blue-square) for a constant weight W applied to the PDC bit. The green and blue squares represent the 2D friction lines for the homogeneous cases when the bit is fully engaged in the soft and hard rock layers, respectively. Increasing the weight W moves the solid lines close to the red *cutting line* (reflecting the ideal - no dissipation condition). The cutting points also evolve during the transition as a *cutting line* indicated by the red solid line and only dependent on the bit/rock parameters – conforming Eq. (3.32) for E_{cp} and Eq. (3.33) for S_{cp}.

Figure 3.10 shows the 2D projections of the 3D E–S diagram (in Figure 3.9) based on several selected values of u. The dashed lines show the friction lines for each u; see also the analytical sketch in Figure 3.8. In addition, Figure 3.11 shows the 2D projection (in solid gray lines) of the 3D $E-S$ diagram for each constant level of the applied weight W, when the bit traverses the interface from the soft-upper layer to the hard-lower one. An important observation on the basis of Figures 3.9 and 3.11 is that the bit is constrained to *nonlinear* curves in $E-S$ space during the transition at a constant weight-on-bit.

3.5.2 Drilling efficiency in transitional phase

Now we illustrate the variation of drilling efficiency given by Eq. (3.34) in a *soft-to-hard* layers transition. As shown in Figure 3.12, the drilling efficiency increases with the increasing applied weight W, and these efficiency lines move closer to an efficiency $\eta = 1$ (the red cutting line) in which no frictional contact

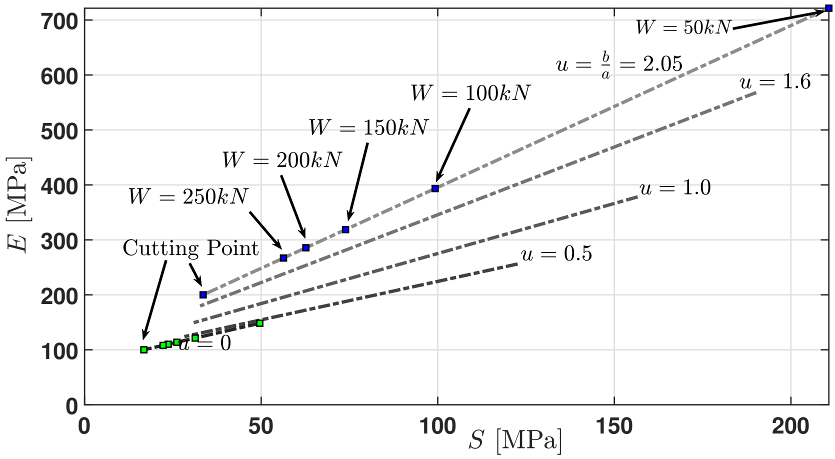

Figure 3.10: 2D projection for the selected values of u (of 3D $E-S$ diagram) for the transitional phase of bit motion from the soft-upper layer (green-square) to the hard-lower layer (blue-square).

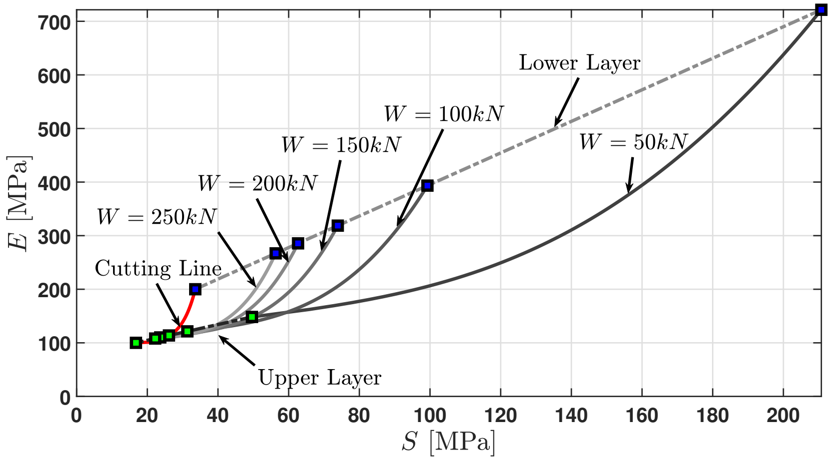

Figure 3.11: 2D projection based on the variations of W (of 3D $E-S$ diagram) for the transitional phase of bit motion from the soft-upper layer (green-square) to the hard-lower layer (blue-square).

dissipation occurs. As expected, in a *soft-to-hard* layers transition the drilling efficiency decreases with the progression of u, and this confirms the reduction in the depth-of-cut d.

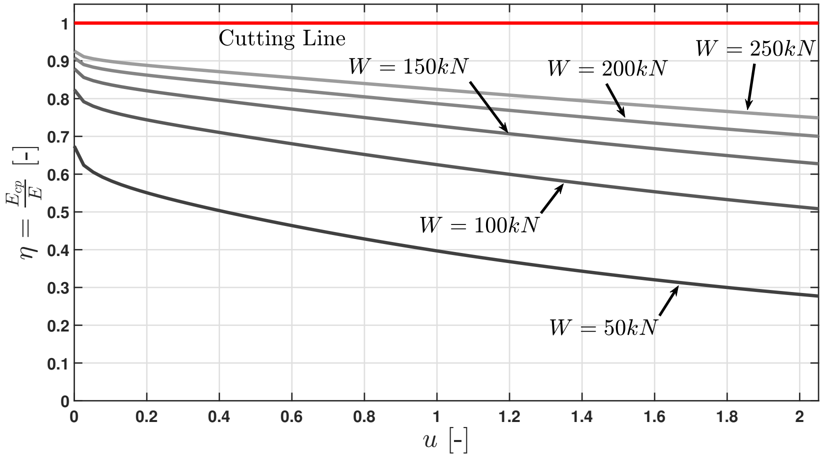

Figure 3.12: Drilling efficiency with the variations of applied weight W during the transitional phase of bit motion (with a parabolic profile) from a soft-upper layer to a hard-lower layer ($u = 0$: fully in soft layer, $u = {}^{b}/_{a} = 2.05$: fully in hard layer).

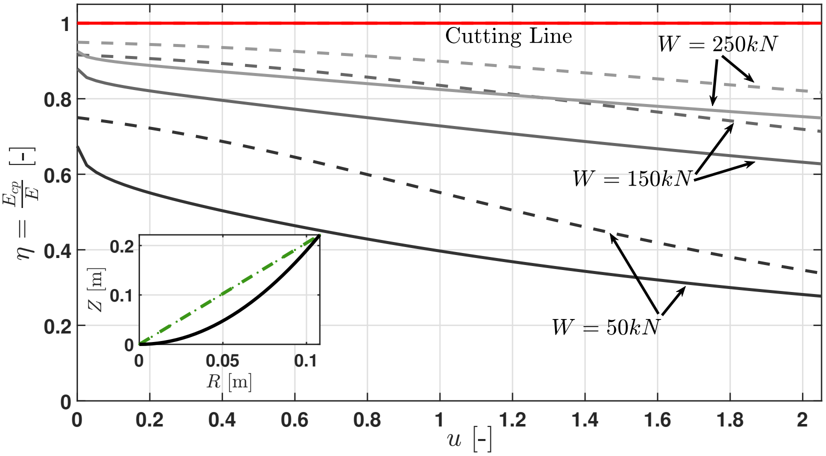

Figure 3.13: Drilling efficiencies comparison for both linear (dashed line) and parabolic (solid line) bit profiles during the transitional phase of bit motion from a soft-upper layer to a hard-lower layer ($u = 0$: fully in soft layer, $u = {}^{b}/_{a} = 2.05$: fully in hard layer).

3.5.2.1 Comparison of the drilling efficiency for different bit profiles within the transition from soft to hard layers

Notably, the transition of the drilling efficiency shows a nonlinear dependency on u, which is related to the bit shape embodied in the function $f(r)$. To assess the effect of bit profile on the drilling efficiency, we compare two different ideal bit profiles: *(i)* a linear function $f(r) = A_z r$, *(ii)* a parabolic function $f(r) = A_z r^2$), both for a *soft-to-hard* layers transition.

Figure 3.13 reveals that the drilling efficiency for the parabolic profile shows more drop-off in the early phase of the transition (i.e., for small values of the engagement u) as compared to the drilling efficiency of the linear profile. This can also be understood by realizing that, for small values of u for the parabolic bit shape, a larger (radial) portion of the bit is engaged within the lower (hard) layer than for the same value of u for the linear bit profile – see in the inset in Figure 3.13. This inset shows both the linear and parabolic bit profiles with the same height and radius of which the values are listed in Table 3.1. Consequently, these give different values of the coordinate q and the bit parameters ϑ^l_ζ and ϑ^l_ξ for the cutting and frictional components, respectively, (see Eq. (3.29)) for the calculations of drilling efficiency in Eq. (3.34).

3.6 Conclusions

This study has extended the bit/rock interface laws of fixed cutter (PDC) bits, developed earlier in [58, 59, 194] for homogeneous formations, to the case of a bit transitioning between two different rock layers. In particular, the extended formulation of the interface laws involves the adaptation of the rock mechanical properties and bit-design parameters used in the cutting and frictional contact components of the laws. Based on this novel bit/rock interaction model we, firstly, constructed 3D $E - S$ diagrams and, secondly, analyze the drilling efficiency as a function of the bit engagement in the transitional phase between two layers. From the numerical examples, these aspects have shown distinct characteristics of dynamic and kinematic variables between the homogeneous formation and two-layered formation. In addition, it has been shown that the 3D $E - S$ diagram and the drilling efficiency are highly dependent on the bit shape for such transitional phase (via the bit engagement) and deviate essentially from the well-known 2D $E - S$ diagram for homogeneous formation. This shows the relevance of these novel bit/rock interface laws for analyzing drilling efficiency. In addition, these interface laws can also be used in the scope of dynamic drill-string models for layered formations (e.g., for the analysis of vibrations).

Chapter 4

Dynamic analysis of a down-hole regulator for drilling in interbedded formations

Abstract[1] - This chapter investigates the effect of a down-hole passive regulator (AST) on the dynamics of rotary drilling systems in interbedded formations. Drilling in interbedded formations can significantly affect the vibrational signature of these systems and the associated drilling performance. Hence models to assess the impact of drilling in such formations are needed. Hereto we construct a dynamic model of the drill-string system which incorporates the bit/rock interface laws for the transitional phase of bit motion between rock layers with distinct mechanical properties. In the model, the axial and torsional dynamics of the drill-string systems are coupled by these interface laws and cast in the form of discontinuous (state-dependent) delay differential equations. Next, we include the AST in the dynamic model to enable the assessment of the influence of this down-hole tool on drilling performance, in particular in terms of rate-of-penetration (ROP) and drilling efficiency. Furthermore, we also investigate the mechanical specific energy (MSE) and steady-state power losses at the bit (due to frictional torque) for different operational conditions and rock layer thicknesses. The analysis reveals that an increased drilling efficiency and lower MSE are obtained by incorporating the down-hole tool in the drill-string, resulting in a higher ROP and a lower frictional contact between the bit and rock in interbedded formations.

---

[1] This chapter is based on: [19] **A.G. Aribowo**, R. Wildemans, E. Detournay, N. van de Wouw, “Dynamic analysis of a downhole regulator for drilling in interbedded formations", *Society of Petroleum Engineers (SPE) Journal*, Volume 28, Issue number 04, pp. 1611–1635, Paper number: SPE-214310-PA, 2023. Related preliminary results are reported in [18] and the main findings of this chapter are summarized in [14].

4.1 Introduction

Drilling deep well-bores is required for the exploration and production of energy resources trapped in the rock formations located in the subsurface. Furthermore, drilling operations play an important role in a full-scale carbon capture and storage (CCS) project – as an effort to mitigate the effects of global climate change by reducing CO_2 emission into the atmosphere [130]. One of the keystones for the economic feasibility in completing these operations is to improve the drilling performance and consequently reducing the capital and operational expenditures.

Although rotary drilling systems equipped with fixed cutter bits (also known as Polycrystalline-Diamond-Compact or simply PDC bits) are widely recognized as being the most efficient for drilling operations [87, 9], they are prone to severe self-excited vibrations that are generated by the bit/rock interaction [76, 147, 57, 169]. The vibrations inevitably lead to damage to the drilling equipment, early fatigue of drill pipes and premature failure of the bits [190, 54, 37, 72]. In particular, layered rock formations, which consist of soft and hard layers with distinct rock mechanical properties, further influence the dynamical response of the rotary drilling systems and result in a decrease of drilling performance [113, 26, 134, 63].

To face these operational challenges and improve the performance of drilling operations in interbedded formations, the development of new technologies has been pursued, including the development of a down-hole passive regulator, the so-called AST, as reported in [53]. An impression of AST is given in Figure 4.1 (left) with the green-colored section of drill-string, above the bit. Field results have shown that the use of the AST can improve the drilling performance in terms of the drilling efficiency and ROP [141]. This passive mechanical down-hole tool installed in a section of the Bottom-Hole-Assembly (BHA) also improves the life-time of the drill-bit (i.e., less damage on the drill-bit after one run), especially when drilling in heterogeneous formations that contain hard and soft layers [158, 140, 10].

In previous studies to investigate the effect of the AST on drilling performance, a model-based approach was pursued, particularly to study the effect of the tool in terms of ROP and drilling efficiency when drilling vertical [181] and deviated wells [187]. For this purpose, a two degrees-of-freedom (2 DOFs) discrete model of the rotary drilling system (here referred to as the RGD model [147]) was extended to incorporate the AST.

In the RGD model and its extensions with the AST, the (rate-independent) bit/rock interface laws for homogeneous formation were applied as the boundary conditions at the bit [58, 59]. All these works considered homogeneous rock formations and did not account for interbedded rock formations and their effect on the bit/rock interaction and, in turn, on the drilling response. Therefore in this chapter, a scenario of drilling in a layered formation is considered, as sketched in Figure 4.1 (right). Thus, the main aim of this chapter is to investigate: *(i)* the drill-string dynamics when drilling interbedded formations with distinct mechanical properties (e.g., soft and hard layers), and *(ii)* the impact of the AST tool on

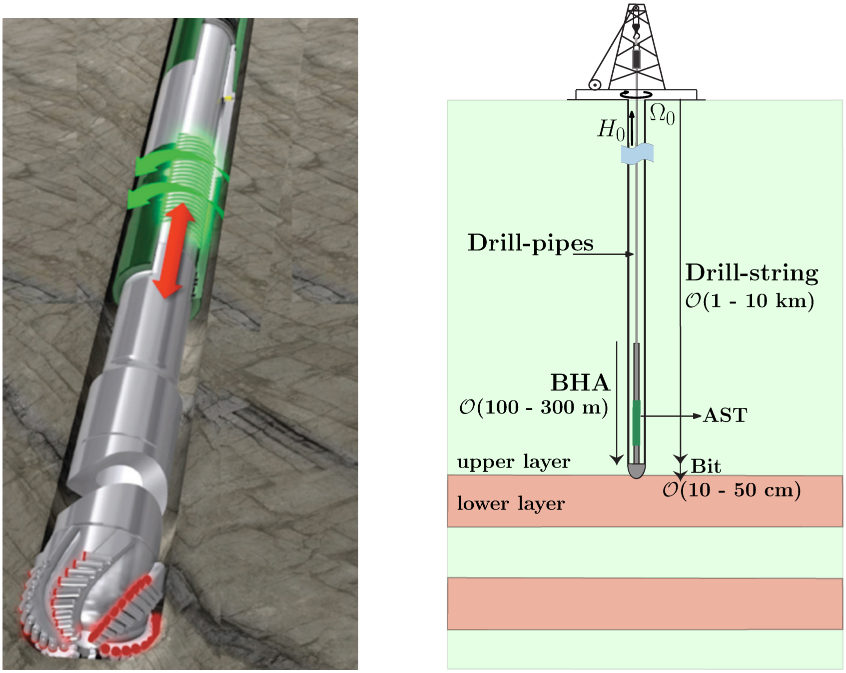

(a) (b)

Figure 4.1: (a) AST tool (Source: Tomax AS). (b) Schematic overview of rotary drilling system equipped with PDC bit and the AST in a vertical well-bore during a transitional phase between two rock layers.

the drilling performance in such scenarios.

With these goals in mind, the main contributions of this work can be summarized as follows:

- Firstly, we extend the dynamic drill-string model in [147, 57], originally limited to drilling homogeneous formations, to account for heterogeneous, interbedded formations. Hereto, we exploit novel bit/rock interface laws [17] that relate the dynamic variables to the kinematic variables at the bit and involve the transitional phase of the bit motion between two rock layers.
- Secondly, we further extend this model by including a model for the AST tool and thereby extend existing models for drilling systems with the AST tool in [181, 187].
- Thirdly, we perform a comparative dynamic analysis of these two models to investigate: *i)* the effect of the interbedded rock formation on the drilling response, and *ii)* the effect of the AST tool on the drilling performance.
- Finally, the effect of AST on the frictional dissipation at the bit is also

analyzed within the same scenario of drilling interbedded formations. This investigation sheds light on how the AST tool helps to prevent bit damage (due to friction-induced (heat) loading of the cutters) in drilling interbedded formations.

The chapter is organized as follows. Section 4.2 summarizes the two foundations for this study: *(i)* the bit/rock interface laws for the transition between two layers, and *(ii)* the dynamic models of a drill-string system without and with AST. In Section 4.3, a dynamic analysis is performed to investigate the effect of the heterogeneous nature of the formation on the drilling response and the impact of the AST tool on this response in terms of ROP, drilling efficiency, and MSE. Subsequently, this section is closed by further discussing the effect of AST on the frictional torque dissipation and power losses within the same drilling scenario. Finally, conclusions are drawn in Section 4.4.

4.2 Modeling of the Drill-String Dynamics in Interbedded Formations

In this section, the bit/rock interface laws including the transitional phase and both dynamic models of drill-string systems (benchmark model without AST tool (BM) and a model with AST (AST)) in drilling interbedded formations are presented. Referring to the schematic overview of a rotary drilling system in Figure 4.1 (right), we employ the interface laws as the boundary conditions (BC) at the bottom of the drill-string. The applied hook-load H_0 and prescribed angular velocity (RPM) Ω_0 act as the BC at the surface.

4.2.1 Bit/Rock Interface Laws for the Transitional Phase between Two Layers

The (rate-independent) bit/rock interface laws constructed in [17] are a set of relations between the dynamic variables, namely weight on bit (WOB) W and torque on bit (TOB) T, and two physical quantities of the bit motion (in steady-state drilling condition): *(i)* the kinematic variable d as the depth-of-cut (DOC) produced per bit revolution, and *(ii)* the evolution parameter Z_b as the bit engagement in the associated lower layer during the transition between two layers. The interface laws account for both cutting and frictional contact processes. The forces associated to these two processes depend on the mechanical properties of the rock layers and on the bit-design parameters.

4.2.1.1 Bit Profile

In the interface laws, a simplified representation of PDC bit is considered. The bit is characterized by its height b and its radius a as depicted in Figure 4.2,

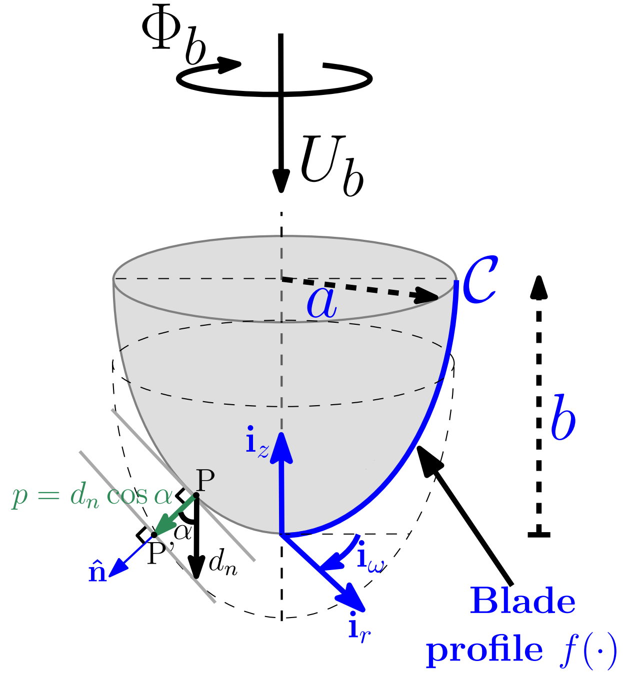

Figure 4.2: Bit profile and local penetration p of a single bit blade [194, 17].

and consists of n symmetric radial blades separated by an angular distance ${}^{2\pi}/_{n}$ between two successive blades. The radial distance between a point located on the edge of the blade profile (the cutting edge curve $\mathcal{C}$) and the bit axis of symmetry is denoted by R (i.e., $0 \leq R \leq a$), while the vertical distance between a point located on the bit axis of symmetry and the origin at the lowest point on the bit is denoted by Z (i.e., $0 \leq Z \leq b$).

The cylindrical coordinate basis $(\mathbf{i}_r, \mathbf{i}_\omega, \mathbf{i}_z)$ on the bit is introduced where the $\mathbf{i}_z$-axis coincides with the bit axis of symmetry while pointing upward and the origin is selected at the reference point of the bit (located at the lowest point on the bit profile). In this coordinate basis, the bit profile (the shape of the cutting edge curve $\mathcal{C}$) is characterized by a (dimensionless) function $f(\cdot)$ with the following mapping:

$$z = f\left(r\right), \tag{4.1}$$

where the variables are obtained by scaling the two distance quantities on the bit with the bit radius a : *(i)* $z = {}^{Z}/_{a}$, and *(ii)* $r = {}^{R}/_{a}$. In this chapter, we consider a parabolic bit shape function $f(r) = a_z r^2$ with a positive constant a_z.

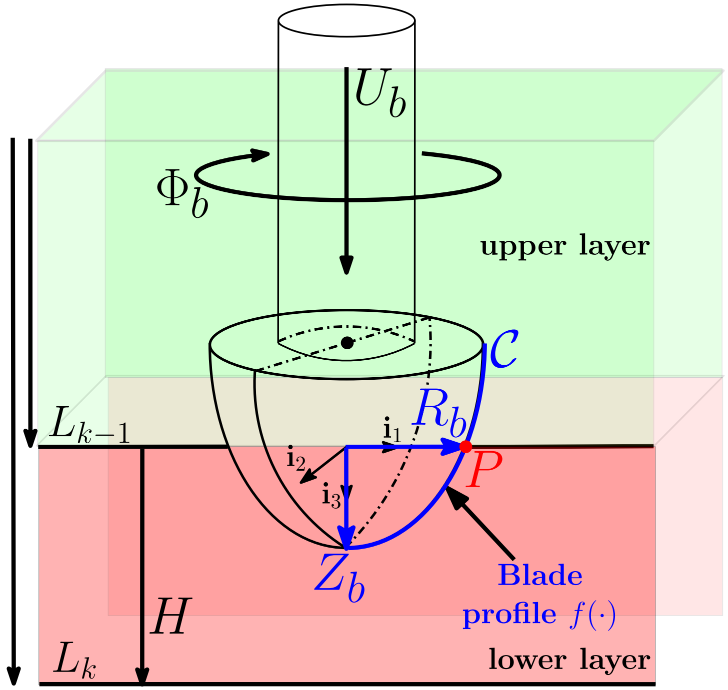

Figure 4.3: The bit engagement during the transitional phase.

4.2.1.2 Interbedded Formations

The interbedded formations, as considered here, are represented by a layered structure of alternating soft and hard, thin layers with the total number of layers equal to K. We index each rock layer with $k \in \{1, 2, 3, \ldots, K\}$. To distinguish the two layers involved in a transitional phase of the bit motion, the upper layer is denoted as the $(k-1)^{th}$ layer, while the lower layer is as k^{th} layer; see Figure 4.3. The interface between these two subsequent distinct layers is located at the depth L_{k-1} with $L_0 = 0$. For simplicity [2], each layer is assumed to have the same thickness H, where $L_k - L_{k-1} = H$ for all $k \in \{1, 2, 3, \ldots, K\}$.

In this chapter, we consider scenarios where the layer thickness H is equal to or larger than the bit height b. This constraint implies that the bit is at most engaging in two consecutive layers during the transitional phase. Hence, the bit/rock interface laws described below distinguish between two conditions: *(i)* the bit is fully engaged in a single rock layer (as a temporarily homogeneous phase), and *(ii)* the bit is partially engaged in two consecutive layers as depicted in Figure 4.3 (as a transitional phase).

---

[2] The models presented here are, however, also valid for the layer thickness H dependent on the layer index k, i.e., varied thickness of each layer in the rock formations

4.2.1.3 Bit Engagement

At the interface of two rock layers, let consider the coordinate basis $(\mathbf{i}_1, \mathbf{i}_2, \mathbf{i}_3)$. The $\mathbf{i}_3$-axis coincides with the bit axis of symmetry while pointing ahead of the bit, and the $\mathbf{i}_1$-axis coincides with the layer interface (see Figure 4.3). The origin of this coordinate system is selected at the intersection between the bit axis of symmetry and the interface.

As the advance of the bit in the $\mathbf{i}_3$ direction during a transitional phase, the coordinate system on the bit $(\mathbf{i}_r, \mathbf{i}_\omega, \mathbf{i}_z)$ also moves relatively to this coordinate system at the interface $(\mathbf{i}_1, \mathbf{i}_2, \mathbf{i}_3)$. Now let consider a point P (in red as depicted in Figure 4.3) located at the intersection of the cutting edge curve $\mathcal{C}$ with the horizontal interface line. At P, we define the evolution parameter Z_b as the vertical distance that represents how deep the bit has entered into the lower layer relative to the layer interface. At the same point, we also define the radial distance R_b calculated from P to the origin of the coordinate system $(\mathbf{i}_1, \mathbf{i}_2, \mathbf{i}_3)$ located on the interface. Note that these two parameters evolve as the bit progresses into the lower layer.

Furthermore, by scaling these quantities at the interface with the bit radius a, firstly we have the dimensionless engagement (evolution) parameter

$$z_b = \frac{Z_b}{a}, \quad \text{for } 0 \leq Z_b \leq b, \tag{4.2}$$

such that $z_b \in [0, {}^{b}\!/_{a}]$. Secondly, we have an alternative evolution parameter r_b that is given by

$$r_b = \frac{R_b}{a}. \tag{4.3}$$

Under the coordinate system on the bit $(\mathbf{i}_r, \mathbf{i}_\omega, \mathbf{i}_z)$, we relate these two dimensionless evolution parameters via the bit profile function in Eq. (4.1) and arrive into the following mapping for the bit engagement in the lower layer:

$$z_b = f(r_b), \quad \text{for } 0 \leq r_b \leq 1. \tag{4.4}$$

Parameter r_b is used to identify which part of the bit is engaged in the upper and lower rock layers; r_b can also be expressed uniquely in terms of z_b due to the invertibility of $f(\cdot)$ (due to its monotonicity): $r_b = f^{-1}(z_b)$, for $0 \leq z_b \leq {}^{b}\!/_{a}$.

4.2.1.4 Bit Kinematics: Depth-of-Cut and Time-Delay

In Figure 4.4, the generalized coordinates for describing the drill-string response at the bit are the axial and angular displacements of the drill bit, respectively denoted as U_b and Φ_b. The quantity t_n denotes the (state-dependent) time-delay arising from the bit/rock interaction due to the cutting process (also known as

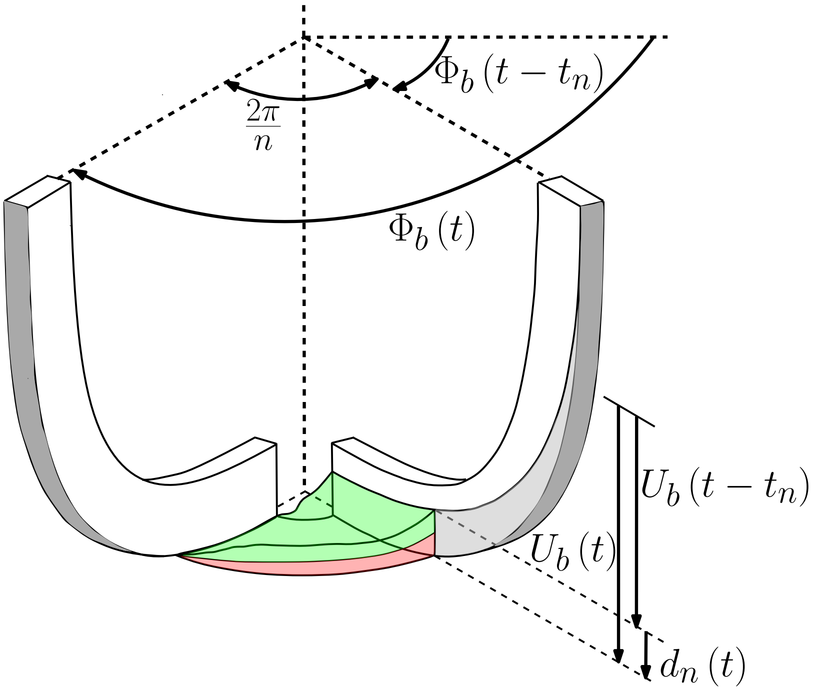

Figure 4.4: Bottom-hole profile between two successive blades of a drill-bit.

the *regenerative cutting effect*), which is equal to the time interval in which the bit rotates $^{2\pi}/_{n}$ rad (the angle between two-successive blades on the PDC bit). Thus, the delayed axial and angular displacements are denoted by $U_b(t-t_n)$ and $\Phi_b(t-t_n)$, respectively. Note also that the axial displacement U_b corresponds to the lowest point at the bit [147].

The time-delay t_n is characterized by the following implicit relation based on the angular displacements (as illustrated in Figure 4.4):

$$\int\limits_{t-t_n(t)}^{t} \frac{\mathrm{d}\Phi_b(s)}{\mathrm{d}s}\mathrm{d}s = \Phi_b(t) - \Phi_b(t-t_n(t)) = \frac{2\pi}{n}. \tag{4.5}$$

The time-delay t_n plays a key role in the reaction force and torque acting on the bit due to the cutting process, in particular for calculating the instantaneous depth-of-cut produced by each blade that is given by

$$d_n(t) = U_b(t) - U_b(t-t_n). \tag{4.6}$$

Note that we also employ the concept of local penetration [194, 17] that gives the local depth p produced per revolution as depicted in Figure 4.2. This local depth p varies along the cutting profile of the blade (the curve $\mathcal{C}$) due to the effect of the bit shape in terms of the profile function $f(\cdot)$, and is calculated as the projection of vector $\overrightarrow{PP'}$ onto the normal direction $\hat{\mathbf{n}}$ as follows:

$$p = d_n \cos\alpha, \text{ with } \cos\alpha = \frac{1}{\sqrt{(f'(r))^2+1}}. \tag{4.7}$$

This depth is used to calculate the part of the cutting component of the WOB W and TOB T.

Furthermore, the bit engagement Z_b in the lower rock layer is updated via

$$Z_b(t) = \min(b, U_b(t) - L_{k_*-1}), \tag{4.8}$$

where k_* is the minimum $k \in \{1,2,3,\ldots,K\}$ such that it holds that $U_b(t) - L_{k_*-1} \geq 0$, with $L_0 = 0$. The layer index k_* is also updated based on the latest displacement $U_b(t)$ relative to the depth L_{k-1} as the bit progresses into the lower layer.

4.2.1.5 Cutting Component of the Torque and Weight On the Bit

According to [17], the reaction torque acting on the bit due to the cutting process in interbedded formations (either in temporary-homogeneous or transitional phase) is expressed:

$$T^c = \frac{a^2}{2} d\left(\varepsilon_{k-1}\left(1-r_b^2\right) + \varepsilon_k r_b^2\right). \tag{4.9}$$

with $d = nd_n$ as the total depth-of-cut of n identical blades on the bit. The mechanical properties influencing the cutting component of the bit/rock interface laws are the rock intrinsic specific energies in upper and lower layers, ε_{k-1} and ε_k, respectively (in the unit of pressure).

The contribution of the cutting process on the weight on bit can be written as

$$W^c = a\,\zeta^*\,d\left(\varepsilon_{k-1}\left(1-\vartheta_k^\zeta\right) + \varepsilon_k\,\vartheta_k^\zeta\right). \tag{4.10}$$

Herein, the nominal bit-design parameter ζ^* is defined as $\zeta^* := \zeta\,\vartheta^\zeta$ with a positive constant ζ and

$$\vartheta^\zeta := \int_0^1 \frac{1}{\sqrt{\left(f'(r)\right)^2+1}} \mathrm{d}r, \tag{4.11}$$

that describes the orientation of the local cutting force in each cutter and thus depends on the bit profile function $f(r)$. Parameter ϑ_k^ζ in Eq. (4.10) is the bit design parameter of the cutting component in the lower layer and is defined as

$$\vartheta_k^{\zeta}(r_b) := \frac{1}{\vartheta^{\zeta}} \int\limits_0^{r_b} \frac{1}{\sqrt{\left(f'(r)\right)^2 + 1}} \mathrm{d}r. \tag{4.12}$$

This parameter depends on the bit engagement Z_b in Eq. (4.8) via Eqs. (4.2) – (4.4).

4.2.1.6 Wear-Flat-Induced Component of the Torque and Weight On the Bit

In the contributions associated with the frictional contact between the cutter wear-flat and rock, the reaction contact force acting on the wear-flats λ_a is formulated as a set-valued force law at the velocity level (reflecting the unilateral contact law; see [104]) by the following inclusion [17]:

$$\lambda_a \in -\left(\bar{\sigma}_{k-1}\,(1 - r_b) + \bar{\sigma}_k\, r_b\right) n\, a\, \ell_n\, g\left(\dot{U}_b\right), \tag{4.13}$$

with $\bar{\sigma}_{k-1}$ and $\bar{\sigma}_k$ as the maximum contact pressure at the wear-flat interface in upper and lower layers, respectively. The axial velocity of the drill bit is denoted by $\dot{U}_b$, and ℓ_n is the length of the wear-flat. The function $g(\cdot)$ is the velocity-dependent set-valued function defined as

$$g\left(\dot{U}_b\right) := \frac{1}{2}\left(1 + \mathrm{Sign}\left(\dot{U}_b\right)\right), \quad \text{with} \quad \mathrm{Sign}\,(y) := \left\{ \begin{array}{ccc} 1 & & y > 0 \\ {[-1, 1]} & , & y = 0 \\ -1 & & y < 0 \end{array} \right. . \tag{4.14}$$

In addition, as a consequence of the set-valued nature of the law in Eq. (4.13), the admissible values of the reaction contact force λ_a on the wear-flat form a convex set C_a given by

$$C_a = \left\{\lambda_a \,\middle|\, -\left(\bar{\sigma}_{k-1}\,(1 - r_b) + \bar{\sigma}_k\, r_b\right) n\, a\, \ell_n \leqslant \lambda_a \leqslant 0\right\}. \tag{4.15}$$

Furthermore, this frictional contact results in a frictional torque acting on the bit. This torque, as formulated in [17], is associated with the Coulomb friction law and thus obeys the set-valued force law on velocity level via the following inclusion:

$$\lambda_t(\lambda_a) \in \frac{\left(\mu_{k-1}\,\bar{\sigma}_{k-1}\,(1 - \vartheta_k^{\xi}) + \mu_k\,\bar{\sigma}_k\,\vartheta_k^{\xi}\right) a\,\xi\,\lambda_a}{2\left(\bar{\sigma}_{k-1}\,(1 - r_b) + \bar{\sigma}_k\, r_b\right)}\,\mathrm{Sign}\left(\dot{\Phi}_b\right), \tag{4.16}$$

with μ_{k-1} and μ_k as the frictional coefficients (for the bit-rock contact) in upper and lower layers, respectively, and $\dot{\Phi}_b$ the angular velocity of the drill bit. The nominal bit-design parameter ξ in Eq. (4.16) represents the orientation and the distribution of wear-flats that are dependent on the bit shape function $f(r)$, and is expressed as

$$\xi := 2 \int_{0}^{1} r \sqrt{\left(f'(r)\right)^2 + 1}\, \mathrm{d}r. \tag{4.17}$$

Parameter ϑ_k^{ξ} in Eq. (4.16) is the bit design parameter of the frictional component in the lower layer and is defined as

$$\vartheta_k^{\xi}(r_b) := \frac{2}{\xi} \int_{0}^{r_b} r \sqrt{\left(f'(r)\right)^2 + 1}\, \mathrm{d}r. \tag{4.18}$$

This parameter also depends on the bit engagement Z_b in Eq. (4.8) via Eqs. (4.2) – (4.4); see also the bit design parameter of the cutting component in Eq. (4.12). In addition, the admissible values of the frictional torque λ_t in Eq. (4.16), which depends on the reaction (normal) contact force λ_a, also form a convex set C_t given by

$$C_t = \left\{\lambda_t \mid \beta\lambda_a \leqslant \lambda_t \leqslant -\beta\lambda_a\right\}, \tag{4.19}$$

with

$$\beta = \frac{a\,\xi\,(\mu_{k-1}\,\bar{\sigma}_{k-1}\,(1-\vartheta_k^{\xi}) + \mu_k\,\bar{\sigma}_k\,\vartheta_k^{\xi})}{2\,(\bar{\sigma}_{k-1}\,(1-r_b) + \bar{\sigma}_k\,r_b)}. \tag{4.20}$$

4.2.1.7 Total WOB and TOB

The total weight and torque acting on the bit due to the cutting process and frictional contact in the bit/rock interaction can be summarized as follows:

$$W = W^c + W^f, \tag{4.21}$$

$$T = T^c + T^f, \tag{4.22}$$

where W^c and T^c are given by Eqs. (4.10) and (4.9), respectively. We also have $W^f = -\lambda_a$ and $T^f = -\lambda_t$, with λ_a and λ_t obeying Eqs. (4.13) and (4.16), respectively. Note that the superscripts c and f are associated with the cutting and frictional contact components of the bit/rock interaction, respectively, while the subscripts a and t refer to the axial and torsional directions, respectively. See also the list of bit parameters in Table B.2 in Appendix B.1.

4.2.2 Dynamic Drill-String Models without and with AST

In this work, we consider the lumped-parameter modeling approach (similar to the works in [181, 187]) for constructing the equations of motion (EOMs) of the benchmark model (BM) and the AST model (AST) for drilling in interbedded formations. Note that the difference between the developed model in this work and that in the earlier works [181, 187] is related to the fact that the bit/rock interface laws change essentially from a scenario of homogeneous rock formation to the scenario of an interbedded formation. This chapter presents a dynamic drill-string model, including the AST and a bit/rock interaction in a layered formation. The bit/rock interface laws, summarized in the previous section, represent boundary conditions that couple the axial and torsional dynamics of the drill-string, as depicted in Figures 4.5 and 4.7 for the BM and AST models, respectively. Hence, the dynamics of these models are written in the following compact general form:

$$\mathbf{M}\ddot{\mathbf{q}}\left(t\right)-\mathbf{h}\left(t,\mathbf{q}\left(t\right),\dot{\mathbf{q}}\left(t\right),\mathbf{q}\left(t-t_n\left(t\right)\right)\right)=\mathbf{W}\boldsymbol{\lambda}, \tag{4.23}$$

or in a simpler form for notational convenience by omitting the dependence of $\mathbf{q}$ on the time variable t:

$$\mathbf{M}\ddot{\mathbf{q}}-\mathbf{h}\left(t,\mathbf{q},\dot{\mathbf{q}},\mathbf{q}_{t_n}\right)=\mathbf{W}\boldsymbol{\lambda}. \tag{4.24}$$

Herein, $\mathbf{q}$ is the column vector with the generalized coordinates. Furthermore, we define the column vector $\mathbf{q}_{t_n}:=\mathbf{q}\left(t-t_n\left(t\right)\right)$ for storing the delayed generalized coordinates. The matrix $\mathbf{M}$ is the symmetric, positive-definite mass matrix. The generalized forces and torques related to smooth processes (i.e., they exclude the contact force and frictional torque acting on the bit) are collected in the column $\mathbf{h}$, i.e., damping, stiffness, gravitational forces, the top-side boundary conditions (hook-load, imposed angular velocity) and cutting process taking place at the bit/rock interface. The force and torque acting on the bit due to the frictional contact between the cutter wear-flat and rock are collected in the column $\boldsymbol{\lambda}$. In addition, the generalized directions of these contact force and frictional torque acting on the bit are collected in the matrix $\mathbf{W}$. The low-frequency dynamics of the real system are embedded in this discrete model of the drill-string system in Eq. (4.24).

4.2.2.1 *Benchmark (BM) Model*

In Figure 4.5, the lumped-parameter benchmark (BM) model is schematically depicted, and the EOMs are written in the compact form of Eq. (4.24), where its components are detailed as follows. The generalized coordinates $\mathbf{q}$ in the BM model are given by

$$\mathbf{q}=\left[\begin{array}{cc} U_b & \Phi_b \end{array}\right]^{\top}. \tag{4.25}$$

The delayed coordinates $\mathbf{q}_{t_n}$ are given by

$$\mathbf{q}_{t_n}=\mathbf{q}\left(t-t_n\left(t\right)\right)=\left[\begin{array}{cc} U_b\left(t-t_n\left(t\right)\right) & \Phi_b\left(t-t_n\left(t\right)\right) \end{array}\right]^{\top}. \tag{4.26}$$

In the BM model, the mass matrix reads

$$\mathbf{M}=\left[\begin{array}{cc} M & 0 \\ 0 & I \end{array}\right], \tag{4.27}$$

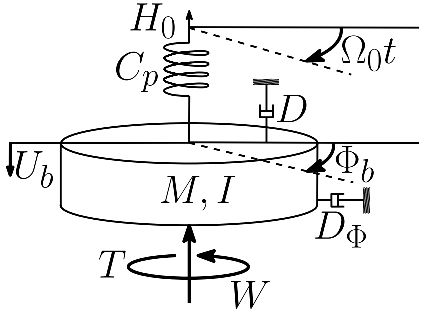

Figure 4.5: Benchmark model of a drill-string system equipped with a PDC bit in a vertical well-bore (BM model).

with M denoting the total mass of drill-string and I the total inertia.

The column $\mathbf{h}$ in Eq. (4.24) for the BM model reads as follows:

$$\mathbf{h}\left(t, \mathbf{q}, \dot{\mathbf{q}}, \mathbf{q}_{t_n}\right) = \begin{bmatrix} -D\dot{U}_b \\ -D_\Phi \dot{\Phi} - C_p\left(\Phi_b - \Omega_0 t\right) \end{bmatrix} + \begin{bmatrix} W_a \\ 0 \end{bmatrix} + \begin{bmatrix} -W^c \\ -T^c \end{bmatrix}, \quad (4.28)$$

with D the axial damping coefficient and D_Φ the torsional damping coefficient – all to represent the viscous friction terms along the drill-pipes and the BHA. The stiffness of the drill-string is represented by the torsional stiffness C_p. As the imposed boundary conditions at the topside, we have the followings: *(i)* the top angular velocity (RPM) Ω_0, and *(ii)* the hook-load H_0 (in upward direction, driven by the top-drive system of the rig). Then, the applied force (weight) at the bit W_a is expressed as

$$W_a = W_s - H_0. \quad (4.29)$$

Herein, $W_s = B_f M g$ is the total drill-string weight that is submerged in the drilling fluids (mud), where B_f is the buoyancy factor due to the mud and g is the gravitational acceleration. The force W^c and torque T^c acting on the bit due to the cutting process in the bit/rock interaction follow Eq. (4.10) and Eq. (4.9), respectively.

The column $\boldsymbol{\lambda}$ for the BM model is constructed in the following way:

$$\boldsymbol{\lambda} = \begin{bmatrix} \lambda_a & \lambda_t \end{bmatrix}^\top, \quad (4.30)$$

with the generalized directions of these frictional components given by

$$\mathbf{W} = \begin{bmatrix} 1 & 0 \\ 0 & 1 \end{bmatrix}. \quad (4.31)$$

The axial contact force λ_a and frictional torque λ_t obey the set-valued force laws in Eqs. (4.13) and (4.16), respectively.

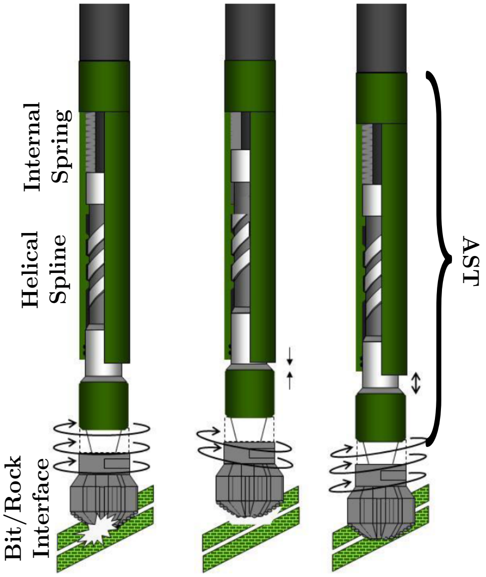

Figure 4.6: The key components and an example of the contraction movement of the Anti-Stall Tool (AST) [158, 140, 141].

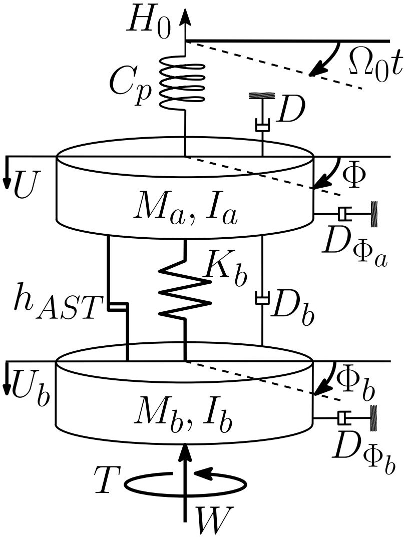

Figure 4.7: Model of drill-string system equipped with PDC bit and the AST in a vertical well-bore (AST model).

4.2.2.2 ***AST Model***

Figure 4.6 describes the two key components of the AST: an internal preloaded spring and a helical spline. The AST couples the axial and torsional dynamics of the drill-string as an increase of torque causes the contraction of the tool. In Figure 4.7, the lumped-parameter model including the AST (here referred as the AST model) is schematically depicted. The EOMs for the AST model are also written in the form of Eq. (4.24). In this model, the drill-string system is divided into two sections: *(i)* the section above the AST and *(ii)* the section below the AST. The generalized coordinates $\mathbf{q}^{\mathbf{g}}$ of the AST model read

$$\mathbf{q}^{\mathbf{g}} = \begin{bmatrix} U & \Phi & U_b & \Phi_b \end{bmatrix}^{\top}. \tag{4.32}$$

The additional coordinates, U and Φ, are the axial and angular displacements of the (lumped) drill-string section above the AST, respectively (see Figure 4.7). Due to the presence of the AST, the generalized coordinates $\mathbf{q}^{g}$ are subject to a kinematic, holonomic constraint that is representative of the design of the AST; via the lead p as a function of lead angle β and the spline radius r_{sp} (see also [181, 187]). This kinematic constraint can be written as

$$(U(t) - U_b(t)) = \frac{p}{2\pi r_{sp}} \left(r_{sp}\Phi(t) - r_{sp}\Phi_b(t)\right), \tag{4.33}$$

or alternatively as follows:

$$h_{AST} = \alpha\left(\Phi(t) - \Phi_b(t)\right) - \left(U(t) - U_b(t)\right) = 0, \tag{4.34}$$

where we define

$$\alpha := \frac{p}{2\pi}, \quad \text{with} \quad p := 2\pi r_{sp}\tan\beta. \tag{4.35}$$

As detailed in [187], the set of dependent generalized coordinates $\mathbf{q}^{g}$ in Eq. (4.32) can be transformed into the following independent generalized coordinates $\mathbf{q}$ due to this kinematic constraint of AST:

$$\mathbf{q} = \begin{bmatrix} U & U_b & \Phi_b \end{bmatrix}^{\top}. \tag{4.36}$$

The delayed coordinates $\mathbf{q}_{t_n}$ for the AST model are then given by

$$\mathbf{q}_{t_n} = \mathbf{q}\left(t - t_n(t)\right) = \begin{bmatrix} U\left(t - t_n(t)\right) & U_b\left(t - t_n(t)\right) & \Phi_b\left(t - t_n(t)\right) \end{bmatrix}^{\top}. \tag{4.37}$$

Furthermore, the mass M_a and the inertia I_a lump the drill-string section above the AST (see Figure 4.7). The torsional stiffness C_p and the axial damping coefficient D for this section above the AST are the same as in the BM model. We also consider the torsional damping coefficient D_{Φ_a} as one of the viscous friction terms on the section above the AST.

The mass M_b and the inertia I_b are considered for the drill-string section below the AST, including another torsional damping coefficient D_{Φ_b} as the viscous friction term in this section. Note also that the total mass and total inertia of the drill-string sections above and below the AST (in the AST model) is equal to the mass and inertia in BM model, respectively, i.e., $M = M_a + M_b$ and $I = I_a + I_b$. This also applies on the total torsional damping coefficients of the sections above and below the AST, which is equal to the torsional damping coefficient in the BM model, i.e., $D_\Phi = D_{\Phi_a} + D_{\Phi_b}$.

In addition, we denote the total submerged drill-string weights above and below the AST as $W_{as} = B_f M_a g$ and $W_{bs} = B_f M_b g$, respectively. The boundary conditions imposed at the topside in the AST model are also the top angular velocity Ω_0 and the hook-load H_0. The flexibility in the AST are described by the stiffness K_b and damping coefficient D_b.

Hence, the EOMs of AST model can be formulated in the form of Eq. (4.24) in terms of three independent coordinates $\mathbf{q}$ as in Eq. (4.36). The mass matrix $\mathbf{M}$, column $\mathbf{h}$ and matrix $\mathbf{W}$ are given by:

$$\mathbf{M} = \begin{bmatrix} M_a + \frac{1}{\alpha^2} I_a & -\frac{1}{\alpha^2} I_a & \frac{1}{\alpha} I_a \\ -\frac{1}{\alpha^2} I_a & M_b + \frac{1}{\alpha^2} I_a & -\frac{1}{\alpha} I_a \\ \frac{1}{\alpha} I_a & -\frac{1}{\alpha} I_a & I_a + I_b \end{bmatrix}, \tag{4.38a}$$

$$\begin{aligned} \mathbf{h}\left(t, \mathbf{q}, \dot{\mathbf{q}}, \mathbf{q}_{t_n}\right) = \left[\begin{array}{c} -K_b\left(U - U_b\right) - D\dot{U} - D_b\left(\dot{U} - \dot{U}_b\right) + W_{as} - H_0 \cdots \\ K_b\left(U - U_b\right) + D_b\left(\dot{U} - \dot{U}_b\right) + W_{bs} - W^c \cdots \\ -D_{\Phi_a}\left(\frac{1}{\alpha}\left(\dot{U} - \dot{U}_b\right) + \dot{\Phi}_b\right) - D_{\Phi_b}\dot{\Phi}_b - T^c \cdots \end{array}\right. \\ \begin{array}{c} \cdots - D_{\Phi_a}\left(\frac{1}{\alpha^2}\left(\dot{U} - \dot{U}_b\right) + \frac{1}{\alpha}\dot{\Phi}_b\right) - C_p\left(\frac{1}{\alpha^2}\left(U - U_b\right) + \frac{1}{\alpha}\Phi_b\right) \cdots \\ \cdots + D_{\Phi_a}\left(\frac{1}{\alpha^2}\left(\dot{U} - \dot{U}_b\right) + \frac{1}{\alpha}\dot{\Phi}_b\right) + C_p\left(\frac{1}{\alpha^2}\left(U - U_b\right) + \frac{1}{\alpha}\Phi_b\right) \cdots \\ \cdots - C_p\left(\frac{1}{\alpha}\left(U - U_b\right) + \Phi_b\right) \cdots \end{array} \\ \left.\begin{array}{c} \cdots + \frac{1}{\alpha} C_p \Omega_0 t \\ \cdots - \frac{1}{\alpha} C_p \Omega_0 t \\ \cdots + C_p \Omega_0 t \end{array}\right], \end{aligned} \tag{4.38b}$$

$$\mathbf{W} = \begin{bmatrix} 0 & 0 \\ 1 & 0 \\ 0 & 1 \end{bmatrix}, \tag{4.38c}$$

where the frictional/contact components to the weight- and torque-on-bit in $\boldsymbol{\lambda}$ again obey the set-valued force laws in Eqs. (4.13) and (4.16), and are expressed as in Eq. (4.30). The lists of drill-string parameters and variables used in the BM and AST models are given in Table B.3 in Appendix B.1 and Table B.4 in Appendix B.4, respectively. In order to reduce the number of parameters and

Table 4.1: Bit and rock mechanical properties for soft and hard layers.

Parameter Name	Soft Layer	Hard Layer	Unit
Intrinsic specific energy (ε)	150	200	MPa
Contact pressure (σ)	150	200	MPa
Friction coefficient (μ)	0.75	1.0	[–]
Bit height (b)	22.2	22.2	cm
Bit radius (a)	10.8	10.8	cm

to facilitate the numerical simulations effectively, the equations of motion in the form of Eq. (4.24) for both BM and AST models are expressed in dimensionless forms; see the detailed derivations for both models in Appendix B.1 and the list of associated parameters in Table B.1. In addition, the computational scheme employed to simulate the responses of these models is summarized in Appendix B.2.

4.3 Drill-String Responses in Interbedded Formations and the Effect of the AST Tool on Performance

In this section, we employ the developed models to analyze, firstly, the effect of the interbedded nature of the rock formation on the dynamic response characteristics for the benchmark model and, secondly, the effect of the AST tool on the dynamic responses (and the related drilling performance) of the drill-string system. The effect of both aspects on the drilling performance in terms of rate-of-penetration and drilling efficiency, including mechanical specific energy, is also investigated.

In the simulations, thin layers in terms of the ratio $^{H}/_{b} \in \{1, 2, \cdots, 10\}$ between the layer thickness and bit height are considered, and the bit parameters and the rock mechanical properties are listed in Table 4.1. For the boundary conditions applied at the top surface, we apply the following representative values for hook-load and surface angular velocity: *(i)* hook-load $H_0 \in \{420, 440\}$ kN corresponding to higher and lower weights W_a applied on the bit, respectively, based on Eq. (4.29), and *(ii)* prescribed angular velocity $\Omega_0 = 80$ rpm. We focus on the variation of the hook-load to investigate how the tool performance behaves over the combination of these nominal operational settings.

In the first subsection, we discuss the main response characteristics of the axial and torsional dynamics of the BM model under the effect of layered formation. The effect of the AST tool on the drilling performance in such drilling scenario is investigated further in the second subsection, which is divided into two parts: *(i)* the emphasis on its effect on the rate-of-penetration, and *(ii)* the emphasis on its effect on the drilling efficiency and mechanical specific energy. The last subsection discusses the effect of the AST tool on the (steady-state) power losses due to the frictional torque in the bit/rock interaction.

4.3.1 Axial and Torsional Responses of the Benchmark Model

Figure 4.8 depicts the time-domain responses of the axial and torsional velocities at the bit of the BM model for a drilling scenario in an interbedded formation. The simulation uses the following settings: *(i)* layer thickness $H = b$, *(ii)* hook-load $H_0 = 440$ kN, and *(iii)* surface angular velocity $\Omega_0 = 80$ rpm. The first initial rock layer is set as a soft rock type (colored in green in the response plots) then followed by a hard rock type (colored in red), with a spatially periodic sequence of soft-hard rock layer structure afterwards. The black vertical lines between these green and red areas show the time when the bit contacts a new layer. Note that in this simulation scenario, we let the drill-string system first converge to a steady-state limit-cycling condition in a homogeneous formation (i.e., in the first soft layer for this case) and subsequently let it enter the layered formation.

In general, the responses of the BM model exhibit axial and torsional (stick-slip) limit-cycles, with a periodicity reflecting the spatial periodicity of the formation layering. The responses also show that due to the limited thickness of the layers (in terms of $^{H}/_{b}$) the vibrational responses do not have sufficient time to converge to the steady-state responses associated with a homogeneous (either hard or soft) layer. Thus, this shows that the response in interbedded formations (i.e., the right-zoomed plots in Figure 4.8) is essentially different from those in homogeneous layers (i.e., the left-zoomed plots in the same figure).

Furthermore, the axial bit velocity in the BM model, as expected, increases in soft layers and decreases in hard layers, however with a complex vibrational signature. By noting that each layer has the same thickness, this leads to shorter elapsed time in drilling soft layers than the hard ones as seen in the responses, e.g., the time duration in the green areas is significantly shorter than in the red areas in Figure 4.8.

4.3.1.1 Rate-Of-Penetration And Drilling Efficiency

In this section, we analyze the effect of the interbedded nature of the rock formation on the rate-of-penetration (ROP) and drilling efficiency. First, the periodicity of the solutions as depicted in Figure 4.8 allows to perform time-based averaging of the solutions over two consecutive rock layers to analyze the drilling performance in terms of the averaged response.

As detailed in [18], the total time required to drill two consecutive layers is $\mathit{\Delta} t = \mathit{\Delta} t_{k-1} + \mathit{\Delta} t_k$, where $\mathit{\Delta} t_{k-1}$ is the time needed for drilling through the $(k-1)^{th}$ (upper) layer and $\mathit{\Delta} t_k$ the time needed for drilling through the k^{th}

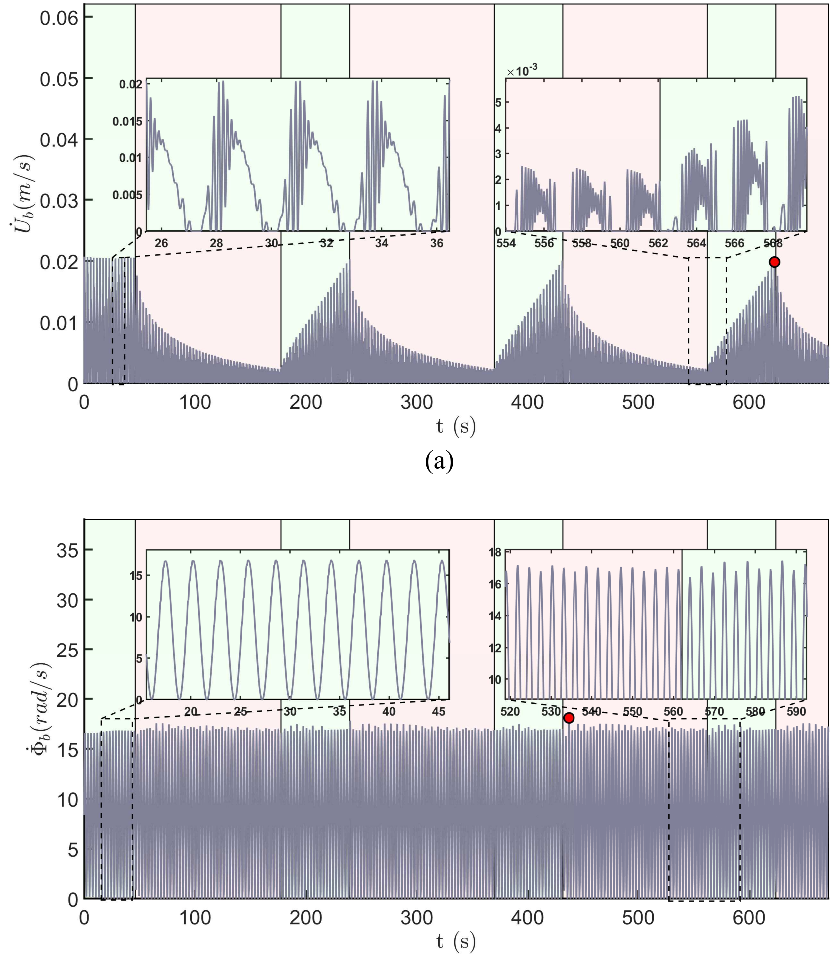

(a)

(b)

Figure 4.8: Effect of the layered formation on (a) the axial and (b) the torsional dynamic responses of the drill-string model without AST (BM model) with the layer thickness $H = b$ and the top boundary conditions: hook-load $H_0 = 440$ kN and prescribed angular velocity $\Omega_0 = 80$ rpm. The red dots show the peak values of the associated responses in the steady-state region.

(lower) layer. Let $\left\langle \hat{f}_{k-1} \right\rangle$ and $\left\langle \hat{f}_k \right\rangle$ be the harmonic means of a time-varying response function $\hat{f}(t)$ in the upper layer over an elapsed time Δt_{k-1} and in the lower layer over another elapsed time Δt_k, respectively. Thus, a generic form for the total harmonic mean of a time-varying response function $\hat{f}(t)$ over the total time Δt is given by

$$\left\langle \hat{f} \right\rangle = \frac{1}{\varDelta t}\left(\int\limits_{0}^{\varDelta t_{k-1}} \hat{f}\left(\tau\right) d\tau + \int\limits_{\varDelta t_{k-1}}^{\varDelta t_{k-1}+\varDelta t_k} \hat{f}\left(\tau\right) d\tau \right) = \frac{\left\langle \hat{f}_{k-1} \right\rangle \varDelta t_{k-1}}{\varDelta t} + \frac{\left\langle \hat{f}_{k} \right\rangle \varDelta t_{k}}{\varDelta t}. \tag{4.39}$$

As each layer thickness is assumed to be identical, the following relations hold

$$\frac{\varDelta t_{k-1}}{\varDelta t} = \frac{\langle \dot{U}_b \rangle}{2\left\langle \dot{U}^b_{k-1} \right\rangle}, \qquad \frac{\varDelta t_{k}}{\varDelta t} = \frac{\langle \dot{U}_b \rangle}{2\left\langle \dot{U}^b_{k} \right\rangle}, \tag{4.40}$$

where $\left\langle \dot{U}^b_{k-1} \right\rangle$ and $\left\langle \dot{U}^b_{k} \right\rangle$ denote to the averaged ROP in the upper and lower layers, respectively. Noting that

$$\frac{\varDelta t_{k-1}}{\varDelta t} + \frac{\varDelta t_{k}}{\varDelta t} = 1, \tag{4.41}$$

and substituting the relations in Eq. (4.40) into Eq. (4.41) yield the following expressions for the averaged ROP $\left\langle \dot{U}_b \right\rangle$ in the layered formation:

$$\left\langle \dot{U}_b \right\rangle = \frac{2\left\langle \dot{U}^b_{k-1} \right\rangle \left\langle \dot{U}^b_{k} \right\rangle}{\left\langle \dot{U}^b_{k-1} \right\rangle + \left\langle \dot{U}^b_{k} \right\rangle}. \tag{4.42}$$

Second, we consider the definition of drilling efficiency in [187] that is expressed as the ratio between the (averaged) torque on bit used for removing rock and the (averaged) total torque on bit (which includes the torque lost due to the frictional dissipation). Thus the drilling efficiency for the k^{th} layer can be expressed as follows:

$$\eta_k = \frac{\langle T^c_k \rangle}{\langle T^c_k \rangle + \left\langle T^f_k \right\rangle}. \tag{4.43}$$

Here $\langle T^c_k \rangle$ and $\left\langle T^f_k \right\rangle$ refer to the averaged TOB resulting from the cutting and frictional contact, respectively, in the bit/rock interaction for each layer (see also Eqs. (4.9) and (4.16)). Hence, the averaged value of the drilling efficiency η in interbedded formations can be calculated via Eqs. (4.39) – (4.40) by considering the drilling efficiencies in the $(k-1)^{th}$ (upper) layer and the k^{th} (lower) layer calculated from Eq. (4.43).

Figure 4.9 depicts the averaged ROP $\left\langle \dot{U}_b \right\rangle$ (top) and averaged drilling efficiency η (bottom) in a layered formation, as a function of the ratio $^{H}/_{b} \in \{1, 2, \cdots, 10\}$, for hook-load $H_0 = 440$ kN and surface angular velocity $\Omega_0 = 80$ rpm. The

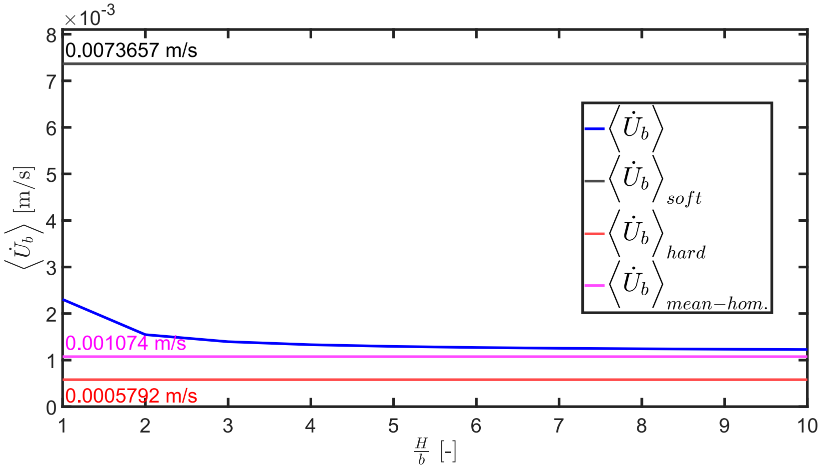

(a)

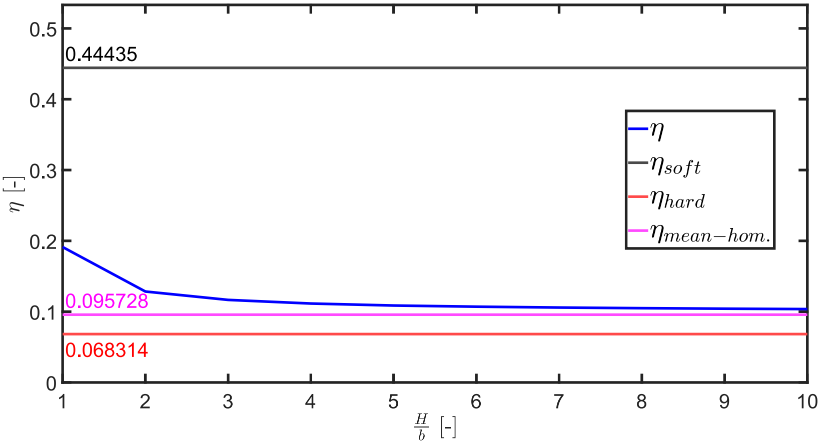

(b)

Figure 4.9: Effect of the layered formation for the drill-string model without AST (BM model) in terms of (a) the (averaged) ROP and (b) the (averaged) drilling efficiency with the layer thickness variations $^H/_b \in \{1, 2, \cdots, 10\}$ with $H_0 = 440$ kN and $\Omega_0 = 80$ rpm.

averaged ROP $\langle \dot{U}_b \rangle$ and averaged drilling efficiency η under this drilling scenario of layered formation (see the blue lines in both plots in Figure 4.9) are observed to increase about 88% and 85%, respectively, with decreasing layer thickness ratio $^H/_b$ (e.g., these averaged values for thinner layers increase relative to the ones for thicker layers). Furthermore, we observe in Figure 4.9 that with increasing ratio $^H/_b$, both the averaged ROP $\langle \dot{U}_b \rangle$ and the averaged drilling efficiency η

are asymptotically converging to the mean values of the averaged steady-state responses of the associated homogeneous formation cases.

In addition, for the case of drilling homogeneous formations (either for hard or soft rock layer), the bit response can be averaged over an axial (stick-slip) limit-cycle. Thus, Figure 4.9 (top) also shows the averaged rates-of-penetration/ROPs of the soft-homogeneous (in black line) and hard-homogeneous (in red line) formations, $\langle \dot{U}_b \rangle_{soft}$ and $\langle \dot{U}_b \rangle_{hard}$, respectively. Moreover, the averaged ROP $\langle \dot{U}_b \rangle$ of the layered formation case, as expected, lies in between these homogeneous averaged ROPs. In the same figure, the mean value of these homogeneous ROPs, $\langle \dot{U}_b \rangle_{mean-hom}$, is the asymptotic line (in magenta) for the averaged ROP $\langle \dot{U}_b \rangle$.

In the same settings, Figure 4.9 (bottom) also depicts the averaged drilling efficiencies, η_{soft} and η_{hard}, of the soft-homogeneous (in black line) and hard-homogeneous (in red line) formations, respectively. The drilling efficiency η of the layered formation case also lies in between the drilling efficiencies of these homogeneous formations. In the same figure, the mean value of these drilling efficiencies of homogeneous formations, $\eta_{mean-hom}$, is the asymptotic line (in magenta) for the drilling efficiency η. As a remark, these findings indeed show that in the case of drilling layered formations, the drill-string dynamics can no longer be described through homogeneous models and the developed model for drilling layered formations is indeed required.

4.3.2 Effect of the AST Tool on the Drilling Performance.

In this subsection, the effect of the AST tool on the dynamic responses of the drill-string system and on the drilling performance in terms of rate-of-penetration and drilling efficiency is investigated.

4.3.2.1 Effect of the AST Tool on the ROP

Figure 4.10 shows the effect of the AST tool on the axial dynamic response of the drilling system in interbedded formation (AST model) in the same drilling scenario considered for the BM Model ($H = b$, $H_0 = 440$ kN, $\Omega_0 = 80$ rpm). Comparing the axial responses of the BM model in Figure 4.8 (top) with the AST model shows that the presence of the AST significantly increases the ROP when drilling both soft and hard layers.

In addition, the amplitudes of the bit axial velocity response of the AST model are increased, e.g., the peak values of the AST model (see the red dots in Figure 4.10) are up to 5 times the amplitude of the axial vibrations in the BM model (see the red dots in Figure 4.8 – top). These findings suggest that stronger axial vibrations are induced due to the presence of AST and consequently these affect the drilling performance in interbedded formations, i.e., higher rate-of-penetration.

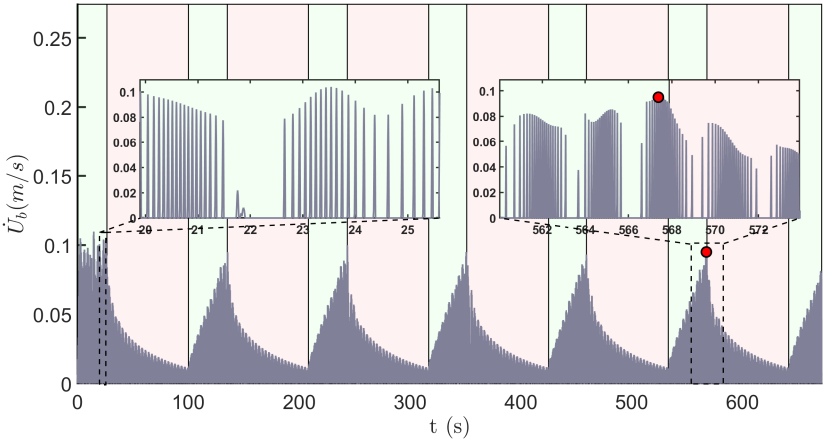

Figure 4.10: Effect of the AST tool on the axial dynamic response of the drilling system in interbedded formation (AST model) with the layer thickness $H = b$, with $H_0 = 440$ kN and $\Omega_0 = 80$ rpm. The red dot shows the peak value of the response in the steady-state region.

Performing a frequency-domain analysis of the axial bit responses for both models reveals that the first harmonic of the response of the BM model lies at 2 Hz, while it lies at 4 Hz for the model with AST. Hence, the presence of the AST tool increases both the amplitude and frequency of the axial vibrations of the bit.

4.3.2.2 Effect of the AST Tool on the Contact Force (at Bit/Rock Interaction)

Figure 4.11 shows the comparison of contact force responses ($W^f = -\lambda_a$ in Eq. (4.13)) between the benchmark and AST models. The dashed lines in both responses show the averaged magnitudes of the contact forces in each layer for both models.

Firstly, this comparison explains that the extra axial vibrations induced by the AST give an effect to lower the contact force (in the bit/rock interaction) for the AST model (in an averaged sense). This is shown by the reduced (averaged) magnitudes of the contact forces for the AST model as compared to the ones for the BM model (see the dashed lines in Figure 4.11 - top and bottom). Secondly, these reduced contact forces in the bit/rock level support to improve the drilling performance (the ROP increase) in the AST model, as the frictional torque ($T^f = -\lambda_t$ in Eq. (4.16)) decreases. This shows more energy used for the rock cuttings than loosed for the frictional dissipation in the AST model, which will be more emphasized via the analyses on drilling efficiency and frictional power losses in

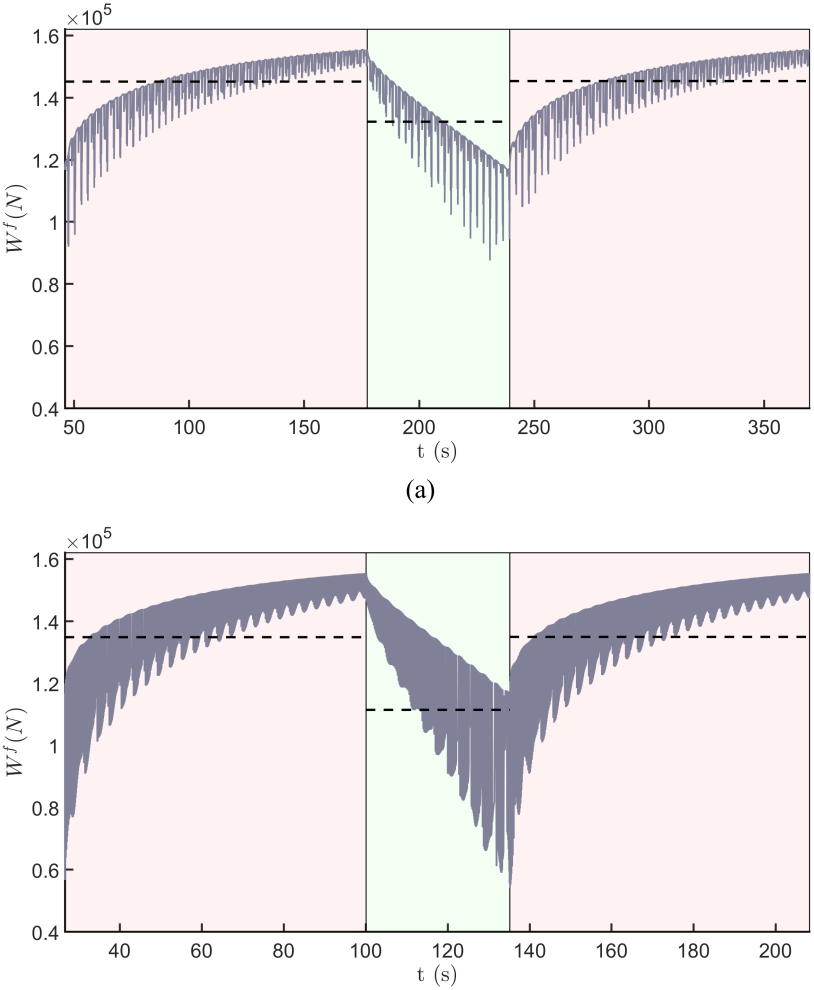

(a)

(b)

Figure 4.11: Comparison of the contact force responses between (a) the benchmark and (b) the AST models in drilling interbedded formation with the layer thickness $H = b$, with $H_0 = 440$ kN and $\Omega_0 = 80$ rpm. The dashed lines show the averaged magnitudes of the contact forces in each layer.

the next subsections.

4.3.2.3 Averaged ROP Comparison.

The essential difference in the axial responses becomes even more apparent when comparing the averaged axial bit velocity (ROPs) of the BM and AST models,

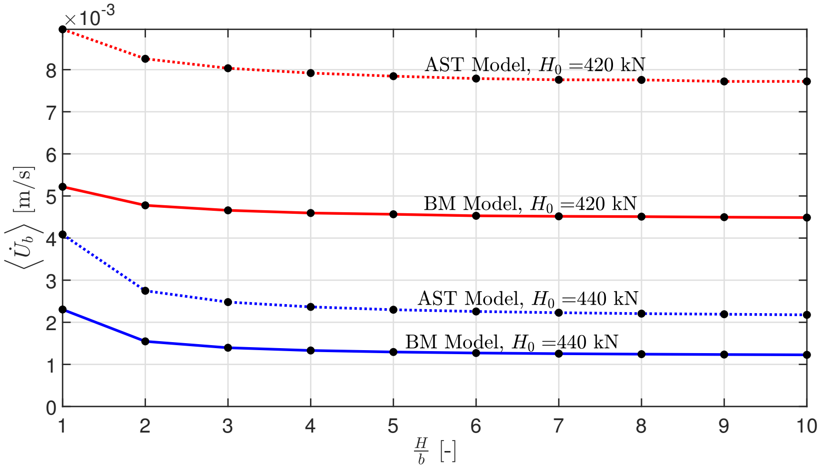

Figure 4.12: Comparison of the averaged ROPs between the benchmark (BM, with solid line) and AST (dashed line) models under the effects of the layer thickness variation ($^H/_b \in \{1, 2, \cdots, 10\}$), for $H_0 = 440$ kN (blue line) and $H_0 = 420$ kN (red line) with $\Omega_0 = 80$ rpm.

which is depicted in Figure 4.12. This figure compares the averaged ROPs between the benchmark (BM, with solid line) and AST (dashed line) models for different layer thicknesses ($^H/_b \in \{1, 2, \cdots, 10\}$) and the nominal set of hook-loads $H_0 \in \{420, 440\}$ kN with a fixed surface angular velocity $\Omega_0 = 80$ rpm.

When drilling interbedded formations, the averaged ROP in the AST model (dashed lines) increases almost 2 times compared to the one in the BM model (solid lines). In addition, the averaged ROPs of both models significantly increase within thinner layers. Overall, lowering the hook-load increases the averaged ROPs in both BM and AST models for all variations of ratio $^H/_b$.

As a remark, these findings suggest that increasing axial vibrations associated with the presence of the AST lead to more efficiency in the cutting process, e.g., more rock volume being removed in a given amount of time, higher depth-of-cut in Eq. (4.6) and consequently higher averaged ROP in Eq. (4.42). Moreover for supporting the findings, the cutting force ratio increases and the contact force ratio decreases more in the AST model than in the BM model; see further numerical results in Appendix B.3.

4.3.2.4 Effect of the AST Tool on the Drilling Efficiency and the Mechanical Specific Energy

To support further analysis on the effect of the AST, we also investigate the drilling efficiency and the $E - S$ diagrams [59, 17]. Hereto, we need to define both the mechanical specific energy E and the drilling strength S for drilling interbedded formations (in an averaged sense). The mechanical specific energy (MSE) E is the quantity representing the amount of energy required to drill a unit volume of rock accounting for both cutting and frictional contact at the bit/rock interface. The drilling strength S is defined as the quantity (with the unit of pressure) that reflects the axial force imposed on the PDC bit for producing the depth-of-cut.

These quantities of MSE and drilling strength for the k^{th} layer can be expressed as follows:

$$\overline{E}_k = \frac{2\left\langle T_k \right\rangle}{a^2 \left\langle d_k \right\rangle}, \quad \text{and} \quad \overline{S}_k = \frac{\left\langle W_k \right\rangle}{a \left\langle d_k \right\rangle}. \tag{4.44}$$

Herein, $\langle T_k \rangle$ and $\langle W_k \rangle$ refer to the averaged values of the total TOB and WOB, respectively, due to the bit/rock interaction for the k^{th} layer; see also Eqs. (4.22) and (4.21). In addition, $\langle d_k \rangle$ is the averaged value of depth-of-cut in the k^{th} layer. Thus, the averaged values of the MSE E and the drilling strength S over the total time Δt in drilling interbedded formations can also be calculated according to Eqs. (4.39) and (4.40).

Figure 4.13 (top) compares the averaged drilling efficiency η for the benchmark (BM, with solid line) and the AST (dashed line) models for the same drilling scenario that was presented previously. In the presence of the AST, we observe that the averaged drilling efficiency in the model including AST increases almost twice compared to the one in the BM model; also with a comparable tendency to the averaged ROP plot in Figure 4.12. These findings suggest that the increased axial vibrations associated with the presence of the AST lead to a larger depth-of-cut as reflected by the increase of the averaged cutting torque applied on the bit in Eq. (4.9) for the AST model.

Figure 4.13 (bottom) shows the $E-S$ diagram including the comparison of the $E-S$ values between the BM (in circle markers) and AST (in square markers) models. From this figure, the decreasing tendencies of the $E-S$ values are visible in the $E-S$ diagram when comparing the results of the AST model to the ones of the BM model for a particular value of hook-load H_0 ($H_0 = 440$ kN in blue and $H_0 = 420$ kN in red).

Note that the lower $E-S$ values are desired, such that these values are getting closer to the so-called cutting line where the ideal cutting process occurs without any frictional dissipation (i.e., the bit produces higher depth-of-cut); see [59, 17]. Therefore, a decrease in the $E-S$ values of the AST model in Figure 4.13 shows the positive impact of the presence of the AST tool for the drilling efficiency in interbedded formation.

As expected, lowering the hook-load increases the averaged drilling efficiency in both BM and AST models for all variations of ratio $^{H}/_{b}$. In accordance with these results, $E-S$ values of both models decrease as the hook-load decreases for all

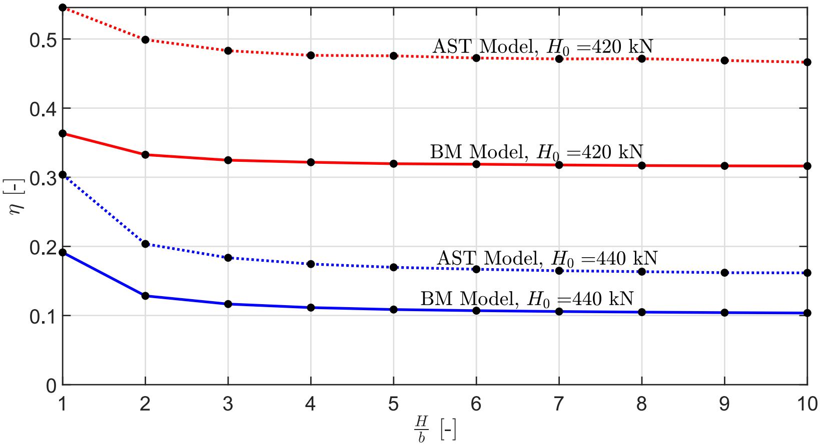

(a)

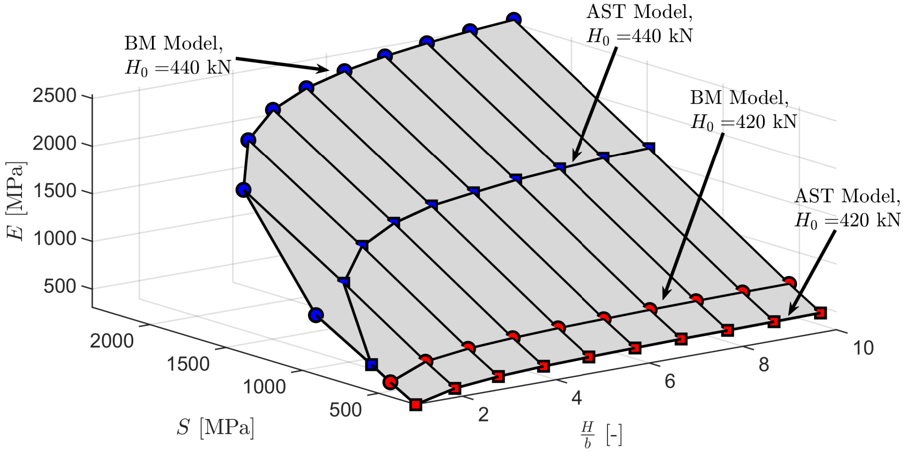

(b)

Figure 4.13: Comparison of (a) the averaged drilling efficiency and (b) the $E - S$ diagram between the benchmark (BM, with solid line or circle in $E - S$ diagram) and AST (dashed line or square in $E - S$ diagram) models under the effects of the layer thickness variation ($^H/_b \in \{1, 2, \cdots, 10\}$), for $H_0 = 440$ kN (blue color) and $H_0 = 420$ kN (red color) with $\Omega_0 = 80$ rpm.

variations of ratio $^H/_b$. In addition, the averaged drilling efficiencies in both BM and AST models significantly increase within thinner layers, which are reflected by a decrease of the $E - S$ values.

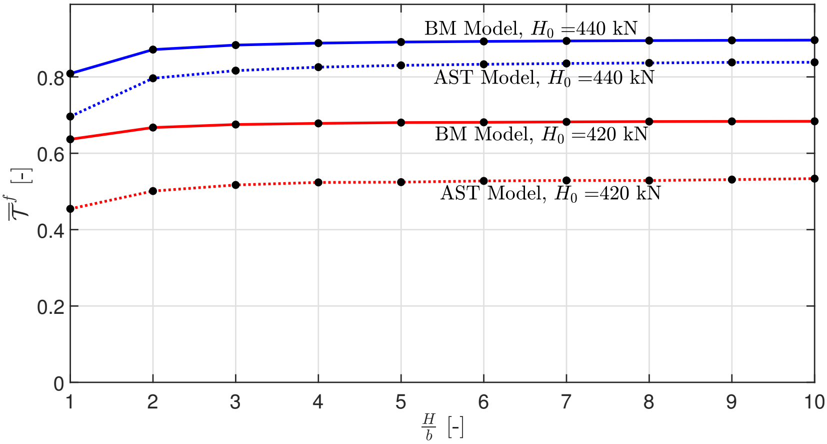

Figure 4.14: Comparison of the averaged frictional torque ratios between the benchmark (BM, with solid line) and AST (dashed line) models under the effects of the layer thickness variation ($^H/_b \in \{1, 2, \cdots, 10\}$) and for $H_0 = 440$ kN (blue line) and $H_0 = 420$ kN (red line) with $\Omega_0 = 80$ rpm.

4.3.3 Analysis of Frictional Power Losses: Effect of the AST

This section investigates the effect of the AST on the averaged frictional torque at the bit and the (steady-state) power loss due to this frictional torque. This investigation is motivated by the fact that large frictional dissipation at the bit is associated with bit damage and wear [72], since high frictional dissipation can lead to high thermal loading on the bit.

4.3.3.1 Frictional Torque at the Bit

The averaged frictional torque ratio for the k^{th} layer is expressed as follows:

$$\overline{\mathcal{T}}_k^f = \frac{\left\langle T_k^f \right\rangle}{\left\langle T_k^c \right\rangle + \left\langle T_k^f \right\rangle}. \tag{4.45}$$

Hence, the averaged value of the frictional torque ratio $\overline{\mathcal{T}}^f$ is calculated according to Eqs. (4.39) and (4.40).

Figure 4.14 shows the comparison of the frictional torque ratio values between the benchmark (BM, with solid line) and AST (dashed line) models for the same drilling scenarios – under the variation of layer thicknesses ($^H/_b \in \{1, 2, \cdots, 10\}$)

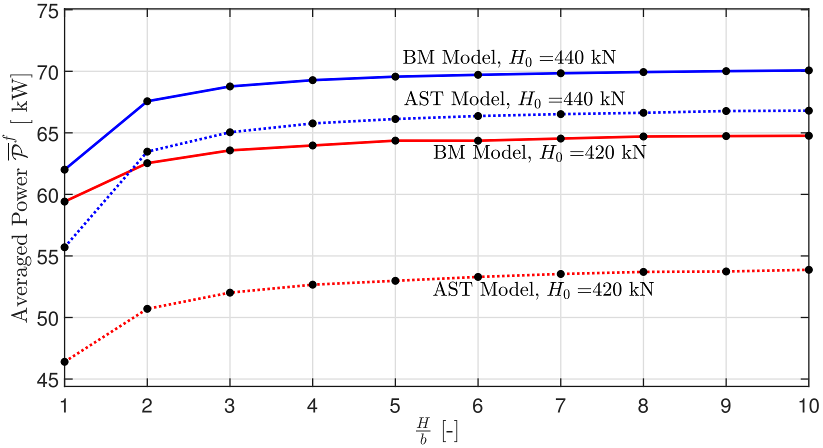

Figure 4.15: Comparison of the averaged power losses due to the frictional torque at the bit between the benchmark (BM, with solid line) and AST (dashed line) models under the effects of the layer thickness variation ($H/b \in \{1, 2, \cdots, 10\}$) and for $H_0 = 440$ kN (blue line) and $H_0 = 420$ kN (red line) with $\Omega_0 = 80$ rpm.

and the nominal set of hook-loads $H_0 \in \{420, 440\}$ kN with a fixed surface angular velocity $\Omega_0 = 80$ rpm. The frictional torque ratio is overall reduced with the presence of the AST as compared with the results of the benchmark (BM) model (for each hook-load value) as depicted in Figure 4.14. This indicates the occurrence of more axial vibrations associated with the presence of the AST, such that this can trigger lower contact force in the bit/rock interaction (in Eq. (4.13)) and lead to reduce the frictional torque in averaged sense (see Eq. (4.16)). In Appendix B.3, we also provide comparisons on the averaged values of the force ratios for each component in the bit/rock interaction between the BM and AST models for supporting this indication.

4.3.3.2 Frictional Power Dissipation

The power loss P_f is defined as the quantity (with the unit of power) that reflects the losses due to the frictional torque imposed on the PDC bit during its rotation. In drilling interbedded formations, this quantity is defined for the k^{th} layer as follows:

$$\overline{\mathcal{P}}_k^f = \left\langle T_k^f \cdot \dot{\Phi}_k^b \right\rangle . \tag{4.46}$$

The averaged value of power losses $\overline{\mathcal{P}}^f$ can also be assessed from Eqs. (4.39) and (4.40).

Figure 4.15 shows the comparison of the averaged power losses between the benchmark (BM, with solid line) and AST (dashed line) models for the same drilling scenario applied in investigating the frictional torque ratio. Clearly, due to the presence of the AST, the power loss decreases as compared with the results of the benchmark (BM) model (based on the same hook-load value for each drilling scenario). In [72], it is reported that the excessive amount of frictional torque can lead to produce (thermally induced) damage on the bit. Hence, the simulation cases show that the presence of the AST tool in the BHA will result in a reduction of the average frictional torque (i.e., lower friction-induced heat loading on the cutters).

4.4 Conclusions

In this study, we present the dynamic modeling of drill-string systems equipped with the Anti-Stall Tool (AST) drilling in interbedded formations. A novel bit/rock interface law involving the transitional phase between two distinct layers couples the axial and torsional dynamics of the systems. The developed simulation tool for the drill-string models is used to investigate the effect of the tool on the total dynamics of drill-string systems in terms of response characteristics, drilling performance and efficiency for some particular drilling cases in interbedded formations.

Numerical analysis results have revealed that the AST tool significantly improves the ROP and efficiency in drilling interbedded formation, which is also observed in terms of mechanical specific energy (MSE). Including the AST in the drilling system induces extra axial vibrations that cause less frictional contact in the bit/rock interaction. Hence, this leads to less (frictional) dissipation on the bit and thus potentially prolong the bit life-time (due to lower thermal loading of the bit). Further research on the parametric study of AST involving higher modes of axial and torsional vibrations and also drilling scenario in interbedded formations is required to determine an optimal and robust tool design over a larger range of operational conditions.

Chapter 5

Analysis of a downhole passive regulator in drilling: a distributed parameter system modeling approach

Abstract[1] - This chapter pursues a model-based investigation of the effect of a downhole passive regulator (AST) on the performance of a rotary drilling system. In this work, the drill-pipe is represented as a continuum model in the form of partial differential equations (PDEs), capturing all modes of axial and torsional dynamics; the bottom-hole-assembly (BHA) is described by a discrete model governed by ordinary differential equations (ODEs); and the evolution of the rock surface under the bit is characterized by another PDE. These sub-systems are assembled and form a coupled PDE-ODE-PDE system model. We perform simulation-based studies on the proposed model for cases without and with the AST, and analyze the drilling performance in terms of the nonlinear behavior of both drilling systems, particularly in terms of depth-of-cut (rate-of-penetration) and drilling efficiency in the rock cutting process (torque-on-bit). In addition, we also analyze the friction-induced loading on the drill-bit and the dynamic loading on the drill-string. These numerical studies show that the use of the AST regulator can assist to improve the drilling performance and to decrease both the frictional loading on the bit and the dynamic loading on the string - this observation is robust under a realistic parametric space of the drilling operations, the drill-string, and the rock formation. Moreover, the robust performance - optimal AST design is investigated using the proposed model.

---

[1] This chapter is based on: [16] **A.G. Aribowo**, U. J. F. Aarsnes, K. Chen, E. Detournay, N. van de Wouw, “Analysis of a downhole passive regulator in drilling: a distributed parameter modeling approach", to be submitted to the Journal of Sound and Vibration. Related preliminary results are reported in [15].

5.1 Introduction

The AST technology developed by Tomax AS (a Norwegian-based drilling technology company) has been widely used as a downhole passive regulator for improving drilling performance in exploration and production activities of hydrocarbon resources stored in deep subsurface rock formations [53, 158, 140, 141, 10]. The field results reported in [26, 103, 99] have shown that application of such a downhole tool can bring economical benefits in executing drilling projects, particularly by improving the drilling efficiency and rate-of-penetration (ROP) that leads to reduced non-productive time (NPT).

Figure 5.1 shows the schematic of the AST basic design. Figure 5.2 visualizes the working principle of the AST, where the AST is installed in the bottom-hole-assembly (BHA) of the drill-string, i.e., in the green-colored section at the middle (above the drill-bit).

To study the effect of the AST on drilling performance, modeling of a rotary drilling system equipped with the AST has been started in [181], where the so-called RGD model of drill-string dynamics proposed in [147] was used as the basis. This extended RGD model with the AST considers that the drill-string is divided into two parts, where the upper part is a lumped rigid body to represent mainly the drill-pipe structure and the rig at surface, and the lower part is a lumped section of BHA, including the drill-bit. The AST is modeled by an ideal linear spring and a kinematic constraint of its helical spline (that couples the axial and torsional dynamics of the drill-string), which connects the upper and lower parts. In this model setup, the bit-rock interaction law developed in [58, 59] acts as the bottom boundary conditions, which is mainly affected by two components: the rock cutting process and the frictional contact between the rock surface and the bit wearflat.

The lumped-parameter model of drill-string dynamics with the AST is then extended for drilling cases involving deviated wellbore trajectory in [187] and for the case of drilling interbedded formations in [19]. In these studies, the influence of the AST on drilling performance was studied numerically. In addition, the modeling works in [55, 131] have considered the internal friction of the AST, particularly due to the frictional contact located on the mounted parts of the helical spline.

The lumped-parameter (discrete) modeling approach (i.e., the RGD model) simplifies the drill-string structure to a two-degrees-of-freedom (2-DOFs) dynamical model, while neglecting all higher dynamical modes apparent in the long, slender structure of the drill-pipes that can reach $1 - 10$ km in length [147, 78, 27, 57]. To overcome this simplification, the continuum modeling approach of the drill-string system is considered in [77], where the partial differential equations of the drill-string axial and torsional dynamics are solved via the finite-element-method (FEM). In [2, 5, 3, 6], a distributed parameter modeling approach was used to study the multiple modes of the axial and torsional dynamics of the drill-string,

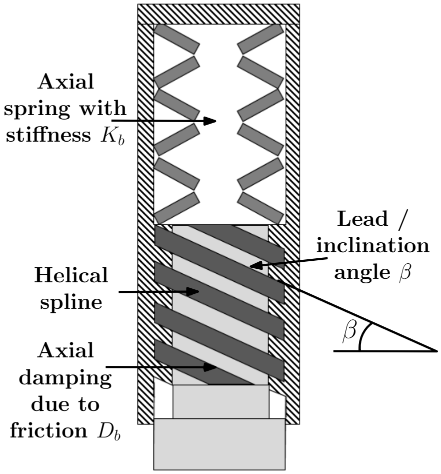

Figure 5.1: The schematic design overview of the AST [30].

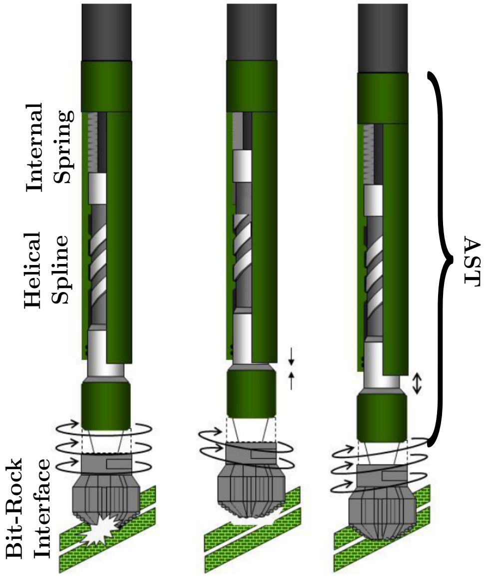

Figure 5.2: The working principle of the downhole passive regulator AST installed in the BHA [158, 140, 141].

which are coupled by the bit-rock interface law developed in [58, 59]. Moreover, in the cutting component of the interface law, this work used a PDE to describe the evolution of the depth-of-cut (DOC) [80], that is inspired by the study of the regenerative effect in the metal cutting process [184]. In [4], this distributed model of drill-string dynamics was extended to include an axial elastic tool (the so-called shock-sub) for studying its feasibility for a stabilizing effect on the dynamics.

The present work is motivated by the following findings from the prior studies:

1. The previous studies [77, 3, 6] have shown that higher-order modes can cause instability and vibrations which are not captured by the low-order models, e.g., the RGD model.
2. The topside boundary conditions, i.e., the top angular velocity and hook-load, have a significant impact on both the stability of the drill-string system and the limit-cycle signatures arising from instability [77].
3. Furthermore, it is reported that the effect of the AST on the increase of axial instability in the drill-string system leads to higher performance in terms of ROP and drilling efficiency as compared to the performance in the benchmark model (the model without the AST) for drilling scenarios in homogeneous formation [181] as well as in interbedded formation [19]. These results indicate that more torque is used for the cutting process (e.g., lower mechanical-specific-energy (MSE)) and that lower frictional loading occurs on the drill bit in drilling processes with the use of the AST.
4. The study [19] has also revealed that the heterogeneity of rock formations is indicated as a more dominant factor affecting the steady-state responses of drill-string dynamics.

In this work, we derive dynamic models of rotary drilling systems without and with the AST (here referred to as the benchmark (BM) and AST distributed models, respectively) by employing the distributed-parameter approach presented in [2, 5, 3]. Moreover, we consider the (set-valued) bit-rock interface law developed in [59, 17] for the case of homogeneous rock properties and the PDE-based evolution of the depth-of-cut in [80] is used for the interface law.

Given these findings, we intend to assess whether the distributed model response of the drill-string with the AST is still possessing the same tendency (i.e., consistent results in terms of increasing drilling performance) as observed in the lumped-parameter (lower-dimensional) model in [181, 187, 19]. In addition, if the performance improvement with the use of the AST can be shown via the numerical studies, it is also interesting to explore how to optimize the design of the AST for performance.

The main contributions of this work can be summarized as follows:

1. Firstly, we derive distributed models of drill-string dynamics without and with the AST in the form of a coupled PDE-ODE-PDE system.
2. Secondly, we investigate and compare the steady-state responses of both models, particularly under a set of operational drilling parameters (imposed

as the topside boundary conditions), to reveal the impact of the AST on the distributed dynamics.

3. Thirdly, the effect of the AST on drilling performance in terms of rate-of-penetration is investigated by comparing the averaged steady-state responses of these two models. In addition, the frictional loading on the bit and the dynamic loading on the drill-string on both models are also studied as additional performance metrics.

4. Finally, a parametric study on the AST design parameters (the stiffness and the lead angle of the helical spline), including their robustness, is performed under the variation of characteristic parameters of the drill-string (i.e., its length), the physical properties of rock formations (soft vs hard rocks), and the operational drilling parameters.

The remainder of this chapter is structured as follows: Section 5.2 presents the distributed parameter models of rotary drilling systems without and with the AST. Section 5.3 details the numerical method for analyzing the resulting (set-valued) PDE-ODE-PDE models. Dynamic analyses of both models and a parametric study on the robust performance-optimal AST design are presented in Section 5.4 and 5.5, respectively. Conclusions are drawn in Section 5.6.

5.2 Distributed parameter models of drilling systems without and with AST

This section details the coupled PDE-ODE-PDE system for the BM and AST models as depicted in Figures 5.3 and 5.4, respectively. The drill-string system in both models is divided into two main parts, namely the drill-pipe (upper) and the BHA (lower) parts. The upper part mainly represents the long-slender structure of the drill-pipe and the rig where the operational drilling parameters are imposed (here also referred as the drill-pipe model). The lower part is mainly for the BHA (i.e., drill-collar, stabilizers, and other downhole components such as the AST) and the drill-bit with the bit-rock interface law (here also referred as the BHA model).

First, we present the distributed-parameter model developed for the drill-pipe parts of both BM and AST models. Second, we describe the lumped-parameter models for the BHA parts of both models for a drilling scenario in vertical wellbore with homogeneous rock formation - see the zoomed parts in Figures 5.3 and 5.4. In both models, the drill-pipe and BHA are coupled through a rigid interface, i.e., located at the drill-collar (the top part of the BHA).

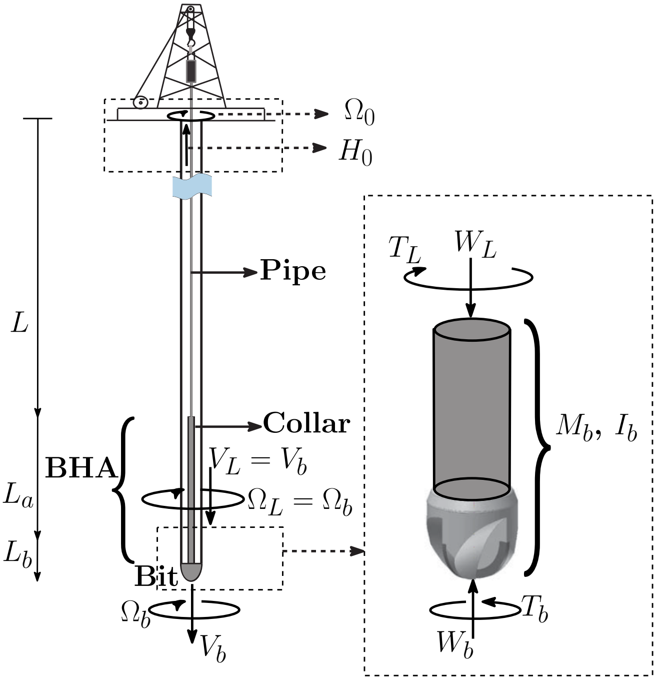

Figure 5.3: Schematic overview of the drill-string without the AST (benchmark (BM) model) in a vertical well-bore (left). The zoomed schematic of the lower part of the drill-string (BHA), including the drill-bit (right).

5.2.1 The distributed model of the drill-pipe (the upper part of drill-string)

On the basis of earlier works in [77, 2, 5, 3], the dynamics of the drill-pipe for both BM and AST models in Figures 5.3 and 5.4, respectively, are modeled with the wave equations. Hereto, two sets of (first-order linear hyperbolic) PDEs of the axial and torsional dynamics of the drill-pipes in both models are considered and detailed as follows.

First, let the state variables $V(t,x)$, $W(t,x)$ denote the axial velocity and the applied weight (axial force) of the drill-string system, respectively, where $(t,x) \in [0,\infty) \times [0,L]$ with the time variable t, the spatial (axial) coordinate x and the drill-pipe length L. Likewise, in torsional direction we denote the state variables $\Omega(t,x)$ and $T(t,x)$ as the angular velocity and the applied torque, respectively. The variable $U(t,x)$ and $\Phi(t,x)$ are the axial and angular displacements in the pipe, respectively, such that the axial and angular velocities are given by $\frac{\partial U(t,x)}{\partial t} = V(t,x)$ and $\frac{\partial \Phi(t,x)}{\partial t} = \Omega(t,x)$, respectively.

Second, in the axial dynamics of the drill-pipe, the applied weight is related to

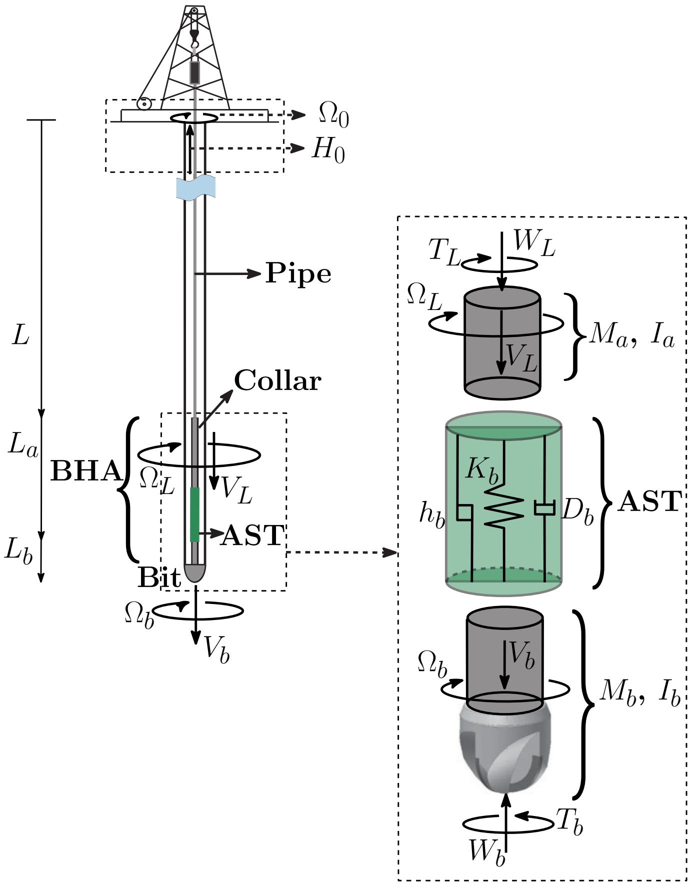

Figure 5.4: Schematic overview of the drill-string equipped with the AST (AST model) in a vertical well-bore (left). The zoomed schematic of the lower part of the drill-string (BHA, AST), including the drill-bit (right).

the axial strain in the pipe as the local relative compression:

$$W(t,x) = -AE\frac{\partial U(t,x)}{\partial x} = AE\frac{(U(t,x) - U(t,x+\delta x))}{\delta x}, \tag{5.1}$$

where δx is an infinitesimal increment of the axial position. The drill-pipe parameters for the axial dynamics consider the cross-sectional area of the drill-pipe element A and the Young's modulus E. Therefore, the partial differential equations (PDEs) for the axial dynamics of the upper part are then given by

$$\frac{\partial W(t,x)}{\partial t} + AE\frac{\partial V(t,x)}{\partial x} = 0, \tag{5.2a}$$

$$A\rho\frac{\partial V(t,x)}{\partial t} + \frac{\partial W(t,x)}{\partial x} = -k_a \rho A V(t,x), \tag{5.2b}$$

where Eqs. (5.2a) and (5.2b) are based on the elasticity relationship in Eq. (5.1) and the Newton's second law, respectively. The parameter ρ is the pipe mass density and the damping coefficient k_a represents the effect of viscous dissipation (shear stresses, structural damping) in the axial direction.

For the torsional dynamics of the drill-pipe, the torque is proportional to the shear strain in the pipe (i.e., twist per unit length) according to the elasticity:

$$T(t,x) = -JG\frac{\partial\Phi(t,x)}{\partial x} = JG\frac{(\Phi(t,x) - \Phi(t,x+\delta x))}{\delta x}. \tag{5.3}$$

The drill-pipe parameters for the torsional dynamics consider the polar moment J and the shear modulus G. The PDEs for the torsional dynamics of the upper part can then be written as follows:

$$\frac{\partial T(t,x)}{\partial t} + JG\frac{\partial\Omega(t,x)}{\partial x} = 0, \tag{5.4a}$$

$$J\rho\frac{\partial\Omega(t,x)}{\partial t} + \frac{\partial T(t,x)}{\partial x} = -k_t\rho J\Omega(t,x). \tag{5.4b}$$

Eqs (5.4a) and (5.4b) are derived based on Eq. (5.3) and the Newton's second law, respectively. The damping coefficient k_t represents the combined effect of the shear stress and structural damping in the torsional direction.

5.2.1.1 Boundary conditions of the drill-pipe models

The top boundary conditions for the PDEs (of the axial and torsional dynamics of the upper part of the drill-string) in Eqs. (5.2a) – (5.2b) and Eqs. (5.4a) – (5.4b) are based on the drilling operational parameters applied on the drilling rig as follows:

$$W(t,x=0) = -H_0, \tag{5.5a}$$

$$\Omega(t,x=0) = \Omega_0, \tag{5.5b}$$

where H_0 is the hookload applied by the hoisting system and Ω_0 is the top angular velocity imposed by the rotary table system of the rig. Moreover, at the bottom of the drill-pipe (i.e., at the rigid interface with the BHA at the depth $x = L$; see Figure 5.3 and 5.4), the kinematic boundary conditions are given by

$$V(t,x=L) = V_L, \tag{5.6a}$$

$$\Omega(t,x=L) = \Omega_L, \tag{5.6b}$$

where the velocities V_L and Ω_L are, respectively, the axial and torsional velocities at the interface.

5.2.2 The lumped model of the BHA (the lower part of drill-string)

The dynamics of the lumped BHA parts of both BM and AST models are modeled in terms of ordinary differential equations (ODEs) following the discrete models developed in [187, 19]. These ODEs for the axial and torsional dynamics of the BHA parts in both models are coupled with the reactive forces and torques due to the bit-rock interaction in [59, 17]. In addition, the depth-of-cut evolution in the rock cutting process of this bit-rock interaction is described by a PDE [80].

In this section, firstly, we summarize the bit-rock interface law and the equation governing the evolution of the rock cutting. Secondly, the lumped-parameter models for the BHA parts of both BM and AST models (as a coupled system with the interface law) are presented.

5.2.2.1 Bit-rock interface law

The bit-rock interaction is essentially composed of two fundamental processes, namely the frictional contact at the interface of the bit wearflat and rock surface and the rock cutting process [59]. Total contributions of each component in the bit-rock interaction into the weight and torque acting on the bit, respectively, are as follows:

$$W_b = W_f + W_c, \tag{5.7a}$$

$$T_b = T_f + T_c. \tag{5.7b}$$

The subscripts f and c are used for the frictional and the cutting components of the interaction, respectively, while the subscript b denotes the variable at the bit. The bit velocities for the axial and torsional directions are denoted by V_b and Ω_b, respectively.

Frictional contact (set-valued force laws) The weight-on-bit (WOB) and torque-on-bit (TOB) due to the frictional contact between the bit and rock are given, respectively, by the following inclusions on velocity level [17]:

$$W_f \in n\,\sigma\,a\,\ell_n\,g\left(V_b\right), \tag{5.8a}$$

$$T_f \in \frac{1}{2}\mu\,a\,\xi\,W_f\,\mathrm{Sign}\left(\Omega_b\right), \tag{5.8b}$$

with σ the normal contact stress, ℓ_n the wearflat length (per blade), a the bit radius, n the number of the bit blades, μ the friction coefficient, and $g\left(y\right)$ is a set-valued function defined as

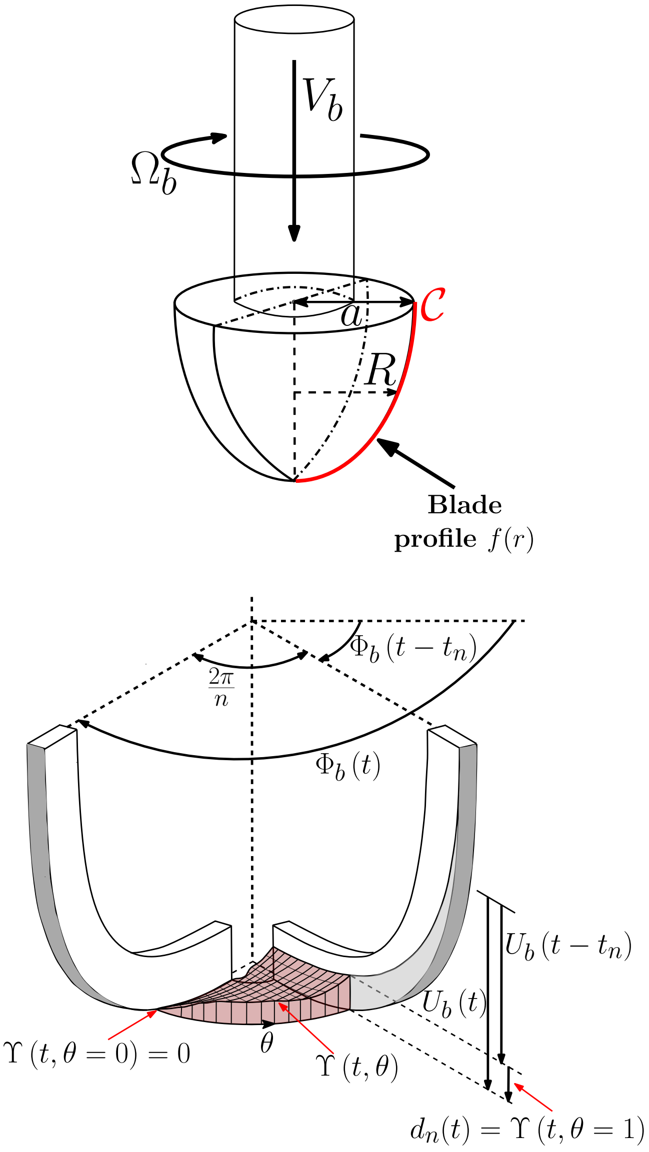

Figure 5.5: The bit profile (top) and the depth-of-cut evolution in the bit-rock interaction (bottom) after [80, 3].

$$g\left(y\right) := \frac{1}{2}\left(1+\mathrm{Sign}\left(y\right)\right) \quad \text{with} \quad \mathrm{Sign}\left(y\right) := \left\{ \begin{array}{ccc} 1 & & y>0 \\ \left[-1,1\right] & , & y=0 \\ -1 & & y<0 \end{array} \right. . \tag{5.9}$$

The bit-design parameter ξ representing the distribution of the wearflat is expressed as

$$\xi := 2\int_0^1 r\sqrt{\left(f'\left(r\right)\right)^2+1}\,\mathrm{d}r, \tag{5.10}$$

with a (dimensionless) bit profile function $f(\cdot)$ [59, 17]. In Figure 5.5 (left), a radial coordinate R on the bit is considered as the radial distance of a point located along the curve of the blade profile $\mathcal{C}$ from the bit axis of symmetry (i.e., $0 \leq R \leq a$). Here the bit profile is considered as a parabolic function, i.e., $f(r) = a_z r^2$ for a positive constant a_z and a (dimensionless-scaled) bit radius $r = {}^{R}\!/_{a}$ with $0 \leq r \leq 1$. The bit parameter ξ in Eq. (5.10) is associated to the orientation of the contact force on the wearflat with respect to the bit profile $f\left(r\right)$.

Cutting process The WOB and TOB due to the cutting process are given, respectively, by

$$W_c = a\,\zeta^*\,\varepsilon\,d, \tag{5.11a}$$

$$T_c = \frac{1}{2}a^2\varepsilon\,d, \tag{5.11b}$$

with ε the intrinsic specific energy of the rock and d the total depth-of-cut. The bit-design parameter representing the orientation of the cutting force is represented by $\zeta^* = \zeta\vartheta_\zeta$ with a positive constant ζ and

$$\vartheta_\zeta := \int_0^1 \frac{1}{\sqrt{\left(f'\left(r\right)\right)^2+1}}\mathrm{d}r, \tag{5.12}$$

following [59, 17]. The evolution of the rock cutting process (with a single bit blade) can be described by the following transport equation [80]:

$$\frac{\partial\Upsilon(t,\theta)}{\partial t} + \Omega_b(t)\frac{n}{2\pi}\frac{\partial\Upsilon(t,\theta)}{\partial\theta} = V_b(t) \tag{5.13}$$

with its evolution state variable $\Upsilon(t,\theta)$ that represents the depth of *uncut* rock at the angular position θ relative to the axial bit position at time t, see Figure 5.5. The angular position $\theta \in [0, 1]$ is the (normalized) angle between an arbitrary surface point on the rock (at a blade) and the reference (next) blade, i.e., initiated at $\theta = 1$ and at $\theta = 0$ after a rock cutting evolution. Herein, the following boundary condition holds:

$$\Upsilon(t,\theta = 0) = 0. \tag{5.14}$$

The depth-of-cut (DOC) produced by a single blade of the drill-bit is then given by

$$d_n(t) = \Upsilon(t, \theta = 1) \tag{5.15}$$

Subsequently, the total depth-of-cut produced by all n identical blades is

$$d = n d_n(t). \tag{5.16}$$

5.2.2.2 The lumped-parameter models of the BHA dynamics

The BHA (lower) parts of the drill-string dynamics are modeled as the lumped-parameter models depicted in Figure 5.6 for the BM model (in left) and for the AST model (in right). These lumped-parameter models of each drill-string system are later to be coupled with the PDEs in Eqs. (5.2a) – (5.2b) and Eqs. (5.4a) – (5.4b) for both axial and torsional dynamics, respectively, of the drill-pipe. We write the equations-of-motion (EOMs) of both lumped-parameter models for the BHA parts into the following generic form:

$$\mathbf{M}\ddot{\mathbf{q}} - \mathbf{H}(t, \mathbf{q}, \dot{\mathbf{q}}) = \mathbf{W}\boldsymbol{\lambda}, \tag{5.17}$$

with the mass matrix $\mathbf{M}$, the generalized smooth forces column $\mathbf{H}$, the non-smooth forces column $\boldsymbol{\lambda}$ and the associated force direction matrix $\mathbf{W}$. The generalized coordinate vector is denoted by $\mathbf{q}$.

BM model In the BM model, the BHA is essentially represented by a lumped section including the drill-bit and the bit-rock interface law in Section 5.2.2.1 plays as its bottom boundary conditions. The generalized coordinates $\mathbf{q}$ of the BHA part in the BM model are given by $\mathbf{q} = \begin{bmatrix} U_b & \Phi_b \end{bmatrix}^\top$ where the axial and torsional displacements at the bit are denoted by U_b and Φ_b, respectively. Note that we use the notation $V_b = \dot{U}_b$ and $\Omega_b = \dot{\Phi}_b$ for the bit axial and torsional velocities, respectively. Herein, the matrices of the EOMs in Eq. (5.17) for the BHA dynamics of the BM model in Figure 5.6 (left) are given by

$$\mathbf{M} = \begin{bmatrix} M & 0 \\ 0 & I \end{bmatrix}, \tag{5.18a}$$

$$\mathbf{H} = \begin{bmatrix} W_L + W_g - W_c \\ T_L - T_c - D_\phi \Omega_b \end{bmatrix}, \tag{5.18b}$$

$$\mathbf{W} = \begin{bmatrix} 1 & 0 \\ 0 & 1 \end{bmatrix}, \tag{5.18c}$$

$$\boldsymbol{\lambda} = \begin{bmatrix} \lambda_a & \lambda_t \end{bmatrix}^\top, \tag{5.18d}$$

with M the total mass of the BHA, I the total inertia, and D_ϕ the torsional damping coefficient representing the viscous friction terms along the BHA. Herein,

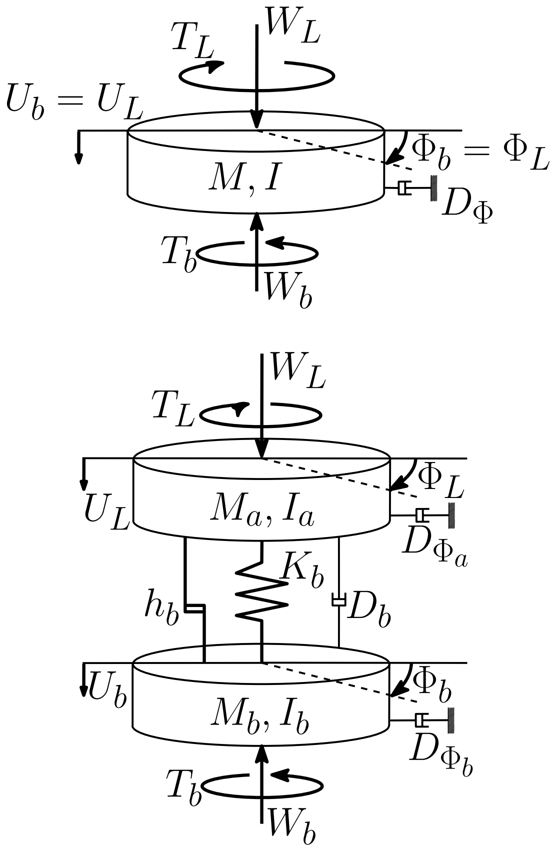

Figure 5.6: The lumped-parameter models of the BHA (lower) parts, including the drill-bit, of drill-string systems for the BM model (top) and the AST model (bottom).

$W_g = Mg$ is the total BHA weight and g is the gravitational acceleration. For the non-smooth component, the force $\lambda_a = -W_f$ and the torque $\lambda_t = -T_f$ abide by the inclusions in Eqs. (5.8a) and (5.8b), respectively. The force W_L and the torque T_L are the interaction forces acting at the interface between the drill-pipe and BHA parts of the drill-string system. The cutting component of the bit-rock interaction follows Eq. (5.11a) and Eq. (5.11b) for the weight W_c and the torque T_c, respectively.

Following the schematic of the BHA (lower) part for the BM model in Figure 5.6 (left), the axial and torsional displacements for the bottom side of the drill-pipe part are denoted by U_L and Φ_L, respectively. As the drill-pipe and BHA parts of the drill-string system are rigidly interconnected at the interface located at the spatial coordinate $x = L$, this condition implies that the bottom side of the drill-pipe is kinematically connected to the BHA, and, consequently, the following kinematic relations at the interface hold:

$$U_L = U_b, \tag{5.19a}$$

$$\Phi_L = \Phi_b. \tag{5.19b}$$

On velocity level, this kinematic condition also implies the boundary conditions for the PDEs of the drill-pipe in Eqs. (5.6a) – (5.6b) as follows:

$$V(t, x = L) = V_b, \tag{5.20a}$$

$$\Omega(t, x = L) = \Omega_b. \tag{5.20b}$$

In addition, the interaction forces at the interface are also coupled with the state variables of the drill-pipe distributed model as follows:

$$W(t, x = L) = W_L, \tag{5.21a}$$

$$T(t, x = L) = T_L. \tag{5.21b}$$

AST model In the AST model, the lumped model of the BHA part is divided into two lumped sections, which are connected by the AST. The bit-rock interface law acts as the bottom boundary condition of the lumped section below the AST – where the drill-bit is mounted. The generalized coordinates $\mathbf{q}$ of the BHA part in the AST model are given by $\mathbf{q} = \begin{bmatrix} U_L & U_b & \Phi_b \end{bmatrix}^\top$. The axial and torsional displacements for the lumped BHA section above the AST are U_L and Φ_L, respectively, see Figure 5.6 (right). Note that we also use the notations $V_L = \dot{U}_L$ and $\Omega_L = \dot{\Phi}_L$ for the velocities of this lumped section above the AST. The matrices of the EOMs in Eq. (5.17) for the BHA dynamics of the AST model in Figure 5.6 (right) are given by

$$\mathbf{M} = \begin{bmatrix} M_a + \frac{I_a}{\alpha^2} & -\frac{I_a}{\alpha^2} & \frac{I_a}{\alpha} \\ -\frac{I_a}{\alpha^2} & M_b + \frac{I_a}{\alpha^2} & -\frac{I_a}{\alpha} \\ \frac{I_a}{\alpha} & -\frac{I_a}{\alpha} & I_a + I_b \end{bmatrix}, \tag{5.22a}$$

$$\mathbf{H} = \begin{bmatrix} -D_b(V_L - V_b) - K_b\left(U_L - U_b\right) + W_L + W_{ag} + \frac{1}{\alpha}\left(T_L - D_{\phi_a}\Omega_L\right) \\ D_b(V_L - V_b) + K_b\left(U_L - U_b\right) + W_{bg} - W_c + \frac{1}{\alpha}\left(D_{\phi_a}\Omega_L - T_L\right) \\ T_L - T_c - D_{\phi_a}\Omega_L - D_{\phi_b}\Omega_b \end{bmatrix}, \tag{5.22b}$$

$$\mathbf{W} = \begin{bmatrix} 0 & 0 \\ 1 & 0 \\ 0 & 1 \end{bmatrix}, \tag{5.22c}$$

$$\boldsymbol{\lambda} = \begin{bmatrix} \lambda_a & \lambda_t \end{bmatrix}^\top. \tag{5.22d}$$

The mass M_a and the inertia I_a lump the BHA section above the AST, and the torsional damping coefficient D_{ϕ_a} is the viscous terms for this BHA section. In addition, the mass M_b and the inertia I_b are for the lumped section below the

AST, with the torsional damping coefficient D_{ϕ_b} as the viscous terms along this section. The weights $W_{ag} = M_a g$ and $W_{bg} = M_b g$ are the weights for the BHA sections above and below the AST, respectively.

The AST consists of an internal spring with a stiffness K_b, a structural damping D_b, and a (holonomic) kinematic constraint (due to the helical spline in the AST) that couples the axial and torsional kinematics of the BHA. This constraint is accounted as follows (written on velocity level):

$$(V_L - V_b) = \frac{p_{sp}}{2\pi r_{sp}} \left(r_{sp}\Omega_L - r_{sp}\Omega_b \right), \tag{5.23}$$

or alternatively on position level as follows:

$$h_b(\mathbf{q}) := \alpha \left(\Phi_L - \Phi_b \right) - \left(U_L - U_b \right) = 0, \quad \text{with}\, \alpha = \frac{p_{sp}}{2\pi},\ p_{sp} = 2\pi r_{sp} \tan\beta. \tag{5.24}$$

The lead p_{sp} is a function of the lead angle β and the spline radius r_{sp} [181, 187, 19]. Based on the BHA schematic for the AST model in Figure 5.6 (right), the lumped BHA section above the AST is set to be kinematically connected to the bottom side of the drill-pipe at the interface located at the spatial coordinate $x = L$. This implies the following boundary conditions of the drill-pipe in Eqs. (5.6a) – (5.6b) (on velocity level):

$$V(t, x = L) = V_L, \tag{5.25a}$$

$$\Omega(t, x = L) = \Omega_L. \tag{5.25b}$$

Besides, the interaction force W_L and torque T_L at the interface between the bottom side of the drill-pipe and the lumped BHA section above the AST are also coupled with the state variables of the drill-pipe distributed model and exactly following Eqs. (5.21a) – (5.21b).

Now, we have presented the distributed model of the drill-pipe part and the lumped models of the BHA part for both the BM and AST models, which include the depth-of-cut evolution (produced by the drill-bit) in the form of a PDE in the bit-rock interface law. The combination of these models of the drill-pipe dynamics, BHA dynamics and the depth-of-cut evolution results in two coupled PDE-ODE-PDE systems for the axial and torsional drill-string dynamics without and with the AST. Besides, a non-smooth (set-valued) formulation for the frictional contact at the bit is included in the reacting forces and torques of the bit-rock interface law for both coupled models.

In the following section, we will detail the numerical scheme used to solve this type of set-valued PDE-ODE-PDE model.

5.3 Numerical scheme

In this section, we present the numerical scheme employed to solve the coupled PDE-ODE-PDE systems of equations for both BM and AST models presented in the previous section. Note that such numerical analysis is challenged by the combined infinite-dimensional and set-valued nature of the dynamics. In support of numerical computations, we first pursue a coordinate transformation in the next section.

5.3.1 Riemann invariants

The wave equations of the drill-pipe dynamics in Eqs. (5.2a) - (5.2b) and Eqs. (5.4a) - (5.4b) are numerically solved by first transforming them into a formulation involving their Riemann invariants. This transformation decouples the interconnection between the states in the original PDEs and thus results in four 1-D transport (advection) equations which can be solved by a finite-difference method (i.e., first-order upwind scheme [3, 4]). We introduce the following Riemann invariants as the function of the state variables for the axial dynamics of the drill-pipe:

$$\alpha_a(t,x) = V(t,x) + \frac{c_a}{AE} W(t,x), \tag{5.26a}$$

$$\beta_a(t,x) = V(t,x) - \frac{c_a}{AE} W(t,x), \tag{5.26b}$$

with the axial wave speed $c_a = \sqrt{\frac{E}{\rho}}$, and for the torsional dynamics of the drill-pipe:

$$\alpha_t(t,x) = \Omega(t,x) + \frac{c_t}{JG} T(t,x), \tag{5.27a}$$

$$\beta_t(t,x) = \Omega(t,x) - \frac{c_t}{JG} T(t,x), \tag{5.27b}$$

with the torsional wave speed $c_t = \sqrt{\frac{G}{\rho}}$. Note that the Riemann invariants α_i for $i \in \{a, t\}$ are the downward traveling waves for both axial and torsional dynamics of the drill-pipe, while the Riemann invariants β_i are the upward traveling waves.

5.3.1.1 PDEs of the drill-pipe dynamics in terms of Riemann invariants.

For the axial dynamics, we write the PDEs in Eqs. (5.2a) – (5.2b) in terms of Riemann invariants as follows:

$$\frac{\partial \alpha_a(t,x)}{\partial t} + c_a \frac{\partial \alpha_a(t,x)}{\partial x} = -S_a(t,x), \tag{5.28a}$$

$$\frac{\partial \beta_a(t,x)}{\partial t} - c_a \frac{\partial \beta_a(t,x)}{\partial x} = -S_a(t,x), \tag{5.28b}$$

with the associated source term,

$$S_a(t,x) = \frac{k_a}{2}\left(\alpha_a(t,x) + \beta_a(t,x)\right). \tag{5.29}$$

As for the torsional dynamics, the PDEs in Eqs. (5.4a) – (5.4b) in terms of Riemann invariants are given by

$$\frac{\partial \alpha_t(t,x)}{\partial t} + c_t \frac{\partial \alpha_t(t,x)}{\partial x} = -S_t(t,x), \tag{5.30a}$$

$$\frac{\partial \beta_t(t,x)}{\partial t} - c_t \frac{\partial \beta_t(t,x)}{\partial x} = -S_t(t,x), \tag{5.30b}$$

with the associated source term,

$$S_t(t,x) = \frac{k_t}{2}\left(\alpha_t(t,x) + \beta_t(t,x)\right). \tag{5.31}$$

5.3.1.2 Boundary conditions in terms of Riemann invariants.

For the top boundary conditions in Eqs. (5.5a) - (5.5b) in terms of Riemann invariants and considering Eqs. (5.26a) – (5.27b), we read

$$\alpha_a(t,x=0) = -\frac{2c_a}{AE}H_0 + \beta_a(t,x=0), \tag{5.32a}$$

$$\alpha_t(t,x=0) = 2\Omega_0 - \beta_t(t,x=0). \tag{5.32b}$$

For the bottom boundary conditions in Eqs. (5.6a) - (5.6b) in terms of Riemann invariants, we write

$$\beta_a(t,x=L) = 2V_L - \alpha_a(t,x=L), \tag{5.33a}$$

$$\beta_t(t,x=L) = 2\Omega_L - \alpha_t(t,x=L). \tag{5.33b}$$

5.3.2 The upwind scheme for the PDEs

The PDEs of the drill-pipe dynamics in terms of Riemann invariants in Eqs. (5.28a) – (5.31) and the PDE of the rock cutting evolution in Eq. (5.13) are hyperbolic PDE systems, which can be solved numerically via a finite-difference method, namely the first-order upwind scheme. To describe this scheme, let consider a generic form of a non-homogeneous transport equation as follows:

$$\bar{\gamma}_t + \bar{c}\bar{\gamma}_x = S(t,x), \tag{5.34}$$

with the subscripts x and t denoting for the spatial and time partial derivatives, respectively, of the state variable $\bar{\gamma}$, a wave propagation speed $\bar{c}$, and a source term S. We perform a first-order discretization on Eq. (5.34) as follows:

$$\bar{\gamma}_p^{n+1} = \bar{\gamma}_p^n - \bar{c}\frac{\Delta\bar{t}}{\Delta\bar{x}}\left(\bar{\gamma}_p^n - \bar{\gamma}_{p-1}^n\right) + S_p^n\Delta\bar{t}, \qquad \text{for } \bar{c} > 0, \tag{5.35a}$$

$$\bar{\gamma}_p^{n+1} = \bar{\gamma}_p^n + \bar{c}\frac{\Delta\bar{t}}{\Delta\bar{x}}\left(\bar{\gamma}_{p+1}^n - \bar{\gamma}_p^n\right) + S_p^n\Delta\bar{t}, \qquad \text{for } \bar{c} < 0, \tag{5.35b}$$

as the standard first-order upwind scheme with the grid index n and p for the temporal and spatial domains, respectively. The increments of the axial position and time are denoted by $\Delta\bar{x}$ and $\Delta\bar{t}$, respectively.

5.3.3 The time-stepping scheme for the BHA model

For solving the ODEs of the BHA dynamics in both BM and AST models, we rewrite the EOMs in Eq. (5.17) into a velocity-level form and apply first-order discretization on its velocity coordinates (based on Moreau's midpoint rule for the time-stepping scheme [165]) as follows:

$$\mathbf{u}^E = \mathbf{M}^{-1}\left(\mathbf{H}^M + \mathbf{W}^M\boldsymbol{\lambda}\right)\Delta t + \mathbf{u}^B, \tag{5.36}$$

In the form of Eq. (5.36), the velocity vectors for the BM and AST models at the discrete time instant t^j are denoted by $\mathbf{u}^j = \begin{bmatrix} V_b^j & \Omega_b^j \end{bmatrix}^\top$ and $\mathbf{u}^j = \begin{bmatrix} V_L^j & V_b^j & \Omega_b^j \end{bmatrix}^\top$, respectively, for $j \in \{B, E\}$. We consider a timestep $\Delta t = t^E - t^B > 0$, of which the superscripts B and E denote the begin and end points, respectively. In Eq. (5.36), the generalized smooth forces column $\mathbf{H}^M$ and the nonsmooth force direction matrix $\mathbf{W}^M$, respectively, are given by

$$\mathbf{H}^M := \mathbf{H}(t^M, \mathbf{q}^M, \mathbf{u}^B), \tag{5.37a}$$

$$\mathbf{W}^M := \mathbf{W}(t^M, \mathbf{q}^M), \tag{5.37b}$$

which are approximated at the (mid-step) time instant $t^M = t^B + \frac{\Delta t}{2}$. Note that we also use the notations $\mathbf{u}^B = \dot{\mathbf{q}}^B$ for the generalized velocity vector in Eq. (5.36). The generalized coordinate vector at the mid-step time instant is denoted by

$$\mathbf{q}^M = \mathbf{q}^B + \mathbf{u}^B\frac{\Delta t}{2}. \tag{5.38}$$

Note that the mass matrix $\mathbf{M}$ in Eq. (5.36) is not necessarily a diagonal matrix. Hereto, we can rewrite the discretized EOMs in Eq. (5.36) as follows:

$$\mathbf{u}^E = \frac{\operatorname{adj}(\mathbf{M})\left(\mathbf{H}^M + \mathbf{W}^M\boldsymbol{\lambda}\right)\Delta t}{\det(\mathbf{M})} + \mathbf{u}^B, \tag{5.39}$$

where $\operatorname{adj}(\mathbf{M})$ and $\det(\mathbf{M})$ are the classical adjoint (adjugate) and the determinant of the mass matrix $\mathbf{M}$, respectively. In solving for the kinematic responses, we substitute the associated matrices in Eqs. (5.18a) – (5.18d) for the BM model into Eq. (5.36). For the AST model, we refer to the matrices in Eqs. (5.22a) – (5.22d).

In this scheme, the inclusions in Eqs. (5.8a) - (5.8b) for the contact force λ_a and the frictional torque λ_t of the bit-rock interaction are stored in the vector $\boldsymbol{\lambda} = \begin{bmatrix} \lambda_a & \lambda_t \end{bmatrix}^\top$ in Eqs. (5.36) – (5.39) and can be rewritten equivalently as the following implicit proximal point equations [104]:

$$\lambda_a = \operatorname{prox}_{C_a}\left(\lambda_a - r_a V_b\right), \tag{5.40a}$$

$$\lambda_t = \operatorname{prox}_{C_t}\left(\lambda_t - r_t \Omega_b\right). \tag{5.40b}$$

These proximal point formulations can be solved by an iterative technique [165], e.g., JOR scheme, with the parameters r_a and r_t being strictly positive constants and the associated convex sets being defined as follows:

$$C_a := \left\{\lambda_a \mid -n\,\sigma\,a\,\ell_n \le \lambda_a \le 0\right\}, \tag{5.41a}$$

$$C_t := \left\{\lambda_t \mid \frac{1}{2}\mu\,a\,\xi\,\lambda_a \le \lambda_t \le -\frac{1}{2}\mu\,a\,\xi\,\lambda_a\right\}. \tag{5.41b}$$

Please also refer to [19] for the details on this time-stepping scheme implementation for solving the drill-string dynamics, in the scope of a lumped-parameter modelling approach.

5.3.4 The interconnection of the drill-pipe and BHA dynamics

For both the BM and AST models, we construct the interconnection of the subsystems models of the drill-string at an interface between the bottom side of the drill-pipe (the upper part) and the top side of the BHA (the lower part). In this section, we first describe the kinematic and dynamic interconnections at the interface for both BM and AST models, in which the information of each sub-system obtained from the implementation of the numerical schemes detailed in the previous sections are exchanged. Second, we present the workflow of the numerical solver used for this type of coupled PDE-ODE-PDE system of both models.

5.3.4.1 BM model

In the benchmark model, the dynamic interconnection at the interface possesses the kinematic conditions in Eqs. (5.20a) – (5.20b). Since the BHA, including the drill-bit, is assumed to be a rigid body, this kinematic constraint implies that the velocities at the interface are equal to the bit velocities (see also Figure 5.6 – left). Note that the bit velocities are obtained by solving the BHA dynamics in Eqs. (5.36) – (5.39) via the time stepping scheme. Hereto, these kinematic conditions are written as follows (at the end of a time-stepping step):

$$V(t, x = L) = V_L = V_b^E, \tag{5.42a}$$

$$\Omega(t, x = L) = \Omega_L = \Omega_b^E. \tag{5.42b}$$

These kinematic conditions are essential for updating the boundary conditions of the PDEs of the drill-pipe dynamics (in terms of Riemann invariants) in Eqs. (5.33a) – (5.33b) based on the latest conditions of the BHA dynamics. These updates are used in solving the PDEs in Eqs. (5.28a) – (5.31) for the responses of the drill-pipe dynamics via the upwind scheme in Section 5.3.2.

On the other hand, the interaction force W_L and torque T_L at the interface are required as the inputs of the BHA dynamics; see in Eq. (5.17) with the associated matrices for the BM model in Eqs. (5.18a) – (5.18d). Updating the force and torque at the interface requires the latest boundary conditions of the PDEs of the drill-pipe dynamics. Thus, they can be updated in terms of the Riemann invariants in Eqs. (5.26a) – (5.27b) (after a time step) in the following way:

$$W_L = \left(\alpha_a(t, x = L) - \beta_a(t, x = L)\right) \frac{AE}{2c_a}, \tag{5.43a}$$

$$T_L = \left(\alpha_t(t, x = L) - \beta_t(t, x = L)\right) \frac{JG}{2c_t}. \tag{5.43b}$$

Moreover, the PDE of the depth-of-cut evolution in Eq. (5.13) is also solved via the upwind scheme (in Section 5.3.2) while incorporating the latest conditions of the BHA dynamics. The evolution state variable is updated as follows:

$$\Upsilon_p^{n+1} = \Upsilon_p^n - \Omega_b^E \frac{n}{2\pi} \frac{\Delta \bar{t}}{\Delta \theta} \left(\Upsilon_p^n - \Upsilon_{p-1}^n\right) + V_b^E \Delta \bar{t}, \qquad \text{for } \Omega_b^E \geq 0, \tag{5.44}$$

with $\Delta \bar{t}$ and $\Delta \theta$ as the increments of the time and the normalized angular position θ in the cutting process evolution, respectively. In this work, we do not consider the backward rotation of the drill-bit. The total depth-of-cut produced by the drill-bit is calculated via Eq. (5.15) – (5.16) by incorporating this latest evolution state obtained in Eq. (5.44). This total depth is then used for updating the reaction force and torque of the cutting component in the interface laws in Eqs. (5.11a) – (5.11b), which are required for solving the BHA dynamics in Eq. (5.17).

5.3.4.2 AST model

In the model with AST, we also have the kinematic condition at the interface between the drill-pipe and the lumped section of BHA above the AST in Eqs.

(5.25a) – (5.25b). Following the kinematic condition of the BM model in Eqs. (5.42a) – (5.42b), the kinematic condition at the interface of the AST model implies that the velocities at the interface are equal to the velocities of the lumped BHA section above the AST (see also Figure 5.6 – right).

Note that in the AST model, as with the bit velocities, the velocities of the lumped BHA section above the AST are obtained by both solving the BHA dynamics in Eqs. (5.36) – (5.39) (via the time stepping scheme, with the associated matrices in Eqs. (5.22a) – (5.22d)) and utilizing the kinematic constraint in Eqs. (5.23) – (5.24). Hence, we have the following kinematic conditions at the interface of the AST model:

$$V(t, x = L) = V_L^E, \tag{5.45a}$$

$$\Omega(t, x = L) = \Omega_L^E. \tag{5.45b}$$

The axial velocity at the interface, V_L^E, is calculated via Eq. (5.39), i.e., as the first element of the vector $\mathbf{u}^E$. While the angular velocity at the interface is calculated via the kinematic constraint in Eq. (5.23) as follows:

$$\Omega_L^E = \Omega_b^E + \frac{\left(V_L^E - V_b^E\right)}{\alpha}. \tag{5.46}$$

Furthermore, in the AST model, the interaction force W_L and torque T_L at the interface are calculated in the same way as for the BM model by following Eqs. (5.43a) – (5.43b) with the Riemann invariants in Eqs. (5.26a) – (5.27b). In addition, the depth-of-cut evolution for the AST model is also solved by utilizing Eq. (5.44) as in the BM model.

In overall, these BM and AST models (in terms of a coupled PDE-ODE-PDE system) allow us to capture the multiple modes of axial and torsional oscillations of the long drill-pipe structure and also to interconnect them with the BHA dynamics incorporating the nonlinearity due to the frictional contact and the delay (regenerative) effect of the cutting process at the bit-rock interface.

5.3.4.3 Workflow of the numerical solver

Algorithm 5.1 describes the workflow for numerically solving the coupled PDE-ODE-PDE system of the BM and AST models. Moreover, the steady-state solutions derived in Appendix C.1 are also used for the initial conditions in the numerical solvers of these models.

In the next section, we will provide practically representative, illustrative numerical examples for investigating the effect of the AST on drilling performance under the influence of multiple modes of axial and torsional dynamics of the drill-pipe structure.

Algorithm 5.1 Pseudo code for the numerical solver for the coupled PDE-ODE-PDE system of the BM and AST models.

```
Input: Initial conditions & parameter settings for the PDEs and ODEs
Input: Simulation parameters (final simulation time, spatial cell size (spatial discretization))    ▷ the CFL condt.

for $i = 1 : n$ do    ▷ $n$: number of temporal discretization based on the CFL condt.
    1) Calculate the Riemann invariants at the top ($x = 0$) using the top BCs ($V_0, \Omega_0$), see Eqs. (5.32a) - (5.32b).
    2) Update the interaction forces at the interface ($W_L, T_L$) using the latest Riemann invariants, see Eqs. (5.43a) - (5.43b).

    Solve the BHA dynamics in Eq. (5.17)
    3) Update the total depth-of-cut in Eqs. (5.15) - (5.16) based on the latest evolution state in Eq. (5.44).
    4) Solve the proximal point of the frictional component in Eqs. (5.40a) - (5.40b) using the JOR scheme.
    5) Solve the EOMs in Eq. (5.39) using the time-stepping scheme with the Moreau's midpoint method.
    6) Update the bit velocities ($V_b^E, \Omega_b^E$) and the interface velocities ($V_L$, $\Omega_L$), using Eqs. (5.42a) - (5.42b) for the BM model and Eqs. (5.45a) - (5.46) for the AST model.
    7) Update the WOB and TOB due to bit/rock interaction ($W_b, T_b$) in Eqs. (5.7a) - (5.7b).

    Update the interface condition:
    8) Update the Riemann invariants at the interface ($x = L$) in Eqs. (5.33a) - (5.33b) using $V_L$ and $\Omega_L$

    Solve the PDEs of the drill-pipes and rock surface evolution:
    9) Solve the PDEs of the drill-pipe in Eqs. (5.2a) - (5.4b) with the upwind scheme in Eqs. (5.35a) - (5.35b)
    10) Solve the PDE for the depth-of-cut evolution in Eq. (5.13) with the upwind scheme in Eq. (5.35a)

    Update for the next iteration, including for the interface:
    11) Update the time step: $t_k^B = t_k^B + \Delta t_s$
    12) Update the bit velocities ($V_b^B = V_b^E$ and $\Omega_b^B = \Omega_b^E$) using the latest solutions of the BHA dynamics
    13) Update the bit positions ($U_b^B = U_b^E$ and $\Phi_b^B = \Phi_b^E$)
    14) Update the axial and angular positions at the inteface ($U_L, \Phi_L$) with the associated velocities ($V_L, \Omega_L$)
end for

Store all the state variables for response plotting
```

5.4 Dynamic analyses of drill-string dynamics without and with the AST

In this section we present the simulation results of the BM and AST models. In particular, we focus on the following aspects:

1. Comparison of the steady-state responses between the BM and AST models,
2. Comparison of the time-averaged steady-state responses of both models to evaluate drilling performance, the contact forces (frictional loading at the bit) and the torque-on-interface (TOI; representing the dynamic loading on the drill-string) under variation of the drilling operational parameters.

For the numerical simulations, we consider the system parameters used in the earlier works in [187, 3, 192, 19].

5.4.1 Effect of the AST on the drilling performance

In this subsection, we analyze first the characteristics of the dynamic responses of both BM and AST models. Second, we continue the investigation of the effect of the AST on drilling performance in terms of rate-of-penetration, drilling efficiency and frictional loading at the bit.

5.4.1.1 The dynamic response of the BM and AST models

Figure 5.7 depicts the steady-state responses of the axial velocities at the bit for the BM model (on top side) and the AST model (on bottom side) for hookload $H_0 = 56.6$ kN and top-drive angular velocity $\Omega_0 = 60$ rpm. Figure 5.8 shows the angular bit velocity responses of the BM and AST models in the steady-state region. The black dashed lines in all responses show the averaged magnitudes of the velocities for both BM and AST models.

In general, the steady-state responses of both BM and AST distributed models exhibit axial and torsional limit-cycles, with a stick-slip phenomenon in the axial dynamics. This limit cycling behavior is induced by the fact that the nominal (constant angular and axial velocities) solution is unstable. These periodic responses are dominated by lower dynamic modes of the axial and torsional dynamics in both models. By comparing these responses for each model, the limit-cycles in the AST model show higher frequency contents than the limit-cycles in the BM model.

Furthermore, Figure 5.7 shows that the presence of the AST increases the ROP. The peak values of the axial bit velocity response in the AST model are up to three times the peak values of the axial vibrations in the BM model. These

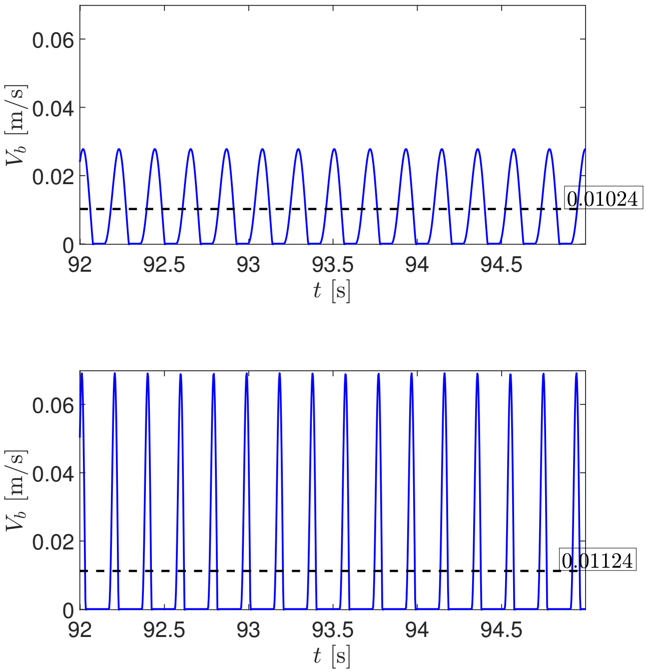

Figure 5.7: The axial dynamic response of the distributed models of drill-string without AST (BM model - top) and with AST (AST model - bottom) with drilling operational parameters: hookload $H_0 = 56.6$ kN and top-drive angular velocity $\Omega_0 = 60$ rpm.

findings suggest that stronger axial vibrations are induced due to the presence of AST and these significantly affect the drilling performance (i.e., higher ROP). As a remark, these results are inline with the conclusions presented in the earlier works in [181, 187, 19] on low-order lumped-parameter models.

5.4.1.2 Comparison of frictional contact at the bit between the BM and AST models

Figure 5.9 shows the comparison of the contact force responses between the BM and AST models (see Eq. (5.18d) or Eq. (5.22d)). The black dashed lines in both responses show the averaged magnitudes of the contact forces for both BM and AST models.

First, this comparison shows that the stronger axial vibrations induced by the AST result in a lower averaged contact force at the bit (in Eq. (5.8a)) for the AST model. As indicated in Figure 5.9, the averaged magnitude of the contact force for the AST model shows about 25% reduction compared to the BM model.

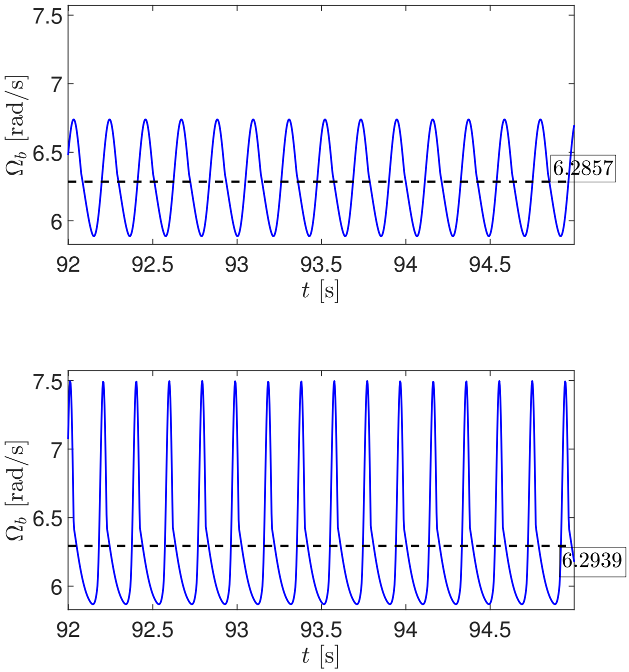

Figure 5.8: The torsional dynamic responses of the distributed models of drill-string without AST (BM model - top) and with AST (AST model - bottom) with drilling operational parameters: hookload $H_0 = 56.6$ kN and top-drive angular velocity $\Omega_0 = 60$ rpm.

This effect arises because the AST leads to longer axial sticking periods (see Figure 5.7), during which that axial contact force W_f can be lower than its maximum value (which is always attained during axial slip periods); see the set-valued force law for W_f in Eq. (5.8a).

Second, the average decrease of the contact force in the bit-rock interaction shows that in the AST model more energy applied by the rig at surface is used more in the rock cutting process (i.e., producing more DOC) and less frictional dissipation at the bit-rock interface (wearflat). Note that the frictional torque decreases as the contact force gets reduced - following their relation in Eq. (5.8b). This will be further explored in the analyses on drilling efficiency in the next subsection.

5.4.1.3 Comparison of drilling performance and frictional loading (at the bit) under the variation of drilling operational parameters

The influence of the AST on drilling performance becomes even more apparent when comparing the averaged axial bit velocity (ROP) and drilling efficiency of

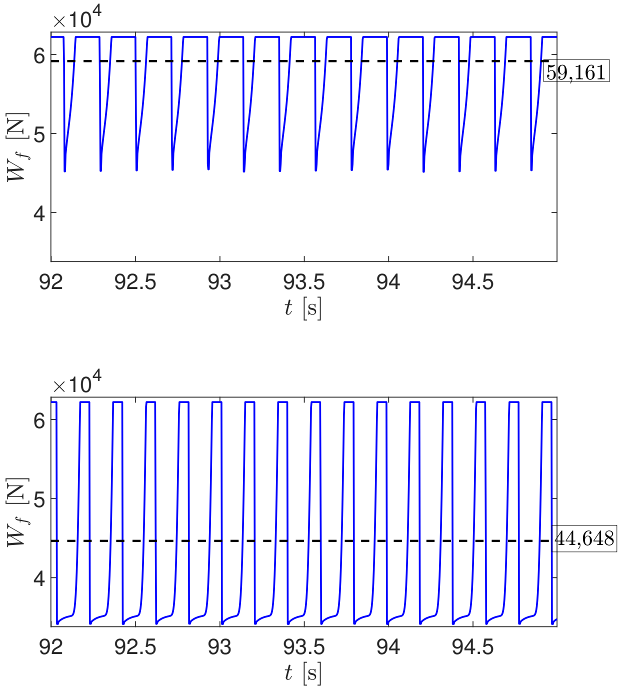

Figure 5.9: The evolution of contact forces at the bit for the distributed models of drill-string without AST (BM model - top) and with AST (AST model - bottom) with drilling operational parameters: hookload $H_0 = 56.6$ kN and top-drive angular velocity $\Omega_0 = 60$ rpm. The dashed lines show the averaged magnitudes of the contact forces in both models.

the BM (red-dots) and AST (blue-dots) models, as depicted in Figure 5.10. In these plots, these comparisons are conducted under drilling operational parameter variations: hookload $H_0 \in \{16.9, 39.6, 56.6, 73.6, 96.2\}$ kN and top angular velocity $\Omega_0 \in \{30, 60, 120\}$ rpm.

Note that the applied weight on the drill-string increases as the hookload decreases; see Figures 5.3 and 5.4. The hookload acts as a control parameter for drilling performance in the axial direction, i.e., we expect an increase of ROP when decreasing the hookload.

Inline with previous studies [187, 19], the average drilling efficiency is expressed as the ratio between the average TOB used in the rock cutting process T_c and the total of the average TOB due to the bit-rock interaction (which includes the torque lost due to the frictional dissipation T_f):

$$\eta = \frac{\langle T_c \rangle}{\langle T_c \rangle + \langle T_f \rangle}, \tag{5.47}$$

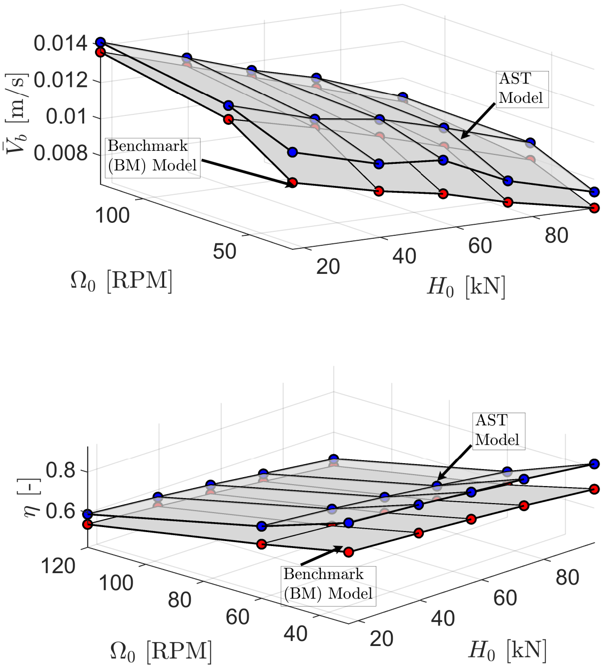

Figure 5.10: The comparison of averaged rate-of-penetrations (ROP; top) and drilling efficiency (bottom) for the distributed models of drill-string without AST (BM model) and with AST (AST model) under drilling operational parameter variations: $H_0 \in \{16.9, 39.6, 56.6, 73.6, 96.2\}$ kN and $\Omega_0 \in \{30, 60, 120\}$ rpm.

where $\langle T_c \rangle$ and $\langle T_f \rangle$ are the average values of the (periodic) steady-state solutions of TOB from the cutting and frictional components in the bit-rock interaction, respectively.

From Figure 5.10, first, the top plot shows that the average ROP in the AST model consistently outperforms the ROP in the BM model over the employed ranges of drilling operational conditions. Second, the bottom plot supports the result established in the top plot by visualizing that the rock cutting process in the AST model is more energy-efficient than in the BM model and thus brings higher ROPs.

Moreover, the average ROP increases in both BM and AST models with decreasing hookload H_0 and increasing top angular velocity Ω_0. A decrease in hookload H_0, under a prescribed contact top angular velocity Ω_0, results in increasing drilling efficiencies. However, increasing top angular velocity Ω_0 leads to slightly decreasing drilling efficiencies for both BM and AST models. This indicates that relatively less energy is used in rock cutting process.

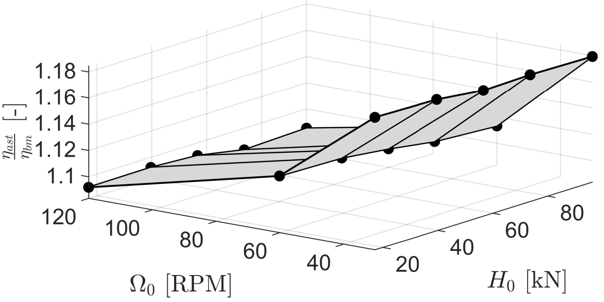

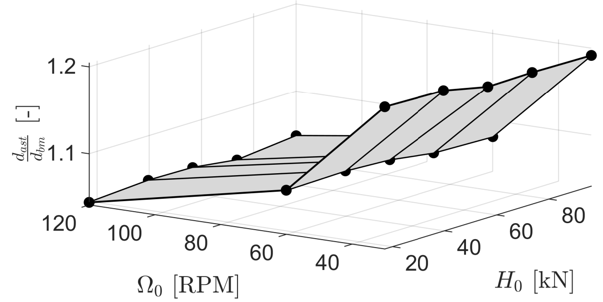

Figure 5.11: The gain ratios of drilling efficiency (top) and depth-of-cut (bottom) of the distributed AST model relative to the distributed BM model under drilling operational parameter variations: $H_0 \in \{16.9, 39.6, 56.6, 73.6, 96.2\}$ kN and $\Omega_0 \in \{30, 60, 120\}$ rpm.

In a more detailed investigation, the gains in terms of drilling efficiency (top) and depth-of-cut (bottom) of the AST model relative to these types of quantities obtained from the BM model (i.e., $\frac{\eta_{ast}}{\eta_{bm}}$ and $\frac{d_{ast}}{d_{bm}}$, respectively) are plotted in Figure 5.11 for the same ranges of operational drilling conditions. In this way, the essential benefits of using the AST to improve drilling performance are clearly seen, i.e., positive gain in drilling efficiency with the AST up to 18% (in the top plot) and positive gain in depth-of-cut with the AST up to 20% (in the bottom plot).

Moreover, Figure 5.12 compares the contact force ratios of the BM and AST models under the same drilling operational variations, where this contact force ratio is given by

$$\bar{W}_f = \frac{\langle W_f \rangle}{\langle W_c \rangle + \langle W_f \rangle}. \tag{5.48}$$

The quantities $\langle W_c \rangle$ and $\langle W_f \rangle$ are the averaged values of WOB from the cutting and frictional components of the bit-rock interface law in steady-state region, respectively. This figure shows the consistency over the varied drilling operational region of the reduction of the contact force at the bit in the AST model compared

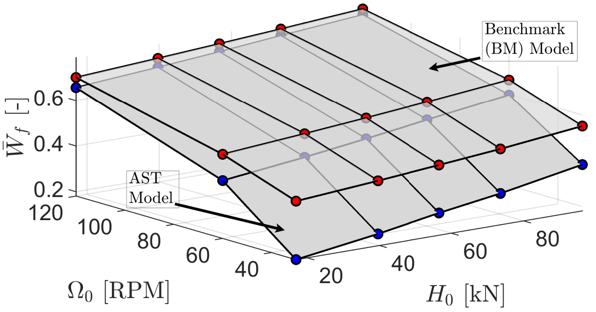

Figure 5.12: The comparison of averaged contact force ratio at the bit wearflat for the distributed models of drill-string without AST (BM model) and with AST (AST model) under drilling operational parameter variation: $H_0 \in \{16.9, 39.6, 56.6, 73.6, 96.2\}$ kN and $\Omega_0 \in \{30, 60, 120\}$ rpm.

to that in the BM model. This indicates that the frictional loading at the bit (in Eq. (5.8b)) in the AST model is less than in the BM model, and this helps to performance improvement (i.e., higher ROP) over the drilling parameters region. As mentioned above, this reduction in the relative contribution of the wearflat force in the total weight-on-bit also reduces the frictional losses at the bit which, in turn, reduce heat-induced bit damage and prolong the operational time of the drill-bit.

5.4.2 Effect of the AST on the dynamic loading on the drill-string

In this part, we analyze the effect of the AST on the dynamic loading at the interface between the drill-pipe and BHA parts of the drill-string system in both benchmark (BM) and AST models. In Section 5.4.2.1, we focus on comparing the steady-state responses of torques-on-interface (TOI), that represent the dynamic loading at the interface (i.e., on the drill-string), for both models. In Section 5.4.2.2, we investigate the average values of the steady-state responses of TOI for both models under varied drilling operational conditions in soft and hard rock formations.

5.4.2.1 The torque responses at the interface of the drill-pipe (upper) and BHA (lower) parts

Figure 5.13 shows the steady-state responses of TOI T_L (in red) and torques-on-bit T_b (TOB; in blue) for the BM model (top) and the AST model (bottom). We consider at the top: hookload $H_0 = 56.6$ kN and top angular velocity $\Omega_0 = 60$ rpm.

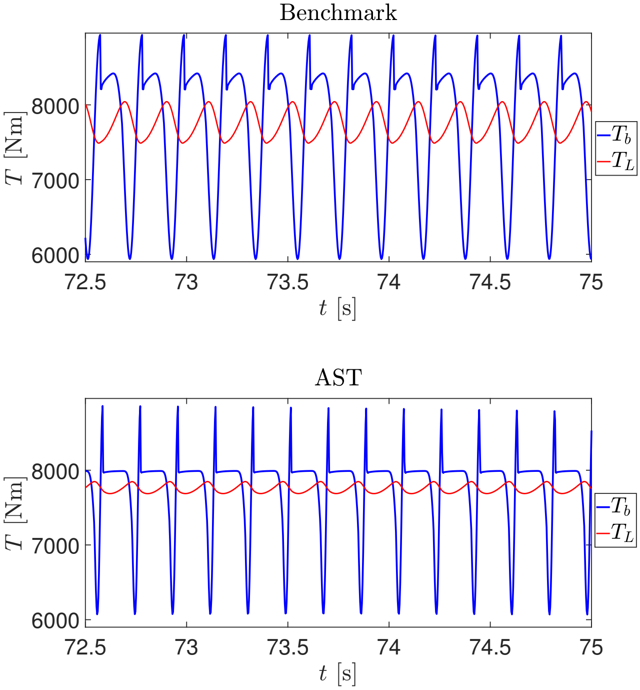

Figure 5.13: The dynamic responses of torque-on-bit (TOB T_b; in blue) and loading at the interface of the drill-pipe and BHA parts (torque-on-interface/TOI T_L; in red) for the BM model (in top) and AST model (in bottom) with drilling parameters: hookload $H_0 = 56.6$ kN and top angular velocity $\Omega_0 = 60$ rpm, and rock parameters $\varepsilon = \sigma = 120$ MPa.

In this comparison on the steady-state responses of TOI, the peak-to-peak value in the BM model is significantly larger than the one in the AST model, while the peak-to-peak value of the TOB is comparable in both cases. This indicates that dynamic loading on the drill-pipe is mitigated by the presence of the AST, which, in turn, can reduce detrimental effects such as drill-string fatigue.

5.4.2.2 Dynamic loading comparison

As a performance indicator of the TOI response, we use the following 'amplitude'-to-mean loading ratio at the interface

$$\frac{T_L^{pp}}{T_L^{ss}} := \frac{T_L^{max} - T_L^{min}}{T_L^{ss}}, \tag{5.49}$$

where T_L^{pp} and T_L^{ss} reflect the amplitude (peak-to-peak) and average (mean) values, respectively, of the torque-on-interface T_L (steady-state) response. The

(Rock parameters: $\varepsilon = \sigma = 120$ MPa)

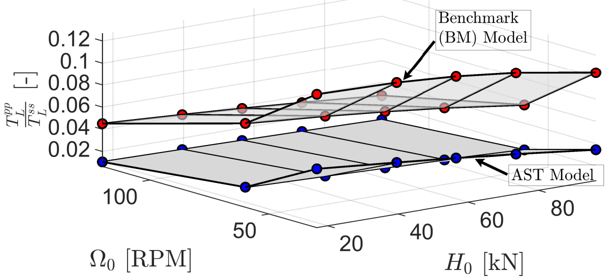

(Rock parameters: $\varepsilon = \sigma = 60$ MPa)

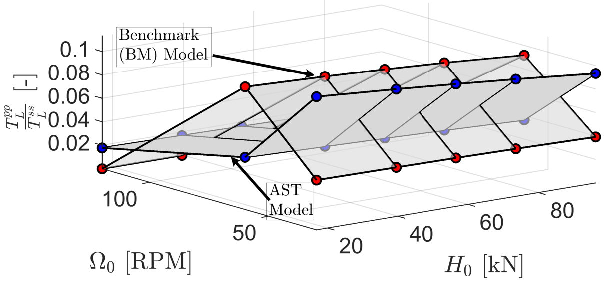

Figure 5.14: The comparison of the amplitude-to-mean loading ratios at the interface (between the drill-pipe and BHA parts of the drill-string systems) for the BM (red-dots) and AST (blue-dots) distributed models in hard rock formation ($\varepsilon = \sigma = 120$ MPa; top figure) and soft rock formation ($\varepsilon = \sigma = 60$ MPa; bottom figure) – under drilling operational parameter variations: $H_0 \in \{16.9, 39.6, 56.6, 73.6, 96.2\}$ kN and $\Omega_0 \in \{30, 60, 120\}$ rpm.

maximum and minimum peaks of the response are denoted by T_L^{max} and T_L^{min}, respectively.

Figure 5.14 presents the comparison of these amplitude-to-mean loading ratios at the interface between the BM (red-dots) and AST (blue-dots) distributed models for drilling cases in hard rock formation ($\varepsilon = \sigma = 120$ MPa; top) and soft rock formation ($\varepsilon = \sigma = 60$ MPa; bottom) under operational parameter variations: hookload $H_0 \in \{16.9, 39.6, 56.6, 73.6, 96.2\}$ kN and top angular velocity $\Omega_0 \in \{30, 60, 120\}$ rpm. For the case of hard rock formation, we show a positive effect of AST in reducing the amplitude-to-mean loading ratio at the interface over the given parametric space of drilling operations. This is consistent with the results in Figure 5.13.

In the case of soft rock formation, we see the same positive effect of the AST in reducing the amplitude-to-mean loading ratio at the interface for a nominal top angular velocity $\Omega_0 = 60$ rpm (in the entire range of hookloads). However, for other operating points, particularly related to the cases of lower and higher top angular velocities, we observe that the amplitude-to-mean loading ratios at the interface in the AST model are higher than the ones in the BM model. Therefore, we investigate further the dynamic responses of both models associated with these two particular operating points, namely the top angular velocity $\Omega_0 \in \{30, 120\}$ rpm with a nominal hookload $H_0 = 16.9$ kN for the case of soft rock formation.

The case of soft rock formation: with lower and higher top angular velocities Ω_0 Figure 5.15 shows the investigation results; the top plots show the steady-state responses of TOB T_b (in blue) and TOI T_L (in red) for both BM and AST models with the lower top angular velocity $\Omega_0 = 30$ rpm. Figure 5.16 shows the plots of the same responses for both models with the higher angular velocity $\Omega_0 = 120$ rpm. In the case of $\Omega_0 = 30$ rpm, we observe that the response of the torque T_L in the BM model indeed has a lower peak-to-peak value than the same response in the AST model. This leads to lower the amplitude-to-mean loading ratio at the interface in Eq. (5.49) for the BM model.

For $\Omega_0 = 120$ rpm, the BM model exhibits a stabilizing effect on the steady-state responses of both torques, which leads to a near-zero amplitude-to-mean loading ratio at the interface. In this case, the AST model also shows a slightly higher peak-to-peak TOI. We care to stress, however, that in these scenarios the TOB response between the two models differs significantly: the peak-to-peak value of the TOB is significantly higher than for the AST model. Taking this fact into account, the AST, in fact, realizes a higher level of mitigation of the TOB towards the TOI, even in these scenarios.

5.5 Performance-based design of the AST parameters

In this section, we tune the key parameters of the AST design, namely its spring stiffness K_b and the lead angle β of its helical spline for drilling performance improvement [187, 181], and also perform robustness analysis on the tuned parameters of the AST under parametric variations of drilling operational conditions, drill-string parameters, and rock formation characteristics. In Section 5.5.1, the tuning process is conducted to find the optimal parameters of the AST, K_b^{opt} and β_{ast}^{opt} for optimal performance (in terms of drilling efficiency) over the variations of drill-string parameter (the drill-pipe length L) and rock parameters (intrinsic specific energy ε and normal contact stress of rock σ) under a set of drilling operational parameters (hookload H_0 and top angular velocity Ω_0). In Section 5.5.2, we perform a comparative study on the robustness of the tuned and standard/existing design parameters of AST in the scope of drilling performance, frictional loading at the bit and dynamic loading on the drill-string. In particular, we focus to assess the robustness under some sets of parametric variations of drilling operational conditions, drill-string, and rock formation parameters.

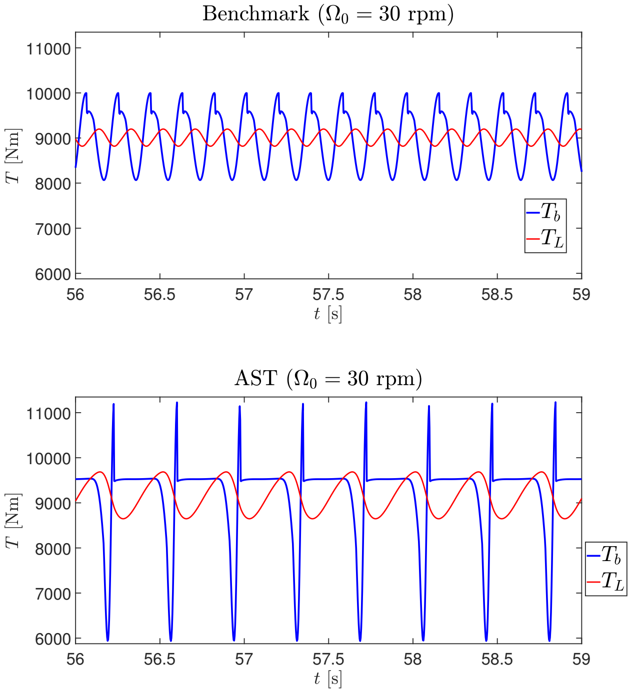

Figure 5.15: The dynamic responses of torque-on-bit/TOB (T_b; in blue) and loading at the interface of the upper and lower parts of drill-string (torque-on-interface/TOI T_L; in red) for the BM model (in top) and AST model (in bottom) with hookload $H_0 = 16.9$ kN and soft rock formation ($\varepsilon = \sigma = 60$ MPa) for the case of lower top angular velocity ($\Omega_0 = 30$ rpm).

5.5.1 The tuned design parameters of the AST

To tune the design parameters of AST, first, we consider the following parametric sets:

1. The stiffness of the AST spring,

$$K_b \in \{456.7, 1065.7, 1522.5, 1979.2\} \, \frac{\text{kN}}{\text{m}}, \tag{5.50a}$$

2. The lead angle of the AST helical spline,

$$\beta_{ast} \in \{15, 30, 45, 60\} \ \text{deg}, \tag{5.50b}$$

3. The drill-string parameter (the drill-pipe length),

$$L \in \{700, 1000, 1500\} \, \text{m}, \tag{5.50c}$$

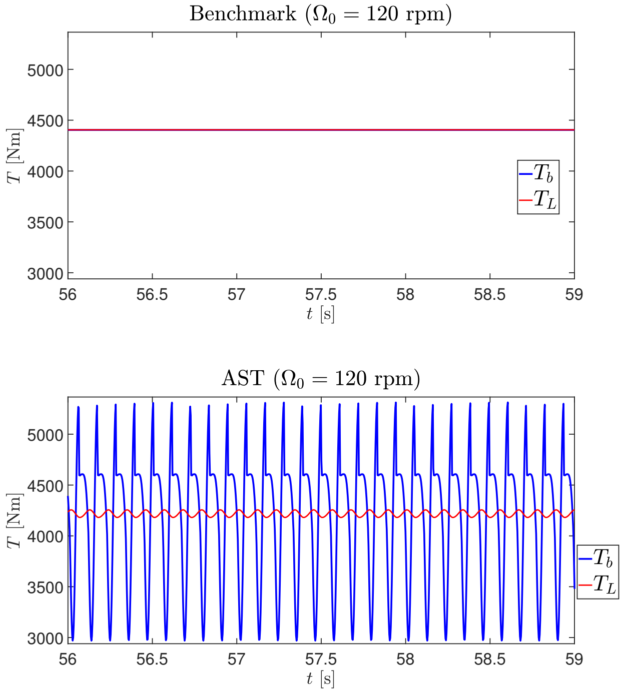

Figure 5.16: The dynamic responses of torque-on-bit/TOB (T_b; in blue) and loading at the interface of the upper and lower parts of drill-string (torque-on-interface/TOI T_L; in red) for the BM model (in top) and AST model (in bottom) with hookload $H_0 = 16.9$ kN and soft rock formation ($\varepsilon = \sigma = 60$ MPa) for the case of higher top angular velocity ($\Omega_0 = 120$ rpm).

4. The rock parameters (e.g., indicating hard and soft rock properties) for both cutting and frictional components of the bit-rock interaction,

$$\varepsilon = \sigma \in \{60, 90, 120\} \ \text{MPa}. \tag{5.50d}$$

Based on the earlier work [187], we use the stiffness $K_b = 1522.5 \frac{\text{kN}}{\text{m}}$ and the lead angle $\beta_{ast} = 45$ deg as the standard (nominal) design parameters of AST (design baseline). Nominal drilling operational parameters, hookload $H_0 = 56.6$ kN and top angular velocity $\Omega_0 = 60$ rpm, are used in the numerical simulations. Second, for the tuning process, the average drilling efficiency η in Eq. (5.47) is set as the performance indicator to find the optimal design of AST. The tuning procedure is detailed as follows:

1. Simulate the distributed AST model for every AST design parameter in the parameter sets in Eqs. (5.50a) - (5.50b) with considering particular drill-string and rock parameters (e.g., $L = 700$ m and $\varepsilon = \sigma = 60$ MPa).

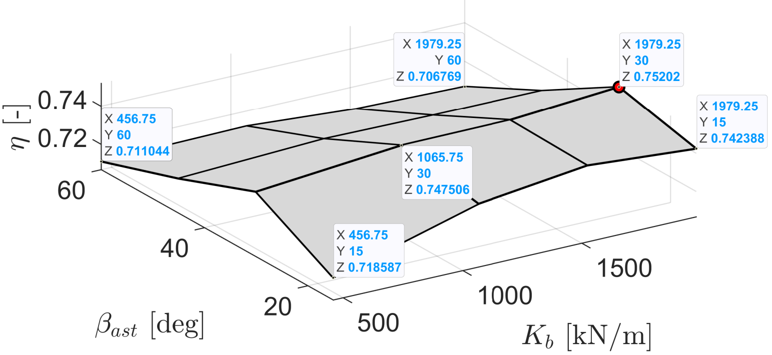

Figure 5.17: The drilling efficiency for the AST model under the variation of the design parameters of the AST for nominal drilling operational parameters: $H_0 = 56.6$ kN and $\Omega_0 = 60$ rpm, and for drill-string and rock parameters: $L = 1000$ m and $\varepsilon = \sigma = 60$ MPa, respectively.

2. Collect all drilling efficiency η values (Eq. (5.47)) based on the steady-state responses for every design parameter of the AST in the sets, and then determine the optimal design parameters of AST, K_b^{opt} for the optimal stiffness and β_{ast}^{opt} for the optimal lead angle, based on the maximum (optimal) efficiency for this particular drill-string and rock parameters used in step 1.
3. Repeat steps 1 and 2 above for the other values of drill-string and rock parameters in Eqs. (5.50c) - (5.50d).

Figure 5.17 shows the averaged drilling efficiency plot for the distributed AST model under the sets of AST design parameters in Eqs. (5.50a) - (5.50b) for a couple of drill-string and rock parameters: $L = 1000$ m and $\varepsilon = \sigma = 60$ MPa, and with a nominal drilling operational parameters: hookload $H_0 = 56.6$ kN and top angular velocity $\Omega_0 = 60$ rpm. In this particular set of drill-string and rock parameters, the optimal drilling efficiency (see the red dot) is achieved with a higher stiffness K_b and lower lead angle β of the AST design, i.e., $K_b = 1979.2\frac{\text{kN}}{\text{m}}$ and $\beta_{ast} = 30$ deg.

After we run the tuning procedure above for all the variations of the drill-pipe length and the rock parameters in Eqs. (5.50c) - (5.50d), we then collect all optimal values of drilling efficiencies into a single plot in Figure 5.18 (for each point of drill-string and rock parameters in the sets), together with the plots of their associated optimal design parameters (the AST stiffness and lead angle). As the result of this tuning process, Figure 5.18 shows in overall that the optimal drilling efficiencies are achieved with the higher stiffness $K_b^{opt} = 1979.2\frac{\text{kN}}{\text{m}}$ (middle plot) and lower lead angle $\beta_{ast}^{opt} = 30$ deg (bottom plot) – although for some specific parameter settings, $\beta_{ast} = 15$ deg seems optimal. Hence, these parameters, $K_b^{opt} = 1979.2\frac{\text{kN}}{\text{m}}$ and $\beta_{ast}^{opt} = 30$ deg, are obtained as the tuned design parameters of AST for optimal drilling efficiency under the variations of the drill-pipe length: $L \in \{700, 1000, 1500\}$ m and the rock parameters: $\varepsilon = \sigma \in \{60, 90, 120\}$ MPa with a nominal drilling operational parameters: $H_0 = 56.6$ kN and $\Omega_0 = 60$ rpm.

Next, we analyze the robustness of these tuned design parameters of AST under some variations of drilling operational conditions and drill-string and rock parameters.

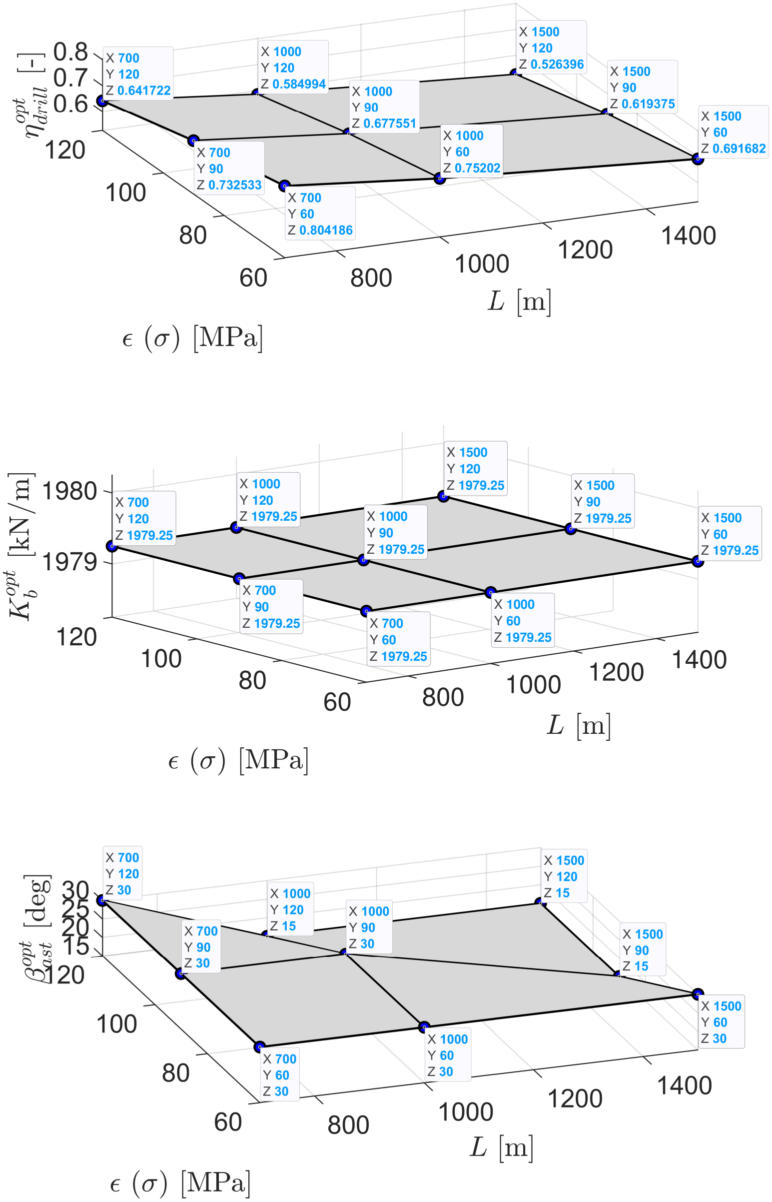

Figure 5.18: The optimal drilling efficiency (top plot) results from the tuned design parameters of AST: $K_b^{opt} = 1979.2\frac{\text{kN}}{\text{m}}$ (middle plot) and $\beta_{ast}^{opt} = 30$ deg (bottom plot) applied in the AST model under the variations of the drill-string parameter (the drill-pipe length): $L \in \{700, 1000, 1500\}$ m and the rock parameters: $\varepsilon = \sigma \in \{60, 90, 120\}$ MPa and a nominal drilling operational parameters: $H_0 = 56.6$ kN and $\Omega_0 = 60$ rpm.

5.5.2 Robustness analysis

In this section, we present the robustness analysis on the tuned design parameters of the AST (also called the tuned AST model) for three indicators: drilling performance, frictional loading at the bit, and dynamic loading at the interface - all under the parametric variations of drilling operational conditions, rock and drill-string physical characteristics. We also perform this robustness analysis on the standard/existing design parameters of the AST (also called the standard AST model) and the benchmark (BM) model and compare the three indicators among these three models. We consider the following parametric sets of drilling operational conditions: $H_0 \in \{16.9, 56.6\}$ kN for the hookload, and $\Omega_0 \in \{60, 120\}$ rpm for the top angular velocity.

5.5.2.1 Drilling performance and frictional loading at the bit

Figures 5.19 and 5.20 show the comparison of the average drilling efficiencies (as a ratio relative to the drilling efficiency of the BM model) based on the steady-state responses of

1. The standard/nominal AST model with the stiffness $K_b = 1522.5\frac{\text{kN}}{\text{m}}$ and the lead angle $\beta_{ast} = 45$ deg, and
2. The tuned AST model with the optimal stiffness $K_b^{opt} = 1979.2\frac{\text{kN}}{\text{m}}$ and the optimal lead angle $\beta_{ast}^{opt} = 30$ deg.

In addition, Figures 5.21 and 5.22 show the comparison of the average depths-of-cut (also as a ratio relative to the depth-of-cut of the BM model) obtained from the same AST models responses. These comparisons are conducted under the variations of the drill-string parameter (the drill-pipe length): $L \in \{700, 1000, 1500\}$ m and the rock parameters: $\varepsilon = \sigma \in \{60, 72, 90, 120\}$ MPa and with the parametric sets of drilling operational conditions above.

First, these two comparisons show that the tuned AST model consistently gives higher drilling efficiency and a superior cutting process (reflected in the depth-of-cut) than the standard AST model. Relative to the efficiency and the DOC obtained from the BM model (without the AST), the tuned AST model can gain its average efficiency and DOC up to 18% and 20%, respectively, depending also on the drilling operational parameters being employed. The standard AST model gains up to 12% for the average efficiency and 15% for the average DOC with the same operational conditions. Second, these comparisons also show the robustness of the tuned and standard design parameters of the AST over the parametric spaces of drilling operational conditions, rock and drill-string physical characteristics.

Figures 5.23 and 5.24 support the findings above by showing the comparison of contact force ratio (in Eq. (5.48)) obtained from the steady-state responses of the

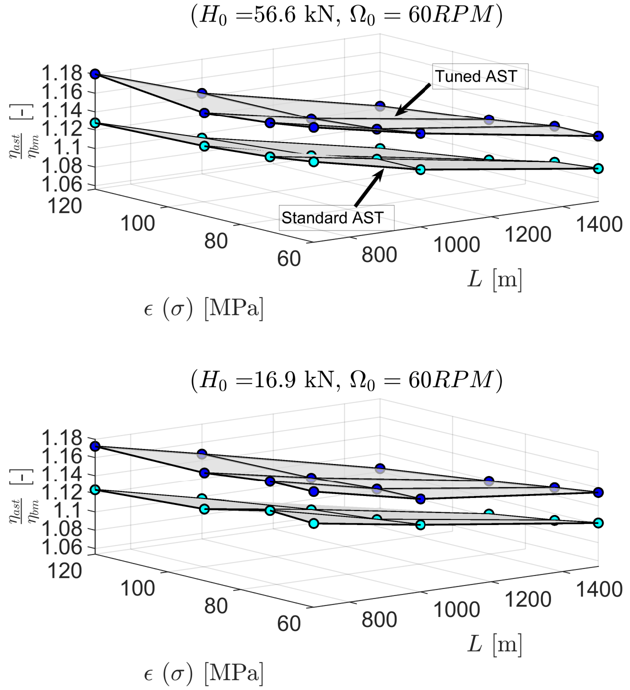

Figure 5.19: The comparison of the drilling efficiency (relative to the drilling efficiency of the BM model) for the distributed AST models with the standard (nominal) design parameters ($K_b = 1522.5\frac{\text{kN}}{\text{m}}$ and $\beta_{ast} = 45$ deg) and with the tuned design parameters ($K_b^{opt} = 1979.2\frac{\text{kN}}{\text{m}}$ and $\beta_{ast}^{opt} = 30$ deg), under the variations of the drill-string parameter (the drill-pipe length): $L \in \{700, 1000, 1500\}$ m and the rock parameters: $\varepsilon = \sigma \in \{60, 72, 90, 120\}$ MPa and with the variation of drilling operational parameters: 1) $H_0 = 56.6$ kN and $\Omega_0 = 60$ rpm (top), and 2) $H_0 = 16.9$ kN and $\Omega_0 = 60$ rpm (bottom).

tuned and standard AST models and BM model for the same ranges of operating conditions, drill-string, and rock parameters.

First, this comparison explains that the extra axial vibrations induced by the tuned AST model gives a lower contact force than the standard AST and BM models. This is shown by the reduced magnitudes of the contact forces for the tuned AST model. Second, these reduced contact forces support to improve the drilling performance in the tuned AST model, as the frictional torque (in Eq. (5.8b)) decreases. Hence, this indicates that more energy used for the rock cutting in the tuned AST model. Third, this reduction of the contact force magnitudes in both tuned and standard AST models is robust over the parametric spaces of operating conditions, drill-string, and rock physical characteristics.

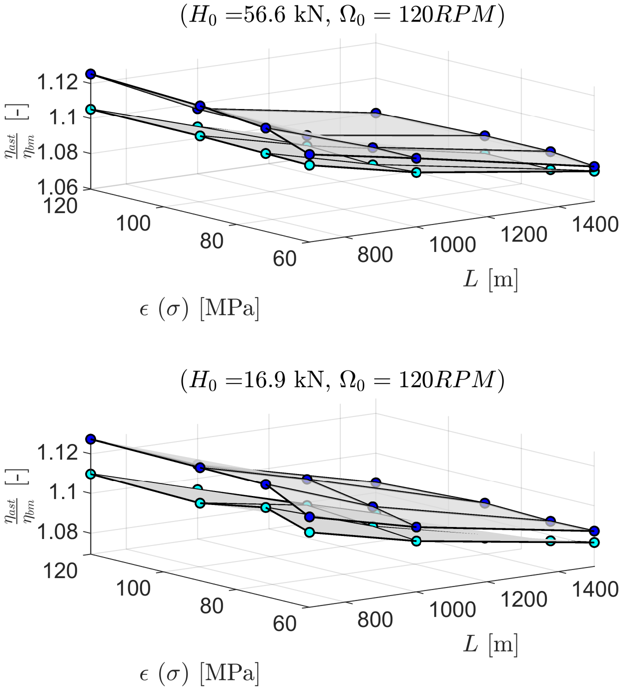

Figure 5.20: The comparison of the drilling efficiency (relative to the drilling efficiency of the BM model) for the distributed AST models with the standard (nominal) design parameters ($K_b = 1522.5\frac{\text{kN}}{\text{m}}$ and $\beta_{ast} = 45$ deg) and with the tuned design parameters ($K_b^{opt} = 1979.2\frac{\text{kN}}{\text{m}}$ and $\beta_{ast}^{opt} = 30$ deg), under the variations of the drill-string parameter (the drill-pipe length): $L \in \{700, 1000, 1500\}$ m and the rock parameters: $\varepsilon = \sigma \in \{60, 72, 90, 120\}$ MPa and with the variation of drilling operational parameters: 1) $H_0 = 56.6$ kN and $\Omega_0 = 120$ rpm (top), and 2) $H_0 = 16.9$ kN and $\Omega_0 = 120$ rpm (bottom).

5.5.2.2 Dynamic loading on the drill-string

In this part, we focus to investigate the dynamic loading on the drill-string, particularly at the interface of the upper and lower parts of the string, for the tuned and standard AST models and the BM model within the same ranges of operating conditions, drill-string, and rock parameters. This type of dynamic loading affects the drill-string structure performance, which can impact the fatigue level and the reliability of the drill-string structure to support the downhole equipment in the BHA.

Figures 5.25 and 5.26 show the comparison of the 'amplitude'-to-mean loading ratios at the interface (in Eq. (5.49)). This comparison shows that the loading ratio of the tuned AST model gives the lowest value among the three models within

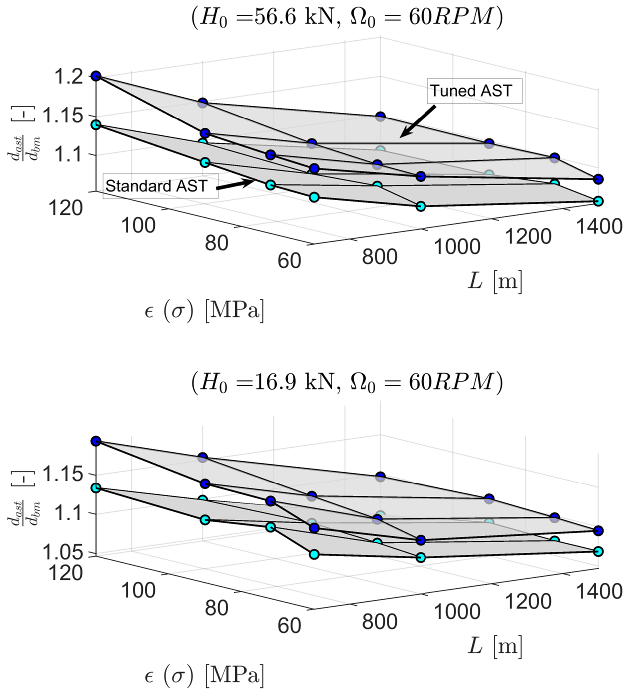

Figure 5.21: The comparison of averaged depth-of-cut (DOCs, relative to the depth-of-cut of the BM model) for the distributed AST models with the standard (nominal) design parameters ($K_b = 1522.5\frac{\text{kN}}{\text{m}}$ and $\beta_{ast} = 45$ deg) and with the tuned design parameters ($K_b^{opt} = 1979.2\frac{\text{kN}}{\text{m}}$ and $\beta_{ast}^{opt} = 30$ deg), under the variations of the drill-string parameter (the drill-pipe length): $L \in \{700, 1000, 1500\}$ m and the rock parameters: $\varepsilon = \sigma \in \{60, 72, 90, 120\}$ MPa and with the variation of drilling operational parameters: 1) $H_0 = 56.6$ kN and $\Omega_0 = 60$ rpm (top), and 2) $H_0 = 16.9$ kN and $\Omega_0 = 60$ rpm (bottom).

the operational condition of low top angular velocity ($\Omega_0 = 60$ rpm). For the case of high top angular velocity ($\Omega_0 = 120$ rpm), in general the same tendency of lower loading ratio for the tuned AST model is also observed, except for ratios with the soft rock parameter ($\varepsilon = \sigma = 60$ MPa). As discussed in the Section 5.4.2.2, we observe that the BM model has the lowest 'amplitude'-to-mean loading ratio at the interface in this parametric condition (a high top angular velocity within a soft formation) due to experiencing a stabilizing effect; see also Figures 5.15 and 5.16.

Overall, Figures 5.25 and 5.26 show that the tuned and standard AST models give low loading ratios at the interface, i.e., the ratios below 0.05. In addition, this reduction of the loading ratio at the interface in both tuned and standard AST models is robust in general over the parametric spaces of operating conditions, drill-string, and rock physical characteristics. Hence, this leads to better drill-

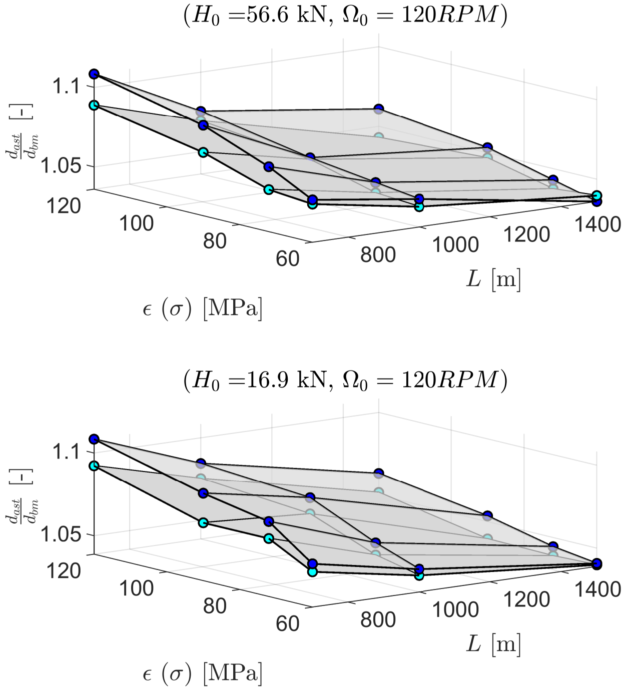

Figure 5.22: The comparison of averaged depth-of-cut (DOCs, relative to the depth-of-cut of the BM model) for the distributed AST models with the standard (nominal) design parameters ($K_b = 1522.5\frac{\text{kN}}{\text{m}}$ and $\beta_{ast} = 45$ deg) and with the tuned design parameters ($K_b^{opt} = 1979.2\frac{\text{kN}}{\text{m}}$ and $\beta_{ast}^{opt} = 30$ deg), under the variations of the drill-string parameter (the drill-pipe length): $L \in \{700, 1000, 1500\}$ m and the rock parameters: $\varepsilon = \sigma \in \{60, 72, 90, 120\}$ MPa and with the variation of drilling operational parameters: 1) $H_0 = 56.6$ kN and $\Omega_0 = 120$ rpm (top), and 2) $H_0 = 16.9$ kN and $\Omega_0 = 120$ rpm (bottom).

string structure performance by including the AST in the drill-string.

5.6 Conclusions

The main conclusions from this study are drawn as follows:

- Drilling performance (in terms of ROP and drilling efficiency) is improved by including the AST. This is due to a reduction in the (frictional) contact force at the bit on average as induced by the AST dynamics, resulting in a higher cutting force (improvement on the rock cutting efficiency). These results are in line with the earlier works [181, 187, 19], which were limited to lumped-parameter models for the drill-string dynamics. While earlier

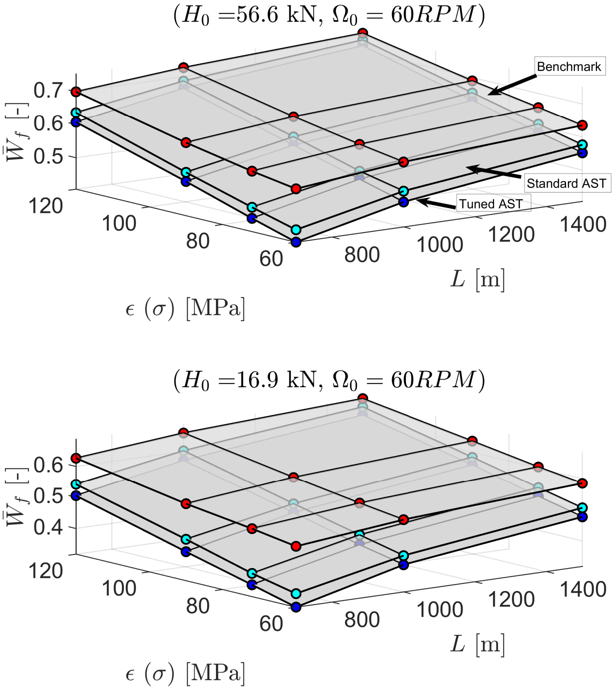

Figure 5.23: The comparison of the averaged (frictional) contact force ratio at the bit wearflat for the distributed AST models with the standard (nominal) design parameters ($K_b = 1522.5\frac{\text{kN}}{\text{m}}$ and $\beta_{ast} = 45$ deg) and with the tuned design parameters ($K_b^{opt} = 1979.2\frac{\text{kN}}{\text{m}}$ and $\beta_{ast}^{opt} = 30$ deg) and for the distributed BM model, all under the variations of the drill-string parameter (the drill-pipe length): $L \in \{700, 1000, 1500\}$ m and the rock parameters: $\varepsilon = \sigma \in \{60, 72, 90, 120\}$ MPa and with the variation of drilling operational parameters: 1) $H_0 = 56.6$ kN and $\Omega_0 = 60$ rpm (top), and 2) $H_0 = 16.9$ kN and $\Omega_0 = 60$ rpm (bottom).

work [2, 5, 3] showed that the high-order drill-string modes, omitted in the models, are essential from a stability perspective, we observe in this chapter that the arising non-local limit cycling behavior is dominated by the lower-frequency modes. This explains the consistency of the observations regarding the effect of the AST on drilling performance between lumped- and distributed-parameter models.

- In-line with the earlier work [187], optimal tuning of the stiffness and lead-angle results in higher stiffness and lower lead angle that deliver improved drilling performance.

- The AST induces increased axial vibrations on the bit, which lowers wearflat loading and the frictional losses at the bit. This mechanism 1) explains the improvement in drilling efficiency and 2) leads to a lower (friction-induced)

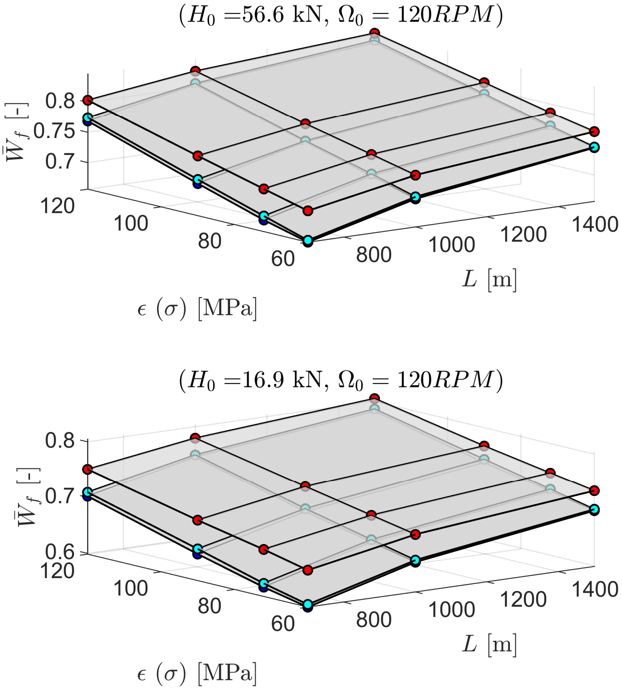

Figure 5.24: The comparison of the averaged (frictional) contact force ratio at the bit wearflat for the distributed AST models with the standard (nominal) design parameters ($K_b = 1522.5\frac{\text{kN}}{\text{m}}$ and $\beta_{ast} = 45$ deg) and with the tuned design parameters ($K_b^{opt} = 1979.2\frac{\text{kN}}{\text{m}}$ and $\beta_{ast}^{opt} = 30$ deg) and for the distributed BM model, all under the variations of the drill-string parameter (the drill-pipe length): $L \in \{700, 1000, 1500\}$ m and the rock parameters: $\varepsilon = \sigma \in \{60, 72, 90, 120\}$ MPa and with the variation of drilling operational parameters: 1) $H_0 = 56.6$ kN and $\Omega_0 = 120$ rpm (top), and 2) $H_0 = 16.9$ kN and $\Omega_0 = 120$ rpm (bottom).

thermal loading on the bit, potentially beneficial for bit life.

- The AST can assist to reduce the dynamic loading on the drill-string, which is beneficial for reducing the fatigue in the drill-string and providing more reliability on the downhole equipment in the BHA.
- From the robustness analysis, it is observed that both the standard AST and optimally tuned AST design can robustly 1) improve drilling efficiency and 2) decrease dynamic loading on the drill-string for a wide range of drill-string parameters, rock formation characteristics, and operational conditions.

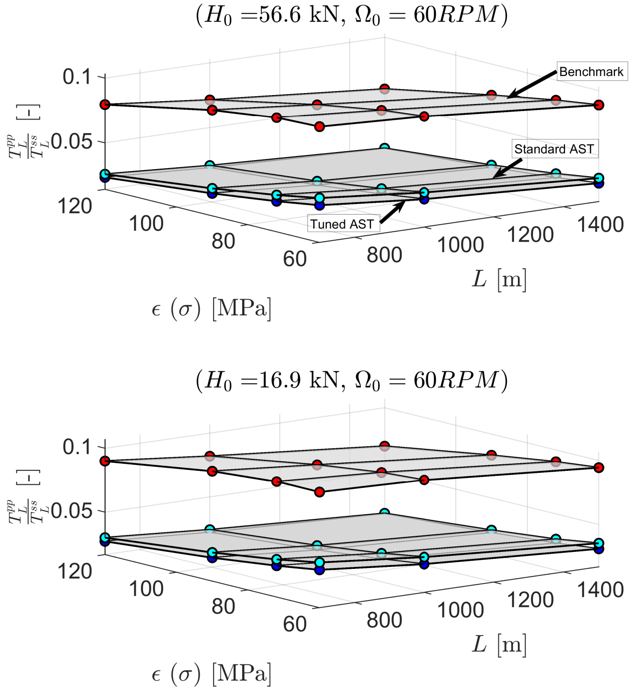

Figure 5.25: The comparison of the 'amplitude'-to-mean loading ratios at the interface for the AST distributed models with the standard (nominal) design parameters ($K_b = 1522.5\frac{\text{kN}}{\text{m}}$ and $\beta_{ast} = 45$ deg) and with the tuned design parameters ($K_b^{opt} = 1979.2\frac{\text{kN}}{\text{m}}$ and $\beta_{ast}^{opt} = 30$ deg) and for the BM distributed model, under the variations of the drill-string parameter (the drill-pipe length): $L \in \{700, 1000, 1500\}$ m and the rock parameters: $\varepsilon = \sigma \in \{60, 72, 90, 120\}$ MPa and with the variation of drilling operational parameters: 1) $H_0 = 56.6$ kN and $\Omega_0 = 60$ rpm (top), and 2) $H_0 = 16.9$ kN and $\Omega_0 = 60$ rpm (bottom).

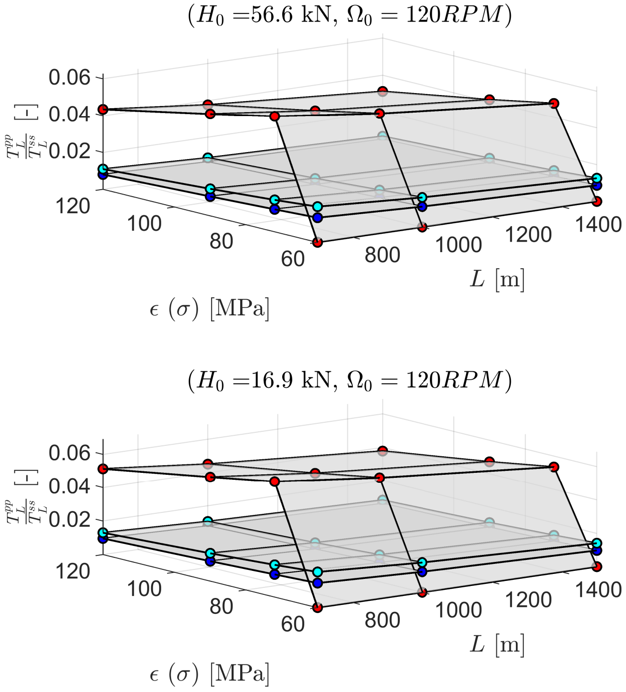

Figure 5.26: The comparison of the 'amplitude'-to-mean loading ratios at the interface for the AST distributed models with the standard (nominal) design parameters ($K_b = 1522.5\frac{\text{kN}}{\text{m}}$ and $\beta_{ast} = 45$ deg) and with the tuned design parameters ($K_b^{opt} = 1979.2\frac{\text{kN}}{\text{m}}$ and $\beta_{ast}^{opt} = 30$ deg) and for the BM distributed model, under the variations of the drill-string parameter (the drill-pipe length): $L \in \{700, 1000, 1500\}$ m and the rock parameters: $\varepsilon = \sigma \in \{60, 72, 90, 120\}$ MPa and with the variation of drilling operational parameters: 1) $H_0 = 56.6$ kN and $\Omega_0 = 120$ rpm (top), and 2) $H_0 = 16.9$ kN and $\Omega_0 = 120$ rpm (bottom).

Chapter 6

Conclusions and Recommendations

6.1 Conclusions

In this thesis, the dynamic modeling and analysis of drilling systems equipped with the AST downhole regulator has been considered. In particular, this thesis has studied the effect of the AST on drilling performance (in terms of ROP and drilling efficiency) under realistic scenarios closer to real drilling operations in fields. Based on field data, incorporating the AST in the BHA results in less damage to the drill bit (i.e., prolonging the bit life) and improves drilling performance in a single run of the drill bit, i.e., higher drilling efficiency (lower MSE) and less bit tripping (replacement). Therefore, it is of great practical interest to understand the basic mechanism of the tool's working principle for maintaining optimal drilling performance in more realistic drilling scenarios.

The objectives of this thesis are divided into the following three categories. The first category is related to the development of dynamic models of drilling systems without and with the AST regulator for three separated drilling scenarios incorporating: 1) deviated wellbore trajectories where the contact between the BHA and the borehole is considered; 2) interbedded formations composed of hard and soft rock properties; and 3) continuum behavior of long, slender drill-pipe structures. The second category is about developing numerical simulators associated with these three drilling scenarios and conducting performance analyses, where the effect of the AST on drilling performance is analyzed under these scenarios, including the associated underlying mechanism of such an effect. The last category is related to a parametric study of the AST design for optimal drilling performance, including its robustness analysis under the variation of drilling system parameters and operational conditions.

The main contributions of this thesis addressing the objectives above can be summarized in terms of contributions in the following aspects.

6.1.1 The case of drilling deviated wellbores

The key contributions for the study on the influence of the AST on the drilling performance of rotary drilling systems in a deviated wellbore scenario in Chapter 2 are as follows:

- A detailed model was developed that includes coupled axial-torsional drill-string dynamics, bit-rock interaction, the AST, and frictional effects of stabilizers (in the BHA) due to borehole inclination. The model employs a set-valued approach to account for all frictional contact effects, resulting in a delay differential inclusion model. A numerical approach based on the time-stepping method was developed for numerical simulations.
- Simulations revealed that the AST significantly enhances both drilling efficiency and ROP across a wide range of deviated wells. The AST's positive impact on drilling performance is evident in various well deviation scenarios, confirming its broad applicability.
- Moreover, the study found that spatial friction has a minimal effect on ROP responses. This is attributed to the relatively small axial component of the spatial friction compared to its tangential component. However, the simulation results highlighted that when spatial friction acts entirely above the AST, there is a slight improvement in drilling performance compared to cases without spatial friction (i.e., vertical drilling) or when friction acts below the tool.

6.1.2 The case of drilling in interbedded formations

In this case, the first contribution, as detailed in Chapter 3, is the extension of the bit-rock interface laws of PDC bits, initially developed for homogeneous formations, to scenarios involving a bit transitioning between two different rock layers. The extended formulation incorporates adaptations in rock mechanical properties and bit-design parameters for both cutting and frictional contact components. Key findings and contributions of this part include:

- The novel bit-rock interaction model enabled the construction of 3D $E-S$ diagrams, which illustrate the characteristics of dynamic and kinematic variables distinctly different from those observed in homogeneous formations.
- The study also analyzed drilling efficiency as a function of bit engagement during the transitional phase between two rock layers. In addition, the numerical results highlight that both the 3D $E-S$ diagrams and drilling efficiency are highly dependent on the bit shape during the transitional phase.

These dependencies significantly deviate from the known 2D $E-S$ diagrams applicable to homogeneous formations, underscoring the importance of the novel interface laws for accurately assessing drilling efficiency in interbedded formations.

- The new interface laws are also applicable in dynamic drill-string models for layered formations, providing a framework for analyzing vibrations during drilling. Overall, the extended bit/rock interface laws provide a more comprehensive understanding of drilling dynamics in layered formations, enhancing the ability to optimize bit design and operational parameters for improved drilling performance.

The second contribution, developed in Chapter 4, is related to the dynamic modeling of drill-string systems with AST drilling in interbedded formations, where the novel bit-rock interface law, which incorporates the transitional phase between distinct layers, couples axial and torsional dynamics. Key contributions of this part are highlighted as follows:

- By utilizing the developed simulation tool for the drill-string models, the effect of AST on the drill-string systems, particularly regarding response characteristics, drilling performance, and efficiency, was explored. It is revealed that the AST notably enhances the ROP and drilling efficiency in interbedded formations. Improvement in this drilling performance was corroborated by MSE observations, i.e., lower MSE for the model with the AST.
- The inclusion of AST results in additional axial vibrations; as such, these vibrations reduce frictional contact at the bit-rock interface. Lower frictional dissipation on the bit potentially also extends bit lifetime due to reduced thermal loading, which appears to be consistent with field observations on the post-drilling conditions of drill bits in Figure 1.9 in Chapter 1.

6.1.3 On the influence of distributed behavior of long-slender drill-pipe structures

This aspect is studied on the basis of a novel infinite-dimensional model of rotary drilling systems without and with the AST and the associated numerical simulator developed in Chapter 5. The key contributions and findings of this study are listed as follows:

- The AST induces increased axial vibrations on the bit, which lowers wearflat loading and the frictional losses at the bit. This mechanism leads to a lower (friction-induced) thermal loading on the bit, potentially beneficial for bit life, and results in a higher cutting force (improvement on the rock cutting efficiency). Overall, the simulation results of the developed models reveal that drilling performance (in terms of ROP and drilling efficiency) is improved by including the AST.

- The limit cycling behavior is dominated by the lower-frequency modes of the drill-string dynamics. This explains the consistency of the observations regarding the effect of the AST on drilling performance between lumped-parameter and distributed-parameter models.
- Moreover, by reducing dynamic loading on the drill-string, the AST contributes to decreased fatigue, enhancing the reliability and longevity of downhole equipment in the BHA.
- Overall, the AST's ability to reduce frictional forces at the bit and dynamic loading on the string makes it a valuable tool for improving both the efficiency and reliability of drilling operations.

6.1.4 Performance-based parametric study of the AST design and the associated robustness analysis

In Chapter 2, a parametric design study indicates that an optimal tool design can be achieved, maximizing drilling efficiency. This optimal design is robust, performing well across a wide range of wellbore inclinations and various operational conditions. In Chapter 5, the analysis reveals several key points regarding the tuning of stiffness and lead-angle in the AST design and its impact on drilling performance. Optimally tuning the stiffness leads to higher overall stiffness in the drill-string, while adjusting the lead angle to a lower value further contributes to enhanced drilling performance.

In addition, Chapter 5 confirms that both the standard and optimally tuned AST designs significantly enhance drilling performance and are effective in reducing dynamic loading on the drill-string, which is crucial for operational stability and tool longevity. Moreover, the robustness analysis indicates that these benefits are consistent across a wide range of parametric conditions, including different drill-string parameters, varying rock formation characteristics, and diverse operational conditions. This robustness underscores the adaptability and reliability of both AST designs in real-world drilling scenarios.

In summary, the use of a passive downhole tool in rotary drilling systems significantly improves drilling efficiency and rate of penetration under the influence of three drilling conditions mentioned above.

6.2 Recommendations

This study has revealed significant results in the development of dynamic models, including the associated numerical simulators, and the analysis of performance of drilling systems without and with the AST – where drilling scenarios involving deviated wellbore trajectory, interbedded formations, and continuum behavior of long-slender drill-pipe structure are considered. In addition, performance-based parametric studies on the AST design and its robustness analysis are also pursued. However, there remain several aspects for further investigation, as proposed below.

6.2.1 Aspects related to the modeling and its validation via experimental and field data

6.2.1.1 Bit-rock interaction

The interface laws used in both lumped-parameter model in Chapters 3 and 4 and distributed-parameter model in Chapter 5 are mainly dependent on the evolution of depth-of-cut and the bit-rock physical parameters associated with cutting and friction at the bit-rock interface. Furthermore, the bit-rock interaction model involving a bit transitioning between two distinct rock layers in Chapter 3 has emphasized how significant the influence of different bit-rock parameters in each layer is on the reaction force and torque on the bit.

Therefore, it is recommended in the next research steps that an accurate estimation of bit-rock parameters is considered for improving the prediction of the drilling responses of PDC bits. For example, in [59, 30], an offline (least-square-based) estimation technique has been used to estimate the bit-rock parameters based on field data. More recent advanced system-identification techniques, i.e., data-driven and machine-learning-based techniques, can potentially improve the parametric accuracy of the estimation results in the presence of uncertainties in field data. It is also worth noting that information gathered from post/while-drilling activities are essential to estimate the rock parameters (e.g., intrinsic specific energy and contact pressure) based on the formation lithology types (e.g., limestone, shale, etc.).

In addition, drilling test facilities (e.g., on a lab scale), where a kinematically controlled condition can be imposed, are also essential for supporting further validation and verification of the estimated bit-rock parameters and the developed models. Examples of such facilities have been developed in recent works [96, 47, 95, 185].

In terms of the bit parameters, the bit profile (shape) is found to be an essential factor in quantifying the bit parameters associated with the cutting and frictional components of the interface laws, particularly for the bit engagement during the bit transition between rock layers; see Chapters 3 – 4. Thus, it is interesting to consider in future works the more complex (realistic) bit design in the bit-rock interface laws, e.g., as developed in [168, 171, 169], for predicting the bit responses, in particular for drilling cases in interbedded formations. Note that, based on field case studies [26, 135], advanced bit design can also improve drilling efficiency.

6.2.1.2 The lateral dynamics of drill-string systems and the spatial friction between the drill-pipes and borehole wall

In this thesis, the modeling has been focused on the axial and torsional dynamics of the drill-string system, for cases without and with the AST regulator. In future works, it is an interesting aspect to include the lateral dynamics of drill-string systems into the dynamic system model, including the development of the associated numerical simulators. The lateral vibrations of the drill-string systems can lead to the phenomenon of bit whirling where the BHA part (e.g., stabilizers, drill collar) has contact with the borehole wall [105]. In [105], the coupling of torsional and lateral dynamics of drill-string systems was developed to analyze the (torsional) stick slip vibrations and bit whirling phenomena. Given the fact that it is clear from this thesis that the interaction between the drill-string dynamics and the bit-rock interaction is key in the modelling and prediction of drill-string vibrations and drilling performance, it will also be interesting to further investigate the role of the bit-rock interaction and the borehole - drill-string interaction in the lateral dynamics (and its coupling to the axial and torsional modes).

In Chapter 2, the spatial friction due to the contact between the stabilizers (in the BHA) and borehole wall due to the inclined trajectory is considered. This case can be extended to the case of spatial friction at multiple points between the long-slender drill-pipe structure and borehole wall, utilizing the distributed-parameter modeling approach in Chapter 5. It is envisioned that this spatial friction at the drill-pipe with the borehole wall can be studied together with the lateral dynamics of drill-string systems leading to the bit whirling.

Moreover, recent works in the milling process [45, 46] have developed an alternative approach for calculating the chip thickness in which the regenerative effect that induces time delay in the cutting process and acts as the root cause of the self-excited vibrations in such a process is considered. This approach can be extended for computing the evolution of depth-of-cut in the bit-rock interaction, where the lateral motion of the bit can be involved. This would be an essential stepping stone towards drill-string models including torsional, axial and lateral dynamics.

6.2.2 AST design

In Chapters 2 and 5, parametric studies of the AST design in terms of its spring stiffness and the lead angle of its helical spline have been pursued. In particular, Chapter 5 has discussed the robustness of these two design parameters for drilling performance under the variations of drilling operational conditions and drill-string and rock physical parameters.

Therefore, it is interesting to further analyze other parametric quantities of the AST physical design, such as the length of the spline (for its stroking moves) and the optimal placement of the AST in the BHA relative to the drill-bit. In particular, the effect of these AST design aspects on lowering the wearflat contact force on the bit (as the main actor for drilling performance improvement with the AST) and the dynamic loading on the drill-string structure should be investigated. Besides, it is also interesting to explore the effect of AST on stick-slip vibration mitigation via the current modeling approaches.

However, the design exploration of and the study of stick-slip mitigation with the AST require to be supported by lab-scale experimental and field data for analysis, in line with the earlier works [182, 177]. Lab-scale experimental testing and field data can surely provide a better physical understanding of the phenomena and essential support for design and validation purposes. For example, the downhole kinematic and dynamic data at the bit and the AST are useful for assessing the contact force at the bit and the reaction torque on the AST (or on the BHA), respectively, which can provide further insight for design and verification purposes.

6.2.2.1 Linearized models of drill-string dynamics with the AST

In a nominal drilling condition, a linearized model of drill-string dynamics with the AST can be pursued for performing a stability analysis (in the frequency domain) to explore in more depth the parametric design of the AST. The linearization procedure and the method for the stability analysis can be based on previous works for the benchmark model (a drilling system without the AST), such as in [27, 108, 28] based on the lumped-parameter approach, and in [5, 3, 4] for the distributed-parameter approach. Moreover, these linearized models can also be useful in designing active control strategies (applied to the rig) and performing its stability analysis for finding the optimal drilling operational envelope for performance and mitigating the onset/growth of (torsional) stick-slip vibrations. In the next subsection, the recommended aspects of active control strategies are detailed.

6.2.3 Active control strategy at surface (drilling rig)

Based on the field report in [99], a combined implementation of PDC bits, Z-Torque (an active control module), and AST technologies in drilling operations involving carbonate and interbedded shale lithology can bring more improvement to drilling performance (ROP). On the other hand, the robustness analysis in Chapter 5 has indicated that an optimal tuning of drilling operational parameters imposed by the rig (i.e., hookload and top angular velocity) can further assist the AST in delivering better drilling performance under variations of the formation lithology types (i.e., soft and hard rock formations). Therefore, it is interesting for the next research lines to explore the design, analysis, and implementation of an active control strategy where it is combined with the AST application in a unified framework for performance improvement and mitigating the onset and growth of undesired vibrations in drill-string systems.

As an option, the unified framework can be in a cascade control scheme as depicted

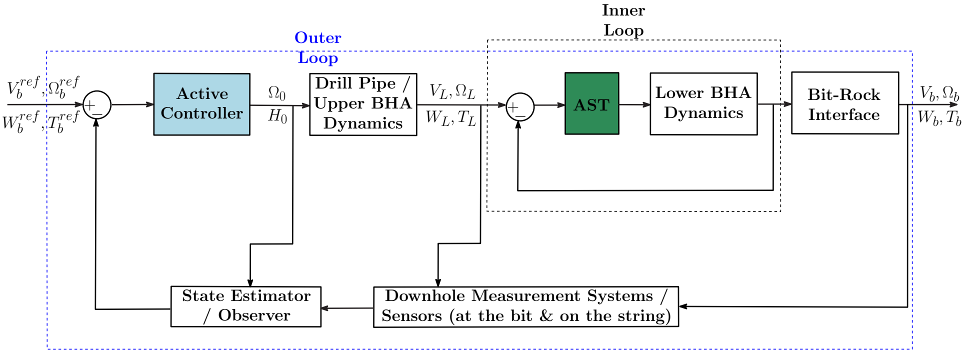

Figure 6.1: The schematic of the cascade control scheme composed of the AST for the inner loop and the active controller for the outer loop.

in Figure 6.1, which consists of two control loops. First is the inner loop, in which the AST is mainly responsible for stabilizing the dynamics of the lower BHA part (below the AST) and directly driving the downhole states at the bit (e.g., the bit velocities V_b and Ω_b, and the WOB W_b and TOB T_b). Second is the outer loop, in which the active controller imposes the optimal drilling operational parameters on the rig (e.g., the top angular velocity Ω_0 and hookload H_0) to drive the inner loop dynamics (via the drill pipe and the upper BHA part) for achieving the desired kinematic and dynamic variables at the bit (e.g., the desired bit velocities V_b^{ref} and Ω_b^{ref}, and the desired WOB W_b^{ref} and TOB T_b^{ref}).

Note that the performance of the cascade control scheme has been successfully proven in process control strategy, i.e., for composition control in the distillation column [117]. This scheme is more efficient than a single feedback controller for disturbance rejection purposes involving long time-delays or lags. In addition, an effective cascade control scheme is essentially indicated by faster inner loop response (typically about five times faster) than the outer loop response. Therefore, this cascade control scheme is envisioned to be a suitable framework for drill-string dynamics, as the (lower) BHA dynamics are typically having much faster responses than the dynamic responses of the long-slender drill-pipe structure.

Moreover, by utilizing the control-oriented modeling approaches presented in this thesis, this recommendation can be categorized in the following ways:

6.2.3.1 Active control design based on the lumped-parameter approach

In this thesis, it is observed that the responses of drill-string dynamics are dominated by lower frequency modes. Thus, it is relevant to design an active control strategy based on the lumped-parameter model of drill-string dynamics equipped with the AST.

As an example, the earlier work [183] has presented a robust output-feedback control design to eliminate torsional stick-slip vibrations in a drilling system. This active control strategy is designed based on the dynamics of the drill-string represented as a Lur'e-type lumped-parameter system (e.g., separating the nonlinearity term of the bit-rock interaction from the linear dynamics of the nominal system) and, interestingly, the uncertainties of the bit-rock parameters taken into account in the controller design. Furthermore, it has also been implemented in a lab-scale experimental drill-string setup that represents such a drilling system with multiple dominant torsional flexibility modes [182, 177]. Hence, it is interesting to extend such an active control strategy with the presence of the AST in a cascade scheme, as depicted in Figure 6.1.

The work [28] presented the stability analysis for the state- and output-feedback controllers designed based on the linearized model of drill-string dynamics in terms of nonsmooth delay-differential equations (DDEs) with state-dependent delays. This analysis can also be extended later in the case of drill-string dynamics equipped with both an active controller and the AST to find the optimal parametric designs of both the AST and the controller. In addition, other examples of active control strategies designed with lumped-parameter models of drill-string dynamics are as follows: pole-placement technique [189], Proportional-Integral (PI) controller [91], Proportional-Derivative (PD) controller [149], H_∞ control approach [159], and H_∞ gain-scheduled active control strategy developed with a linear-parameter-varying (LPV) modeling approach of drill-string dynamics [49].

State estimator/observer for the downhole kinematics and dynamics
It is worth noting that rotary drilling systems can be categorized as non-collocated systems, where the placement of sensors and actuators is at different positions within the system. Therefore, in the design of active controller, e.g., within the cascade control scheme in Figure 6.1, state observer design is often taken into account, particularly for estimating the downhole states (e.g., bit angular velocity, weight-on-bit, torque-on-bit, torque at the interface on the drill-string) when sensors are not available at the desired locations. The work [182] provides a relevant example of state observer design and implementation based on the torsional dynamics of a drill-string system. This work can be extended to the case involving the axial drill-string dynamics and the AST under the cascade scheme.

6.2.3.2 Active control design based on the distributed-parameter approach

As an example of an active controller design based on a distributed-parameter model, the earlier works [166, 70] show the procedures for designing a prediction-based state-feedback controller that stabilizes the coupled axial-torsional drill-string vibrations while dealing with the distributed behavior of the dynamics and the associated delays induced by the bit-rock interaction. Moreover, in [129, 128], a combination of torsional damping subs distributed along the drill string and an On-Off control scheme with a proportional controller is studied, particularly on its effectiveness to mitigate (torsional) stick-slip vibrations. In that work, a distributed-parameter approach is used to model the drill-string system equipped with such damping subs and to design the active control strategy. All these works provide the first stepping stone for designing an active controller for performance improvement and mitigating unwanted vibrations where the AST application is also involved in the drill-string dynamics.

6.2.4 High-frequency torsional oscillations (HFTO)

In [191], it is reported that recently, high-frequency torsional oscillations (HFTO) have attracted increased attention in the drilling industry. This phenomenon, as observed via field measurement and lab experiments, is characterized by high-frequency self-excited torsional oscillations (often encountered while drilling harder rock formations) and is localized in the lower BHA or lower part of the drill-string only. These oscillations are generally excited by the bit-rock interaction [90, 86] and can induce high-frequency torsional loads in different locations of the drill-string. The severity of these loads is dependent on the BHA design, vibrational modes, bit type, drilling mud parameters, rock hardness, and drilling operational parameters (e.g., WOB, TOB, angular bit velocity, etc.). As an impact, HFTO can cause very harmful conditions for the downhole equipment, including bit damage.

Given this fact, it is interesting to extend the distributed models of drill-string dynamics in Chapter 5 to further analyze the physical mechanism (root cause) leading to the onset or growth of such an HFTO phenomenon. Subsequently, a parametric study of the AST application to assist in attenuating the HFTO can be pursued via the distributed model of drill-string dynamics with the AST in Chapter 5. To optimize this attenuation effort and the drilling efficiency improvement, the synergy between the AST and an active control strategy within the cascade scheme, as depicted in Figure 6.1, can also be the next feasible path-forward.

Appendix A

Appendix to Chapter 2

A.1 Coordinate transformation

The drill-string dynamics including AST are expressed in a set of dependent coordinates $\mathbf{q}^c = \begin{bmatrix} U & \Phi & U_b & \Phi_b \end{bmatrix}^\top$ combined with the following holonomic constraint:

$$h_{ast} = \alpha \left(\Phi - \Phi_b\right) - \left(U - U_b\right) = 0. \tag{A.1}$$

The dynamics of the constrained system can also be given in variational form:

$$\left(\delta \mathbf{q}^c\right)^\top \left(\mathbf{M}^c \ddot{\mathbf{q}}^c - \mathbf{h}^c \left(t, \mathbf{q}^c, \dot{\mathbf{q}}^c\right) - \mathbf{W}^c \boldsymbol{\lambda}\right) = 0, \tag{A.2}$$

which holds for all the virtual displacements $\delta \mathbf{q}^c$ that satisfy the variational holonomic constraint given by

$$\mathbf{W}_c^\top \delta \mathbf{q}^c = 0, \tag{A.3}$$

where $\mathbf{W}_c^\top$ is the constraint Jacobian:

$$\mathbf{W}_c^\top = \frac{\delta h_{ast}}{\delta \mathbf{q}^c} = \begin{bmatrix} -1 & \alpha & 1 & -\alpha \end{bmatrix}^\top. \tag{A.4}$$

Expressions for $\mathbf{M}^c$ and $\mathbf{h}^c \left(t, \mathbf{q}^c, \dot{\mathbf{q}}^c\right)$ can be found in [186]. The set of independent coordinates $\mathbf{q} = \begin{bmatrix} U & U_b & \Phi_b \end{bmatrix}^\top$ is introduced, such that it uniquely determines $\mathbf{q}^c = \mathbf{q}^c(\mathbf{q})$. The relation between the set of dependent and independent coordinates is explicitly given by a constant transformation matrix $\mathbf{T}$. Hence, the following relations hold:

$$\mathbf{q}^c = \mathbf{T}\mathbf{q}, \qquad \dot{\mathbf{q}}^c = \mathbf{T}\dot{\mathbf{q}}, \qquad \ddot{\mathbf{q}}^c = \mathbf{T}\ddot{\mathbf{q}}, \tag{A.5}$$

with

$$\mathbf{T} = \begin{bmatrix} 1 & 0 & 0 \\ \frac{1}{\alpha} & \frac{-1}{\alpha} & 1 \\ 0 & 1 & 0 \\ 0 & 0 & 1 \end{bmatrix}. \tag{A.6}$$

Moreover, the virtual displacement in terms of the independent coordinates can be written as follows:

$$\delta \mathbf{q}^c = \mathbf{T}\delta \boldsymbol{q}. \tag{A.7}$$

Substitution of Eqs. (A.5) and (A.7) into Eq. (A.2) results in the following equation

$$(\delta \mathbf{q})^\top \left(\mathbf{T}^\top \mathbf{M}^c \mathbf{T}\ddot{\mathbf{q}} - \mathbf{T}^\top \mathbf{h}^c \left(t, \mathbf{T}\mathbf{q}, \mathbf{T}\dot{\mathbf{q}}\right) - \mathbf{T}^\top \mathbf{W}^c \boldsymbol{\lambda}\right) = 0, \quad \forall \delta \mathbf{q}. \tag{A.8}$$

Since the generalized coordinates $\mathbf{q}$ are independent, all virtual displacements $\delta \mathbf{q}$ are admissible and therefore the dynamics in independent coordinates can be written as follows:

$$\mathbf{T}^\top \mathbf{M}^c \mathbf{T}\ddot{\mathbf{q}} - \mathbf{T}^\top \mathbf{h}^c \left(t, \mathbf{T}\mathbf{q}, \mathbf{T}\dot{\mathbf{q}}\right) = \mathbf{T}^\top \mathbf{W}^c \boldsymbol{\lambda}. \tag{A.9}$$

The new system matrices, explicitly given in Eq. (2.5), are now given by

$$\begin{aligned} \mathbf{M} &= \mathbf{T}^\top \mathbf{M}^c \mathbf{T}, \\ \mathbf{h}\left(t, \mathbf{q}, \dot{\mathbf{q}}\right) &= \mathbf{T}^\top \mathbf{h}^c \left(t, \mathbf{T}\mathbf{q}, \mathbf{T}\dot{\mathbf{q}}\right), \\ \mathbf{W} &= \mathbf{T}^\top \mathbf{W}^c. \end{aligned} \tag{A.10}$$

Appendix B

Appendix to Chapter 4

B.1 Dimensionless models

To reduce the number of parameters and to facilitate the numerical simulations, the equations of motion (in the generic form in Eq. (4.24)) are scaled to render them dimensionless. The following scales for length and time, respectively, are used for constructing the dimensionless models:

$$L_* = \frac{2C_p}{\bar{\varepsilon}a^2}, \quad \text{and} \quad t_* = \sqrt{\frac{I}{C_p}}. \tag{B.1}$$

Here, parameter $\bar{\varepsilon}$ denotes the mean value of the intrinsic specific energy for all rock layers involved in drilling interbedded formations. Typically, we select around $t_* = 1$ sec and $L_* = 1$ mm.

Dimensionless coordinates The characteristic length L_* and characteristic time t_* are utilized to introduce the following dimensionless generalized coordinates at the bit:

$$u_b(\tau) := \frac{U_b(t)}{L_*}, \qquad \phi_b(\tau) := \Phi_b(t). \tag{B.2}$$

In Eq. (B.2), the dimensionless time τ is defined as follows:

$$\tau := \frac{t}{t_*}. \tag{B.3}$$

In addition, in the AST model the following dimensionless coordinate is introduced to describe the motion of the drill-string section above the AST in the axial direction:

$$u(\tau) := \frac{U(t)}{L_*}. \tag{B.4}$$

The nominal angular velocities imposed at the surface can be written in dimensionless form as $\omega_0 = \Omega_0 t_*$.

Furthermore, the dimensionless delayed axial and angular displacement coordinates are denoted by $u_b(\tau-\tau_n)$ and $\phi_b(\tau-\tau_n)$, respectively, with the dimensionless time delay $\tau_n := \frac{t_n}{t_*}$. Hence, the implicit equation (4.5) reads in a dimensionless formulation as follows:

$$\phi_b(\tau) - \phi_b(\tau - \tau_n) = \frac{2\pi}{n}, \tag{B.5}$$

which is used for calculating τ_n. The total depth-of-cut d, as given by Eq. (4.6), is also scaled according to:

$$\delta\left(\tau\right) = n\delta_n\left(\tau\right) := \frac{d\left(t\right)}{L_*} = n\,\left(u_b(\tau) - u_b(\tau - \tau_n)\right). \tag{B.6}$$

Bit/rock parameters in layered formations Following the interface laws in Section 4.2.1, we define the ratio of the associated rock mechanical parameters in the cutting and frictional contact components of two consecutive rock layers with distinct mechanical properties as follows:

$$g_k^{\varepsilon} := \frac{\varepsilon_{k-1}}{\varepsilon_k}, \qquad g_k^{\mu} := \frac{\mu_{k-1}}{\mu_k}, \qquad g_k^{\sigma} := \frac{\bar{\sigma}_{k-1}}{\bar{\sigma}_k}, \tag{B.7}$$

for the intrinsic specific energy, the frictional coefficients, and the contact pressures, respectively. The ratios for the intrinsic specific energy and the contact pressures describe the following conditions:

$$\begin{cases} g_k^{\star} > 1, & \text{(a) transition from hard to soft layer,} \\ g_k^{\star} = 1, & \text{(b) no transition (homogeneous),} \\ g_k^{\star} < 1, & \text{(c) transition from soft to hard layer,} \end{cases} \tag{B.8}$$

with $\star \in \{\varepsilon, \sigma\}$.

In addition, we also define the ratio between the intrinsic specific energy of the lower (k^{th}) layer and the mean value of the intrinsic specific energy of all rock layers as:

$$\bar{g}_k^{\varepsilon} := \frac{\varepsilon_k}{\bar{\varepsilon}}. \tag{B.9}$$

The rock parameters (and their ratios) are associated to the current layer(s) and updated based on the layer index k, in which the bit engages during drilling the interbedded formations (see the condition in Eq. (4.8)).

Furthermore, in drilling layered formations as considered here, the evolution of both normalized bit-design parameters in Eqs. (4.12) and (4.18) is based on the dimensionless bit engagement z_b as described by the dimensionless formulation of condition Eq. (4.8). Precisely, this engagement z_b is utilized to update the dimensionless engagement radius r_b at the bit via the bit profile relation in Eq. (4.4). Subsequently, this radius is used for updating both bit-design parameters.

The dimensionless value of the depth L_k is given by

$$l_k := \frac{L_k}{L_*}. \tag{B.10}$$

Hence, we can rewrite the update of the bit engagement in Eq. (4.8) into the following dimensionless form:

$$z_b(\tau) = \min\left(\frac{b}{a}, \frac{L_*}{a}\left(u_b(\tau) - l_{k_*-1}\right)\right), \tag{B.11}$$

considering Eq. (4.2) and the bit radius a. The index k_* is the minimum $k \in \{1, 2, 3, \ldots, K\}$ such that it holds that $\frac{L_*}{a}\left(u_b(\tau) - l_{k_*-1}\right) \geq 0$, with $l_0 = 0$. The layer index k_* is also updated based on the latest axial displacement $u_b(\tau)$ relative to the depth l_{k-1} as the bit progresses into the lower layer.

Generic form of the dimensionless models The generic form of equations of motion with original generalized coordinates $\mathbf{q}$ in Eq. (4.24) is expressed in dimensionless form as follows:

$$\mathcal{M}\mathbf{z}'' - \mathcal{H}\left(\tau, \mathbf{z}, \mathbf{z}', \mathbf{z}_{\tau_n}\right) = \mathcal{W}\mathcal{L}. \tag{B.12}$$

The single and double prime symbols denote the derivatives of the generalized coordinates $\mathbf{z}$ w.r.t. time τ in Eq. (B.3). Next, this generic form is used to express the dimensionless BM and AST models as the basis for developing the numerical solver.

Dimensionless benchmark (BM) model The dimensionless generalized coordinates used in the dimensionless BM model are defined as follows:

$$\mathbf{z}(\tau) := \begin{bmatrix} u_b(\tau) & \phi_b(\tau) \end{bmatrix}^\top. \tag{B.13}$$

We construct the following relations between the original and dimensionless coordinates in matrix form:

$$\mathbf{q} = \mathbf{\Gamma}\mathbf{z}, \tag{B.14}$$

by considering a transformation matrix

$$\mathbf{\Gamma} = \begin{bmatrix} L_* & 0 \\ 0 & 1 \end{bmatrix}. \tag{B.15}$$

The delayed axial and angular displacements in Eq. (4.26) are stored in $\mathbf{z}_{\tau_n}$ defined as:

$$\mathbf{z}_{\tau_n} := \mathbf{z}\left(\tau - \tau_n\right) = \begin{bmatrix} u_b\left(\tau - \tau_n\right) & \phi_b\left(\tau - \tau_n\right) \end{bmatrix}^\top, \tag{B.16}$$

such that $\mathbf{q}_{t_n} = \mathbf{\Gamma}\mathbf{z}_{\tau_n}$ holds.

With these dimensionless coordinates and considering Eqs. (4.27) – (4.31), the dimensionless equations of motion of the BM model in the generic form of Eq. (B.12) are characterized by the following matrices and columns:

$$\mathcal{M} = \left[\begin{array}{cc} 1 & 0 \\ 0 & 1 \end{array}\right], \tag{B.17a}$$

$$\begin{aligned} \mathcal{H} &= \left[\begin{array}{c} -\gamma u_b' \\ (-\gamma_\phi \phi_b' - (\phi_b - \omega_0\,\tau)) \end{array}\right] \cdots \\ &\cdots + \left[\begin{array}{c} -\bar{\psi} n \delta_n \bar{g}_k^\varepsilon \left(g_k^\varepsilon \left(1 - \vartheta_\zeta^l(r_b)\right) + \vartheta_\zeta^l(r_b)\right) \\ -n\delta_n \bar{g}_k^\varepsilon \left(g_k^\varepsilon \left(1 - r_b^2\right) + r_b^2\right) \end{array}\right] + \left[\begin{array}{c} \bar{\psi}\mathcal{W}_a \\ 0 \end{array}\right], \end{aligned} \tag{B.17b}$$

$$\mathcal{W} = \left[\begin{array}{cc} \bar{\psi} & 0 \\ 0 & 1 \end{array}\right], \tag{B.17c}$$

$$\mathcal{L} = \left[\begin{array}{cc} \mathcal{L}_{b_a} & \mathcal{L}_{b_t} \end{array}\right]^\top. \tag{B.17d}$$

In Eq. (B.17d), the column $\mathcal{L}$ is the dimensionless form of the column $\boldsymbol{\lambda}$ in Eq. (4.30) describing the non-smooth dynamics and defined via the following scaling:

$$\mathcal{L} := \left[\begin{array}{cc} \frac{a}{2C_p\zeta^*} & 0 \\ 0 & \frac{1}{C_p} \end{array}\right] \boldsymbol{\lambda} = \left[\begin{array}{cc} \frac{a}{2C_p\zeta^*} & 0 \\ 0 & \frac{1}{C_p} \end{array}\right] \left[\begin{array}{c} \lambda_a \\ \lambda_t(\lambda_a) \end{array}\right]. \tag{B.18}$$

The first entry of the column $\mathcal{L}$ is the dimensionless form of the total contact force λ_a in Eq. (4.13) and is written as an inclusion:

$$\mathcal{L}_{b_a} \in -\frac{a}{2C_p\zeta^*} \bar{\lambda}_{b_a} g\left(u_b'\right), \tag{B.19}$$

with the set-valued function $g\left(u_b'\right)$ following the definition in Eq. (4.14). In Eq. (B.19), $\bar{\lambda}_{b_a}$ is the nominal value of the total contact force λ_a in the k^{th} rock layer:

$$\bar{\lambda}_{b_a} := \left(g_k^\sigma \left(1 - r_b\right) + r_b\right) n\, a\, \ell_n\, \bar{\sigma}_k. \tag{B.20}$$

The second entry of the column $\mathcal{L}$ in Eq. (B.18) is the dimensionless form of the total frictional torque λ_t in Eq. (4.16) and is given by the following inclusion:

$$\mathcal{L}_{b_t} \in \beta_k \mathcal{L}_{b_a} \mathrm{Sign}\left(\phi_b'\right), \tag{B.21}$$

with

$$\beta_k := \frac{(g_k^\sigma g_k^\mu (1 - \vartheta_\xi^l(r_b)) + \vartheta_\xi^l(r_b))}{(g_k^\sigma \left(1 - r_b\right) + r_b)} \mu_k \xi \zeta^*. \tag{B.22}$$

Note that the sign-dependency of the frictional torque $\mathcal{L}_{b_t}$ on the sign of the torsional bit velocity ϕ_b' also models a torsional sticking mode, and hence can be a beneficial insight for studying the onset of (torsional) stick-slip vibrations.

The dimensionless form of the applied weight at the top surface is given by

$$\mathcal{W}_a = \frac{a}{2C_p\zeta^*} W_a. \tag{B.23}$$

Moreover, the dimensionless physical parameters of benchmark drill-string system and the bit/rock parameters involved in the equations of motion are listed in Table B.1 (on the basis of the properties of a real drilling system: in Table B.2 for the bit parameters and in Table B.3 for the drill-string parameters).

Table B.1: Characteristic system parameters.

Parameter Name	Symbol	Value
Characteristic length	$L_* = \frac{2C_p}{\varepsilon_{avg}a^2}$	0.82
Characteristic time	$t_* = \sqrt{\frac{I_{tot}}{C_p}}$	0.45
Scaled axial damping	$\gamma = \frac{D}{M}\sqrt{\frac{I}{C_p}}$	6.4×10^{-3}
Scaled torsional damping (for BM)	$\gamma_\phi = \frac{D_\Phi}{\sqrt{IC_p}}$	2.13×10^{-4}
Drill-string design	$\bar{\psi} = \frac{aI\zeta^*\bar{\varepsilon}}{C_pM}$	31.83
Drill bit design (nominal)	$\beta_{nom} = \xi\zeta^*$	0.64
Mass ratio	$m_* = \frac{M_a}{M}$	0.92
Inertia ratio	$\iota = \frac{I_a}{I}$	0.86
Torsional damping above AST	$\gamma_{\phi_1} = \frac{D_{\Phi_a}}{\sqrt{C_pI}}$	2.05×10^{-4}
Torsional damping below AST	$\gamma_{\phi_2} = \frac{D_{\Phi_b}}{\sqrt{C_pI}}$	7.39×10^{-6}
Inertia mass ratio	$\kappa = \frac{I}{\alpha^2 M}$	0.56
Scaled lead of AST	$\nu = \frac{\kappa\alpha}{L_*}$	44.31
Scaled axial stiffness of AST	$\eta_b = \sqrt{\frac{K_bI}{MC_p}}$	2.06
Scaled axial damping of AST	$\gamma_b = \frac{D_b}{M}\sqrt{\frac{I}{C_p}}$	0.45

Table B.2: Bit parameters (see also [181, 187]).

Parameter Name	Symbol	Value	Unit
Wear-flat length	ℓ_n	1.2×10^{-3}	m
Cutting-face orientation	ζ	0.625	—
Number of blades	n	6	—

Dimensionless AST model The dimensionless generalized coordinates of the AST model are defined as follows (by referring to the original coordinates in Eq.

Table B.3: Drill-string parameters (see also [181, 187]).

Parameter Name	Symbol	Value	Unit
Steel density	ρ	8000	kg/m^3
Steel shear modulus	G	77	GPa
Steel elasticity modulus	E	200	GPa
Drill pipe length	L_p	1500	m
Length BHA below AST	L_b	40.9	m
Length BHA above AST	L_{hp}	113.1	m
Drill pipe outer radius	r_{po}	0.067	m
Drill pipe inner radius	r_{pi}	0.056	m
Heavy drill pipe outer radius	r_{hpo}	0.083	m
Heavy drill pipe inner radius	r_{hpi}	0.038	m
AST outer radius	r_{bo}	0.083	m
AST inner radius	r_{bi}	0.038	m
AST helix (spline) radius	r_{sp}	0.0640	m
AST Lead angle	β	$\frac{\pi}{4}$	rad
AST Lead	$p = 2\pi r_{sp} \tan\beta$	0.4021	m
AST constraint constant	$\alpha = \frac{p}{2\pi}$	0.0640	m/rad
Drill pipe mass	$M_p = \rho\pi(r_{po}^2 - r_{pi}^2)L_p$	5.1×10^4	kg
Heavy drill pipe mass	$M_{hp} = \rho\pi(r_{hpo}^2 - r_{hpi}^2)L_{hp}$	1.548×10^4	kg
BHA below AST mass	$M_b = \rho\pi(r_{bo}^2 - r_{bi}^2)L_b$	5.597×10^3	kg
Area of cross section pipe	$A_p = \pi(r_{po}^2 - r_{pi}^2)$	0.0043	m^2
Area of cross section BHA	$A_{hp} = \pi(r_{hpo}^2 - r_{hpi}^2)$	0.0171	m^2
Area of cross section AST	$A_b = \pi(r_{bo}^2 - r_{bi}^2)$	0.0171	m^2
Drill pipe inertia	$I_p = \rho L_p \frac{\pi}{2}(r_{po}^4 - r_{pi}^4)$	194.4638	kg.m^2
BHA inertia - above AST	$I_{hp} = \rho L_{hp} \frac{\pi}{2}(r_{hpo}^4 - r_{hpi}^4)$	64.4869	kg.m^2
BHA inertia - below AST	$I_b = \rho L_b \frac{\pi}{2}(r_{bo}^4 - r_{bi}^4)$	23.3202	kg.m^2
Drill pipe torsional stiffness	$C_p = \frac{GJ_p}{L_p}$	831.8729	N.m/rad
Drill-string axial damping	D	1035	N.s/m
Torsional damping - above AST	D_{Φ_a}	0.0765	Nm.s/rad
Torsional damping - below AST	D_{Φ_b}	0.00275	Nm.s/rad
AST axial spring stiffness	K_b	1522.5×10^3	N/m
AST axial damping	D_b	72×10^3	N.s/m

(4.36)):

$$\mathbf{z}(\tau) := \begin{bmatrix} u\,(\tau) & u_b\,(\tau) & \phi_b\,(\tau) \end{bmatrix}^\top . \tag{B.24}$$

We construct the same matrix relations as in Eq. (B.14) between the original and dimensionless coordinates of AST model, such that we consider the following transformation matrix:

$$\mathbf{\Gamma}_{AST} = \left[\begin{array}{ccc} L_* & 0 & 0 \\ 0 & L_* & 0 \\ 0 & 0 & 1 \end{array} \right], \tag{B.25}$$

and later replace matrix $\mathbf{\Gamma}$ in Eq. (B.14) with matrix $\mathbf{\Gamma}_{AST}$ to read:

$$\mathbf{q} = \mathbf{\Gamma}_{AST}\mathbf{z}, \tag{B.26}$$

The delayed coordinates of the AST model in Eq. (4.37) are defined in this dimensionless coordinate vector form:

$$\mathbf{z}_{\tau_n} := \mathbf{z}\left(\tau - \tau_n\right) = \left[\begin{array}{ccc} u\left(\tau - \tau_n\right) & u_b\left(\tau - \tau_n\right) & \phi_b\left(\tau - \tau_n\right) \end{array} \right]^{\top}, \tag{B.27}$$

such that $\mathbf{q}_{t_n} = \mathbf{\Gamma}_{AST}\mathbf{z}_{\tau_n}$ holds. Thus, with these dimensionless coordinates and considering Eqs. (4.38a) – (4.38c), the dimensionless AST model in the generic form of Eq. (B.12) is described by the following matrices:

$$\mathcal{M} = \left[\begin{array}{ccc} \left(m_* + \kappa\iota\right) & -\kappa\iota & \nu\iota \\ -\kappa\iota & \left(1 + \kappa\iota - m_*\right) & -\nu\iota \\ \frac{\kappa}{\nu}\iota & -\frac{\kappa}{\nu}\iota & 1 \end{array} \right], \tag{B.28a}$$

$$\begin{aligned} \mathcal{H} = & \left[\begin{array}{c} -\eta_b^2\left(u - u_b\right) - \gamma u' - \gamma_b\left(u' - u_b'\right) - \kappa\gamma_{\phi_1}\left(u' - u_b'\right)\cdots \\ \eta_b^2\left(u - u_b\right) + \gamma_b\left(u' - u_b'\right) + \kappa\gamma_{\phi_1}\left(u' - u_b'\right)\cdots \\ -\gamma_{\phi_1}\frac{\kappa}{\nu}\left(u' - u_b'\right) - \gamma_{\phi_1}\phi_b' - \gamma_{\phi_2}\phi_b'\cdots \end{array} \right. \\ & \left. \begin{array}{c} \cdots - \nu\gamma_{\phi_1}\phi_b' - \kappa\left(u - u_b\right) - \nu\phi_b + \nu\omega_0\tau \\ \cdots + \nu\gamma_{\phi_1}\phi' + \kappa\left(u - u_b\right) + \nu\phi_b - \nu\omega_0\tau \\ \cdots - \frac{\kappa}{\nu}\left(u - u_b\right) - \phi_b + \omega_0\tau \end{array} \right]\cdots \\ & \cdots + \left[\begin{array}{c} 0 \\ -n\bar{\psi}\delta_n\bar{g}_k^{\varepsilon}\left(g_k^{\varepsilon}\left(1 - \vartheta_{\zeta}^{l}(r_b)\right) + \vartheta_{\zeta}^{l}(r_b)\right) \\ -n\delta_n\bar{g}_k^{\varepsilon}\left(g_k^{\varepsilon}\left(1 - r_b^2\right) + r_b^2\right) \end{array} \right] + \left[\begin{array}{c} \bar{\psi}\mathcal{W}_{as} \\ \bar{\psi}\mathcal{W}_{bs} \\ 0 \end{array} \right], \end{aligned} \tag{B.28b}$$

$$\mathcal{W} = \left[\begin{array}{cc} 0 & 0 \\ \bar{\psi} & 0 \\ 0 & 1 \end{array} \right]. \tag{B.28c}$$

The dimensionless frictional/contact components of the bit/rock interaction in the AST model is characterized in the same manner as in Eq. (B.17d) for the BM model (with also considering Eqs. (B.18) – (B.22)).

In Eq. (B.28b), the dimensionless applied weight at the top surface, which consists of the total submerged weight of the drill-string section above the AST and the applied hook-load H_0, is given by

$$\mathcal{W}_{as} = \frac{a}{2C_p\zeta^*}\left(W_{as} - H_0\right), \tag{B.29}$$

and the dimensionless total submerged weight of the drill-string section below the AST reads as

$$\mathcal{W}_{bs} = \frac{a}{2C_p\zeta^*}W_{bs}. \tag{B.30}$$

The parameters of the dimensionless AST model listed in Table B.1 are calculated on the basis of Tables B.2 and B.3. The corresponding numerical parameter values also use the cases studied in [181, 187].

B.2 Computational Method for the Dynamic Responses

The equations of motion Eq. (B.12) are solved numerically by employing the time-stepping method with Moreau's midpoint rule at the velocity level (see further details about this time-integration scheme for non-smooth dynamical systems in [8, 165]). In general, this method can be summarized as follows. First, we recall the generic form of EOMs in Eq. (B.12):

$$\mathcal{M}\mathbf{z}'' - \mathcal{H}\left(\tau, \mathbf{z}, \mathbf{z}', \mathbf{z}_{\tau_n}\right) = \mathcal{W}\mathcal{L}. \tag{B.31}$$

The column $\mathbf{z}$ and the matrix $\mathcal{M}$ represent the independent generalized coordinates and the mass matrix, respectively. The column $\mathcal{H}$ contains all the generalized (smooth) forces and torques except the non-smooth (nonlinear) part. The vector $\mathcal{L}$ contains the non-smooth forces and torques associated with the set-valued forces laws, i.e., the contact force and frictional torque arising from the bit/rock interaction. The matrix $\mathcal{W}$ stores the associated directions of these non-smooth forces and torques.

Second, we rewrite Eq. (B.31) as follows:

$$\dot{\mathbf{u}} = \mathcal{M}^{-1}\left(\mathcal{H}\left(\tau, \mathbf{z}, \mathbf{u}, \mathbf{z}_{\tau_n}\right) + \mathcal{W}\mathcal{L}\right), \tag{B.32}$$

with the generalized velocities $\mathbf{u} = \mathbf{z}'$. The first-order discretization of these velocities (based on Moreau's midpoint rule for the time-stepping method and w.r.t. time τ) is then given by

$$\dot{\mathbf{u}} = \frac{\mathbf{u}^E - \mathbf{u}^B}{\Delta\tau}. \tag{B.33}$$

Herein, the velocities at the discrete time instants τ^B and τ^E are denoted by $\mathbf{u}^E$ and $\mathbf{u}^B$, respectively, with a time-step $\Delta\tau = \tau^E - \tau^B > 0$. Hence, we combine Eq. (B.33) into Eq. (B.32) that gives

$$\mathbf{u}^E = \mathcal{M}^{-1}\left(\mathcal{H}^M + \mathcal{W}^M\mathcal{L}\right)\Delta\tau + \mathbf{u}^B, \tag{B.34}$$

for solving the EOMs in Eq. (B.31). In Eq. (B.34), the column $\mathcal{H}^M$ and the matrix $\mathcal{W}^M$, respectively, are given by

$$\mathcal{H}^M := \mathcal{H}(\tau^M, \mathbf{z}^M, \mathbf{u}^B, \mathbf{z}^M_{\tau_n}), \tag{B.35a}$$

$$\mathcal{W}^M := \mathcal{W}(\tau^M, \mathbf{z}^M), \tag{B.35b}$$

that are approximated at the (mid-step) time instant $\tau^M := \tau^B + \frac{\Delta\tau}{2}$. Herein, the generalized coordinates at the mid-step time instant τ^M are denoted by

$$\mathbf{z}^M = \mathbf{z}^B + \mathbf{u}^B \frac{\Delta\tau}{2}, \tag{B.36}$$

and the delayed generalized coordinates prior to the mid-step time instant τ^M are defined by

$$\mathbf{z}^M_{\tau_n} := \mathbf{z}\left(\tau^M - \tau_n\right). \tag{B.37}$$

Two pivotal elements in numerically solving the EOMs in Eq. (B.31) for both BM and AST models are: *(i)* the time-delay calculation arising from the cutting process (i.e., solving for τ_n based on Eq. (B.5)) that is required to evaluate $\mathcal{H}^M$ in Eq. (B.35a), and *(ii)* the nonlinear (non-smooth) parts of the WOB and TOB due to the (frictional) contact in the bit/rock interaction (i.e., solving Eqs. (B.19) and (B.21), respectively).

First, the time-delay τ_n in Eq. (B.5) is state-dependent. Hence, we adopt the technique developed in [181] to calculate the time-delay for each bit rotation, namely based on the interpolation between the generalized coordinates $\mathbf{z}^M$ at the mid-step time instant τ^M in Eq. (B.36) and the delayed generalized coordinates $\mathbf{z}^M_{\tau_n}$ prior to the mid-step time instant τ^M in Eq. (B.37) via the implicit equation in Eq. (B.5).

This time-delay is then utilized with the axial response of the system for updating the depth-of-cut in Eq. (B.6) that is required to compute the WOB and TOB of the cutting component (due to the bit/rock interaction) stored in the column $\mathcal{H}^M$ in Eq. (B.35a). Note also that to evaluate this column $\mathcal{H}^M$ in Eq. (B.35a) at the mid-step discrete time instant τ^M, we refer to Eq. (B.17b) for the BM model and Eq. (B.28b) for the AST model.

Second, the WOB and TOB due to the (frictional) contact are formulated as the set-valued force laws that are solved numerically via the inclusions in Eqs. (B.19) and (B.21), respectively. These inclusions can be rewritten equivalently using a proximal-point formulation on velocity level [104]:

$$\mathcal{L}_{b_a} = \operatorname{prox}_{\overline{C}_a}\left(\mathcal{L}_{b_a} - r_1 u_b'\right), \tag{B.38a}$$

$$\mathcal{L}_{b_t} = \operatorname{prox}_{\overline{C}_t}\left(\mathcal{L}_{b_t} - r_2 \phi_b'\right), \tag{B.38b}$$

with r_1 and r_2 as the strictly positive constants that shall be tuned in the numerical computation, and the associated convex sets defined as follows:

$$\overline{C}_a = \left\{\mathcal{L}_{b_a} \mid -\frac{a}{2C_p\zeta^*}\bar{\lambda}_{b_a} \leqslant \mathcal{L}_{b_a} \leqslant 0\right\}, \tag{B.39a}$$

$$\overline{C}_t = \left\{\mathcal{L}_{b_t} \mid \beta_k \mathcal{L}_{b_a} \leqslant \mathcal{L}_{b_t} \leqslant -\beta_k \mathcal{L}_{b_a}\right\}, \tag{B.39b}$$

considering the definitions in Eqs. (B.20) and (B.22).

Note that the following bit/rock parameters in the case of drilling layered formations are adapted with the bit engagement in Eqs. (4.2) and (4.4): *(i)* the bit parameters for the cutting and frictional components (ϑ^l_ζ in Eq. (4.12) and ϑ^l_ξ in Eq. (4.18), respectively), and *(ii)* the rock parameters for the cutting component (the rock intrinsic specific energy ε) and in the frictional component (the frictional coefficient μ and the maximum contact pressure $\bar{\sigma}$) via Eq. (B.7).

The proximal point formulations in Eqs. (B.38a) – (B.38b) are affected by this bit/rock parameters adaptation (via the associated convex sets in Eqs. (B.39a) – (B.39b)) and solved numerically using an iterative technique, in this case a Jacobian-relaxation (JOR) scheme [165].

Algorithm B.1 summarizes the implementation of this time-stepping method for numerically solving the delay differential inclusions representing the BM and AST models. The developed algorithm for solving these EOMs converges with a computational time approximately less than 10 minutes (on an Intel(R) Core(TM) i7-6700HQ, 2.60GHz CPU) for the case study presented in Section 4.3, i.e., Figure 4.8 for the BM model and Figure 4.10 for the AST model.

Nominal solutions as the initial values for BM and AST models. For the initial conditions in the numerical computation, we assume that the bit is steadily drilling in the first layer (e.g., $k = 1$) and fully engaged in this layer (e.g., $r_b = 1$). Hence, we consider the same nominal values presented in [187] as the initial conditions; in the case of a nominal drilling operation, the axial and torsional velocities are constant and positive (no vibrations), and consequently nominal values of the interface laws are obtained.

B.3 The Ratio of the Weights-On-Bit

The reaction weights due to the cutting process and frictional contact in the bit/rock interaction in drilling interbedded formations are explored to further analyze the effect of the AST on the drill-string dynamics. Let us define the cutting force ratio and the wear-flat contact force ratio for the k^{th} layer as follows:

$$\overline{\mathcal{W}}^c_k = \frac{\langle W^c_k \rangle}{\langle W^c_k \rangle + \left\langle W^f_k \right\rangle}, \quad \text{and} \quad \overline{\mathcal{W}}^f_k = \frac{\left\langle W^f_k \right\rangle}{\langle W^c_k \rangle + \left\langle W^f_k \right\rangle}, \tag{B.40}$$

respectively. Here $\langle W^c_k \rangle$ and $\left\langle W^f_k \right\rangle$ refer to the averaged WOB resulting from the cutting and frictional contact, respectively, in the bit/rock interaction for each layer (see also Eqs. (4.10) and (4.13)). Hence, the averaged values of the

Algorithm B.1 Time-stepping method (with Moreau's midpoint rule) for solving the (dimensionless) EOMs of BM and AST models in interbedded formation.

```
Initialize the generalized coordinates $\mathbf{z}^B$ and the generalized velocities $\mathbf{u}^B$ at the discrete time instant $\tau^B$.
Initialize the rock layer index $k_* = 1$ and the interface depth $l_0 = 0$ (see Eq. (B.10)).
Initialize the frictional component ($\mathcal{L}_{b_a}$ and $\mathcal{L}_{b_t}$) based on the nominal values.
Compute $\tau^M \leftarrow \tau^B + \frac{\Delta\tau}{2}$.    ▷ Start the mid-step; given the time step $\Delta\tau$.
Compute $\mathbf{z}^M \leftarrow \mathbf{z}^B + \mathbf{u}^B \frac{\Delta\tau}{2}$.    ▷ Update generalized coordinates at $\tau^M$. Note that the velocities $\mathbf{u} = \mathbf{z}'$.
Compute the bit engagement $z_b$ in Eq. (B.11).
Update the rock layer index $k_*$ as the minimum $k \in \{1, 2, 3, \ldots, K\}$ such that it holds that $\frac{L_*}{a}\left(u_b(\tau) - l_{k_*-1}\right) \geq 0$ (see Eq. (B.11)).
Update the bit parameters with the bit profile in Eq. (4.4): $\vartheta^l_\zeta$ in Eq. (4.12) and $\vartheta^l_\xi$ in Eq. (4.18).
Update the rock parameters: $\varepsilon$, $\mu$ and $\bar{\sigma}$ via Eqs. (B.7) - (B.8).
Compute the delayed generalized coordinates $\mathbf{z}^M_{\tau_n} \leftarrow \mathbf{z}\left(\tau^M - \tau_n\right)$.
Compute the time delay $\tau_n$ based on the interpolation between $\mathbf{z}^M$ and $\mathbf{z}^M_{\tau_n}$ via the implicit equation in Eq. (B.5).
Compute the depth-of-cut $\delta(\tau^M, \tau_n)$ based on $\mathbf{z}^M$ and $\mathbf{z}^M_{\tau_n}$ using Eq. (B.6).
Approximate $\mathcal{H}^M \leftarrow \mathcal{H}(\tau^M, \mathbf{z}^M, \mathbf{u}^B, \mathbf{z}^M_{\tau_n})$.    ▷ Update generalized (smooth) forces and torques at $\tau^M$.
Update $\mathcal{W}^M \leftarrow \mathcal{W}(\tau^M, \mathbf{z}^M)$.    ▷ Update force directions of non-smooth forces and torques at $\tau^M$.
Solve the proximal point equations for $\mathcal{L}_{b_a}$ and $\mathcal{L}_{b_t}$ in Eqs. (B.38a) - (B.38b) using JOR iterative scheme:
while Not converged do
    Compute the velocities $\mathbf{u}^E$ based on Eq. (B.34).    ▷ Update generalized velocities at $\tau^E = \tau^B + \Delta\tau$.
    Update the velocities $u'_b$ and $\phi'_b$ based on $\mathbf{u}^E$.
    Update $\mathcal{L}^{old}_{b_a} = \mathcal{L}_{b_a}$ and $\mathcal{L}^{old}_{b_t} = \mathcal{L}_{b_t}$.    ▷ From the previous iteration.
    Compute $\mathcal{L}_{b_a} = \min\left(\max\left(-\frac{a}{2C_p\zeta^*}\bar{\lambda}_{b_a}, \left(\mathcal{L}^{old}_{b_a} - r_1 u'_b\right)\right), 0\right)$.    ▷ see Eqs. (B.38a) and (B.39a).
    Compute $\mathcal{L}_{b_t} = \min\left(\max\left(\beta_k \mathcal{L}_{b_a}, \left(\mathcal{L}^{old}_{b_t} - r_2 \phi'_b\right)\right), -\beta_k \mathcal{L}_{b_a}\right)$.    ▷ see Eqs. (B.38b) and (B.39b).
    Converged if: $\left\|\mathcal{L}_{b_a} - \mathcal{L}^{old}_{b_a}\right\|_2 <$ error tolerance value and $\left\|\mathcal{L}_{b_t} - \mathcal{L}^{old}_{b_t}\right\|_2 <$ error tolerance value.
end while
Compute $\mathbf{u}^E$ using Eq. (B.34) with the updated frictional components $\mathcal{L}_{b_a}$ and $\mathcal{L}_{b_t}$.
Compute $\mathbf{z}^E \leftarrow \mathbf{z}^M + \mathbf{u}^E \frac{\Delta t}{2}$.    ▷ Update generalized coordinates at $\tau^E = \tau^B + \Delta\tau$.
```

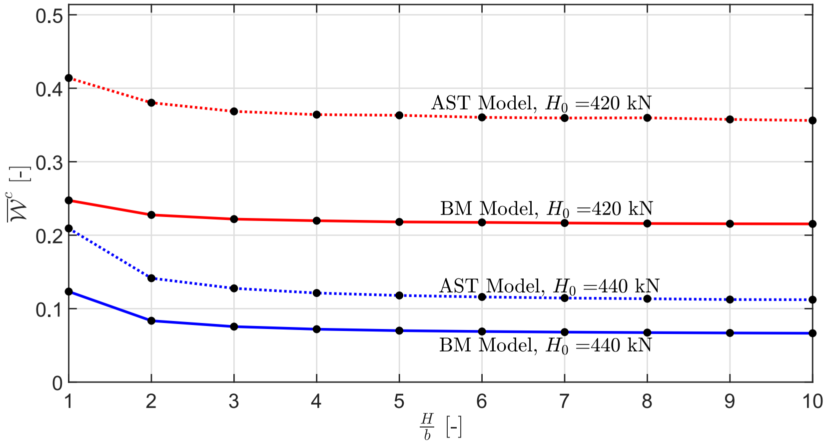

(a)

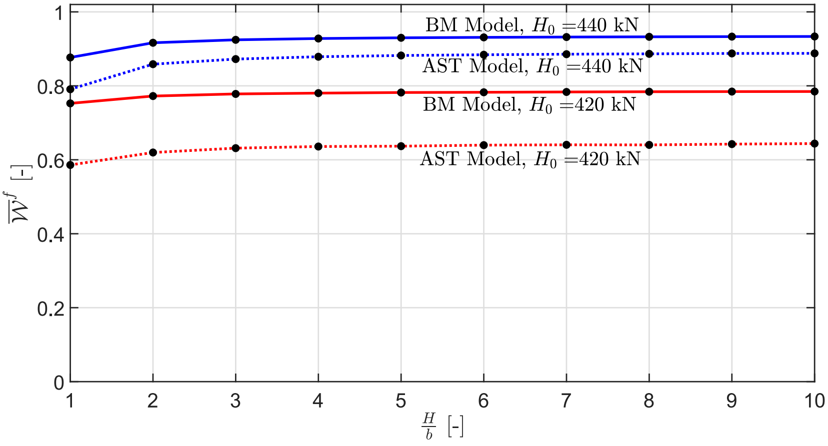

(b)

Figure B.1: Comparison of (a) the averaged cutting force ratio and (b) the averaged wear-flat contact force ratio between the benchmark (BM, with solid line) and AST (dashed line) models under the effects of the layer thickness variation ($^H/_b \in \{1, 2, \cdots, 10\}$) and for $H_0 = 440$ kN (blue line) and $H_0 = 420$ kN (red line) with $\Omega_0 = 80$ rpm.

cutting force ratio and the contact force ratio ($\overline{\mathcal{W}}^c$ and $\overline{\mathcal{W}}^f$, respectively) over the total time Δt in drilling interbedded formations can be also calculated by according to Eqs. (4.39) and (4.40) (also by considering all the force ratios in the $(k-1)^{th}$ and k^{th} layers calculated from Eq. (B.40)).

The values of the cutting force ratio and the contact force ratio based on the

Table B.4: Variable list.

Variable Name	Symbol	Unit
Axial displacement of drill-string above AST	U	m
Bit axial displacement	U_b	m
Torsional displacement of drill-string above AST	Φ	rad
Bit torsional displacement	Φ_b	rad
Axial velocity of drill-string above AST	$\dot{U}$	m/s
Bit axial velocity (its averaged value in k^{th} layer)	$\dot{U}_b(\langle \dot{U}_k^b \rangle)$	m/s
Torsional velocity of drill-string above AST	$\dot{\Phi}$	rad/s
Bit torsional velocity (its averaged value in k^{th} layer)	$\dot{\Phi}_b(\langle \dot{\Phi}_k^b \rangle)$	rad/s
WOB of the cutting component in the interface laws (its averaged value in k^{th} layer)	$W_k^c(\langle W_k^c \rangle)$	N
WOB of the frictional component in the interface laws (its averaged value in k^{th} layer)	$W_k^f(\left\langle W_k^f \right\rangle)$	N
TOB of the cutting component in the interface laws (its averaged value in k^{th} layer)	$T_k^c(\langle T_k^c \rangle)$	Nm
TOB of the frictional component in the interface laws (its averaged value in k^{th} layer)	$T_k^f(\left\langle T_k^f \right\rangle)$	Nm
Averaged depth-of-cut (DOC) in k^{th} layer	$\langle d_k \rangle$	m

dynamic responses of both BM and AST models are presented in Figure B.1 at top and bottom, respectively. In Figure B.1 (top) with the presence of the AST, the cutting force ratio is higher while the contact force ratio is lower, when compared to the results of BM model. These comparison results support the indication on the occurrence of more axial vibrations associated with the presence of the AST that leads to reduce the frictional torque and more weight used for the cutting – all in averaged sense.

B.4 Additional variable list

The additional list of variables used in the model formulations and the simulation analyses are given in Table B.4.

Appendix C

Appendix to Chapter 5

C.1 Steady-state solutions

In the absence of any vibrations, the axial and torsional velocities are given by $V_L = V_b = V_0$ and $\Omega_L = \Omega_b = \Omega_0$, respectively, and assume constant velocities $V_0 > 0$ and $\Omega_0 > 0$. Herein, the steady-state solutions for both BM and AST models are unique and given below. Note that the nominal generalized positions in both BM and AST models are affected by the static deformations of the drill-string structure and the prescribed boundary conditions; see also the works in [77, 187].

C.1.1 BM model

The initial axial displacements (i.e., due to the static deformation at the time-instant $t = 0$) at the bit and at the interface are set to be $U_{bs} = 0$ and $U_{L0} = 0$, respectively. The initial torsional displacements at the bit and at the interface are equal to $\Phi_{bs} = 0$ and $\Phi_{L0} = 0$, respectively. Furthermore, based on the dynamics of the lower part in Eq. (5.17) with the associated matrices in Eqs. (5.18a) – (5.18d) for the BM model, the steady-state force and torque at the interface, denoted by W_{L0} and T_{L0}, respectively, are given by

$$W_{L0} = W_g - W_{b0}, \tag{C.1}$$

$$T_{L0} = T_{b0} + D_\phi \Omega_0. \tag{C.2}$$

The nominal weight-on-bit and torque-on-bit due to the bit-rock interaction, following Eqs. (5.7a) and (5.7b), are, respectively, given by

$$W_{b0} = W_{c0} + W_{f0}, \tag{C.3}$$

$$T_{b0} = T_{c0} + T_{f0}. \tag{C.4}$$

In a nominal operation (where the bit is fully mobilized), the frictional component of the bit-rock interaction (i.e., the weight W_{f0} and torque T_{f0}) are equal to the maximum values of the contact force and frictional torque in Eqs. (5.8a) – (5.9). For the cutting component in Eqs. (5.11a) – (5.11b), the nominal weight W_{c0} and torque T_{c0} are dependent to the following nominal depth-of-cut obtained based on the depth-of-cut evolution in Eq. (5.13):

$$d_{n0} = \frac{2\pi V_0}{n\Omega_0}. \tag{C.5}$$

Note that V_0 is a nominal axial velocity of the drill-string system (e.g., in the steady-state drilling condition).

In a steady-state condition, the PDE of the axial dynamics of the drill-pipe in Eq. (5.2b) becomes

$$W_{L0} - H_0 = k_a \rho A V_0 L. \tag{C.6}$$

By substituting the nominal weight W_{L0} (based on the axial equilibrium at the interface in Eq. (C.1)) into Eq. (C.6) and considering the nominal weight-on-bit in Eq. (C.3) (based on the nominal depth-of-cut in Eq. (C.5)), we obtain the nominal axial velocity as follows:

$$V_0 = \frac{W_g - H_0 - W_{f0}}{\left(\frac{2\pi K_a}{\Omega_0}\right) + k_a \rho A_p L}, \tag{C.7}$$

with $K_a = a\zeta\varepsilon$.

C.1.2 AST model

For the case of a steady-state drilling condition in the AST model, the initial axial and torsional displacements (i.e., due to the static deformation at the time-instant $t = 0$) at the bit are set to be $U_{bs} = 0$ and $\Phi_{bs} = 0$, respectively. Moreover, the equilibria at the interface (of the drill-pipe and BHA parts), based on the BHA dynamics in Eq. (5.17) with the associated matrices in Eqs. (5.22a) – (5.22d), read the nominal weight and torque due the interaction at this interface, respectively, as follows:

$$W_{L0} = K_b U_{L0} - W_{ag} - \frac{1}{\alpha}\left(T_{L0} - D_{\phi_a}\Omega_0\right), \tag{C.8}$$

$$T_{L0} = T_{b0} + \left(D_{\phi_a} + D_{\phi_b}\right)\Omega_0. \tag{C.9}$$

Note that the nominal weight-on-bit in Eq. (C.3) and torque-on-bit in Eq. (C.4) due to the bit-rock interaction also apply in the AST model. In addition, this steady-state force and torque at the interface in Eqs. (C.8) – (C.9) and the holonomic constraint of the AST in Eq. (5.24) give the initial axial and torsional displacements at the interface, respectively, as follows:

$$U_{L0} = \frac{1}{K_b}\left(W_{b0} - W_{bg} + \frac{1}{\alpha}\left(T_{L0} - D_{\phi_a}\Omega_0\right)\right), \tag{C.10}$$

$$\Phi_{L0} = \frac{U_{L0}}{\alpha}. \tag{C.11}$$

In a steady-state condition, the equilibrium in Eq. (C.6) also applies in the AST model. Hence, substituting the nominal weight at the interface W_{L0} into Eq. (C.6) and considering Eqs. (C.9) – (C.11) in this substitution give the nominal axial velocity for the AST model as follows:

$$V_0 = \frac{W_{ag} + W_{bg} - H_0 - W_{f0}}{\left(\frac{2\pi K_a}{\Omega_0}\right) + k_a \rho A_p L}. \tag{C.12}$$

C.2 List of variables and parameters

The additional list of variables used in the model formulations and the simulation analyses are given in Tables C.1 and C.2.

Table C.1: Nomenclature.

Kinematic variables/coordinates		
t	$[s]$	Time coordinate
x	$[m]$	Axial position
U	$[m]$	Axial displacement
Φ	$[rad]$	Angular displacement
State variables – in time-domain		
V	$[m/s]$	Axial velocity
Ω	$[rad/s]$	Angular velocity
W	$[N]$	Force (Weight)
T	$[Nm]$	Torque

Table C.2: Parameter values of the bit-rock interaction, the drill-string, and the AST.

Bit-rock parameters		
ε	[MPa]	Intrinsic specific energy of the rock
σ	[MPa]	Normal contact stress (bit-rock contact)
μ	[−]	Friction coefficient (bit-rock contact)
n	[−]	Number of bit blades
a	[m]	Bit radius
ℓ	[m]	Wearflat length
ζ	[−]	Cutting face orientation
ξ	[−]	Orientation and distribution of wear-flats
Drill-string parameters		
ρ	[kg/m^3]	Density of the drill-string material
E	[GPa]	Young's modulus (elasticity modulus)
G	[GPa]	Shear modulus
L	[m]	Total length of drill-pipe
A	[m^2]	Drill-pipe area
J	[m^4]	Drill-pipe polar inertia
k_a	[−]	Axial domain damping
k_t	[−]	Torsional domain damping
V_0	[m/s]	Top-drive (nominal) axial velocity
Ω_0	[RPM]	Top-drive (nominal) angular velocity
H_0	[kN]	Hook-load
L_a	[m]	Length of the top part of BHA (or above the AST)
L_b	[m]	Length of the bottom part of BHA (or below the AST)
I	[kg.m^2]	Total inertia of the BHA
I_a	[kg.m^2]	Inertia of the top part of BHA (or above the AST)
I_b	[kg.m^2]	Inertia of the bottom part of BHA (or below the AST)
M	[kg]	Total mass of the BHA
M_a	[kg]	Mass of the top part of BHA (or above the AST)
M_b	[kg]	Mass of the bottom part of BHA (or below the AST)
D_ϕ	[Nm.s/rad]	Total torsional damping of the BHA
D_{ϕ_a}	[Nm.s/rad]	Torsional damping of the top part of BHA (or above the AST)
D_{ϕ_b}	[Nm.s/rad]	Torsional damping of the bottom part of BHA (or below the AST)
AST parameters		
p	[m]	AST lead
r_{sp}	[m]	AST helix (spline) radius
β	[rad]	AST lead angle
K_b	[N/m]	AST axial spring stiffness
D_b	[N.s/m]	AST axial damping

Bibliography

[1] B. S. Aadnøy and K. Andersen. Design of oil wells using analytical friction models. *Journal of Petroleum Science and Engineering*, 32(1):53–71, 2001.

[2] Aarsnes U. J. F., Aamo O. M. Linear stability analysis of self-excited vibrations in drilling using an infinite dimensional model. *Journal of Sound and Vibration*, 2016.

[3] Aarsnes U. J. F., van de Wouw N. Axial and torsional self-excited vibrations of a distributed drill-string. *Journal of Sound and Vibration*, 444:127–151, March 2019.

[4] Aarsnes U. J. F., van de Wouw N. Effect of shock subs on self-excited vibrations in drilling systems. *Journal of Petroleum Science and Engineering*, 181:106217, 2019.

[5] Aarsnes U.J.F., van de Wouw N. Dynamics of a distributed drill string system: Characteristic parameters and stability maps. *Journal of Sound and Vibration*, 417:376–412, March 2018.

[6] Aarsnes U.J.F., van de Wouw N. Effect of axial and torsional vibrations on a distributed drill string system. In *5th International Colloquium on Nonlinear Dynamics and Control of Deep Drilling Systems, 27 - 29 June 2022, University of Maryland, College Park, MD, U.S.A.*, 2022.

[7] Abbassian F., Dunayevsky V. A. Application of stability approach to torsional and lateral bit dynamics. *SPE Drilling & Completion*, 13(02):99–107, 06 1998.

[8] Acary V., Brogliato B. *Numerical methods for nonsmooth dynamical systems: applications in mechanics and electronics*, volume Volume 35 of *Lecture Notes in Applied and Computational Mechanics. Springer-Verlag, Berlin*, 2008.

[9] Aird P. *Deepwater drilling: well planning, design, engineering, operations, and technology applications.* Elsevier Ltd., 2019.

[10] Akutsu E., Rødsjø M., Gjertsen J., Andersen M., Reimers N., Granhøy-Lieng M., Strøm E., Horvei K.A. Faster ROP in Hard Chalk: Proving a New Hypothesis for Drilling Dynamics. In *SPE/IADC Drilling Conference and Exhibition, held in London, United Kingdom, 17 - 19 March*, number SPE-173068-MS, 2015.

[11] P. Allan and R. Brogan. Energy transition: optimizing existing E&P value and clean energy potential. In *SPE Annual Technical Conference and Exhibition in Dubai, UAE*, number SPE-206175-MS, September 2021.

[12] Altamimi I.M., Mokrani S., Zulkaf A.H. Axial oscillation tool significantly mitigates the vibration level and enhances drilling performance in conjunction with standard RSS systems. In *Abu Dhabi International Petroleum Exhibition and Conference in Abu Dhabi, UAE*, number SPE-177713-MS, November 2015.

[13] M. Angelone and S.S. Labini. Overcoming research challenges for geothermal energy. Technical report, Energy Research Knowledge Centre (ERKC), 2014.

[14] A.G. Aribowo, U. J. F. Aarsnes, E. Detournay, N. van de Wouw, and N. Reimers. Performance Analysis of a Downhole Regulator on Rate-Of-Penetration and Drilling Efficiency: An Autonomous Load Management at Bit. In *SPE/IADC International Drilling Conference and Exhibition, Stavanger, Norway*, number IADC/SPE-212560-MS, March 2023.

[15] A.G. Aribowo, U.J.F. Aarsnes, K. Chen, E. Detournay, and N. van de Wouw. Model-based drilling performance analysis of a downhole regulator. In *6th International Colloquium on Nonlinear Dynamics and Control of Deep Drilling Systems, 1 - 3 July 2024, Universidade Federal do Rio de Janeiro (UFRJ), Rio de Janeiro, RJ, Brazil*, 2024.

[16] Aribowo A.G., Aarsnes U. J. F., Chen K., Detournay E., van de Wouw N. Analysis of a downhole regulator in drilling: a distributed parameter modeling approach. *To be submitted*, 2024.

[17] Aribowo A.G., Wildemans R., Detournay E., van de Wouw N. Drag bit/rock interface laws for the transition between two layers. *International Journal of Rock Mechanics and Mining Sciences*, 150:104980, 2022.

[18] Aribowo A.G., Wildemans R., Detournay E., van de Wouw N. Dynamic modeling of drill-string systems for layered rock formations. In *5th International Colloquium on Nonlinear Dynamics and Control of Deep Drilling Systems, 27 - 29 June 2022, University of Maryland, College Park, MD, U.S.A.*, 2022.

[19] Aribowo A.G., Wildemans R., Detournay E., van de Wouw N. Dynamic analysis of a downhole regulator for drilling in interbedded formations. *SPE Journal*, 28(04):1611–1635, August 2023. SPE-214310-PA.

[20] P. Astrid, A.K. Singh, J.E. Huhman, M.A. Stoever, M.W. Dykstra, R.H.G.M. Grauwmans, and J.J. Blangé. Optimizing performance of a drilling assembly. Technical Report 9938816, US Patent Office, 2018.

[21] V. Azike-Akubue, S. Barton, R. Gee, and T. Burnett. Agitation Tools Enables Significant Reduction in Mechanical Specific Energy. In *SPE Asia Pacific Oil and Gas Conference and Exhibition*, volume All Days, 10 2012.

[22] M.H. Bahari, A. Bahari, F. Nejati, R. Rajaei, and B. Vosoughi-V. Drilling rate prediction using bourgoyne and young model associated with genetic algorithm. In *4th ACM International Conference on Intelligent Computing and Information Systems (ACM-ICICIS)*, 2009.

[23] Balanov A.G., Janson N.B., McClintock P.V.E., Tucker R.W., Wang C.H.T. Bifurcation analysis of a neutral delay differential equation modelling the torsional motion of a driven drill-string. *Chaos, Solitons & Fractals*, 15(2):381–394, 2003.

[24] Barreau M., Gouaisbaut F., Seuret A. Practical stability analysis of a drilling pipe under friction with a PI-controller. *IEEE Transactions on Control Systems Technology*, 29(2):620–634, 2021.

[25] Barton S., Baez F., Alali A. Drilling performance improvements in gas shale plays using a novel drilling agitator device. In *SPE Unconventional Resources Conference / Gas Technology Symposium in the Woodlands, Texas, USA*, pages SPE–144416–MS, June 2011.

[26] Beeh H.A., Khalil H., Paulus S.L., Tiku A., Karlsen B.A. Thorough analysis and commitment for improvement led to a step change in the drilling performance on valemon field, north sea. In *SPE Norway One Day Seminar, Bergen, Norway*, number SPE-191316-MS, April 2018.

[27] Besselink B., van de Wouw N., Nijmeijer H. A semi-analytical study of stick-slip oscillations in drilling systems. *Journal of Computational and Nonlinear Dynamical*, 6:21006–21009, 2011.

[28] Besselink B., Vromen T., Kremers N., van de Wouw N. Analysis and control of stick-slip oscillations in drilling systems. *IEEE Transactions on Control Systems Technology*, 24(5):1582–1593, 2016.

[29] Black & Veatch Company. 2021: Market dynamics of hydrogen, 2021.

[30] Blatter P. Dynamic modeling and analysis of drilling systems with an anti stick-slip tool. mathesis, Master of Science Thesis, DC 2016.073, Eindhoven University of Technology, Department of Mechanical Engineering, September 2016.

[31] Boualleg R., Sellami H., Menand S. Effect of formations anisotropy on directional tendencies of drilling systems. In *2006 SPE/IADC Drilling Conference, 21 - 23 February 2006, Miami, Florida, U.S.A.*, number SPE/IADC-98865, 2006.

[32] Boussaada I., Cela A., Mounier H., Niculescu S.-I. Control of drilling vibrations: A time-delay system-based approach. *IFAC Proceedings Volumes*, 46(3):226–231, 2013. 11th Workshop on Time-Delay Systems.

[33] Boussaada I., Mounier H., Niculescu S.-I., Cela A. Analysis of drilling vibrations: A time-delay system approach. In *2012 20^{th} Mediterranean Conference on Control & Automation (MED)*, pages 610–614, 2012.

[34] Bresch-Pietri D., Di Meglio F. Prediction based control of linear input-delay system subject to state-dependent state delay - Application to suppression of mechanical vibrations in drilling. In *2nd IFAC Workshop on Control of Systems Governed by Partial Differential Equations CPDE 2016*, volume 49, pages 111–117, 2016.

[35] Bresch-Pietri D., Krstic M. Adaptive output feedback for oil drilling stick-slip instability modeled by wave PDE with anti-damped dynamic boundary. In *2014 American Control Conference*, pages 386–391, 2014.

[36] Bresch-Pietri D., Krstic M. Adaptive output-feedback for wave PDE with anti-damping - application to surface-based control of oil drilling stick-slip instability. In *53rd IEEE Conference on Decision and Control*, pages 1295–1300, 2014.

[37] Brett J.F. The genesis of torsional drillstring vibrations. *Society of Petroleum Engineers (SPE) Drilling Engineering*, 7(3):168–174, September 1992. SPE-21943-PA.

[38] Brown E.T., Green S.J., Sinha K.P. The influence of rock anisotropy on hole deviation in rotary drilling - a review. *International Journal of Rock Mechanics and Mining Sciences and Geomechanics Abstracts*, 18(5):387 – 401, 1981.

[39] Canudas-de-Wit C., Aracil J., Gordillo, F., Salas F. The oscillations killer: a mechanism to eliminate undesired limit cycles in a class of nonlinear systems. *International Journal of Robust and Nonlinear Control*, 24(1):39–53, July 2014.

[40] Canudas-de-Wit C., Rubio F.R., Corchero M.A. D-OSKIL: a new mechanism for controlling stick-slip oscillations in oil well drillstrings. *IEEE Transactions on Control Systems Technology*, 16(6):1177–1191, 2008.

[41] Cayeux E., Ambrus A. Self-attenuation of drillstring torsional vibrations using distributed dampers. *SPE Journal*, pages 1–22, 03 2023.

[42] Challamel N. Rock destruction effect on the stability of a drilling structure. *Journal of Sound and Vibration*, 233(2):235–254, 2000.

[43] Che D., Zhang W., Ehmann K. Chip formation and force responses in linear rock cutting: an experimental study. *Journal of Manufacturing Science and Engineering*, 139(1):011011, January 2017.

[44] Che D., Zhu W.-L., Ehmann K.F. Chipping and crushing mechanisms in orthogonal rock cutting. *International Journal of Mechanical Sciences*, 119:224–236, December 2016.

[45] K. Chen, H. Zhang, N. van de Wouw, and E. Detournay. An alternative approach to compute chip thickness in milling. *Journal of Manufacturing Science and Engineering*, 144(11):111006, 07 2022.

[46] K. Chen, H. Zhang, N. van de Wouw, and E. Detournay. An alternative approach to model the dynamics of a milling tool. *Journal of Sound and Vibration*, 569:117940, 2024.

[47] P. Chen, X. Dai, F. Shao, E. Ozbayoglu, W. Liu, and J. Wang. Review of PDC cutter - rock interaction: Methods and physics. *Geoenergy Science and Engineering*, 228:211995, 2023.

[48] Chen S., Wisinger J., Dunbar B., Propes C. Identification and mitigation of friction- and cutting-action-induced stick/slip vibrations with PDC bits. *SPE Drilling & Completion*, 35(04):576–587, December 2020.

[49] Cheng J., Wu M., Wu F., Lu C., Chen X., Cao W. Modeling and control of drill-string system with stick-slip vibrations using LPV technique. *IEEE Transactions on Control Systems Technology*, 29(2):718–730, 2021.

[50] Christoforou A.P., Yigit A.S. Dynamic modelling of rotating drillstrings with borehole interactions. *Journal of Sound and Vibration*, 206(2):243–260, 1997.

[51] Christoforou A.P., Yigit A.S. Fully coupled vibrations of actively controlled drillstrings. *Journal of Sound and Vibration*, 267(5):1029–1045, 2003.

[52] Cockburn C., Matheus J., Dang K.L. Automatic trajectory control in extended-reach wells. In *SPE Middle East Oil and Gas Show and Conference in Manama, Bahrain*, number SPE-142671-MS, September 2011.

[53] Dagestad V., Reimers N. First field results for extended-reach ct drilling tool. *2006 SPE Coiled Tubing and Well Intervention Conference, The Woodlands (TX)*, IA, 2006.

[54] Dareing D., Tlusty J., Zamudio C. Self-excited vibrations induced by drag bits. *Journal of Energy Resources Technology*, 112:54–61, March 1990.

[55] Dehkordi M. K., Osguei A. T., Khamoushi I., Pavlovskaia E., Wiercigroch M. Internal mechanics of anti stick-slip tool. *International Journal of Mechanical Sciences*, 221:107188, 2022.

[56] Deliac E.P. *Optimisation des Machines d'Abattages à Pics.* PhD thesis, Université Pierre et Marie Curie, 1986.

[57] Depouhon A., Detournay E. Instability regimes and self-excited vibrations in deep drilling systems. *Journal of Sound and Vibration*, 333(7):2019–2039, 2014.

[58] Detournay E., Defourny P. A phenomenological model for the drilling action of drag bits. *International Journal of Rock Mechanics and Mining Sciences and Geomechanics Abstracts*, 29(1):13–23, 1992.

[59] Detournay E., Richard T., Shepherd M. Drilling response of drag bits: theory and experiment. *International Journal of Rock Mechanics and Mining Sciences*, 45(8):1347–1360, 2008.

[60] Di Meglio F., Aarsnes U.J.F. A distributed parameter systems view of control problems in drilling. In *2nd IFAC Workshop on Automatic Control in Offshore Oil and Gas Production OOGP 2015*, volume 48, pages 272–278, 2015.

[61] Dileep G. A survey on smart grid technologies and applications. *Renewable Energy*, 146:2589–2625, 2020.

[62] DiPippo R. 7.07 - Geothermal Power Plants. In Ali Sayigh, editor, *Comprehensive Renewable Energy*, pages 209–239. Elsevier, Oxford, 2012.

[63] Dupriest F. E., Noynaert S., Cunningham T., Rendon M. Maximizing drilling performance through the Delaware Basin Brushy Canyon and interbedded formations. In *IADC/SPE Drilling Conference, 3-5 March 2020, in Galveston, Texas, U.S.A.*, number IADC/SPE-199599-MS, 2020.

[64] Dwars S. Recent advances in soft torque rotary systems. In *SPE/IADC Drilling Conference and Exhibition in London, United Kingdom*, number SPE/IADC-173037-MS, March 2015.

[65] Dwars S., Lien M., Øydna S., Baumgartner T. Curing stick-slip: Eureka. In *SPE/IADC Drilling Conference and Exhibition in The Hague, The Netherlands*, number SPE-194108-MS, March 2019.

[66] Elsayed M.A., Raymond D.W. Analysis of coupling between axial and torsional vibration in a compliant model of a drillstring equipped with a PDC bit. In *ASME Engineering Technology Conference on Energy, in Houston, TX, USA*, pages 897–904, February 2002.

[67] Faassen R.P.H., van de Wouw N., Oosterling J.A.J., Nijmeijer H. Prediction of regenerative chatter by modelling and analysis of high-speed milling. *International Journal of Machine Tools and Manufacture*, 43(14):1437–1446, 2003.

[68] Faghihi M.A., Tashakori S., Yazdi E.A., Eghtesad M. Multiple regenerative effects of the bit-rock interaction in a distributed drill-string system. In Dimitrovová, Z., Biswas, P., Gonçalves, R., Silva, T., editor, *Recent Trends in Wave Mechanics and Vibrations*, volume 125, pages 491–500, Cham, 2023. Springer International Publishing.

[69] Faghihi M.A., Tashakori S., Yazdi E.A., Eghtesad M., van de Wouw N. Suppression of axial-torsional vibrations of a distributed drilling system by

the eigenvector contradiction method. In *17th IFAC Workshop on Time Delay Systems TDS 2022*, volume 55, pages 109–114, 2022.

[70] Faghihi M.A., Tashakori S., Yazdi E.A., Mohammadi H., Eghtesad M., van de Wouw N. Control of axial-torsional dynamics of a distributed drilling system. *IEEE Transactions on Control Systems Technology*, pages 1–16, 2023.

[71] Fairhurst C., Lacabanne W.D. Hard rock drilling techniques. *Mine and Quarry Engineering*, 23:157–161, 1957.

[72] Fear M.J., Abbassian F., Parfitt S.H.L., McClean A. The destruction of PDC bits by severe stick-slip vibration. In *SPE/IADC Drilling Conference, 4 - 6 March 1997, Amsterdam, Netherlands*, number SPE-37639-MS, 1997.

[73] J. Finger and D. Blankenship. Handbook of best practices for geothermal drilling. Technical Report SAND2010-6048, Sandia National Laboratories, California, USA, 2010.

[74] I. Forster. Axial Excitation as a Means of Stick Slip Mitigation - Small Scale Rig Testing and Full Scale Field Testing. In *SPE/IADC Drilling Conference and Exhibition, Amsterdam, The Netherlands*, number SPE-139830-MS, 03 2011.

[75] Franca L.F.P. Drilling action of roller-cone bits: Modeling and experimental validation. *ASME Journal of Energy Resources Technology*, 132(4):043101–1 043101–9, 2010.

[76] Gerbaud L., Menand S., Sellami H. PDC bits: all comes from the cutter rock interaction. In *IADC/SPE Drilling Conference, 21 - 23 February 2006, in Miami, Florida, U.S.A.*, number *IADC/SPE-98988*, 2006.

[77] Germay C., Denoël V., Detournay E. Multiple mode analysis of the self-excited vibrations of rotary drilling systems. *Journal of Sound and Vibration*, 325:362–381, 2009.

[78] Germay C., van de Wouw N., Nijmeijer H., Sepulchre R. Nonlinear drillstring dynamics analysis. *SIAM Journal Applied Dynamical Systems*, 8(2):527–553, 2009.

[79] Ch. Glocker. *Set-Valued Force Laws: Dynamics of Non-Smooth Systems*. Lecture Notes in Applied and Computational Mechanics. Springer Berlin, Heidelberg, 2001.

[80] Gupta S.K., Wahi P. Global axial-torsional dynamics during rotary drilling. *Journal of Sound and Vibration*, 375:332–352, 2016.

[81] Gupta S.K., Wahi P. Bifurcations in the axial-torsional state-dependent delay model of rotary drilling. *International Journal of Non-Linear Mechanics*, 99:13–30, 2018.

[82] Gupta S.K., Wahi P. Tuned dynamics stabilizes an idealized regenerative axial-torsional model of rotary drilling. *Journal of Sound and Vibration*, 412:457–473, 2018.

[83] Halsey G.W., Kyllingstad Å., Aarrestad T.V., Lysne D. Drillstring torsional vibrations: comparison between theory and experiment on a full-scale research drilling rig. In *SPE 61st Annual Technical Conference and Exhibition*, number SPE-15564-MS, October 1986.

[84] Halsey G.W., Kyllingstad Å., Kylling Å. Torque feedback used to cure slip-stick motion. In *SPE 63rd Annual Technical Conference and Exhibition in Houston, Texas, USA*, number SPE-18049-MS, October 1988.

[85] He X., Xu C. Specific energy as an index to identify the critical failure mode transition depth in rock cutting. *Rock Mechanics and Rock Engineering*, 49:1461–1478, April 2016.

[86] A. Hohl, M. Tergeist, H. Oueslati, J. R. Jain, C. Herbig, G. P. Ostermeyer, and H. Reckmann. Derivation and experimental validation of an analytical criterion for the identification of self-excited modes in drilling systems. *Journal of Sound and Vibration*, 342:290–302, 2015.

[87] Hyne N. J. *Nontechnical Guide to Petroleum Geology, Exploration, Drilling and Production.* PennWell Corporation, 3rd edition, 2012.

[88] Ignova M., Mantle K., Brovko K., Abe V., Gorodnov A., Li L. Downhole trajectory automation of RSS tools: autonomous drilling becomes reality. In *SPE/IADC Drilling Conference and Exhibition, Stavanger, Norway*, number SPE-212519-MS, March 2023.

[89] Insperger T., Stépán G., Turi J. State-dependent delay in regenerative turning processes. *Nonlinear Dynamics*, 47(1-3):275–283, 2007.

[90] J. R. Jain, H. Oueslati, A. Hohl, H. Reckmann, L. W. Ledgerwood III, M. Tergeist, and G. P. Ostermeyer. High-Frequency Torsional Dynamics of Drilling Systems: An Analysis of the Bit-System Interaction. In *SPE/IADC Drilling Conference and Exhibition, held in Texas, USA, 4 - 6 March*, number SPE-167968-MS, 03 2014.

[91] Jansen J.D., van den Steen L. Active damping of self-excited torsional vibrations in oil-well drill-strings. *Journal of Sound and Vibration*, 179(4):647–668, 1995.

[92] Jansen J.D., van den Steen L., Zachariasen E. Active damping of torsional drillstring vibrations with a hydraulic top drive. *SPE Drilling & Completion*, 10(04):250–254, 12 1995.

[93] C.A. Johancsik, D.B. Friesen, and R. Dawson. Torque and drag in directional wells-prediction and measurement. *Journal of Petroleum Technology*, 36(06):987–992, June 1984.

[94] Khulief Y.A., Al-Sulaiman F.A., Bashmal S. Vibration analysis of drillstrings with self-excited stick-slip oscillations. *Journal of Sound and Vibration*, 299(3):540–558, 2007.

[95] A. Koulidis, G. Pelfrene, and S. Ahmed. Experimental investigation of the rock cutting process and derivation of the 3d spatial distribution of the formation strength using in-cutter sensing. *Journal of Petroleum Exploration and Production Technology*, 14:365–380, January 2024.

[96] A. Koulidis, G. Zhan, and S. Ahmed. Embedded force sensing at the cutter. In *Abu Dhabi International Petroleum Exhibition and Conference, Abu Dhabi, UAE*, number SPE-211511-MS, 10 2022.

[97] Kovalyshen Y. Experiments on stick-slip vibrations in drilling with drag bits. In *U.S. Rock Mechanics/Geomechanics Symposium in Minneapolis, MN, USA*, number ARMA-2014-7108, June 2014.

[98] Kovalyshen Y. Understanding root cause of stick-slip vibrations in deep drilling with drag bits. *International Journal of Non-Linear Mechanics*, 67:331–341, 2014.

[99] Kusumawardhani D. A business case for drilling automation: well cost compression by suppressing downhole tool failure in low oil market. In *IPTC International Petroleum Technology Conference, Virtual, March 2021*, number IPTC-21781-MS, March 2021.

[100] Kyllingstad Å. A comparison of stick-slip mitigation tools. In *SPE/IADC Drilling Conference and Exhibition in the Hague, the Netherlands*, number SPE-184658-MS, March 2017.

[101] Kyllingstad Å., Halsey G.W. A study of slip/stick motion of the bit. *SPE Drilling Engineering*, 3(04):369–373, 12 1988.

[102] Kyllingstad Å., Nessjøen P.J. A new stick-slip prevention system. In *SPE/IADC Drilling Conference and Exhibition in the Hague, the Netherlands*, number SPE-119660-MS, March 2009.

[103] Labrousse S., Guner H., Kauffmann C., Caycedo A., Opsahl J., Atallah R., Hatleseth T.A., Moldekleiv R., Nokland M., Andreassen Ø., Nyborg B. How rethinking the drilling system, from the drillbit to the drillstring and the drilling fluid addressed a threatening casing wear and turned a difficult 6-in. section into a perfect 6-in. sidetrack. In *Abu Dhabi International Petroleum Exhibition and Conference, held in Abu Dhabi, UAE, 11 November 2019*, number SPE-197959-MS, 2019.

[104] Leine R., van de Wouw N. *Stability and Convergence of Mechanical Systems with Unilateral Constraints*, volume Volume 36 of *Lecture Notes in Applied and Computational Mechanics*. Springer-Verlag, Berlin, 2008.

[105] Leine R.I., van Campen D.H., Keultjes W.J.G. Stick-slip whirl interaction in drillstring dynamics. *Journal of Vibration and Acoustics*, 124(2):209–220, April 2002.

[106] X. Liu, N. Vlajic, X. Long, G. Meng, and B. Balachandran. Nonlinear motions of a flexible rotor with a drill bit: stick-slip and delay effects. *Nonlinear Dynamics*, 72:61–77, April 2013.

[107] Liu X., Vlajic N., Long X., Meng G., Balachandran B. Coupled axial-torsional dynamics in rotary drilling with state-dependent delay: stability and control. *Nonlinear Dynamics*, 78(3):1891–1906, 2014.

[108] Liu X., Vlajic N., Long X., Meng G., Balachandran B. State-dependent delay influenced drill-string oscillations and stability analysis. *ASME Journal of Vibration and Acoustics*, 136(5):051008–1 – 051008–9, October 2014.

[109] Lobo D.M., Ritto T.G., Castello D.A. Stochastic analysis of torsional drill-string vibrations considering the passage from a soft to a harder rock layer. *Journal of the Brazilian Society of Mechanical Sciences and Engineering*, 39:2341–2349, June 2017.

[110] Ma J., Li L., Wang H., Du Y., Ma J., Zhang X., Wang Z. Carbon Capture and Storage: History and the Road Ahead. *Engineering*, 14:33–43, 2022.

[111] J. Marck. *A nonlinear dynamical model of borehole spiraling.* phdthesis, University of Minnesota, December 2015.

[112] G. Mensa-Wilmot, Y. Harjadi, S. Langdon, and J. Gagneaux. Drilling Efficiency and Rate of Penetration - Definitions, Influencing Factors, Relationships and Value. In *SPE/IADC Drilling Conference and Exhibition, New Orleans, Louisiana, USA*, number SPE-128288-MS, February 2010.

[113] Mensa-Wilmot G., Fear M.J. The effects of formation hardness, abrasiveness, heterogeneity and hole size on PDC bit performance. In *2001 SPE/IADC Drilling Conference, 27 February - 1 March 2001, Amsterdam, Netherlands*, number *SPE/IADC-67698*, 2001.

[114] Mihajlović N., van de Wouw N., Hendriks M.P.M., Nijmeijer H. Friction induced limit cycling in flexible rotor systems: An experimental drill-string set-up. *Nonlinear Dynamics*, 46:273–291, 2006.

[115] Mihajlović N., van de Wouw N., Rosielle P.C.J.N., Nijmeijer H. Interaction between torsional and lateral vibrations in flexible rotor systems with discontinuous friction. *Nonlinear Dynamics*, 50:679–699, January 2007.

[116] Mihajlović N., van Veggel A.A., van de Wouw N., Nijmeijer H. Analysis of friction-induced limit cycling in an experimental drill-string system. *Journal of Dynamic Systems, Measurement, and Control*, 126(4):709–720, 03 2005.

[117] S. Mokhatab and W. A. Poe. *Chapter 14 - Process Control Fundamentals.* Gulf Professional Publishing, Boston, second edition edition, 2012.

[118] K. Nandakumar, Marian Wiercigroch, and Chris Pearson. Bit-bounce and stick-slip in drill-string dynamics. In Marian Wiercigroch and Giuseppe Rega, editors, *IUTAM Symposium on Nonlinear Dynamics for Advanced Technologies and Engineering Design*, pages 323–335, Dordrecht, 2013. Springer Netherlands.

[119] Nandakumar K., Wiercigroch M. Galerkin projections for state dependent delay differential equations with applications to drilling. *Applied Mathematical Modelling*, 37(4):1705–1722, 2013.

[120] Nandakumar K., Wiercigroch M. Stability analysis of a state dependent delayed, coupled two DOF model of drill-string vibration. *Journal of Sound and Vibration*, 332(10):2575–2592, 2013.

[121] A. Nascimento, D. Tamas Kutas, A. Elmgerbi, G. Thonhauser, and M. Hugo Mathias. Mathematical modeling applied to drilling engineering: An application of bourgoyne and young rop model to a presalt case study. *Mathematical Problems in Engineering*, 2015(1):631290, 2015.

[122] Navarro-López E.M. An alternative characterization of bit-sticking phenomena in a multi-degree-of-freedom controlled drillstring. *Nonlinear Analysis: Real World Applications*, 10(5):3162–3174, 2009.

[123] Navarro-López E.M., Cortés D. Avoiding harmful oscillations in a drillstring through dynamical analysis. *Journal of Sound and Vibration*, 307(1):152–171, 2007.

[124] Navarro-López E.M., Cortés D. Sliding-mode control of a multi-DOF oilwell drillstring with stick-slip oscillations. In *2007 American Control Conference*, pages 3837–3842, 2007.

[125] Navarro-López E.M., Licéaga-Castro E. Non-desired transitions and sliding-mode control of a multi-DOF mechanical system with stick-slip oscillations. *Chaos, Solitons & Fractals*, 41(4):2035–2044, 2009.

[126] Navarro-López E.M., Suarez R. Practical approach to modelling and controlling stick-slip oscillations in oilwell drillstrings. In *Proceedings of the 2004 IEEE International Conference on Control Applications, 2004.*, volume 2, pages 1454–1460, 2004.

[127] Nishimatsu Y. Theories of rock cutting. *J. A. Hudson, editor, Comprehensive Rock Engineering: Principles, Practice, and Project, chapter 26*, 1:647 – 662, 1993.

[128] P. M. Nüsse, A. Ambrus, and O. M. Aamo. Decentralized active control of distributed damping subs for stick-slip reduction in drilling. In *SPE/IADC Drilling Conference and Exhibition, Galveston, Texas, USA*, number SPE-217676-MS, 03 2024.

[129] P. M. Nüsse, A. Ambrus, U. J. F. Aarsnes, and O. M. Aamo. Evaluation of distributed damping subs with active control for stick-slip reduction in drilling. *Geoenergy Science and Engineering*, 231:212255, 2023.

[130] Orr Jr. F.M. Carbon capture, utilization, and storage: an update. *SPE Journal*, 23(06):2444–2455, 2018.

[131] Osguei A. T., Khamoushi I., Dehkordi M. K., Pavlovskaia E., Wiercigroch M. Non-smooth dynamics of anti stick-slip tool. *Physica D: Nonlinear Phenomena*, 443:133525, 2023.

[132] Palmov V.A., Brommundt E., Belyaev A.K. Stability analysis of drillstring rotation. *Dynamics and Stability of Systems*, 10(2):99–110, 1995.

[133] Pambudi N.A. Geothermal power generation in Indonesia, a country within the ring of fire: Current status, future development and policy. *Renewable and Sustainable Energy Reviews*, 81:2893–2901, 2018.

[134] Pastusek P., Sanderson D., Minkevicius A., Blakeman Z., Bailey J. Drilling interbedded and hard formations with PDC bits considering structural integrity limits. In *IADC/SPE Drilling Conference and Exhibition, 6 - 8 March 2018, Fort Worth, Texas, U.S.A.*, number SPE-189608-MS, 2018.

[135] Paulus S.L., Shen H., Beeh H.A. Becoming an HPHT World Class Project, the Valemon experience 2012-2017. In *SPE/IADC International Drilling Conference and Exhibition, Stavanger, Norway*, number IADC/SPE-212448-MS, March 2023.

[136] Pavone D.R., Desplans J.P. Application of high sampling rate downhole measurements for analysis and cure of stick-slip in drilling. In *SPE Annual Technical Conference and Exhibition in New Orleans, LA, USA*, number SPE-28324-MS, September 1994.

[137] Perneder L., Detournay E., Downton G. Bit-rock interface laws in directional drilling. *International Journal of Rock Mechanics and Mining Sciences*, 51:81–90, 2012.

[138] Purba D., Adityatama D.W., Agustino V., Fininda F., Alamsyah D., Muhammad F. Geothermal drilling cost optimization in Indonesia: a discussion of various factors. In 45th *Workshop on Geothermal Reservoir Engineering*, number SGP-TR-216, Stanford, California, USA, February 2020. Stanford University.

[139] Rahman M.M., Velayutham E. Renewable and non-renewable energy consumption-economic growth nexus: New evidence from South Asia. *Renewable Energy*, 147:399–408, 2020.

[140] N. Reimers. Antistall tool reduces risk in drilling difficult formations. *Journal of Petroleum Technology*, 64(1):26–29, 2012.

[141] N. Reimers. Mitigation of torsional vibrations and stick-slip induced by aggressive, energy efficient drill-bits. *Third International Colloquium on Nonlinear Dynamics and Control of Deep Drilling Systems, Minneapolis, Minnesota, U.S.A.*, pages 9–14, 2014.

[142] Richard T., Dagrain F., Poyol E., Detournay E. Rock strength determination from scratch tests. *Engineering Geology*, 147-148:91–100, 2012.

[143] Richard T., Detournay E. Stick-slip vibrations of PDC bits. In *4th North America Rock Mechanics Symposium in Seattle, Washington, USA*, number ARMA-2000-0033, July 2000.

[144] Richard T., Detournay E., Drescher A., Nicodeme P., Fourmaintraux D. The scratch test as a means to measure strength of sedimentary rocks. In *SPE/ISRM Rock Mechanics in Petroleum Engineering, Trondheim, Norway*, number SPE-47196-MS, July 1998.

[145] Richard T., Detournay E., Fear M., Miller B., Clayton R.., Matthews O. Influence of bit-rock interaction on stick-slip vibrations of PDC bits. In *SPE Annual Technical Conference and Exhibition in San Antonio, Texas, USA*, number SPE-77616-MS, September 2002.

[146] Richard T., Germay C., Detournay E. Self-excited stick-slip oscillations of drill bits. *Comptes Rendus Mécanique*, 332(8):619–626, 2004.

[147] Richard T., Germay C., Detournay E. A simplified model to explore the root cause of stick-slip vibrations in drilling systems with drag bits. *Journal of Sound and Vibration*, 305:432–456, 2007.

[148] Ritto T.G., Aguiar R.R., Hbaieb S. Validation of a drill string dynamical model and torsional stability. *Meccanica*, 52:2959–2967, September 2017.

[149] Ritto T.G., Ghandchi-Tehrani M. Active control of stick-slip torsional vibrations in drill-strings. *Journal of Vibration and Control*, 25(1):194–202, 2019.

[150] Runia D.J., Dwars S., Stulemeijer I.P.J.M. A brief history of the Shell Soft Torque Rotary System and some recent case studies. In *SPE/IADC Drilling Conference and Exhibition in Amsterdam, Netherlands*, number SPE-163548-MS, March 2013.

[151] Saldivar B., Boussaada I., Mounier H., Mondié S., Niculescu S.-I. An overview on the modeling of oilwell drilling vibrations. *IFAC Proceedings Volumes*, 47(3):5169–5174, 2014. 19th IFAC World Congress.

[152] Saldivar B., Mondié S., Loiseau J.-J., Rasvan V. Stick-slip oscillations in oillwell drilstrings: Distributed parameter and neutral type retarded model approaches. *IFAC Proceedings Volumes*, 44(1):284–289, 2011. 18th IFAC World Congress.

[153] Saldivar B., Mondié S., Loiseau J.-J., Rasvan V. Suppressing axial-torsional coupled vibrations in drillstrings. *Journal of Control Engineering and Applied Informatics*, 15:3–10, 2013.

[154] Saldivar B., Mondié S., Niculescu S.-I., Mounier H., Boussaada I. A control oriented guided tour in oilwell drilling vibration modeling. *Annual Reviews in Control*, 42:100–113, 2016.

[155] Saldivar B., Mondié S., Vilchis J.C.A. The control of drilling vibrations: A coupled PDE-ODE modeling approach. *International Journal of Applied Mathematics and Computer Science*, 26(2):335–349, June 2016.

[156] Saldivar Márquez M.B., Boussaada I., Mounier H., Niculescu S.-I. *Analysis and control of oilwell drilling vibrations: A time-delay systems approach.* Advances in Industrial Control. Springer Cham, 1 edition, March 2015.

[157] Sampaio R., Piovan M.T., Lozano G.V. Coupled axial/torsional vibrations of drill-strings by means of non-linear model. *Mechanics Research Communications*, 34(5):497–502, September 2007.

[158] Selnes K.S., Clemmensen C., Reimers N. Drilling difficult formations efficiently with the use of an antistall tool. *Society of Petroleum Engineers (SPE) Drilling and Completion*, 24(SPE-111874-PA):531–536, December 2009.

[159] Serrarens A.F.A., van de Molengraft M.J.G., Kok J.J., van den Steen L. H_∞ control for suppressing stick-slip in oil well drillstrings. *IEEE Control Systems Magazine*, 18(2):19–30, 1998.

[160] M. C. Sheppard, C. Wick, and T. Burgess. Designing Well Paths to Reduce Drag and Torque. *SPE Drilling Engineering*, 2(04):344–350, 12 1987.

[161] Sinsel S.R., Riemke R.L., Hoffmann V.H. Challenges and solution technologies for the integration of variable renewable energy sources - a review. *Renewable Energy*, 145:2271–2285, 2020.

[162] Smith Bits - A Schlumberger Company. Product catalog, 2018.

[163] Stépán G. Delay-differential equation models for machine tool chatter. *Dynamics and Chaos in Manufacturing Processes, Ed.: F. C. Moon, John Wiley & Sons, New York*, pages 165–192, 1998.

[164] C. Studer, R. I. Leine, and Ch. Glocker. Step size adjustment and extrapolation for time-stepping schemes in non-smooth dynamics. *International Journal for Numerical Methods in Engineering*, 76(11):1747–1781, 2008.

[165] Studer C. *Numerics of Unilateral Contacts and Friction: Modeling and Numerical Time Integration in Non-Smooth Dynamics*, volume Volume 47 of *Lecture Notes in Applied and Computational Mechanics.* Springer-Verlag, Berlin, 2009.

[166] Tashakori S., Vossoughi G., Zohoor H., van de Wouw N. Prediction-based control for mitigation of axial-torsional vibrations in a distributed drill-string system. *IEEE Transactions on Control Systems Technology*, 30(1):277–293, 2022.

[167] Tashakori S., Vossoughi G., Zohoor H., Yazdi E.A. Modification of the infinite-dimensional neutral-type time-delay dynamic model for the coupled axial-torsional vibrations in drill strings with a drag bit. *Journal of Computational and Nonlinear Dynamics*, 15(8):081006, 06 2020.

[168] Tian K. *Influence of bit design on the stability of the rotary drilling system.* PhD Thesis, University of Minnesota, Department of Civil, Environmental and Geo-Engineering, June 2020.

[169] Tian K., Detournay E. Influence of PDC bit cutter layout on stick-slip vibrations of deep drilling systems. *Journal of Petroleum Science and Engineering*, 206:109005, November 2021.

[170] Tian K., Detournay E., Zhang H. An alternative formulation for modeling self-excited vibrations of drillstring with polycrystalline diamond compact bits. *Journal of Computational and Nonlinear Dynamics*, 17(5):051002–1 – 051002–8, May 2022.

[171] Tian K., Ganesh R., Detournay E. Influence of bit design on the stability of a rotary drilling system. *Nonlinear Dynamics*, 100:51–75, March 2020.

[172] Tlusty J., Polacek M. The stability of the machine tool against self-excited vibration in machining. *International research in production engineering, American Society of Mechanical Engineers, New York*, pages 465–474, 1963.

[173] Tomax AS. Products - Tomax AS. `https://tomax.no/products/`, July 2023. Accessed 13-Jul-2023.

[174] Tucker W.R., Wang C. An integrated model for drill-string dynamics. *Journal of Sound and Vibration*, 224(1):123–165, July 1999.

[175] Tucker W.R., Wang C. Torsional vibration control and cosserat dynamics of a drill-rig assembly. *Meccanica*, 38:145–161, January 2003.

[176] U.S. Energy Information Administration and U.S. Geological Survey. The geology of natural gas resources. `https://www.eia.gov/todayinenergy/detail.php?id=110#`, July 2023. Accessed 13 July 2023.

[177] van de Wouw N., Nijmeijer H., Vromen T.G.M., van Helmond M.J.M., Astrid P., Doris A. Experimental validation of torsional controllers for drilling systems. In *Advanced Topics in Nonsmooth Dynamics (Transactions of the European Network for Nonsmooth Dynamics)*. Springer, Cham, 2018.

[178] Viguié R., Kerschen G. Using passive nonlinear targeted energy transfer to stabilize drillstring systems. In *International Colloquium on Non-Linear Dynamics of Deep Drill-String Systems, Liège, 2009*, Liège, Belgium, 2009.

[179] Viguié R., Kerschen G., Golinval J.-C., McFarland D.M., Bergman L.A., Vakakis A.F., van de Wouw N. Using passive nonlinear targeted energy transfer to stabilize drill-string systems. *Mechanical Systems and Signal Processing*, 23(1):148–169, 2009. Special Issue: Non-linear Structural Dynamics.

[180] Viguié R., Kerschen G., Ruzzene M. Exploration of nonlinear shunting strategies as effective vibration absorbers. In *Active and Passive Smart Structures and Integrated Systems 2009*, volume 7288, pages 812–821. SPIE, 2009.

[181] Vromen T., Detournay E., Nijmeijer H., van de Wouw N. Dynamics of drilling systems with an antistall tool: effect on rate of penetration and mechanical specific energy. *SPE Journal*, 24(5):1982–1996, 2019.

[182] Vromen T.G.M. *Control of stick-slip vibrations in drilling systems.* PhD Thesis, Eindhoven University of Technology, Department of Mechanical Engineering, 2015.

[183] Vromen T.G.M., Dai C.H., van de Wouw N., Oomen T.A.E., Astrid P., Doris A., Nijmeijer H. Mitigation of torsional vibrations in drilling systems: a robust control approach. *IEEE Transactions on Control Systems Technology*, 27(1):249–265, January 2019.

[184] Wahi P., Chatterjee A. Self-interrupted regenerative metal cutting in turning. *International Journal of Non-Linear Mechanics*, 43(2):111–123, 2008.

[185] J. Wei, W. Liu, and D. Gao. Modeling of pdc bit-rock interaction behaviors based on the analysis of dynamic rock-cutting process. *Geoenergy Science and Engineering*, 239:212955, 2024.

[186] R. Wildemans. Modeling and dynamic analysis of an anti-stall tool in a drilling system including spatial friction. mathesis, Master of Science Thesis, DC 2018.099, Eindhoven University of Technology, Department of Mechanical Engineering, 2018.

[187] Wildemans R., Aribowo A.G., Detournay E., van de Wouw N. Modelling and dynamic analysis of an anti-stall tool in a drilling system including spatial friction. *Nonlinear Dynamics*, 98(4):2631–2650, 2019.

[188] Yigit A.S., Christoforou A.P. Coupled torsional and bending vibrations of actively controlled drillstrings. *Journal of Sound and Vibration*, 234(1):67–83, 2000.

[189] Yigit A.S., Christoforou A.P. Stick-slip and bit-bounce interaction in oil-well drillstrings. *Journal of Energy Resources Technology*, 128(4):268–274, December 2006.

[190] Zamudio C.A., Tlusty J.L., Dareing D.W. Self-excited vibrations in drillstrings. In *62nd Annual Technical Conference and Exhibition of SPE*, pages 117–124, 1987.

[191] Y. Zhang, H. Zhang, D. Chen, P. Ashok, and E. van Oort. Comprehensive review of high frequency torsional oscillations (hftos) while drilling. *Journal of Petroleum Science and Engineering*, 220:111161, 2023.

[192] Zhang H., Detournay E. A high-dimensional model to study the self-excited oscillations of rotary drilling systems. *Communications in Nonlinear Science and Numerical Simulation*, 112:106549, 2022.

[193] Zhang Z., Pan S.Y., Li H., Cai J., Olabi A.G., Anthony E.J., Manovic V. Recent advances in carbon dioxide utilization. *Renewable and Sustainable Energy Reviews*, 125:109799, 2020.

[194] Zhou Y., Detournay E. Analysis of the contact forces on a blunt pdc bit. In *48th US Rock Mechanics / Geomechanics Symposium 2014*, volume 1, pages 306–314. American Rock Mechanics Association (ARMA), 2014.

Curriculum vitae

Arviandy Aribowo (born in 1985 in Madiun, East Java, the Republic of Indonesia) obtained his B.Sc. degree in Engineering Physics from the Bandung Institute of Technology (ITB), Bandung, Indonesia, in 2007. He also received his M.Sc. degree in Aerospace Engineering from the University of Houston, Texas, USA, in 2015, under the support of the Fulbright Scholarship Program (from the IIE, US Department of State). From 2010 to 2016, he worked in the area of instrumentation and automation systems for offshore processing facilities of oil-gas exploration and production companies (ConocoPhillips, MedcoEnergi), located in the Natuna Sea, Indonesia. From 2008 to 2010, he worked at universities located in Indonesia and Singapore as a research assistant/engineer.

In 2017, with the support of the Indonesia Endowment Fund for Education (LPDP) program of the Republic of Indonesia and the Norwegian company Tomax AS, he started on his PhD research at the Dynamics and Control group within the Department of Mechanical Engineering at the Eindhoven University of Technology (TU/e), Eindhoven, The Netherlands. His PhD research work is under the supervision of Nathan van de Wouw (TU/e) and Emmanuel Detournay (University of Minnesota, USA), of which the results are presented in this dissertation.